A Gas-Phase Approach to Biomolecular Structure:

Combining Ion Mobility-Mass Spectrometry with Spectroscopy

Inaugural-Dissertation
to obtain the academic degree
Doctor rerum naturalium (Dr. rer. nat.)

Submitted to the Department of
Biology, Chemistry and Pharmacy
of Freie Universität Berlin

by

Stephan Warnke

from Kassel, Germany

October 2015

Fritz-Haber-Institut
der Max-Planck-Gesellschaft

Freie Universität Berlin

The work reported in this thesis was performed from October 2010 to October 2015, at the Fritz Haber Institute of the Max Planck Society in Berlin, under the supervision of Dr. Gert von Helden and Prof. Dr. Kevin Pagel.

1st reviewer: Prof. Dr. Kevin Pagel, Freie Universität Berlin

2nd reviewer: Prof. Dr. Gerard J. M. Meijer, Radboud Universiteit Nijmegen

Date of defence: 02.12.2015

Eidesstattliche Erklärung

Hiermit erkläre ich an Eides statt, dass ich die vorliegende Dissertation selbstständig verfasst und keine anderen als die angegebenen Hilfsmittel genutzt habe. Alle wr̈tlich oder inhaltlich übernommenen Stellen habe ich als solche gekennzeichnet.

Ich versichere außerdem, dass ich die vorliegende Dissertation nur in diesem und keinem anderen Promotionsverfahren eingereicht habe und, dass diesem Promotionsverfahren keine endgültig gescheiterten Promotionsverfahren vorausgegangen sind.

Berlin, 28.10.2015

Kurzfassung

Die Struktur und Funktion von Biomolekülen sind eng miteinander verbunden. Um biochemische Prozesse in lebenden Organismen auf molekularer Ebene zu verstehen, ist daher die Kenntnis von strukturellen Details der beteiligten Moleküle von großer Bedeutung. Proteine sind molekulare Maschinen, die lebenswichtige Aufgaben im Organismus erfüllen, und sind als solche eines der wichtigsten Forschungsobjekte in den Lebenswissenschaften. Für Strukturuntersuchungen von Proteinen bieten Gasphasenmethoden vielversprechende Ansätze. Im Gegensatz zu Methoden die auf Untersuchungen in der Flüssig- oder Festphase basieren, bietet die Gasphase eine einzigartige *Reinraumumgebung*, die es erlaubt den Analyten isoliert, und frei von Umgebungseinflüssen zu untersuchen. Ein zentraler Bestandteil der vorliegenden Dissertation ist die Beschreibung, die Charakterisierung und Etablierung eines neuen Versuchsaufbaus in dem verschiedene struktursensible Gasphasenmethoden vereint sind. Durch diesen soll eine detaillierte Untersuchung von Strukturen biologisch relevanter Moleküle ermöglicht werden.

Die Ionenmobilitäts-Massenspektrometrie (IM-MS) erlaubt sowohl die Trennung als auch die Bestimmung der Größe von Molekülionen mit gleichem Masse-zu-Ladungs Verhältnis (m/z), und unterschiedlicher Form. In der vorliegenden Arbeit wird sie zunächst verwendet um den Einfluss der Ladungen eines Proteinions auf dessen Faltung in der Gasphase zu untersuchen. Die Studie zeigt, dass intramolekulare Ladungssolvatation eine wichtige Rolle bei der (Um)Faltung von Proteinen in der Gasphase spielt. Darüber hinaus wird gezeigt wie selektive Mikrosolvatisierung von geladenen Gruppen dazu beitragen kann die Umfaltung potentiell nativer Strukturelemente nach dem Transfer des Proteins in die Gasphase zu verhindern.

IM-MS ist jedoch nur empfindlich auf die äußere Form eines Molekülions. Die Photodissoziation von Proteinionen mittels Photonen im ultravioletten (UV) Wellenlängenbereich hingegen, ist potentiell empfindlich auf Details von Proteinstrukturen. Sie ist ein vielversprechendes Werkzeug zur Sequenzierung von Proteinen, da die Dissoziation des Proteinrückgrates statistisch über die gesamte Proteinsequenz erfolgt. In dem hier beschriebenen neuen Versuchsaufbau wird diese Methode mit IM-MS kombiniert um deren Empfindlichkeit auf höhere Proteinstrukturelemente zu untersuchen. Die präsentierte Studie zeigt, dass UV (193 nm) Photodissoziation strukturelle Ähnlichkeiten zwischen Gruppen verschiedener Proteinkonformere auflösen kann. Des Weiteren wird durch den Vergleich mit theoretischen Modellstrukturen deutlich, dass die hier beobachteten Strukturunterschiede auf die *cis/trans* Isomerisierung einer einzigen Peptidbindung zurückzuführen sind.

Eine Methode, die sehr direkte Information über Molekülstruktur liefern kann, ist die Infrarot-(IR) Spektroskopie. Absorptionsbanden in einem experimentellen Infrarot-Molekülspektrum sind höchst indikativ für bestimmte Vibrationen innerhalb eines Moleküls. Diese wiederum sind stark von der lokalen Struktur der jeweiligen Oszillatoren abhängig. Eine große Anzahl experimenteller und theoretischer Studien haben die Methode auch für die Untersuchung von Gasphasenmolekülen etabliert. Die Kombination von IR-Spektroskopie mit IM-MS zur spektroskopischen Untersuchung von größen- und m/z-selektierten Molekülionen ist einer der Schwerpunkte dieser Dissertation. Es wird zunächst gezeigt, dass die kombinierten Methoden, in Verbindung mit quantenchemischen Rechnungen, eindeutige Indizien für zwei verschiedene Protomere des relativ kleinen Moleküls Benzocain liefern kann. Die Rechnungen zeigen zudem, dass die dielektrischen Eigenschaften der direkten Molekülumgebung großen Einfluss auf die Stabilität bestimmter Strukturen haben können.

Dass der kombinierte Gasphasenansatz auch auf größere Moleküle und Molekülaggregate anwendbar ist, wird im letzten Kapitel dieser Arbeit gezeigt. Hier werden die Strukturen von frühen Oligomeren kurzer, amyloidogener Peptidsequenzen untersucht. Solche amyloidogene Peptide und Proteine spielen eine zentrale Rolle in einer Vielzahl neurodegenerativer Krankheiten wie Alzheimer oder Parkinson. Im Krankheitsfall gehen die involvierten Proteine spontan von einer löslichen, teilweise gefalteten Form zu unlöslichen Fibrillen über, die reich an β-Faltblatt-Sekundärstrukturelementen sind. Größen- und m/z-selektive IR-Spektroskopie bietet hier erste Anhaltspunkte, dass schon frühe Oligomere mit nur vier oder fünf Peptid-Untereinheiten einen erheblichen Anteil an β-Faltblättern besitzen können. Diese Studie stellt die erste direkte Messung von Sekundärstruktur von isolierten Amyloid-Intermediaten dar, und eröffnet somit neue Wege auf dem Feld der Amyloidforschung.

Abstract

The structure and function of a biological molecule is closely connected. Consequently, a detailed knowledge about molecular structure is essential to understand the biochemical processes inside of living organisms. Proteins are the molecular machines that carry out vital tasks and are, as such, an important target of research in life sciences. For the investigation of protein structures, gas-phase methods are on the rise. In contrast to the condensed phase, the gas phase offers a unique *clean room* environment that allows the investigation of isolated species, free from external influences. A central component of the present thesis is the development, characterization, and establishment of a new experimental setup that combines structure-sensitive gas-phase methods to facilitate in-depth structural investigations on protein ions and other biologically relevant molecules.

Ion mobility-mass spectrometry (IM-MS) is a method to separate and measure the overall sizes of molecular ions of identical mass-to-charge (m/z) ratios but different shape. Here, it is initially used to investigate the influence of the charges on a protein ion onto its folding and refolding in the gas phase. It is found that intramolecular charge solvation plays a crucial role in the formation of gas-phase structures. Furthermore, it is shown how selective microsolvation of charged sites can help to prevent the structural reorganization after the transfer from solution into the gas phase.

IM-MS is, however, only sensitive to the overall shape of a molecular ion. The photodissociation of a protein ion using photons in the ultraviolet (UV) wavelength range, on the other hand, is potentially sensitive to structural details. The method recently emerged as a promising tool for protein sequencing applications because of its ability to yield statistically distributed bond cleavages over the entire amino acid sequence of a protein. In the newly fashioned instrument, it is combined with IM-MS to probe its potential for the study of higher order protein structure. The presented data suggests that UV (193 nm) photodissociation can highlight structural similarities between groups of different conformations of a single protein. With the aid of theoretical model structures, it is shown that the here observed similarities may be attributed to *cis/trans* isomerization of a single peptide bond.

A method that can provide more direct information about molecular structure is infrared (IR) spectroscopy. In the IR wavelength range, absorption bands in an experimentally obtained spectrum are highly indicative for specific molecular vibrations. These, in turn, strongly depend on the local structure around the respective oscillators. A large body of experimental and theoretical work established IR spectroscopic techniques for the study of gas-phase molecular ions. The combination of IR spectroscopy with IM-MS to allow the spectroscopic investigation of m/z and shape-selected molecular ions is the main objective of the here presented experimental setup. In an initial study, it is shown how the combined methods can, in conjunction with quantum chemical calculations, unambiguously identify two different protomeric forms of the relatively small molecule benzocaine. The calculations furthermore highlight how the dielectric properties of the molecule's environment can drastically influence the structural preferences.

The applicability of this gas-phase approach to larger molecules and molecular assemblies is illustrated in the last chapter of this thesis. Here, the structures of early oligomers of short, amyloidogenic peptide sequences were investigated. Amyloidogenic peptides and proteins play a crucial role in a variety of neurodegenerative disorders such as Alzheimer's and Parkinson's disease. In the disease case, the involved proteins undergo a spontaneous transition from a soluble, often partially folded form into insoluble, β-sheet rich amyloid fibrils. The m/z and shape selective IR spectroscopic data presented here suggests that already early oligomeric species with as little as four or five peptide subunits can contain a significant amount of β-sheet structure. This study represents the first direct secondary structure analysis of individual amyloid intermediates and opens new possibilities for the field of amyloid research.

Contents

1 Introduction

Life on earth is based on a rich and complex carbon chemistry. This biochemistry involves a gigantic number of molecules with sizes ranging from only a few up to hundreds of thousands of atoms. An important class of biomolecules are α-amino acids. They are composed of an amine (-NH_2) and a carboxylic acid (-COOH) functional group and a side chain (R), all connected *via* covalent bonds to a central carbon atom, C_α. With its four different substituents, the C_α atom represents an element of central chirality, which results in the existence of two enantiomeric forms of a given α-amino acid.[*] The two respective enantiomers are called L- and D-amino acids (Figure 1.1 (a, b)). For reasons that have yet to be discovered, life generally prefers L-amino acids over the D-form. The universal genetic code holds the information for 20 out of the 22 L-enantiomeric amino acids that constitute the building blocks of *proteins.* The amino group of an amino acid can bind to the carboxylic group of another one in a condensation reaction to form a peptide bond. In this manner, hundreds of amino acids can combine to long peptide chains (Figure 1.1 (c)) and the repeating N-C_α-C pattern is known as the protein backbone. Proteins and protein complexes are central to virtually all biochemical processes that take place in the cells of living organisms: They catalyze biochemical reactions, serve the transport of molecules and ions through the organism or cell membranes, are involved in signalling processes, and replicate DNA.

The sequence of amino acids in a protein (the *primary* structure) is the main determinant for how the peptidic backbone folds into a specific three-dimensional structure. This structure will finally determine the protein's activity. The protein folding process is a result of inter- and intramolecular interactions, *i.e.*, an interplay between the molecule and its surroundings as well as between functional groups within the molecule. It is based on ionic interactions, van der Waals forces, hydrogen bonding, and hydrophobic interactions. The resulting structural elements can be further categorized [1]. The local, three-dimensional arrangement of the peptidic backbone is described by the *secondary* structure of a protein and the three main secondary-structural elements are helices, so-called β-sheets, and turns, all of which are supported by hydrogen-bonding networks within the backbone. The three-dimensional arrangement of these secondary structure elements is referred to as the *tertiary* structure. Multiple proteins can arrange together to non-covalently bound multi-subunit complexes and the structure of these large assemblies is referred to as *quaternary* structure.

In order to selectively interact with a target molecule, a so-called *native* structure must be maintained by the protein, which, under physiological conditions, is the structure that is

---

[*] In the case of a chirality in *R*, four different diastereomers result.

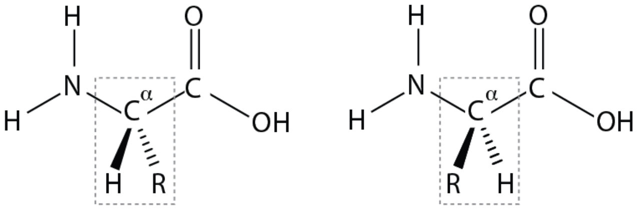

(a) L-amino acid

(b) D-amino acid

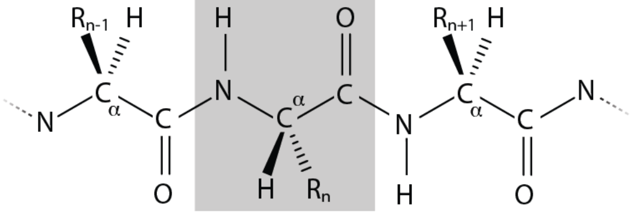

(c) Peptide chain

Figure 1.1: (a) and (b) show the L- and D-stereoisomer of an α-amino acid, respectively. The L-isomeric form is almost exclusively found to form the polypeptide chains (c) that occur in nature. For this, 22 different proteinogenic α-amino acid building blocks are available, which differ in their side chain (R).

most thermodynamically stable [2, 3]. In terms of energy, those structures can be represented as global minima in a free energy landscape (Figure 1.2 (a)). The form of such an energy landscape and the location of the minima are the result of the amino acid sequence but are also strongly influenced by interactions with surrounding molecules. The smooth, funnel-shaped surface helps the protein to efficiently fold into its favoured structure N, thereby solving the Levinthal paradox [4].

Protein misfolding – the adoption of a structure other than the native one – not only diminishes the functionality of the molecule but can, under certain circumstances, also seed the formation of large, insoluble protein assemblies known as amyloid fibrils. The accumulation of such fibrils inside the brain and other organs or tissues are a common hallmark in a variety of amyloidogenic disorders such as Alzheimer's or Parkinson's disease [3, 5–7].

Investigation of biomolecular structures is, therefore, the key to understanding biochemical processes and many methods have been applied to obtain structural information. Amongst techniques of optical microscopy, electron microscopy, and classical spectroscopic approaches (measurement of the absorption of light by the molecules), the methods nuclear magnetic resonance spectroscopy (NMR) and X-ray diffraction have proven particularly useful for structure elucidation of biological molecules. They both provide three-dimensional molecular structures and even though the latter technique requires the analyte to be implanted in an arguably non-physiological environment (a crystal), structures obtained from both X-ray diffraction and NMR are often comparable [9, 10]. All these methods, having their own advantages, face problems that are inherent to the condensed phase. They can only yield ensemble-averaged results, for example, when not a single but a mixture of different protonation states, conformations, aggregation states, or even impurities are present, which is often the case. Additionally, the influence of the surrounding molecules does not allow to study intrinsic molecular properties.

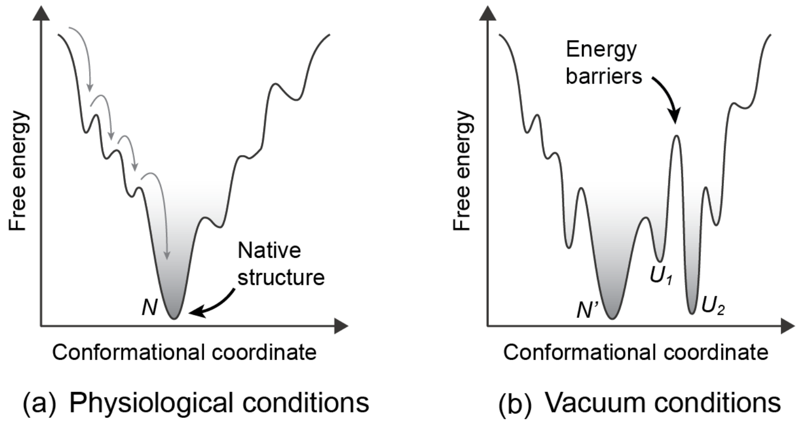

Figure 1.2: Schematic representation of free energy landscapes that govern protein folding under (a) physiological conditions and (b) vacuum conditions. The native, solution structure N will be altered in the absence of solvent interactions, leading to an *in vacuo* equivalent N'. Large energy barriers separate local energy minima that can lead to different coexisting structures (U_1, U_2, *etc.*) under vacuum conditions. Figure adapted from [8].

Mass spectrometry (MS) based methods seem to circumvent these limitations because they allow to isolate and further investigate one particular species in the presence of many others. This advantage resulted in today's success of MS in analytical applications to identify and characterize biomolecular ions [11]. The gas phase of a mass spectrometer provides an ideal *clean room* environment for the investigation of intramolecular interactions and the resulting molecular structures. However, whether or not those gas-phase structures represent the native, solution structure can be viewed with legitimate skepticism because molecule-solvent interactions are often found to support the native fold.

In an aqueous solution, the hydrophobic effect is responsible for hydrophobic residues to be buried inside the core of a protein. This effect is absent in the vacuum, allowing such residues to be exposed. Existing electrostatic interactions such as hydrogen bonds and salt bridges will be further strengthened in the absence of water molecules. On the other hand, repulsive Coulomb interactions come into play when charged sites are no longer solvated. Consequently, if an *in vacuo* equivalent to the native structure exists, it will be somewhat altered to account for the new conditions of the vacuum environment. Additionally, the absence of structure-stabilizing solvent molecules may result in free energy landscapes that have not one, but various local minima that are separated by large barriers (Figure 1.2 (b)) [12, 13]. The coexistence of multiple, stable structures that do not necessarily resemble the native fold may be the result. Despite these fundamental differences between solution and vacuum conditions, there is evidence for a retention of native structural elements even after transfer into the gas phase [13–18]. This will be exemplified in the following paragraphs.

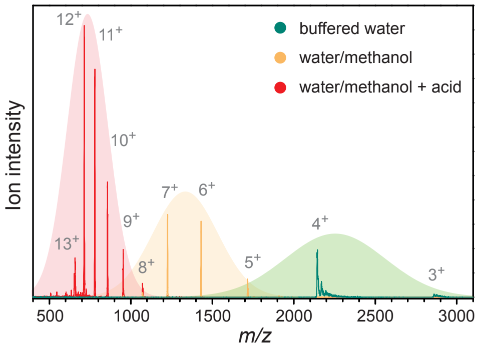

Figure 1.3: Mass spectra of the protein ubiquitin (8.5 kDa). The protein was ionized from different solvents (see colour code) using the standard ionization method electrospray ionization (ESI) and analyzed with the ion mobility-mass spectrometry instrument described later in this thesis.

When a protein is transferred from solution into the gas phase using the standard ionization method electrospray ionization (ESI) and analyzed in a mass spectrometer, a distribution of differently charged ionic species can typically be observed. This is exemplarily illustrated in Figure 1.3 for a protein that is not only ubiquitous in all eukaryotes but also throughout the literature, giving topic to nearly a quarter million publications. Hence, its name – *ubiquitin*. Here, the protein was observed from the 3^+ up to the 13^+ charge state, giving rise to the different mass-to-charge (m/z) ratios in the mass spectrum. The average charge that a protein carries into the mass spectrometer is typically found to depend on the conditions of the solution that the molecules were ionized from [19–21]. Buffered, aqueous solutions yield low charge states (green trace in Figure 1.3), whereas the amount of charges increases when denaturants such as methanol (yellow trace) and acids (red trace) are added to the solvent. In solution, a denaturation is often accompanied by an unfolding of the native structure. The question arises whether this behaviour is reflected in the structures that the differently charged protein ions adopt inside the mass spectrometer.

MS alone can only indirectly yield information about higher order structure such as the hydrogen bonding network and the folding of the molecule. To investigate such structural aspects, MS can be combined with, for example, ion mobility spectrometry (IMS) – a technique that allows to separate ions based on their overall shape and charge. Its operating principle is based on a difference in the drag force that two isobaric species of differing size experience when they drift through a buffer gas, which leads to a spatial separation. When combined with MS to an ion mobility-mass spectrometry (IM-MS) instrument, the size (or size-to-charge) distribution of ions with a particular m/z value can be investigated. Such a measurement is illustrated in Figure 1.4 for differently charged ubiquitin ions with a colour scale (green-yellow-red) indicating the relative size of the ions. Such measurements evidently show that for most species not a single structure is present but rather a distribution of structures with different sizes. Compact structures can be observed for species with lower amount of charges, whereas the proteins tend to unfold to extended structures when the total charge increases. This is often attributed to an increased Coulomb repulsion within the molecule [22]. IM-MS studies show that the most compact, globular conformations observed for ubiquitin ions with a total charge of $< 7^+$ are of similar size as the native fold of the protein, which can be found

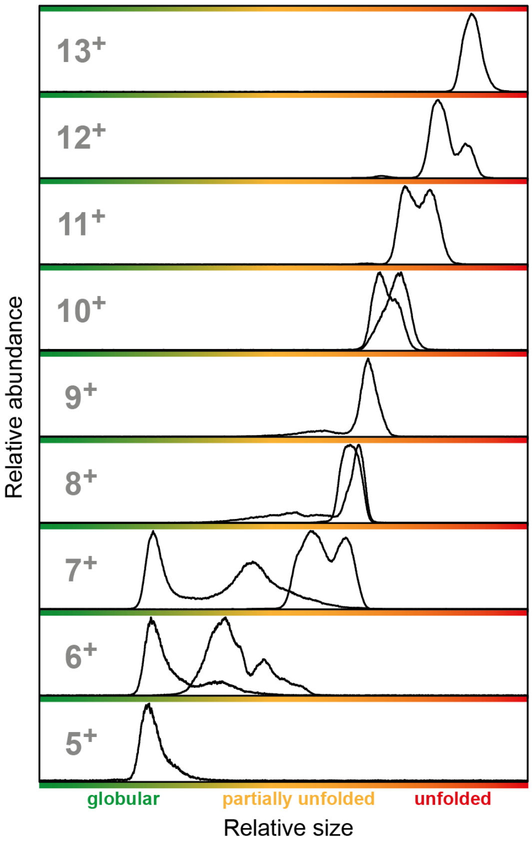

Figure 1.4: Size distributions of ionic ubiquitin gas-phase structures from ion mobility-mass spectrometry (IM-MS) measurements. Compact, globular structures are observed for lower charge states, whereas extended, unfolded structures occur when the total amount of charges within the molecule increases. Multiple data traces for one charge state were acquired for different experimental conditions with the IM-MS instrument described later in this thesis.

in aqueous solutions [19, 20]. Note, that those species that can be considered compact do not form from solutions with a high content of denaturants. Such a result represents one of many instances where IM-MS data suggest a correlation between solution structures and gas-phase structures, which is still topic of active research [21, 23–25]. It is therefore worthwhile to investigate peptide and protein gas-phase structures and the factors that contribute to their folding and unfolding in more detail.

IM-MS has proven to be a valuable tool for structure analysis of biological molecules. Its use, however, is not restricted to investigating single protein structures of different sizes. With the goal to provide information about the processes involved in amyloid diseases, the technique was recently applied to separate and measure the sizes of early peptide oligomers [26–28] some of which are known to form insoluble fibril structures at a later stage. Such fibrils are commonly observed in all amyloidogenic disorders [3, 5]. When analyzed in a mass spectrometer, the non-covalently bound peptide aggregates occur with different numbers of monomer subunits n and different amount of charges z, leading to complex mass spectra as illustrated in Figure 1.5 (a) for an amyloidogenic peptide sequence found in insulin (VEALYL, $m = 707$ Da). The signals can be readily assigned to singly charged monomers ($n/z = 1/1$), singly charged dimers

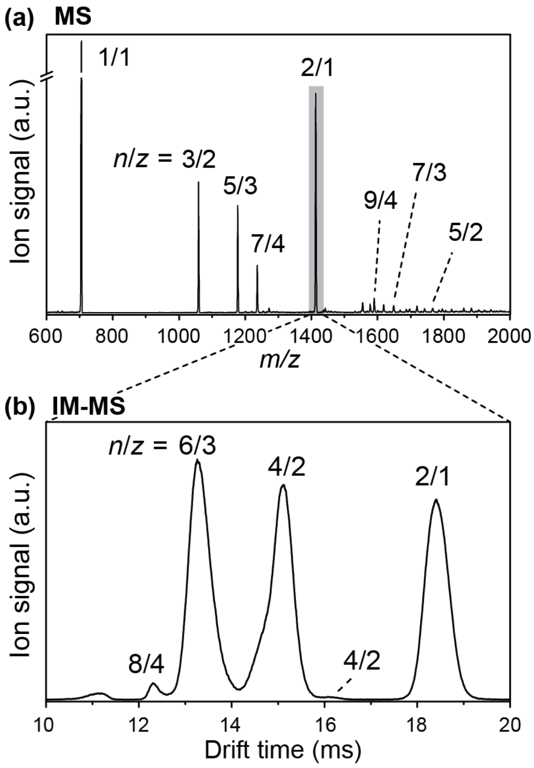

Figure 1.5: (a) Mass spectrum of an amyloidogenic peptide giving rise to extensive aggregation. Aggregation states (n/z) can be readily assigned. (b) Ion mobility data of the $n/z = 2/1$ signal. The coexistence of higher oligomers up to the quadruply charged octamer 8/4 is apparent. These species can only be separated using IM-MS methods. The data was acquired on the drift tube IM-MS instrument described later in this thesis.

(2/1), double charged trimers (3/2), and so on. However, every one of these signals may also be interpreted as an integer multiple of the respective n/z values, making an unambiguous assignment of oligomeric species impossible. Ion mobility spectrometry allows to separate these species with identical m/z values due to their differences in size and charge, as illustrated in Figure 1.5 (b) for ions that correspond to the $n/z = 2/1$ signal in the mass spectrum. Oligomers up to the quadruply charged octamer (8/4) are apparently hidden underneath a single mass peak. In order to benefit from the unique properties of gas-phase experiments in amyloid research, incorporation of ion mobility methods is, therefore, imperative.

The advantage of combined IM-MS methods over MS alone is evident as it can simultaneously provide information about molecular mass and overall shape. To gain a deeper insight into the structural details of the molecular ions inside an IM-MS instrument, however, other techniques need to be interlaced with these experiments. Methods to dissociate mass-selected molecular ions, for example, are routinely applied to probe molecular composition, *i.e.*, the primary structure in case of a protein [29], and can in some cases also yield structural information [25, 30–32]. Most promising, however, are methods that can directly probe molecular structure, such as infra red (IR) spectroscopy. IR absorption measurements are well-established for structure elucidation of molecules in the condensed phase [33, 34], but are difficult to perform on molecular ions in the gas phase. However, with powerful laser sources such as free electron lasers that provide tuneable IR light with high intensities becoming increasingly available to the scientific community, gas-phase IR spectroscopic approaches are on the rise [35–37]. Furthermore, advances in molecular modeling and quantum chemical calculations can help to interpret experimental results from model structures. Together, the here presented gas-phase approach opens new pathways for the investigation of (bio)molecular structures.

Outline of the Thesis

The application of ion mobility spectrometry as a preparative tool in conjunction with mass spectrometry, followed by further interrogation with other structure-sensitive methods is relatively new and its benefits and limits will be explored in the course of this thesis. For this purpose, a new experimental setup that allows to perform photodissociation experiments on size and m/z-selected molecular ions was designed and constructed. The applied methods that were used to separate, excite, and dissociate molecular ions in order to deduce structural information are briefly introduced in Sections 2.1–2.3 of Chapter 2. A detailed description and characterization of the newly fashioned IM-MS instrument, the underlying principles, and the experimental procedures are presented in Sections 2.4–2.6 of the same chapter. Chapter 2 closes with the brief description of a second, commercially available IM-MS instrument that was used continuously throughout this work for IMS and dissociation studies.

As mentioned above, it is still not fully understood in how far the native, solution structure of a protein is represented by the structure that is found in the gas phase of a mass spectrometer. In order to probe to what extent the charges inside a gas-phase molecule influence its structure, the charged sites of two different proteins were selectively solvated and the resulting complexes were investigated using IM-MS methods. The results are presented in Chapter 3 and reveal how interaction of the charged sites with the molecule's peptidic backbone can substantially alter its structure.

The dissociation of a protein upon absorption of UV photons at 193 nm wavelength is potentially structure-sensitive because it is believed that the energy that is imposed onto the molecule by the energetic UV photon does not dissipate through the molecule but leads to cleavage of peptide bonds around the site of photon absorption. In Chapter 4, the potential of UV photodissociation to obtain information about protein structure is investigated. To do so, IMS-separated species of different charge states of ubiquitin are irradiated with UV light and the conformation-dependency of the resulting photofragment spectra is examined. The presented studies represent the first of its kind and show that UV photodissociation can, under certain circumstances, help to reveal structural details and identify similarities between different protein conformations.

IR spectroscopic methods for the investigation of molecular gas-phase structures are of particular interest since they were shown to provide direct structural information not only for small molecules, but also on a protein level [35–37]. To combine IM-MS with its ability to select overall shapes of molecular ions together with IR spectroscopy to probe the structure of the selected species in more detail seems to be the logical consequence. This approach is exercised in Chapter 5 and represents, together with similar approaches [38, 39], one of the first. Its success in unambiguously identifying two structural isomers of the small molecule benzocaine – not a protein but a molecule that interacts with the same – may in the future trigger many similar studies.

One of them follows in Chapter 6 and effectively shows that condensed-phase structural elements like β-sheets of small peptide aggregates can be successfully transferred into the gas phase. They are identified using IM-MS and further investigated with IR spectroscopy to probe structure-characteristic molecular vibrations. The study on amyloid fibril formation presented here, however, does not only represent a proof of principle. It shows how already early oligomeric species of a small amyloidogenic peptide, with as few as four or five monomer subunits, can already contain significant amount of β-sheet structure – the main structural motif of a mature fibril. This study opens new doors for amyloid research and may ultimately help to understand the molecular basis of neurodegenerative diseases.

2 Experimental Methods

The following chapter gives a general overview of the different experimental methods and instruments that have been utilized, individually or in combination, to probe various aspects of molecular structure.

The three-dimensional structure of peptides and proteins or, more generally, the overall size of a molecule or molecular complex can be investigated with ion-mobility spectrometry (IMS, Section 2.1). This technique is today, in combination with mass spectrometry (MS), emerging as an analytical tool in scientific as well as for routine, industrial laboratory applications. In the present work it is used to obtain indirect information about intramolecular protein interactions (Chapter 3) or to preselect molecular ions of a specific size (mobility) followed by further investigations. These are based on the dissociation of the molecules upon energy deposition through energetic collisions with neutrals (collision-induced dissociation, CID) or *via* the absorption of photons in the ultraviolet (UV) or infrared (IR) wavelength range. These methods are briefly discussed in Section 2.2. The frequencies of molecular vibrations, on the other hand, can be highly sensitive to the molecule's structure and are here investigated with IR vibrational spectroscopy, which is introduced in Section 2.3.

A new experimental setup, which incorporates methods of IMS, MS, as well as UV photodissociation and IR spectroscopy, was designed* and constructed in the course of this thesis and is, together with the experimental procedures and the necessary light sources, in detail described and characterized in Section 2.4 of this chapter. The chapter closes with a brief description of a second ion mobility-mass spectrometry instrument, the commercial Synapt G2-S.

2.1 Ion-Mobility Spectrometry

Over the past 25 years ion-mobility spectrometry (IMS) has developed into a mature analytical method [41–44] and is today applied individually or in combination with mass spectrometry (MS) or other techniques in a myriad of ways. In industry IMS is often used in quality control and security applications [45]. On the other hand, the medical interest in the technique steadily grows because of, *e.g.*, its sensitivity to volatile organic compounds in exhaled breath that emerge from cancerous cells [46], or other disease screening approaches [47, 48].

---

*Design based, in part, on a instrument design from the group of Mike Bowers, UCSB [40]

However, military and law enforcement applications for the search of warfare agents, explosives, and narcotics [49, 50] were one of the main driving forces in the development of new IMS instrumentation already in the 1950s and 60s. Today, IMS instruments are an integral part of screening procedures in security-sensitive areas [51]. Comprehensive retrospectives of IMS history and applications can be found throughout the literature, *e.g.*, in recent review articles and the references therein [42–44, 52, 53].

The combination of IMS with MS to IM-MS instruments has proven to be particularly beneficial as these methods yield highly complementary information. Modern mass spectrometers separate ions based on their mass-to-charge (m/z) ratios with extremely high resolution and accuracy, whereas in IMS ions are separated based on their overall size and shape. The separation of ions based on these different aspects occurs on vastly different timescales, making the combination of these methods feasible. Furthermore, combination of IM-MS instruments with other methods for separation or dissociation of molecules is possible as long as they feature compatible timescales. Based on this principle, IM-MS has been combined to a range of different techniques [53], which is also a fundamental element of this thesis.

2.1.1 Basic IMS Theory

The fundamental theoretical considerations of IMS were already laid out more than one century ago by the french scientist Langevin [54]. These form the foundation of todays view on diffusion of ions in gases [55, 56].

In the most basic implementation of IMS, ionized molecules of different sizes-to-charge ratios are separated based on their different velocities attained when they drift through an inert buffer gas under the influence of a weak and constant electric field. For a single species of ions, their average drift velocity v_d is determined by the number of collisions each ion experiences with the neutral drift-gas molecules within the drift region (typically many millions), which is directly proportional to the electric field strength E:

$$v_\mathrm{d} = K\,E\,, \tag{2.1}$$

where K is the *ion mobility*, a combined property of the ion-neutral system often reported in units of cm^2 V^{-1} s^{-1}. In this context, an electric field is considered *weak* when the velocity of the resulting directed motion of the ions is much slower than their random diffusionally driven motion. Only then are the ions in thermal equilibrium with the surrounding buffer gas molecules and the Einstein-Relation [57] connecting the mobility K of ions with their diffusion coefficient D is valid:

$$K = \frac{qD}{k_\mathrm{B}T}\,, \tag{2.2}$$

where $q = ze$ is the total charge of the ion, k_B the Boltzmann constant, and T is the temperature of the buffer gas. Throughout the literature values of K are typically reported as *reduced mobilities*

$$K_0 = K \frac{P}{P_0} \frac{T_0}{T}\,, \tag{2.3}$$

which incorporate standard pressure P_0 and temperature T_0. An expression connecting the mobility of an ion to its size can be obtained from rigorous calculations considering kinetic theory, which will finally lead to the Mason-Schamp Equation [56]

$$K_0 = \frac{3q}{16N_0} \sqrt{\frac{2\pi}{\mu\, k_{\mathrm{B}} T}} \frac{1}{\Omega}\,, \tag{2.4}$$

with the number density N_0 of the buffer gas molecules and the reduced mass of the ion-molecule system $\mu = m_{\mathrm{i}} m_{\mathrm{g}} / (m_{\mathrm{i}} + m_{\mathrm{g}})$ where m_{i} and m_{g} denote the masses of the ion and the neutrals, respectively. The ion-neutral average collision cross-sectional area Ω can be obtained from evaluation of the ion-neutral collision integral under consideration of all possible orientations and collision energies. When electrostatic and charge-induced polarization interactions between ion and buffer gas molecules are small, it reduces to the hard-sphere collision cross-section (CCS), which, under the assumption of spherical molecules, is given by $\Omega_{\mathrm{HS}} = \pi(r_{\mathrm{i}} + r_{\mathrm{g}})^2$, with the radii r_{i} and r_{g} of the ion and the neutral, respectively.

It is apparent from Equation 2.4 that the mobility of an ion is proportional to $q/\sqrt{\mu}\Omega$ at constant temperature and pressure, which implies that for heavier ions with mass $m_{\mathrm{i}} \gg m_{\mathrm{g}}$ the mobility is largely dominated by their charge q and the ionic size and, thus, demonstrates how ions of identical mass-to-charge ratios but different shapes can potentially be separated using IMS. It should be noted that for smaller molecules, ion-neutral interaction may play an increasingly important role in Ω and can even lead to separation of isobaric ions of similar size as demonstrated in Chapter 5.

However, ions of differing CCS can not only be separated but their CCS can be experimentally determined by measuring the time that ions of a particular type need to traverse the drift region, which results in a so-called arrival time distribution (ATD). The equations above can then be used to extract information about the molecules' shapes and comparison of experimentally obtained CCSs to those from computational models can finally help to elucidate molecular structures. Details about the experimental procedures will be given in Section 2.5.2.

2.2 Fragmentation Methods

For the study of molecular structures, so-called tandem MS experiments have proven particularly useful. Such an experiment involves the ionization of molecules, the selection of the precursor ion of interest followed by an ion activation step and subsequent analysis of its fragmentation products. Generally, the involved reactions that lead to the dissociation of a molecular ion AB^+ can be described as

$$AB^+ \xrightarrow{\text{Energy}} (AB^+)^* \xrightarrow{k(E)} A^+ + B\,. \tag{2.5}$$

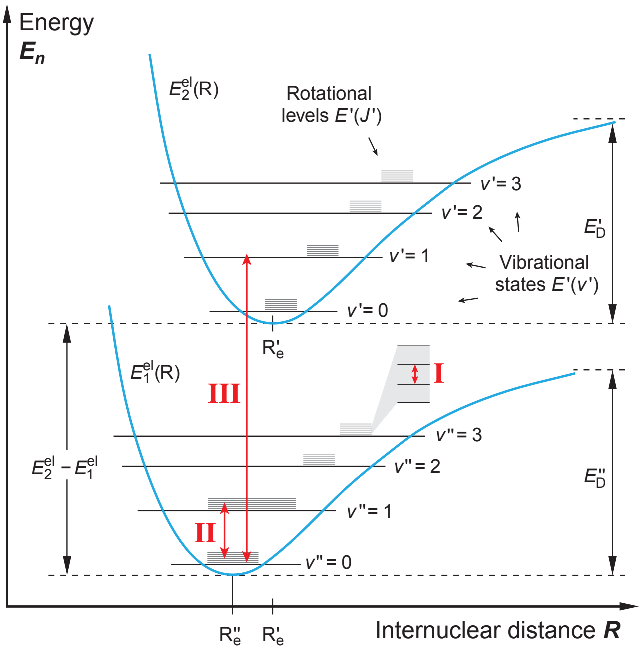

Figure 2.1: Rotational and vibrational energy levels of two electronic states in a diatomic molecule. Transitions can occur between rotational (I), vibrational (II), and electronic states (III) under consideration of certain selection rules [59]. The anharmonic nature of the electronic potential leads to an increase in the density of states with increasing internal energy E_n. Dissociation can occur when the internal energy exceeds the threshold for dissociation E_D.

An activation step involving energy transfer elevates the molecule into an excited state $(AB^+)^*$ followed by a unimolecular dissociation reaction given that the internal energy E is high enough to overcome the dissociation threshold. The charged particle A^+ can subsequently be detected in a mass spectrometer when this reaction occurs at a appreciable rate $k(E)$. As a rule of thumb, one can assume that $k(E)$ needs to be larger than the reciprocal of the time between ion activation and detection [58]. Hence, reaction rates of 10^4–10^5 s^{-1} are required for common tandem MS setups (and those employed here). Energy relaxation through collisions with neutral particles or through the emission of photons may decrease this rate and have to be taken into account when conceiving an experiment.

The activation of ions is the crucial step in the experiment and will determine the products of the unimolecular reaction. Dependent on the method and the energy range of activation, the internal energy of a molecule can be altered in terms of rotational E_rot, vibrational E_vib, or electronic energy E_n^el. To illustrate this, Figure 2.1 exemplarily shows rotational and vibrational energy levels in two different electronic states of a diatomic molecule as a function of the internuclear distance R. Each electronic state n contains many vibrational states v, which each contain many rotational levels J. A transition between two different states is associated with a change in energy and lies in the μeV–meV range (microwave) for transitions between rotational states (I), in the meV–eV range (infrared) for vibrational transitions (II), and in the lower eV range (far-infrared to vacuum UV) for transitions between different electronic states (III) [59]. Current instrumentation for the analysis of molecules with biological relevance employ a large variety of different activation methods that manipulate the internal energies of the analytes in all three energy regimes I–III. Of the many techniques available [58, 60], three will be briefly discussed here.

Collision-induced dissociation (CID) is a technique where inelastic collisions with neutral buffer-gas molecules (often N_2 or Ar) are used to gradually rise the internal energy of the ion until the dissociation threshold is reached [11, 58]. For collisions with up to several tens of eV laboratory frame collision energy mainly rotational and vibrational modes of biological molecules are excited [61]. This is because maximum energy transfer occurs during inelastic collisions when the ion-neutral interaction occurs on timescales that are similar to the associated periods of motion. In the here discussed *low-energy* regime, this involves sub-ps time frames [61].

Coupling between vibrational modes (see below) leads to intramolecular vibrational redistribution (IVR), *i.e.*, a quick randomization of vibrational energy throughout the entire molecule [62]. As a consequence, many collisions are needed to rise the internal energy above the dissociation threshold E_D. As the internal energy is statistically distributed over the entire system, dissociation often occurs over low-energy pathways, which leads to dissociation of the weakest bonds. Reviews of proposed fragmentation mechanisms can be found in the literature [63]. A CID mass spectrum of the singly protonated pentapeptide $[\mathrm{YGGFL} + \mathrm{H}]^+$ is exemplarily shown in the upper panel of Figure 2.3 where fragments are labeled according to standard nomenclature [64]. CID in the low-energy regime mostly yields *b* and *y* type fragments. Additionally, small signals giving rise to internal fragments (*e.g.* GF) can be observed.

Infrared multiple photon dissociation (IRMPD) is an activation technique in which the vibrations of a molecular ion are probed directly by irradiation with IR light [35, 65]. Photons with energies in the range of hundreds of meV are absorbed by the molecule when the corresponding frequency is resonant with an IR active transition between vibrational states (II). Dissociation thresholds are usually much higher than the energy imparted on the system by a single photon, *i.e.*, several eV binding energy need to be overcome by the absorption of $\sim$ 100 meV photons in order to dissociate covalent bonds. Therefore, the absorption of many photons is necessary to dissociate a molecule or molecular complex. However, the naive image of a stepwise multiphoton absorption accompanied by an increase in the rotational quantum number of one and the same vibrational mode ($v = 0 \rightarrow v = 1 \rightarrow ...$) is not realistic for the molecules and photon densities delivered by the mid-IR free electron laser used within this work (Section 2.6.1). During this vibrational ladder-climbing process, the anharmonic nature of the electronic states leads to a decrease in energy separation of vibrational levels as the

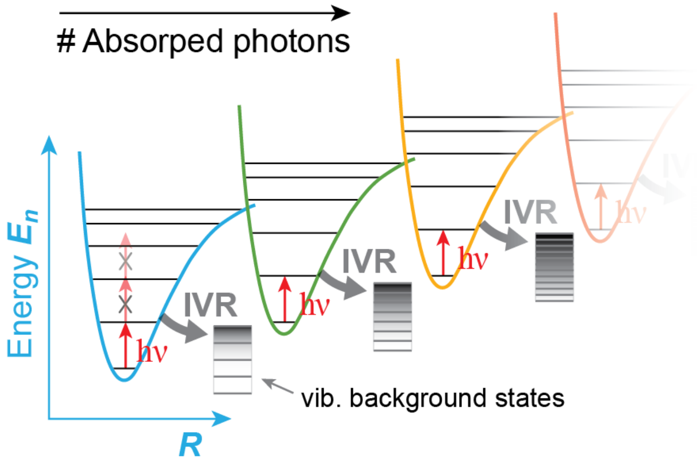

Figure 2.2: Schematic energy diagram of the IR multiple photon dissociation (IRMPD) mechanism. In the resonant regime (a) successive photon absorption by resonant vibrational modes leads to increase in internal energy. Anharmonic coupling of vibrational modes dissipates the energy *via* internal vibrational redistribution (IVR) in a quasi-continuum of states (b). Above the dissociation threshold E_D (c) fragmentation can occur.

vibrational quantum number v increases. This effect it often referred to as the *anharmonicity bottleneck* and would shift the corresponding vibrational transitions out of resonance (towards lower energies) when the wavelength of the IR light is fixed [66].

Instead, a sequential multiple photon absorption scheme applies here, which is schematically depicted in Figure 2.2. It is based on the quick dissipation of vibrational energy after the absorption of a photon by a particular mode *via* IVR, *i.e.*, anharmonic coupling to the bath of vibrational background states, resulting in the depletion of the excited vibrational mode. For larger, polyatomic molecules, this process occurs on a sub-ns timescale (at room temperature). It is the more effective, the higher the density of states that effectively couple to the original vibrational mode, *i.e.*, the larger the molecule and the higher its internal energy [35, 37]. In this picture, successive photon absorption by the same IR active vibrational transition, followed by energy randomization over the entire molecule leads to a gradual increase in internal energy. When the internal energy exceeds the threshold for dissociation E_D, the vibrationally excited molecule can undergo a unimolecular reaction, which usually involves the dissociation of the weakest bonds. A more detailed description of the involved processes can be found throughout the literature, *e.g.*, in [35, 37] and the references therein.

The sequential intake of energy and its subsequent statistical dissipation over many modes of vibration resembles the processes involved in CID [58]. In fact, IRMPD yields fragmentation patterns that are overall similar to those obtained from collisionally activated species, as can be seen from the IRMPD fragment spectra obtained from resonant irradiation of [YGGFL + H]$^+$ ions in the middle panel of Figure 2.3.

Ultraviolet photodissociation (UVPD) makes use of transitions between electronic states in an eV energy regime (III) and is, therefore, considered a *high energy* dissociation method. When biological molecules are of interest, a strong absorption band of the peptidic backbone at wavelengths around 190 nm [60] offers a convenient gateway for energy deposition using 193 nm photons produced by readily available ArF excimer lasers (Section 2.6.1). Thus, upon absorption of a single photon, the molecule can be elevated into an excited electronic state *via* a $\pi \rightarrow \pi^*$ transition of the peptide bond [67], roughly 6.5 eV in energy above the electronic ground state. The excited molecule can subsequently undergo a unimolecular dissociation reaction, in which die 3–4 eV binding energy of the peptide bond is overcome without further photon absorption. Whether dissociation of a peptide occurs *via* curve crossing to a dissociative electronic state, or after a transition to the electronic ground state and subsequent energy redistribution through anharmonically coupled vibrational modes is, to date, not clear [60, 67–69]. There is evidence, however, that energy is not completely randomized over the molecule as in the case of the *slow heating* techniques CID and IRMPD. This will be discussed in Chapter 4 where the UV photofragmentation behavior of ubiquitin conformers is studied.

UVPD at 193 nm was shown to effectively dissociate small peptides already some 30 years ago [70], however, only recently was it applied successfully to analyze the primary structure of proteins or entire protein complexes [71–73]. In contrast to slow heating techniques, which are characteristic for the dissociation of the weakest bonds, fragmentation of the peptide backbone occurs statistically distributed over the entire amino acid sequence [72]. This characteristic fragmentation behaviour of peptides upon absorption of 193 nm photons is shown exemplarily for $[\mathrm{YGGFL} + \mathrm{H}]^+$ ions in the lower panel of Figure 2.3.

A comparison between the fragment spectra of $[\mathrm{YGGFL} + \mathrm{H}]^+$ obtained using the three different activation methods CID, IRMPD, and UVPD reveal the similarity of the first two techniques, where molecules are gradually heated, and the drastic difference to UVPD at 193 nm, where the absorption of a single photon by the peptide bond provides sufficient energy to induce fragmentation of the backbone. Thus, depending on the energy deposited in the molecule, different dissociation channels become available. For $[\mathrm{YGGFL} + \mathrm{H}]^+$ ions at photon energies above 8.8 eV ($\leqslant$ 140 nm), for example, direct detachment of electrons was shown to contribute to the rather complex fragment spectra [68].

2.3 Gas-Phase Vibrational Spectroscopy

The vibrations of a molecule or a molecular complex depend on the interactions of the oscillators within the molecule and therefore on the molecular geometry and structure. Besides information about the type and strength of chemical bonds, a vibrational spectrum also contains information about the various types of non-covalent interactions, such as hydrogen

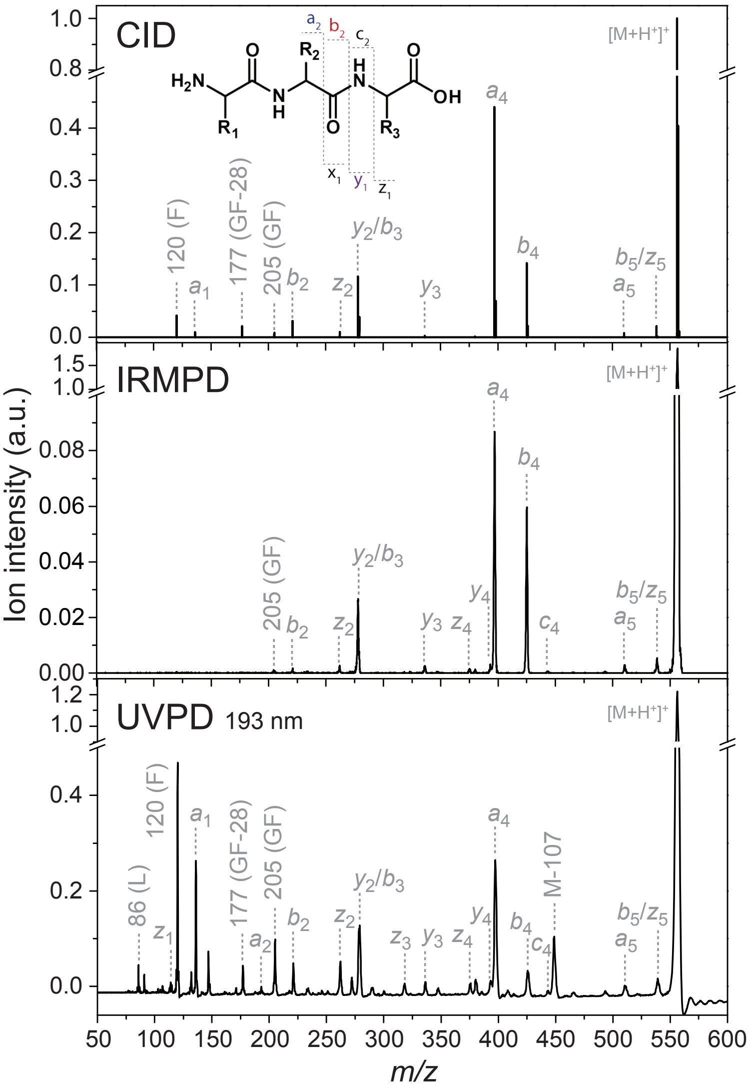

Figure 2.3: Fragment spectra of the singly protonated peptide $[\text{YGGFL} + \text{H}]^+$ using different activation methods. CID (upper panel) and IRMPD (middle panel) generally yield similar fragmentation patterns arising from cleavage of the weakest peptide bonds. In UVPD (lower panel) bond cleavages are distributed statistically over the entire sequence leading to rich fragment spectra. CID data was acquired using the traveling-wave IM-MS setup described in Section 2.7. IRMPD and UVPD data was acquired at the drift-tube IM-MS instrument described in Section 2.4.

bondings or ionic interactions. This information is hidden in the spectrum in the form of absorption bands that may increase or decrease in relative intensities or shift towards higher or lower energies, thereby indicating specific interactions within the molecule and the respective oscillators [33].

Classically, a vibrational spectrum is obtained by measuring the attenuation of a beam of light when it passes through a sample of length l, containing molecules at a number density of n. The intensity of the transmitted light $I(\nu)$ is then determined by the Lambert-Beer law

$$I(\nu) = I_0 \, e^{-\sigma(\nu) \, ln} \, , \tag{2.6}$$

where I_0 is the intensity of the light before it passes through the sample and $\sigma(\nu)$ is the absorption cross section of the molecules in question. For direct absorption measurements on gas-phase molecular ions, however, this approach is not feasible as the product $n \cdot l$ is generally too small in gas-phase experiments, owed to the comparatively low maximum ionic number density of $n_{\mathrm{scl}} \approx 10^6$ cm^{-1} at the space-charge limit [35]. A way to overcome this inherent problem is to employ *action spectroscopy*, *i.e.*, to monitor how the molecules are affected after irradiation with light rather than monitoring the intensity of the light. When the radiation is resonant with a molecular vibration and enough energy can be deposited into the molecule for dissociation to occur as described in the previous Section 2.2, an IRMPD vibrational spectrum can be obtained from the intensities of the precursor and fragment ions in a tandem MS experiment. In a simplified picture of a two-state system, where the precursor ions can be dissociated with a linear photon fluence dependency, the number of precursor ions after irradiation $N_p(\nu)$ can be expressed in analogue to the Lambert-Beer law as [37]

$$N_p(\nu) = N_0 \, e^{-\sigma(\nu) \, F(\nu)} \, , \tag{2.7}$$

which depends on the total number of precursor ions before irradiation N_0 and the photon fluence $F(\nu)$. The number of fragment ions that are produced during the fragmentation then calculates to

$$N_f(\nu) = N_0 \, \left(1 - e^{-\sigma(\nu) \, F(\nu)}\right) \, . \tag{2.8}$$

It is apparent that, in order to achieve an adequate signal in the experiment, a high flux of photons $F(\nu)$ is needed in this gas-phase approach as opposed to direct absorption measurements, where high number densities of the molecule are required. In the here-presented experiments an IR free electron laser (FEL, Section 2.6.1) is utilized to generate IR radiation of high intensity and, therefore, high photon fluence $F(\nu)$.

In order to deduce structural information from a gas-phase IR spectrum one can, *e.g.*, compare positions and, to a certain degree, relative intensities of absorption bands to reference spectra from condensed-phase measurements [33]. A more thorough approach that is so far only feasible for smaller molecules is to calculate and compare vibrational spectra from model structures obtained from calculations at a quantum chemical level [35]. One has to bear in mind, however, that the IRMPD process often causes shifts and/or broadening of experimental vibrational bands. Both can be attributed to the anharmonic nature of the oscillator potentials, leading to decreasing energy differences between excited vibrational levels, decreased lifetimes of excited vibrational states due to high IVR rates, and a somewhat reduced wavelength selectivity in the quasi-continuum of vibrational states at high internal energies [35]. However, in Chapters 5 and 6, comparison of experimental spectra with calculated spectra and with solution reference spectra, respectively, shows that this could nonetheless lead to satisfactory results.

2.4 Experimental Setup I: Linear Drift-Tube Instrument

The following section gives an overview of the drift-tube (DT) IM-MS instrument that was designed* and constructed in the course of this work. Several constructional details and background information about the employed techniques and modes of operation will be given.

Figure 2.4 shows a simplified engineering drawing of the experimental setup. The apparatus consists of a (nano) electrospray ionization (nESI) source (see Section 2.4.2) followed by a radio-frequency (RF) ion funnel (*entrance funnel*) to radially collimate and trap ions over several tens of milliseconds. From there, ions are pulsed into the 805.5 mm long, buffer-gas filled drift tube, which is constructed from four similar segments of conductive glass tubes (Photonis, USA). These are designed to feature a high and homogeneous electric resistance over their entire length of 200 mm (see also Section 2.5.4). A difference in electrical potential between the ends of the drift tube will then lead to a homogeneous electric field inside the tubes, which drives the ions forward. Many collisions with buffer-gas molecules lead to a spacial separation of ions with different size but perhaps identical mass-to-charge ratios m/z, as explained in Section 2.1. To account for the diffusional spread of the ion cloud in radial direction (perpendicular to the directed drift motion), a second RF ion funnel (*exit funnel*) provides radial confinement and ensures the transport of the ions through a small conductance limit followed by a series of cylindrical ring electrode guides (*ring guides*) for the transmission of ions through two differentially pumped stages (for funnels and guides, see Section 2.4.3). An electrostatic einzel lens stack of 25 mm length then focuses ions into a quadrupole mass filter (see Section 2.4.4) followed by a second quadrupole guide of identical dimensions. Ions exiting this guide once more pass an einzel lens stack and an additional set of steering lenses where the focus as well as the horizontal and vertical direction of flight can be manipulated. Subsequently, ions are either directly detected using an off-axis electron multiplier detector (ETP Ion Detect, Australia, model AF632) approximately 160 mm downstream or pulsed in perpendicular direction into a time-of-flight (TOF) mass analyzer (see Section 2.4.4). Also here, ions are detected using an ETP electron multiplier (model AF882). For drift-time and m/z-resolved laser-light induced dissociation experiments, optical access to the ion-light interaction region (quadrupole guide) is provided.

For a more detailed description of the different experimental procedures, see Sections 2.5 and 2.6.

2.4.1 Vacuum System

The different experimental techniques that are combined in the IM-MS instrument require different operating pressures. The nESI source typically operates at ambient pressures, whereas the ion-mobility section is employed in the mbar regime. Mass spectrometry and spectroscopy methods, on the other hand, require high vacuum conditions ($< 10^{-5}$ mbar). Consequently,

---

*Design based, in part, on a instrument design from the group of Mike Bowers, UCSB [40]

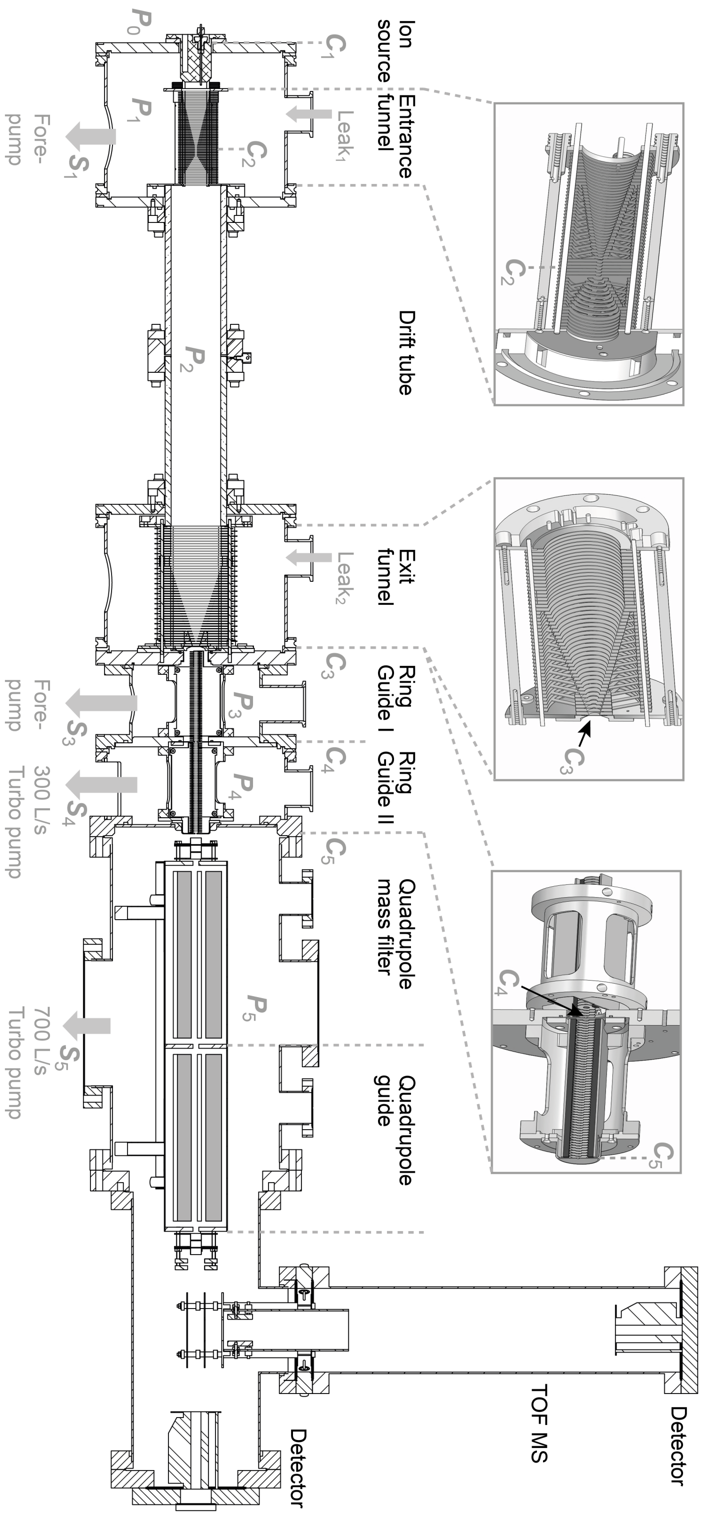

Figure 2.4: Simplified technical drawing of the drift-tube (DT) IM-MS experimental setup. Regions of different pressures P_0–P_5 are connected by the respective conductance limits C_1–C_5.

careful design of the vacuum regions n and implementation of the connecting conductance limits C_n under consideration of the resulting pressures P_n, gas flows S_n, and gas throughputs Q_n is necessary to meet the required vacuum conditions.

The setup (shown in Figure 2.4) comprises six different pressure regions P_0–P_5, where P_0 is the ambient laboratory pressure that surrounds the ion source. The inherent flow of laboratory air through the electrospray capillary (C_1) into the instrument must not contaminate the high-purity buffer gas of inside the drift tube. Therefore, the source region is pumped with a forepump and a constant pressure gradient $\Delta P = P_2 - P_1 > 0$ between the source region (P_1) and the drift tube (P_2) is implemented, leading to a permanent backflow of buffer gas through the conductance limiting orifice C_2. Two manual leak valves are installed at the source region (Leak$_1$) and at the end of the drift region (Leak$_2$), respectively, to control the ingestion of buffer gas into the instrument. The buffer gas pressure P_2 is critical for the accuracy of the collision cross-section determination and is monitored with a high-precision MKS Baratron absolute pressure gauge (type 627). The pressure P_1 in the source region is monitored indirectly by measuring the pressure difference ΔP with a MKS Baratron differential pressure gauge (type 226). Less critical pressures P_3–P_5 as well as foreline pressures are monitored with standard Penning and Pirani-type pressure gauges.

For the dimensions of the gas-flow restricting conductance limits C_n, a compromise between a high ion transmission and effective differential pumping has to be made. At a given geometry of the connecting orifice or tube with conductance C, the gas load Q will be determined by the pressure difference $(P_a - P_b)$ between two consecutive, differentially pumped vacuum chambers a and b. For constant pressures, the pump speed S_p in chamber b needs to be large enough to compensate this load, which can also be expressed as a product of the flow rate S and the pressure P_a in chamber a. These relationships are summarized in Equations 2.9 [74]:

$$Q = \begin{cases} SP_a \\ C(P_a - P_b) \\ S_p P_b \end{cases} \tag{2.9}$$

In order to calculate these vacuum parameters for the IM-MS instrument, the conductances C_n of circular tubes (nESI capillary) and thin apertures can be estimated using the following formulae [74]:

- Viscous flow, tube (air, 20°C): $C^{\text{vis}}_{\text{tube}} = 135 \cdot 10^{-3} \, \frac{D^4}{L} P_{\text{av}}$ L s^{-1}
- Viscous flow, thin aperture (20°C): $C^{\text{vis}}_{\text{aperture}} \approx 0.2 \, A$ L s^{-1}
- Molecular flow, thin aperture: $C^{\text{mol}}_{\text{aperture}} = 37 \cdot 10^{-3} \sqrt{\frac{T}{M}} \, A$ L s^{-1}

with the diameter D and the length L of the tube in mm, the average pressure P_{av} in mbar, the area of the aperture $A = \pi(D/2)^2$ in mm^2, the temperature T and the molecular mass M

of the buffer gas molecules in amu. Molecular flow dominates when the mean free path* λ of the buffer-gas molecules is much larger than the dimensions of the vacuum chambers. In the transition regime, where λ is of similar dimensions as the conductance apertures ($\sim$ mm), the conductance C can be conservatively estimated with the expression for viscous flow.

Table 2.1: Vacuum parameters. The pressures P_n, conductances C_n, throughputs Q_n, and pump speeds at the vacuum chambers S_n are labeled as in Figure 2.4. λ_n is the mean free path in the respective pressure region and D denotes the diameter of the conductance orifice. P_n are determined experimentally. Parameters were calculated for He buffer gas.

n	P_n^{exp} (mbar)	C_n (L s^{-1})	Q_n (mbar L s^{-1})	S_n (L s^{-1})	λ_n (m)	D (mm)
1	4.5	$1.4 \cdot 10^{-3}$	1.4	1	$1 \cdot 10^{-4}$	0.2
2	5.0	$(1.9 - 7.5)^\dagger$	$(1.0 - 3.8)$	–	$9 \cdot 10^{-5}$	3.5
3	$1 \cdot 10^{-2}$	$4.0 \cdot 10^{-2}$	0.2	20	$5 \cdot 10^{-2}$	0.5
4	$3 \cdot 10^{-5}$	1.0	$1 \cdot 10^{-2}$	330	15	2
5	$4 \cdot 10^{-8}$	1.0	$3 \cdot 10^{-5}$	750	$1.2 \cdot 10^{4}$	2

$^\dagger C_2$ estimated as a thin aperture (lower limit) or tube (upper limit).

Calculated and measured vacuum parameters for the IM-MS instrument assuming helium as buffer gas are summarized in Table 2.1 with labels according to Figure 2.4. The throughput Q_2 corresponds to the backflow of buffer gas through the conductance limit C_2, which comprises six adjacent apertures at a short distance (for details see Section 2.4.3). This geometry is difficult to treat using established conductance formulae and it it therefore estimated as a thin aperture (lower conductance limit) or a short tube (upper conductance limit) in Tabe 2.1. The flow rates S_n refer to the necessary displacements of gas at the pump outlet of the vacuum chamber and approximately match the nominal speeds S_p of the connected vacuum pumps including vacuum hoses. The gas flow $S_1 \approx 1$ L s^{-1} is estimated from the nominal pump speed ($\sim$ 4.4 L s^{-1}) of the connected vacuum pump and the measured pressures inside the vacuum chamber ($\sim$ 4.5 mbar) and at the inlet of the pump ($\sim$ 1 mbar) using Equations 2.9. It represents the inflow of gas from the nESI capillary Q_1, the drift tube Q_2 and the manual leak valve (Leak$_1$). The throughput of the leak valves can be estimated from the total flux of gas in the source chamber ($n = 1$) and the drift region ($n = 2$). This yields 1–2 mbar L s^{-1} for each valve.

2.4.2 Ion Sources

In the beginning of every MS experiment stands the ion source. Here, molecules are ionized and transferred from the condensed phase to the gas phase for further investigation. The most commonly used technique in the field of biomolecular mass spectrometry is electrospray

---

*Mean free path in an ideal gas [74]

$$\lambda = \frac{k_{\mathrm{B}} T}{\sqrt{2}\pi d^2 P},$$

with the Boltzmann constant k_{B}, the temperature T, the molecular diameter d, and the pressure P.

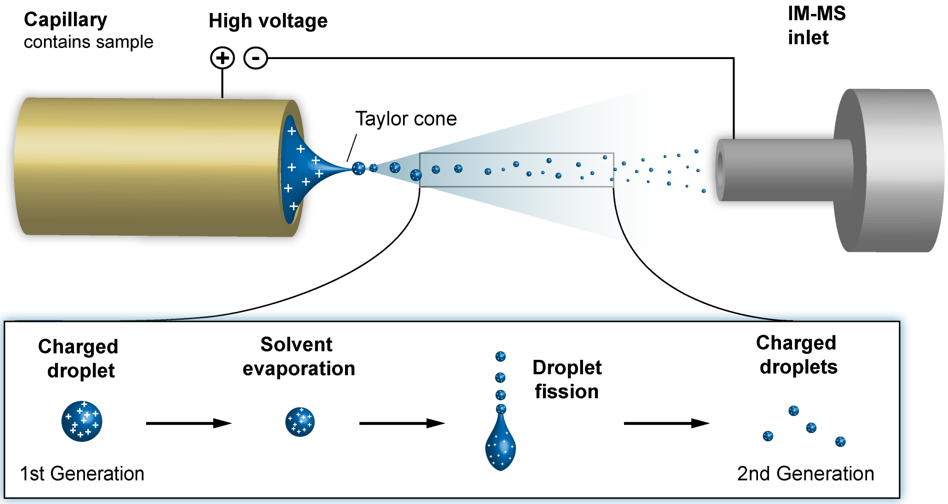

Figure 2.5: Schematic representation of an electrospray ionization (ESI) source. When the electric field generated by the applied voltage is high enough (Equation 2.10), the tip of the liquid (Taylor) cone breaks up into small ion-containing droplets. The solvent quickly evaporates, thereby increasing the charge density inside a droplet. Subsequent fission events and/or direct evaporation of ions from the droplet lead to the final desolvated ions (see text for discussion).

ionization (ESI), which was pioneered by Malcom Dole *et al.* in the 1960s [75] and further improved by John B. Fenn to be applicable to large biomolecules some 20 years later [76]. Using this technique, non-volatile molecules and weakly bound complexes with masses of more than 100 kDa can be readily ionized without inducing fragmentation. This achievement was later rewarded with the Nobel prize in 2002 [77].

In Figure 2.5 the electrospray process is depicted schematically. The solvated analyte molecules are filled into a small capillary and a high voltage is applied with respect to a counter electrode (IM-MS inlet in Figure 2.5). The polarity of this voltage will determine the polarity of the produced ions. The high electric field at the tip of the capillary leads to partial separation of charges close to the surface of the solvent, which consequently expands to a liquid cone (Taylor cone). When the electric field exceeds a critical voltage [78]

$$E_0 = \sqrt{\frac{2\gamma\,\cos(49^\circ)}{\epsilon_0 r_c}}\,, \tag{2.10}$$

where γ is the surface tension of the solvent, r_c the radius of the capillary, and ϵ_0 is the vacuum permittivity, then the liquid filament at the tip of the Taylor cone breaks up into charged droplets which propagate towards the counter electrode. Consequently, for a typical ESI setup where $r_c \approx 500$ μm and a mixture of water/methanol is used as a solvent, an electric field of $E_0 \approx 3$ kV/cm is required. The field at the tip of the capillary E_c can be estimated using [79]

$$E_c = \frac{2V_c}{r_c \ln(4d/r_c)} , \tag{2.11}$$

where V_c is the applied voltage and d the distance of the capillary from the inlet of the setup. Hence, for $d = 10$ mm, the required electric field E_0 can be generated by a voltage of $V_c \approx 3$ kV.

The evolution of the charged ESI droplets is depicted in the bottom panel of Figure 2.5. Depending on the concentration of analyte molecules inside the solvent, one droplet of the first droplet generation, which is typically about 1 μm in size, can contain many thousand ions [80]. In the atmospheric pressure environment of the ESI source, solvent molecules quickly evaporate, leading to a smaller droplet diameter D and an increased charge density, until the so-called Rayleigh limit at a total charge of $q = \sqrt{8\pi\ \epsilon_0 \gamma D^3}$ is reached [81], where the surface tension γ of the solvent droplet can no longer withstand the increased coulomb repulsion of the like charges. As a consequence the next droplet generation is produced as fission products, which are about 2 % in mass of the initial droplet and each carry 15 % of the initial droplet charge [82]. This process may repeat itself many times until only one single ion remains in a small droplet of solvent molecules, which subsequently evaporate and finally leave a fully desolvated ion. This charge residue model (CRM) is assumed to hold for larger molecular ions such as peptides and proteins, which are, dependent on ionization conditions, typically found to adopt a distribution of different charge states (compare Figure 1.3). A second model, the ion evaporation model (IEM), is more likely to apply to smaller molecules and takes into account that the direct evaporation of an ion from a multiply charged droplet may be energetically favorable to the Coulomb fission process [82]. This, of course, is dependent on the type of ions and the solvent composition and a mixture of both processes will be found in most ESI applications [79].

In a more refined version of the ESI source, sample consumption is minimized by using spray emitters with a diameter of only 1–2 μm at the tip, which leads to lower sample flow rates ($\sim$ 10–50 nL min^{-1}) and smaller initial droplets that are only about 200 nm in diameter [80]. The smaller droplet size is beneficial for the sensitivity of the measurement and samples with down to attomolar concentrations can be characterized [83]. With a smaller capillary diameter and capillary-inlet distances of $d \approx$ 1–2 mm, lower voltages of 0.8–1.2 kV are needed to produce the electric field E_0 (Equation 2.10) required for stable operation. This nano electrospray ionization (nESI) technique was used for all measurements that are presented throughout this thesis.

The two types of nESI sources that were employed in the experimental setups are schematically depicted in Figure 2.6 and are briefly described in the following paragraph. In Figure 2.6 (a), the so-called Z-spray source is shown, which is installed on commercial MS instruments, available from the Waters Corporation and in (b) a simpler, in-house constructed linear nESI source is depicted. The ionization and desolvation principles are identical for

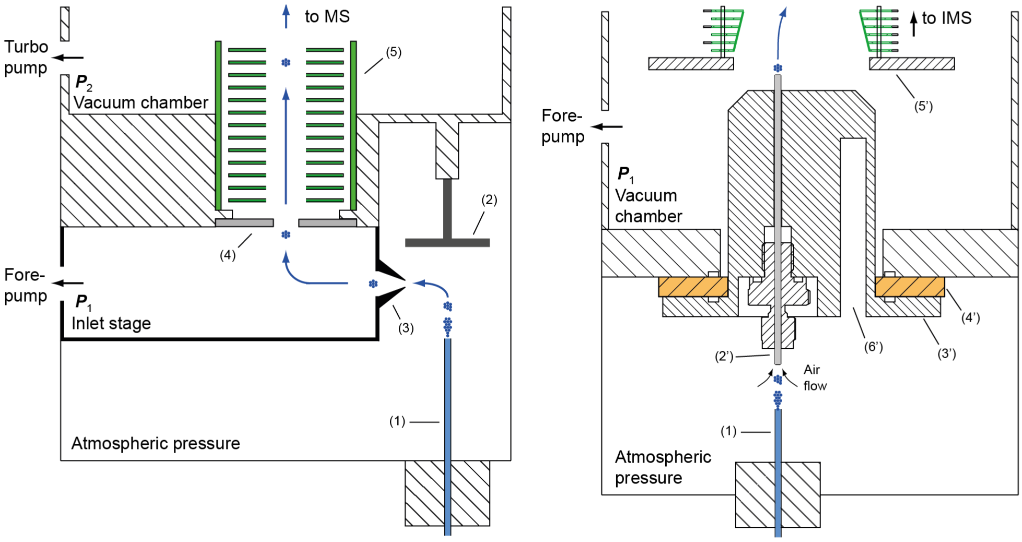

(a) Z-spray nESI **(b)** Linear nESI

Figure 2.6: Schematic representation of the Z-spray (a) and the linear type (b) nano ESI sources utilized in the experiments that are presented within this thesis. In both cases, the analyte-containing solvent is filled into a Pd/Pt coated borosilicate capillary (1) and a high voltage with respect to the counter electrode is applied. Other essential elements of the Z-spray are: (2) grounded baffle, (3) instrument inlet cone, (4) entrance lens to the (5) ion guide. Linear setup: (2') transfer capillary (75 mm) held by the (3') aluminum source block, (4') electrical isolator, (5') entrance electrode of the ion guide, (6') insertion slot for optional heating cartridge. The scheme of the Z-spray source is adapted from [84].

both versions and their main difference lies in the transfer of the charged species into the vacuum environment of the experimental setup. For both setups, the nESI capillaries (1) are prepared from borosilicate capillaries using a needle puller (Flaming/Brown Micropipette P-1000, Sutter Instrument Company, Novato (USA)) following Pt/Pd coating (Sputter Coater HR 208, Cressington, Dortmund (Germany)) [85]. In the Z-spray setup the electrosprayed droplets enter the instrument's inlet stage ($P_1 \approx$ 1–5 mBar) by following the flow of air through a cone-shaped opening (3) of $\sim 800\ \mu$m in diameter. A combination of electric fields and air flow directs the charged species into a second transfer section ($P_2 \approx 10^{-3}$ mBar) where an ion guide (5) transports them towards higher vacuum. The Z-shaped ion trajectory helps to prevent neutral particles to enter the ion guide region. To aid desolvation of the charged droplets, the source block can be heated, which, however, can be disruptive for fragile molecules or molecule complexes.

In the linear nESI setup (Figure 2.6 (b)), the additional instrument inlet stage is omitted and particles are transferred directly after the spray process into an ion guide region ($P_1 \approx$ 2–6 mBar) by following the air flow through a 75 mm stainless steel capillary (2') of 250 μm inner diameter. This transfer capillary, which is mounted in an aluminum source block (3'), is offset with respect to the instrument axis to prevent neutral species to further enter

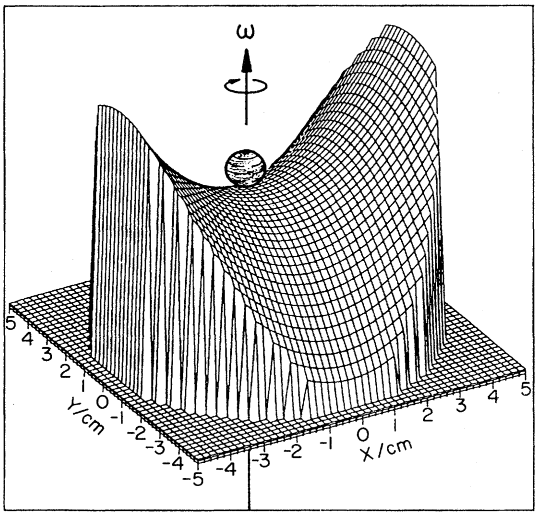

Figure 2.7: Mechanical analogue of an RF confining electrical potential. The ball, placed on the rotating saddle surface, will experience a net force towards the center. Figure adapted from [93].

the instrument. The electric potential of the source block is set ~ 5 V above the potential of the ion guide (5'). Also for this source setup, the temperature can be elevated to help the desolvation process by inserting a heating cartridge in an insertion slot (6'). Practice has shown that the linear source type generally provides more gentle ionization conditions than the Z-spray type. As a result species with high extent of non-covalent interactions can often not be observed using a Z-spray but are readily generated with the linear source type [86]. These performance differences are still not fully understood but are possibly a result of different pressure and voltage gradients, influencing the amount and energy of collisions with neutral gas molecules and the time span of desolvation.

2.4.3 Multipole RF Ion Transport- & Storage Devices

Under high-vacuum conditions, ion trajectories can be influenced with high precision using static electric or magnetic fields. When the ion motion is dominated by collisions with neutral gas molecules, however, such electrostatic methods are little effective. Instead, inhomogeneous, fast oscillatory electric fields can be used to manipulate ion trajectories even at the elevated buffer gas pressures of an ion-mobility spectrometer. Hence, electrode arrangements that carry fast alternating radio-frequency (RF) electric potentials are routinely utilized to guide ions through small apertures [87], or through areas of counter-propagating gas flows, and, most importantly, to trap ions over an extended period of time [88, 89]. The development of RF confining multipole devices for charged particles dates back to the 1950s when Wolfgang Paul *et al.* designed the first multipole lenses for atomic and molecular beams [90, 91], which later resulted in the first quadrupole mass spectrometers [92]. In 1989, these achievements were awarded with the Nobel prize [93].

The necessity of alternating electric fields for the confinement of a charged particle arises from Earnshaw's theorem [94], which states that "A charged particle cannot be held [statically]

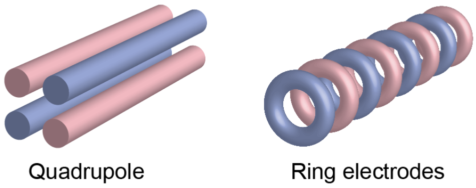

Figure 2.8: Two types of electrode arrangements. Electrodes of different colour differ in the phase of the electric potential $\Phi_0(t)$ by π.

in a stable equilibrium by electrostatic forces alone." Mathematically, this circumstance is described by the Laplace equation [95]

$$\triangle\Phi = 0\,, \tag{2.12}$$

which states that an electric potential Φ cannot have any minima or maxima in free space. An electric potential can, however, have a saddle point in three dimensions and, when this saddle point is inverted with the appropriate frequency, a net force drives a charged particle towards the potentials center. A mechanical analogue of this effect is a rotating saddle surface on which a small ball is placed (Figure 2.7). The position of the ball will be unstable and roll down the potential hill unless the surface rotates with the right frequency, which depends on the potential parameters and the mass of the ball.

Electric Potentials

Two types of electrode arrangements that are employed in the here-described DT setup to generate electric potentials in the form of saddle surfaces (Figure 2.7) are depicted in Figure 2.8; the quadrupole (left) and the ring-electrode arrangement (right). The electric potential Φ_0 that is applied to one set of electrodes (*e.g.* blue electrodes in Figure 2.8) is generally described as the sum of a DC component U and an AC component of amplitude V

$$\Phi_0(t) = U + V\sin(\omega t)\,, \tag{2.13}$$

with the angular frequency $\omega = 2\pi f$ and the frequency of the oscillation f. The second set of electrodes (red electrodes in Figure 2.8) carries a potential that is shifted in the phase of the oscillation by π, with respect to the potential of the first set. Such potentials are depicted exemplarily in Figure 2.8 (a) for $U = 0$. To obtain an analytical expression for the electric potentials of the electrode arrangements in Figure 2.8, the Laplace equation 2.12 has to be solved in consideration of the appropriate boundary conditions [96]. For the simplified example of a quadrupole with infinite extension along the z-direction and an inscribed circle of radius r_0, this solution is given in cylindrical coordinates (r, ϕ) by [92]

$$\Phi_{\text{quad}}(r,\phi,t) = V\sin(\omega t)\left(\frac{r}{r_0}\right)^2\cos(2\phi)\,, \tag{2.14}$$

assuming that the applied potential $\Phi_0(t)$ consists of a AC term only ($U = 0$). A solution of the Laplace equation for the example of an infinitely extended set of stacked ring electrodes (Figure 2.8) with radius ρ_0 and a spacing of d is then given by [96]

$$\Phi_{\text{ring}}(r, z, t) = V \sin(\omega t) \frac{I_0(kr)}{I_0(k\rho_0)} \cos(kz)\,, \tag{2.15}$$

where $k = \pi/d$ and $I_n(x)$ (n, integer) is the modified Bessel function of the first kind [97]

$$I_n(x) = \frac{1}{\pi} \int_0^{\pi} e^{x \cos\theta} \cos(n\theta)\, \mathrm{d}\theta\ . \tag{2.16}$$

A solution for the static DC potential is then straight-forward and superposition of the AC and the DC term yields the total electric potential

$$\Phi_{\text{tot}} = \Phi_{\text{AC}} \sin(\omega t) + \Phi_{\text{DC}}\,. \tag{2.17}$$

The electric potentials 2.14 and 2.15 of the quadrupole and the ring electrode arrangement are plotted exemplarily in Figures 2.9 (b) and (c), respectively, for different moments within one oscillation period of $\Phi_0(t)$ from 0 to π as indicated in (a). The approximate positions of the electrodes are indicated in blue and red. As in the example of the rotating saddle surface in Figure 2.7, the electric potentials invert their shape after $\omega t = \pi$.

Motion of Ions in Oscillatory Fields

Surprisingly, the focusing and defocusing forces that the electric potentials in Figure 2.9 oppose to a charged particle (of the right *m/z*) do not cancel out over time. Instead, the time variation and the inhomogeneity of the RF potentials lead to a net focusing force [96]. When the velocity of the ion is slow enough to discard relativistic effects, the general equations of motion of an ion in an electric potential Φ are given by

$$m\ddot{\vec{r}} = -ze\ \nabla\Phi(x, y, t)\,, \tag{2.18}$$

where m is the mass, ze is the absolute charge of the particle, and $\ddot{\vec{r}}$ denotes the second time derivative of its position coordinate. Analytical solutions for these differential equations can only be found for the linear quadrupole (or the Paul trap) [98, 99]. In these cases, the equations of motion 2.18 have the form of the well-characterized Mathieu equations [97]. Clever substitution of parameters allows the solutions of these equations to be classified as stable or unstable. This, in turn, is highly dependent on the applied voltages, as well as on the mass-to-charge ratio of the particle [88]. For this reason, the linear quadrupole is widely utilized as an effective mass filter in gas-phase experiments and is also employed in the here-described DT setup (see Section 2.4.4).

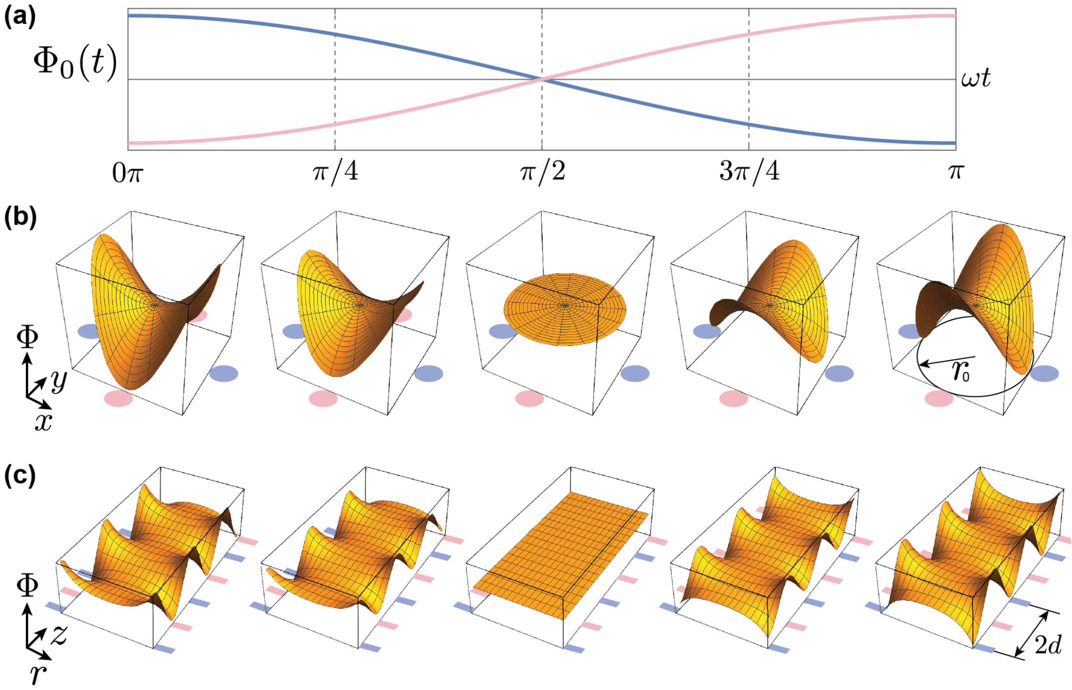

Figure 2.9: (a) Typical time dependency of the RF electrical potential $\Phi_0(t)$. (b) and (c) show electric potentials Φ of a quadrupole electrode and ring electrode arrangement (see Figure 2.8) according to Equations 2.14 and 2.15, respectively, for RF phases corresponding to $\omega t = 0\pi$, $\pi/4$, $\pi/2$, $3\pi/4$, and π. The red and blue coloured areas denote the approximate positions of the electrodes and electrodes of different colour differ in the phase of the RF potential $\Phi_0(t)$ by π.

For the electric potentials of higher multipole arrangements or ring electrode stacks (Equation 2.15), the equations of motion 2.18 become nonlinear coupled differential equations that cannot be solved analytically [96]. Instead, the motion of ions can be described with the aid of an effective, static potential V^* [100]. In this *adiabatic approximation* the motion of an ion is composed of a rapidly oscillating term $\vec{R}_1(t)$ that is superimposed to a smooth drift motion $\vec{R}_0(t)$, so that

$$\vec{r}(t) = \vec{R}_0(t) + \vec{R}_1(t)\,. \tag{2.19}$$

For the micromotion $\vec{R}_1(t)$, an expression is found after a Taylor expansion of the electric field and solving of the resulting equation of motion for short times [96]. This yields

$$\vec{R}_1(t) = \frac{ze}{m\omega^2}\nabla\Phi_{\mathrm{AC}}(\vec{R}_0)\,\sin(\omega t)\,. \tag{2.20}$$

Averaging the equation of motion over one full oscillation yields a differential equation of the secular motion $\vec{R}_0(t)$ [96]

$$m\ddot{\vec{R}}_0(t) = -\nabla V^*(\vec{R}_1)\,, \tag{2.21}$$

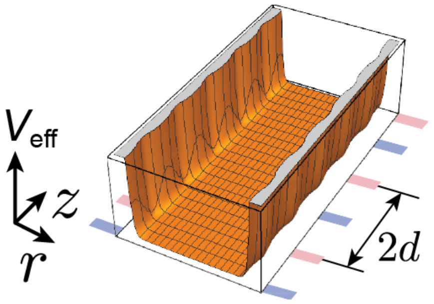

Figure 2.10: Exemplary representation of an effective potential V^* for a ring electrode arrangement as depicted in Figure 2.8.

with the time-indepentent, conservative potential

$$V^*(\vec{R}_0) = \frac{ze}{4m\omega^2}\left|\nabla\Phi_{\mathrm{AC}}(\vec{R}_0)\right|^2 + ze\,\Phi_{\mathrm{DC}}\,, \tag{2.22}$$

often referred to as the *effective potential* [96]. For the stacked ring electrodes, for example, the effective potential calculates to [87]

$$V^*(r,z) = \frac{zeV^2k^2}{4m\omega^2\,I_0^2(k\rho_0)}\left(I_1^2(kr)\cos^2(kz) + I_0^2(kr)\sin^2(kz)\right)\,, \tag{2.23}$$

with the maximum amplitude of the applied RF voltage V and modified Bessel functions according to Equation 2.16. Such an effective potential is exemplarily shown in Figure 2.10. The steep walls and the effectively field free center of the potential are characteristic for ring electrode arrangements (when $d \ll \rho_0$), in contrast to the quadratic behaviour of the effective potential inside a linear quadrupole.

The adiabatic approximation holds as long as the variation of the electric RF-field over one oscillation period of the micromotion R_1 is small. This can be expressed with the following adiabaticity condition [96]

$$\eta = -\frac{2ze\,|\nabla(\nabla\Phi_{\mathrm{AC}})|}{m\omega^2} \ll 1\,. \tag{2.24}$$

Moreover, the ion velocity inside the RF-field needs to be slow with respect to the oscillating field. Additionally, the magnetic component of the electromagnetic field can safely be neglected as long as the ion velocity is small compared to the speed of light. In the here described experiments, however, permanent collisions with buffer gas molecules generally lead to rather slow ions.

Ring Electrode Guides and Funnels

When ions need to be guided through regions of elevated pressures where many collisions with neutral gas molecules occur, ring electrode arrangements are advantageous over other multipole guides because they allow the application of an homogeneous electric field along the flight axis, which drives the ions forward. Using ring electrode ion guides, ions can overcome areas with even counter propagating gas flows. Additionally, when the inner diameter of the

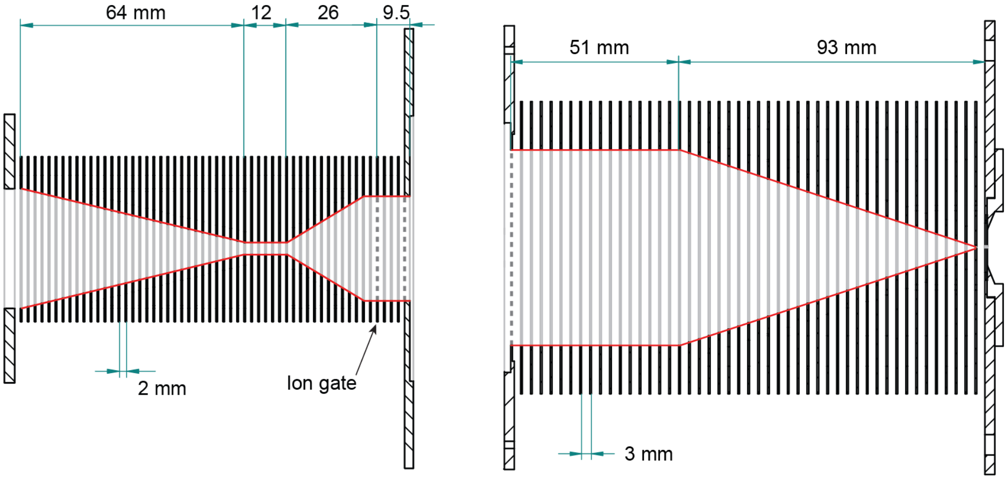

(a) Entrance funnel **(b)** Exit funnel

Figure 2.11: Dimensions of the ring-electrode RF ion funnels that are used to radially collect, focus, and trap ions. The entrance funnel (a) consists of four different regions. The narrow middle section serves as a conductance limit (C_2 in Figure 2.4) and is succeeded by the trap region. Ions are injected into the drift tube over the last 9.5 mm. The exit funnel (b) radially focuses diffusionally spread ion clouds through a 0.5 mm conductance limit (C_3 in Figure 2.4). Grids (denoted by dotted lines) are applied to the ion gate, the last, drift-tube preceding electrode and the first, drift-tube succeeding electrode to homogenize electric fields.

ring electrodes progressively decreases, clouds of ions can be effectively radially focused and guided towards conductance limiting exit orifices [101, 102]. Two of these so-called ion funnels are implemented in the here presented experimental setup, in addition to one segmented, cylindrical ring electrode guide. The funnels are based on a previously published design from the Bowers group [40] and will be described briefly in the following paragraphs.

A CAD model of the ring electrode funnels and guides can be found in Figure 2.4 and in Figure 2.11, a detailed view of the funnel dimensions is provided. The entrance as well as the exit funnel consist of stainless steel electrodes that are stacked onto accurately shaped ceramic rods for proper positioning. Spacing between electrodes is implemented *via* insulating spacers or silicone O-rings. The latter option is chosen when gas flows need to be restricted to the inner part of the funnel. It it worth mentioning that the material of the O-rings can have a severe influence on the electric oscillation behaviour of the electrode stack [103]. Fluorinated elastomers, as for example the standard O-ring material Viton®, are to be avoided since they typically feature higher dissipation factors DF and higher permittivities ϵ_r than other materials, leading to power losses in the electronic oscillator circuit and increased capacities of the electrode arrangements, respectively, both being unfavourable properties from an experimentalists point of view. Electrical contact is established through printed circuit boards (PCBs) that are directly attached to the electrode stacks. These PCBs are fabricated from a vacuum compatible polyimide material and contain the necessary capacitors, resistors, and RF chokes to apply the DC and AC voltages to the electrodes.

The hourglass-shaped entrance funnel (Figure 2.11 (a)) consists of 55 electrodes, which are divided into four sections. The first 64 mm section radially focuses ions that enter the 35 mm funnel opening through the ESI capillary (Figure 2.6 (b)) and transports them towards the conductance limiting section, which is 3.5 mm in diameter and 12 mm in length (C_2 in Figure 2.4). On the following 22 mm, the diameter of the electrodes progressively opens to about 28 mm and remains constant for the remaining 12 mm, or 6 electrodes. A 70 LPI mesh (Ni) is applied to the electrode that is fourth from last (dashed line in Figure 2.11). Applying a higher DC voltage to this *ion gate* with respect to the neighbouring electrodes will create a trapping barrier, which is used to accumulate ions prior injection into the drift tube. The ion gate and the last 9.5 mm section is screened from the RF potentials and carry only DC voltages. This section can be utilized to collisionally activate ions by applying an electric field of up to 200 V cm^{-1} strength (see Section 2.5.3). An additional mesh is attached to the last electrode to prevent inhomogeneous electric fields to penetrate into the drift region. Characteristics of the trap and the injection/activation region will be discussed in Section 2.5.

The exit funnel (Figure 2.11 (b)) is required to guide the diffusionally spread ion cloud through the 0.5 mm conductance limiting orifice at the end of the funnel (C_3 in Figure 2.4). It consists of 47 evenly spaced electrodes (d = 3 mm) that, after a 51 mm section of constant diameter, taper over a length of 93 mm from 59 mm to 2.5 mm inner diameter. A mesh, similar to the ones utilized in the entrance funnel, is attached to the first electrode (dashed line in Figure 2.11 (b)), which marks the end of the drift region. It is needed to homogenize the electric fields at the end of the drift tube and to screen penetrating RF fields.

The cylindrical ring electrode ion guide was designed to transport ions exiting the conductance limit C_3 of the exit funnel through two differentially pumped stages into the high vacuum regime of the quadrupole region (see Figure 2.4 for the CAD model). To accommodate the vacuum ports of a forepump and a small 300 L s^{-1} turbo pump, it has to span over a total distance of approximately 219 mm. It thus consists of two nearly identical segments each comprised 47 electrodes with a 3 mm spacing and an inner diameter of 5 mm, terminated by conductance limits of 2 mm inner diameter (C_4 and C_5 in Figure 2.4, respectively). In contrast to the electrodes of the ion funnels, the ring electrodes of the cylindrical guide are mounted directly onto the connector sockets of the PCBs, which, in turn, are then mounted in a supporting aluminum construction. This sandwich-type assembly greatly simplifies the overall design and reduces the amount of special machined parts. In addition, the fact that no further material is needed between the electrodes helps to minimize the overall capacity of the oscillating circuit.

Electric field strengths reach their highest values at sharp edges and (microscopic) peaks at the surface of the electrodes. To smoothen the electric potential gradients and reduce the risk of electrical discharges, all electrodes of the entrance and exit funnel, as well as of the cylindrical ring guide were electropolished, an electrochemical method to reduce surface roughness. In this procedure, each electrode was placed inside a heated (~ 80°C) electrolyte solution (20% H_2O, 20% H_2SO_4, 60% H_3PO_4) between two parallel Cu-cathodes. A positive voltage was applied to the anode (work piece) with respect to the cathodes to yield an anode current density of ~ 0.26 A cm^{-2}, corresponding to a current of 3–18 A depending on the size of the electrode. After ~ 2.5 minutes, the previously dull surface of the electrode was transformed into a mirror-like finish and sharp edges were visibly removed. This procedure helped to increase the threshold voltages for electrical discharges for the ion funnels and guides.

Stable Operation

After the ion funnels and ion guides have been described in the previous paragraphs, some important relationships and requirements for a successful ion transmission will be presented in the following section. Those will be discussed in consideration of the actual electrode geometries of the ion funnels.

With the Expression 2.23 for the effective potential of the ring electrodes, the potential at the axis of the electrode arrangement ($r = 0$) directly follows

$$V^*(0,z) = \underbrace{\frac{zeV^2k^2}{4m\omega^2\, I_0^2(k\rho_0)}}_{\text{potential well } V_{\max}} \sin^2(kz)\,. \tag{2.25}$$

Expression 2.25 illustrates that the effective potential is of a quadratic sinusoidal form on the axis of the ion guide and, thus, creates potential wells that may influence the ion trajectories. These axial potential wells are negligibly small compared to the steep walls that are formed towards the electrodes as long as the inner diameter is much larger than the distance of two electrodes ($\rho_0 \gg d = \pi/k$), but becomes increasingly important when the inner diameter and the distance are of similar size ($\rho_0 \approx d$). Especially in the case of the exit funnel, where $d/\rho_0 \approx 0.8$ near the exit orifice, this can lead to effective trapping of lighter ions, as $V^* \propto m^{-1}$. To illustrate this, the effective potential is plotted exemplarily for the last section of the exit funnel in Figure 2.12. The detailed view of the potential in (b) (left) shows the formation of axial potential wells with amplitude $V_{\max}$ near the exit orifice where ions will be trapped. Thus, the electric DC field in axial direction needs to be large enough to compensate for these trap potentials as shown in (b) (right).

To estimate approximate values of the electric DC field and the consequences for the transmittable m/z range, the effective axial field can be directly derived from Expression 2.25 using the relation $E^* = -\nabla V^*$. It follows a criterium for the axial DC field E_{DC} [102]

$$E_{\mathrm{DC}} > k\, V_{\max}\,, \tag{2.26}$$

with $V_{\max}$ as defined in Equation 2.25. In Figure 2.13, the electric field E^* corresponding to

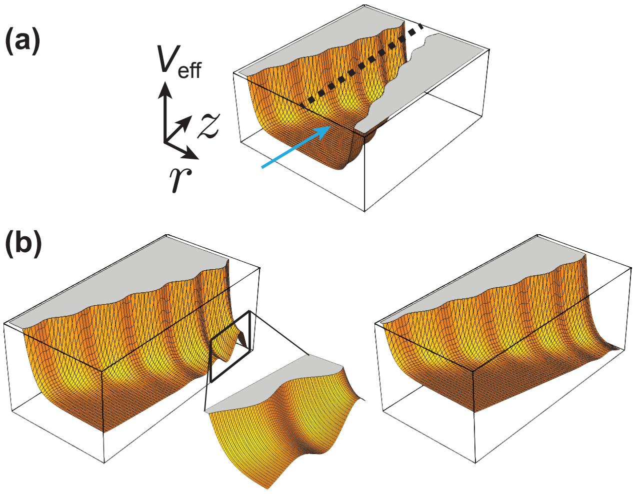

Figure 2.12: Representation of the effective potential V^* near the exit orifice of the exit funnel (Figure 2.11) for arbitrary parameters. (a) The blue arrow indicates the ion flight direction. ((b), left) A detailed view of the potential at the axis illustrates the formation of axial potential wells, which can lead to trapping of ions in regions where $d \sim \rho_0$. ((b), right) The electric DC field must be large enough for the ions to overcome these potential wells.

the axial potential well is evaluated for the exit funnel as a function of the electrode inner diameter for three different m/z values and typical operating parameters; an RF amplitude of $V_{pp} = 80$ V, and two different frequencies of $f = 0.6$ MHz and 1.8 MHz, represented by solid, and dashed lines, respectively. Vertical lines indicate the inner diameters of the last three exit funnel electrodes. The gray area represents typical values of the DC electric field (8–15 V cm^{-1}), which needs to be large enough to compensate the effective field E^* at the last electrode (2.5 mm diameter) for a successful ion transmission. At $f = 0.6$ MHz operation, the m/z 1000 ions (green, solid line) can easily be transmitted, however, lighter ions are effectively blocked (red, solid line). Increasing the frequency to $f = 1.8$ MHz decreases the trapping potential for the lighter ions (red, dashed line), however, might be disadvantageous for the axial focusing of heavier ions. In addition to the DC electric field, the flow of the buffer gas through the conductance limiting exit orifice will have an influence on ion transmission. As this flow occurs in the same direction as the ion motion, this buffer gas drag force may help ions to overcome potential wells that occur close to the exit.

Since the effective potential in Equation 2.23 as well as the stability parameter η in Equation 2.24 are both inversely proportional to m/z and the quadratic frequency. The adiabaticity condition 2.24 may easily be met for a large product of $m\omega^2$, which at the same time decreases the potential V^* necessary to prevent collision of the ions with the electrodes. Thus, finding the best experimental parameters is always a compromise between a broad transmittable m/z-range and effective transmission of particular m/z-windows.

In the case of the entrance funnel one more condition has to be fulfilled for successful ion

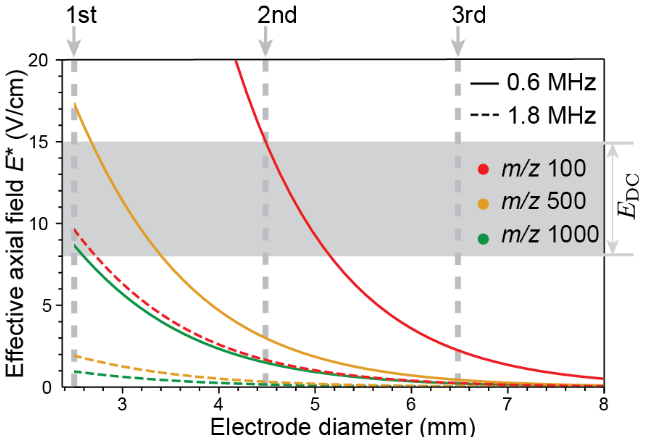

Figure 2.13: The effective electric field $E^* = -\nabla V^*$ near the exit orifice of the exit funnel for m/z 100 (red), 500 (orange), and 1000 (green) ions, and two different RF frequencies (dashed and solid lines). Indicated in gray is the typical experimental range for the DC electric field. Vertical lines indicate the inner diameters of the last three electrodes prior to the exit orifice. The DC field E_{DC} needs to be of higher values than the effective field E^* at the smallest diameter for successful transmission.

transmission. To prevent neutral species to enter the drift tube from the source region, a small pressure gradient is applied between these sections. Therefore, the electric DC field in the 12 mm middle section of the ion funnel ($\o_i \approx 3.5$ mm) has to be large enough to overcome the drag force $F_{\mathrm{drag}} = m v_g / \tau$ [102] that the counter propagating buffer gas imposes on the ion, where v_g and τ are the buffer gas flow velocity and the velocity relaxation time, respectively. In terms of the electric DC field, this leads to the requirement

$$E_{\mathrm{DC}} > \frac{m}{ze}\frac{v_g}{\tau} \,. \tag{2.27}$$

At a pressure difference of ~ 0.5 mbar between the drift tube and the source region, the maximum buffer gas velocity inside the middle section of the entrance funnel can be approximated to $v_g \approx 170$ m s^{-1} assuming laminar flow in tube-like geometries.* For a typical m/z 1000 biomolecular ion with a collision cross section of ~ 1000 Å^2 and a relaxation time of $\tau \approx 10^{-6}$ s, which is typical for the applied pressure regimes† [102], the minimum electric field calculates

---

[*] The maximum laminar flow velocity on the axis of a tube can be calculated using

$$v_{\mathrm{g,max}} = \frac{1}{4\eta}\frac{\Delta P}{\Delta x}R^2 \,,$$

where η is the gas viscosity, ΔP and Δx are the pressure difference and length of the tube of radius R.

[†] For $v_{\mathrm{ion}} < v_{g,\mathrm{th}}$, the relaxation time τ can be calculated using [102]

$$\tau = \frac{m + m_g}{m_g n \Omega\, v_{g,\mathrm{th}}}\left(\frac{0.75}{1 + 0.2\,(v/v_{g,\mathrm{th}})^2}\right) \qquad ; v_{g,\mathrm{th}} = \sqrt{\frac{8k_{\mathrm{B}}T}{\pi m_g}}$$

with the buffer gas number density n, the mean thermal velocity $v_{g,\mathrm{th}}$, and the ion-buffer gas CCS Ω.

to $E_{\mathrm{DC,min}} \approx 20$ V cm^{-1}. This can be achieved by applying a voltage difference of $\sim$ 25 V over this section, which lies well within the usual experimental settings. The effects that may arise when lower DC fields are applied are discussed in Section 2.5.3.

2.4.4 Mass Filters- and Analyzers

Two different mass spectrometers are employed in the DT setup to analyze or filter molecules with respect to their mass-to-charge ratios. A commercial quadrupole mass filter (Extrel, USA; 19 mm rod diameter, 200 mm length) with a mass range of up to 4000 amu is located in the high vacuum region behind the conductance limit C_5 of the second cylindrical ring electrode guide (see Figure 2.4). It is preceded by an einzel lens stack of 25 mm length and a focusing lens, 5 mm in diameter. This mass filter is operated at 440 kHz and is typically used to select ions of a specific *m/z* following either direct detection to record arrival time distributions of a specific species or to further interrogate the *m/z*- and drift-time separated species with intense laser light.

Fast *m/z*-analysis is achieved *via* time-of-flight (TOF) mass spectrometry with a Wiley-McLaren type setup [104]. The extraction plates at a distance of 20 mm are pulsed to high voltages of several kilovolts ($\sim$ 4–5 kV) and the *m/z*-dependent flight time of the ions is measured to yield a mass spectrum. The flight time follows the relationship

$$t_{\mathrm{tof}} = \frac{L_{\mathrm{tof}}}{\sqrt{2Ue}} \sqrt{\frac{m}{z}} \ , \tag{2.28}$$

where L_{tof} is the length of the flight tube ($\sim$ 0.5 m), e the elementary charge, and U the applied acceleration voltage, and is for the here described setup typically on the order of a few tens of μs. To account for the initial velocity of the ions, which is perpendicular to the velocity towards the TOF detector, two parallel deflection plates are mounted at the beginning of the flight tube and a voltage of ± (50–100) V is typically applied to compensate the $\sim$ 5–10 eV transversal kinetic energy of the ions, which would otherwise lead to a displacement of a few cm. With this setup, a mass resolution $M/\Delta M$ of $\sim$ 500 is achieved.

2.4.5 Electronics & Software

Most DC voltages are provided by manually adjustable and in-house designed electronic power supplies. These include the source voltages, all funnel and guide voltages as well as voltages for ion optics and deflection. High voltages for detectors ($\sim$ 1–10 kV) and TOF plates ($\sim$ 3–5 kV) are generated using commercial power supplies.

Various different RF power supplies and oscillator designs are used to generate the high frequency oscillating voltages (0.5–1.8 MHz, 50–600 $\mathrm{V_{pp}}$) for ion funnels, ion guides, and the quadrupole guide. The most basic LC oscillator consists of a parallel circuit of the respective ion guide (C – capacitor) and a manually adjustable coil (L – inductor). The resonance frequency f_0 follows [105]

$$f_0 = \frac{1}{2\pi\sqrt{LC}} \; , \tag{2.29}$$

where L and C are the inductance and the capacitance, respectively. In case of the exit funnel and the quadrupole guide (see 2.4.3), the oscillator circuits are driven externally in resonance with relatively low-amplitude oscillations (maximum $\sim 60\ \mathrm{V_{pp}}$) generated by sine wave generators following amplification and transformation with hand-wound electrical transformer cicuits. More compact, in-house designed RF power supplies, which are based on this principle, are used to operate the entrance funnel and the ring ion guides.

A LabVIEW controlled National Instruments PXIe-1073 platform equipped with three modules provides analogue and digital in- and outputs that are used to generate control voltages for, *e.g.*, the quadrupole mass filter and the drift voltage power supply, to generate trigger sequences controlling the experimental cycle, and, most importantly, to record the signals from the two ion detectors. Control voltages can be generated using the 32 AO channels of a PXI-6723 module, which at a later stage will be used to control all DC power supplies. Signals from arrival time distributions are first amplified (typical gain 10^4–10^5, FEMTO DHPCA-100) and subsequently recorded with 16 Bit resolution and a maximum acquisition rate of 2 MHz using a NI PXIe-6363 module that also provides several digital ports, which are used for trigger generation. A ZTEC 4420 M-series oscilloscope module is used to record the amplified ($\sim 10^2$) signals from TOF measurements with 12 Bit resolution and a sampling rate of 1 GHz.

Several LabVIEW routines were programmed for hardware control, data acquisition, processing, storage, and visualization. Subroutines enable the direct determination of cross-section values, or the extraction of m/z-gate information from wavelength- (Section 2.6) or drift-time (Section 2.5.2) TOF scans, which are stored in an hierarchic data format called HDF5. Data from ATD as well as from TOF measurements can be processed with a repetition rate of up to 50 Hz.

2.5 Machine Performance & Characteristics

This section provides data from test and benchmark measurements that serve the characterization of the drift-tube (DT) instrument and the explanation of experimental procedures. The setup's capabilities in terms of, *e.g.*, ion-mobility resolving power or ion transmission (Sections 2.5.2 and 2.5.5, respectively) are discussed alongside with current deficiencies such as ATD peak broadening effects, ion heating in RF ion guides (Section 2.5.3) or errors in the determination of collision cross-sections (Section 2.5.4). In the following Section 2.5.1, however, the different possible modes of operation are briefly explained and typically applied instrument parameters are summarized, which may serve instrument optimization at a later point.

2.5.1 Typical Operating Conditions

Depending on the purpose, the DT instrument can be utilized as a mass spectrometer, as an ion-mobility spectrometer, or as a preparative tool for m/z and ion-mobility selective laser experiments. The experimental procedures are the following:

Mass Spectra. Mass spectra of an electrosprayed sample can be acquired by either scanning the quadrupole mass filter and simultaneous recording of the m/z dependend ion current using the linearly aligned detector or by pulsing the TOF mass spectrometer and recording of the m/z dependent flight time. Both methods require a continuous ion current. The acquisition of quadrupole spectra is generally more time consuming.

Arrival Time Distributions. For the acquisition of arrival time distributions (ATDs) of a specific species, ions are first accumulated in the trap by applying a small trapping voltage to the ion gate with respect to the neighbouring electrodes and then pulsed into the drift tube at a repetition rate of typically 5–20 Hz. The quadrupole mass filter is fixed at the m/z value corresponding to the species of interest. The ion current as a function of the drift time of the m/z-selected species is recorded using the linear detector to yield the ATD.

Photodissociation. For drift-time and m/z selective photodissociation experiments, the trap is pulsed and only ions within a narrow drift-time window ($\sim 100\,\mu$s) are allowed to enter the quadrupole mass filter, which is fixed at the m/z value of interest. Ions that do not arrive at the mass filter within the desired drift-time window are deflected electrostatically at the first einzel lens. After drift-time and m/z selection, ions are irradiated with intense laser light and subsequently analyzed using the TOF mass spectrometer to yield photofragment mass spectra. For further details, see Section 2.6.

Parameter Scans. Hypothetically, TOF mass spectra of drift-time and m/z-selected species can be acquired as a function of any parameter that can be systematically changed (or scanned). At the current stage the LabVIEW software is capable of recording and processing TOF mass spectra as a function of the drift time (see discussion at the end of this section) and of the FEL wavelength. For the latter option, photofragment TOF mass spectra of drift-time and m/z-selected species are simply acquired while scanning the wavelength of the FEL (see Section 2.6 for details).

A list of typical experimental parameters and characteristic reference values is given in Table 2.2. The exact values for pressures, electric fields, etc., depends on the species of interest. For an increased ion transmission for species with $m/z \lesssim 300$, the higher RF frequency limit is applied. For weakly bound or structurally fragile species, the amplitude of the RF oscillation as well as the electric fields in the entrance funnel middle-, trap-, and injection section are of particular importance and should be reduced to establish *soft* conditions. The effects that

Table 2.2: Typical parameters for instrument operation. Ion optics and bias voltages are listed in the order of ion transmission (Figure 2.4). Higher RF frequencies are used for ions with $m/z \lesssim 300$.

Pressures:	(mbar)	
Drift pressure (Nitrogen / Helium)	2–3 / 3–6	
Differential pressure	0.3–0.6	
Electric fields:	(V cm^{-1})	
Entrance funnel, entrance section	1.5	
Entrance funnel, middle section	8–33	
Entrance funnel, trap section	2–12	
Entrance funnel, injection section	20–200	
Drift field	5–18	
Exit funnel	8–15	
Ring guide I	0.5–0.9	
Ring guide II	0.4	
Bias voltages & Ion optics:	(V)	
Gate – adjacent electrode (differential)	2–20	
Exit funnel – Guide I (differential)	0–5	
Guide I – Guide II (differential)	1	
Einzel lens 1 / (deflection)	-150 / (200)	
Quadrupole lens 1	-60	
Quadrupole (resolving) bias	25	
Quadrupole lens 2	-80	
Quadrupole guide bias	10	
Quadrupole lens 3	9	
Einzel lens 2	-50	
TOF Bias	12	
RF voltages:	(V_{pp})	(MHz)
Entrance funnel	50–180	0.56–0.78
Exit funnel	50–110	0.6–1.8
Ring guides	100–250	1.2–1.8
Quadrupole guide	200–600	0.48
Miscellaneous:		
Pulse rate	5–20 Hz	
IMS resolving power $t_d/\Delta t$	~ 40	
IMS duty cycle†	0.1–0.4	
TOF resolving power $M/\Delta M$	~ 500	
TOF duty cycle†	$0.25 \cdot 10^{-3}$–$1 \cdot 10^{-3}$	

†Time period that a measurement is being made over one measurement cycle.

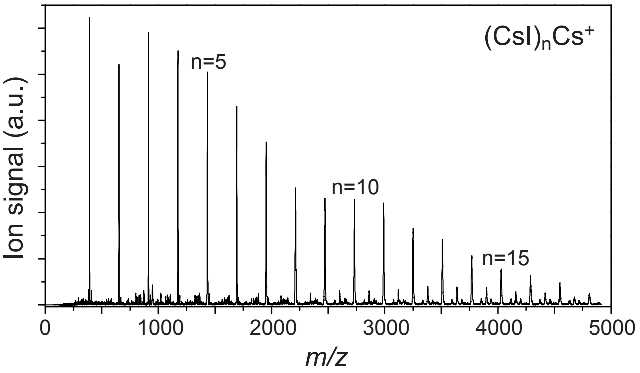

Figure 2.14: TOF mass spectrum of CsI clusters measured at the DT setup, illustrating the the high *m/z* transmission range of the instrument of up to $m/z \approx$ 5000. CsI clusters are often used for *m/z*-calibration.

these parameters may have on the molecular structure are discussed later in this section.

In order to illustrate the transmittable *m/z* range of the instrument, a typical TOF mass spectrum of CsI clusters generated by electrospraying a $\sim$ 100 mM solution of CsI is shown in Figure 2.14. The cluster distribution starts with the smallest species (CsI)Cs$^+$ and extends to the largest observed cluster (CsI)$_{18}$Cs$^+$ with an *m/z* of 4810. The *m/z* range of the TOF measurement is limited by the 50 μs acquisition time, which roughly corresponds to an *m/z* of 5000. The bare Cs$^+$ ion is also generated but can not be transmitted with the instruments settings that are needed for the transmission of larger clusters. Such TOF measurements of species with evenly spaced *m/z* values are usually recorded for fight-time to *m/z* calibration of the instrument.

2.5.2 Drift-Time Measurements

Direct determination of ion-neutral CCSs from arrival time distribution (ATD) measurement of *m/z*-selected ions is a key-feature of the DT instrument. It is often useful to compare experimental ion signals with the theoretical shape of an ATD. When only ions of a single structure that does not interconvert or react on the timescale of the experiment is present, the time-dependent signal of the ion cloud exiting the drift region is given by the gaussian-like distribution [56]

$$\Phi(t) = \int \underbrace{\frac{C}{\sqrt{2\pi D t'}}\left(v_\mathrm{d} + \frac{L}{t'}\right)\exp\left[\frac{-(v_\mathrm{d}t' - L)^2}{4Dt'}\right]}_{\text{signal with } \delta\text{-pulse ion source } \Phi_\mathrm{p}(t')} \underbrace{P(t-t')}_{\text{gate pulse}} \,\mathrm{d}t' \,, \tag{2.30}$$

where C is a scaling factor, L the length of the drift tube, and v_d and D are the average drift velocity and the diffusion coefficient of the ions, respectively. The fact that ions do not enter the drift region in form of a δ-pulse but are injected by the ion gate pulse $P(t)$ of finite length (typically a rectangular function) is accounted for by a convolution of the theoretical signal $\Phi_\mathrm{p}(t)$ with the gate pulse $P(t)$.

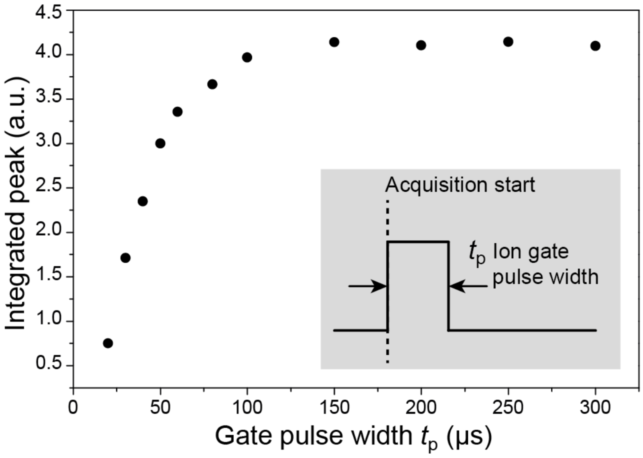

Figure 2.15: Integral of the $(CsI)_5Cs^+$ ion current in ATD mode (pulsed ion trap) as a function of the ion gate pulse width t_p. The integral is proportional to the number of ions that is released from the ion trap.

A series of instrument-characterizing measurements of ATDs is presented in the following paragraphs.

Trap Release Time

Ion trajectory simulations using SIMION reveal that the electric DC and RF fields inside the ion trap lead to accumulation of ions inside a toroidal geometry [40]. On basis of these simulations, the time that ions need to exit the ion trap, once the blocking voltage is switched off, is estimated to 80–100 μs. To experimentally confirm this, the ion current (within one experimental ATD cycle) of a particular species was integrated as a function of the gate pulse width t_p in a range of 20–300 μs. This integral is directly proportional to the number of ions that is released from the ion trap at a repetition rate of 20 Hz and a buffer gas pressure of $\sim$ 4 mbar. For this experiment the $(CsI)_5Cs^+$ cluster was chosen, as its mass and size are representative for the types of ions that are typically studied with the DT instrument (see next paragraph). The result, shown in Figure 2.15, indicates that the ion trap is effectively depleted after $\sim$ 100 μs and therefore confirms the simulation. However, the exact value strongly depends on the type of ions and instrument parameters such as the buffer gas pressure and the electric fields inside the ion trap. This measurement may serve as a reference point as average ion species and parameters were chosen (see Table 2.2).

ATDs and CCS Determination

After determination of the optimal trapping and injection conditions for the proband molecule $(CsI)_5Cs^+$, the drift voltage V_d was varied to confirm its linear relationship to the arrival time

$$t_\mathrm{D} = t_\mathrm{d} + t_0 = \underbrace{\frac{L^2}{K}}_{\text{slope}} \frac{1}{V_\mathrm{d}} + \underbrace{t_0}_{\text{offset}} . \tag{2.31}$$

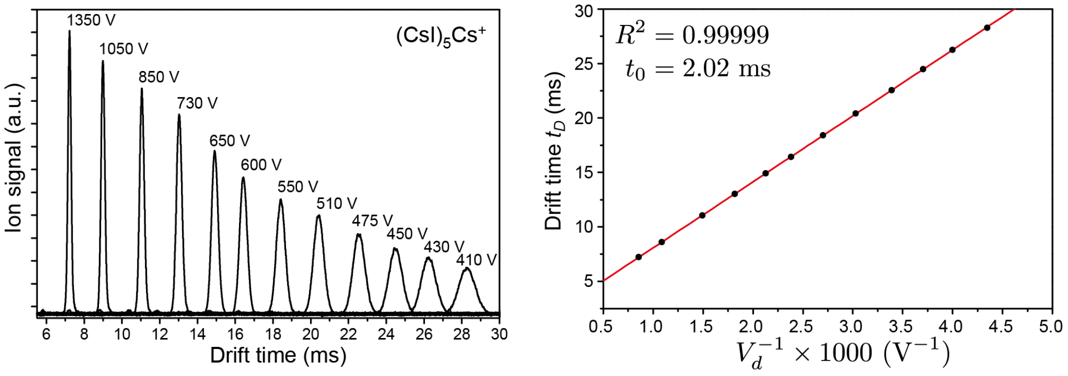

(a) ATDs of $(\mathrm{CsI})_5\mathrm{Cs}^+$ **(b)** t_D–V_d^{-1} plot

Figure 2.16: (a) Arrival time distributions (ATDs) of $(\mathrm{CsI})_5\mathrm{Cs}^+$ clusters at different drift voltages V_D. (b) t_D–V_d^{-1} plot for the drift time data on the left to confirm the high linearity between drift time t_D and inverse drift voltage V_d^{-1}.

This expression simply represents the definition of the mobility K (Equation 2.1), with the length of the drift tube L and the substitution for the electric field $E = V_\mathrm{d}L^{-1}$. The time constant t_0 is instrument and species dependent to some extent and represents the time that the ions under investigation spend outside the drift tube, *i.e.* inside ion funnels, guides, and the quadrupole mass filter region. Thus, the experimentally determined drift time t_D is always greater than the *real* drift time t_d, the time that ions spend inside the drift region. In Figure 2.16 (a) several ATDs of $(\mathrm{CsI})_5\mathrm{Cs}^+$ ions at drift voltages corresponding to electric drift fields of 5–17 V cm^{-1} are shown. The linear relationship between t_D and V_d^{-1} is confirmed by the highly linear regression ($R^2 = 0.99999$) in Figure 2.16 (b), where the position of the drift peaks in (a) are plotted as a function of V_d^{-1}. As indicated in Equation 2.31, the mobility K of the ions can then directly be determined from the slope of this linear regression curve and the Mason-Schamp Equation 2.4 allows to calculate the collision cross-section (CCS) when experimental parameters such as the buffer gas pressure and temperature are known. In this particular example helium buffer gas was used at a pressure of $\sim$ 4 mbar at room temperature and the CCS calculates to 135 Å^2.

IMS Peak Width and Resolving Power

The peak shape of an ATD can contain various information, for example, about the size and the structural variety (or uniformity) of a species, or about structural dynamics, ion-neutral interaction or even molecular reactions inside the drift tube. A drift-time measurement of ions of a single non-reactant species will result in an ATD according to Equation 2.30. However, ATD peak shapes other than the theoretical one can also be of experimental origin, for example, due to coulomb repulsion (at high ion densities), due to diffusion in ion transfer regions, or due to an electronically limited bandwidth.

To test whether any of these peak broadening mechanisms play a role in the DT instrument,

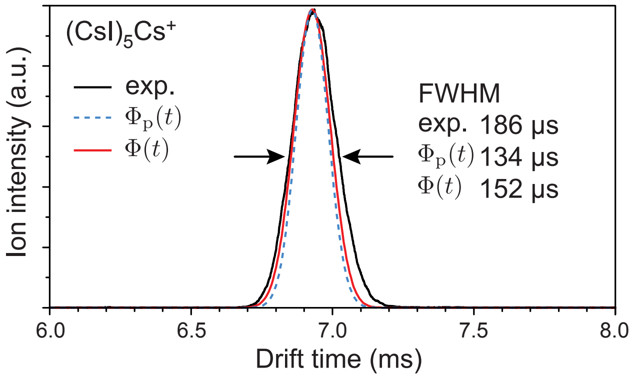

Figure 2.17: Arrival time distribution (ATD) of $(CsI)_5Cs^+$ clusters. The width (FWHM) of the experimental drift peak (black) is only marginally larger than the width of a theoretical drift peak $\Phi(t)$ (red). The 100 μs injection pulse leads to a slight broadening of the theoretical drift peak $\Phi_p(t)$ (dashed) assuming a δ-pulse-like initial ion distribution.

the experimentally determined ATD of $(CsI)_5Cs^+$ was compared to the theoretical signal of a single ion species. The choice of ion is motivated by previous IM-MS studies on CsI clusters of different sizes, where only narrow drift peaks were observed for all investigated species [106, 107]. This suggests that a single structure is present in each case (or that all coexisting structures of the same species are of similar sizes or quickly interconverting). A representative ATD of $(CsI)_5Cs^+$ measured at the DT instrument at intermediate conditions is shown in Figure 2.17 (black line). The dashed line represents the theoretical ATD $\Phi_p(t)$ of ions with an initial ion distribution having the form of a δ-pulse and traversing the drift tube and the exit funnel, assuming the previously determined CCS of the CsI cluster (see above; 135 Å^2). This ATD was subsequently convoluted with the 100 μs injection pulse $P(t)$ to yield the final theoretical form of the ATD $\Phi(t)$ (red) according to Equation 2.30. For ions of this size, the injection pulse only marginally contributes to the overall peak shape but may become more important for smaller species. Here, $\sim$ 13 % (18 μs) of the theoretical peak width can be attributed to the finite injection pulse. The peak width of the experimentally determined ATD differs little from the theoretical value and the deviation of 34 μs may be attributed to many of the above-mentioned experimental or molecular peak broadening mechanisms. It is likely that additional diffusion of the ion cloud inside ion funnels and guides or a structural heterogeneity of the proband molecules plays a role at these intermediate experimental conditions. This reassuring result demonstrates that the ATD peak shape is mainly given by diffusion inside the drift region and, therefore, it can be diagnostic in ion structure studies.

The capability to separate species of different cross-sections is essential for any IM-MS instrument. In this context, it is useful to consider how the width of a theoretical drift peak evolves with changing instrument parameters, such as the drift voltage V_d. An expression for the width of a drift peak can be directly deduced from Equation 2.30 for the theoretical drift peak and comparison with a Gaussian distribution

$$f(x) = \frac{1}{\sigma\sqrt{2\pi}} \exp\left(\frac{-(x-\mu)^2}{2\sigma^2}\right) , \qquad (2.32)$$

with the mean μ and the variance σ^2. Under consideration of the Einstein Relation 2.2, the parameters μ and σ can be identified as

$$\mu \mathrel{\hat{=}} t_\mathrm{d} \qquad \text{and} \qquad \sigma \mathrel{\hat{=}} \sigma(t) = \sqrt{2\frac{k_\mathrm{B}T}{ze}\frac{t_\mathrm{d}}{V_\mathrm{d}}\,t} \tag{2.33}$$

and therefore for the full width at half-maximum (FWHM, Δt) of a drift peak of an ion cloud after having traversed the drift region at $t = t_\mathrm{d}$

$$\Delta t = 2\sqrt{2\ln(2)}\,\sigma(t_\mathrm{d}) = \sqrt{16\ln(2)\frac{k_\mathrm{B}T}{ze}}\,\frac{t_\mathrm{d}}{\sqrt{V_\mathrm{d}}}\,, \tag{2.34}$$

The width Δt is, thus, a linear function of $t_\mathrm{d}/\sqrt{V_\mathrm{d}}$, which should hold for the widths of the $(\mathrm{CsI})_5\mathrm{Cs}^+$ drift peaks in Figure 2.16 (a). To confirm this linear behaviour, Figure 2.18 shows the experimentally determined widths Δt_exp of these drift peaks as a function of $t_\mathrm{d}/\sqrt{V_\mathrm{d}}$ (open circles). To account for diffusion that occurs outside the drift region, the previously determined time offset t_0 was used to calculate the additional gain in peak width Δt_0, under the assumption that t_0 mostly represents the time that ions spend inside the drift-pressure region of the exit funnel. Subsequently this constant gain in peak width $\Delta t_0 \approx 85\,\mu\mathrm{s}$ was subtracted from the experimental width Δt_exp to yield the widths of the drift peaks after the time $t = t_\mathrm{d}$ when ions exit the drift tube (solid circles). For larger values of $t_\mathrm{d}/\sqrt{V_\mathrm{d}}$ the data is in good agreement with the linear relationship found in Equation 2.34 (red line), however, increasingly deviates from the theoretical model for values of $t_\mathrm{d}/\sqrt{V_\mathrm{d}} \lesssim 0.4$.

This deviation clearly is of instrumental origin. While the center of the drift peaks, *i.e.* the drift time t_d, follows the expected behaviour (Figure 2.16), the width of the signals does not. Any mechanisms that permanently contribute to the peak width will be more pronounced when the overall peak width is small – at short drift times t_d, high drift voltages V_d, and consequently at small values of $t_\mathrm{d}/\sqrt{V_\mathrm{d}}$. The finite injection pulse, for example, will then increasingly contribute to the overall peak width. Additionally, the ion transient time inside the guides may also lead to further diffusion of the ion cloud. Furthermore, an increased transient time for ions that enter the exit funnel with a radial displacement (and thus, travel a longer distance to the exit orifice than ions at the radial center) may lead to broadening of the drift peak of up to a few tens of μs. Yet another reason for the observation of non-ideal drift signals are small inhomogeneities of the electric field inside the drift region. In fact, as will be shown in Section 2.5.4, any deviation of the drift field from the optimal, homogeneous form will lead to an increase in drift time and may also influence the ATD peak shape.

These effects that contribute to the deviation of Δt_exp from the theoretical line have a profound impact on the IMS resolving power $R = t_\mathrm{d}/\Delta t$, for which an expression follows

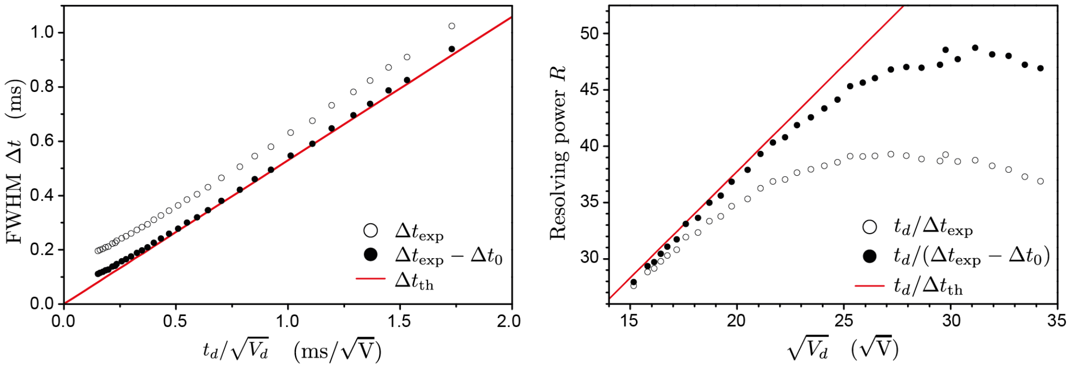

(a) ATD peak width Δt **(b)** IMS resolving power R

Figure 2.18: (a) The ATD peak width Δt as a function of $t_{\mathrm{d}}/\sqrt{V_{\mathrm{d}}}$ and (b) the corresponding resolving power R as a function of $\sqrt{V_{\mathrm{d}}}$. Open circles represent the experimentally determined widths of the $(\mathrm{CsI})_5\mathrm{Cs}^+$ drift peaks in Figure 2.16 and the resulting resolving power, respectively. Solid circles represent the widths and the resolving power, respectively, obtained after subtraction of the constant width Δt_0 that is attributed to diffusion of the ion cloud during the time t_0, under the assumption that t_0 mostly represents the ion transient time inside the exit funnel. The red lines represent the theoretical curve progressions. The data deviates from the theoretical model for high drift voltages V_{d} (see discussion).

directly from Equation 2.34:

$$R = \frac{t_{\mathrm{d}}}{\Delta t} = \left(16\ln(2)\frac{k_{\mathrm{B}}T}{ze}\right)^{-1/2}\sqrt{V_{\mathrm{d}}}\,. \tag{2.35}$$

This expression* implies a linear relationship between the resolving power R and the square root of the drift voltage V_{d}, which is shown in Figure 2.18 (b) for the example of the $(\mathrm{CsI})_5\mathrm{Cs}^+$ cluster ions (red line). The open circles represent the experimentally determined resolving power from the ATDs in Figure 2.16 (a) and the solid circles represent the DT resolving power obtained after subtraction of the additional broadening Δt_0 inside the transfer regions. The resolving power linearly increases until $\sqrt{V_{\mathrm{d}}} \approx 22$, reaches a maximum at $\sqrt{V_{\mathrm{d}}} \approx 31$ and subsequently declines at higher values of $\sqrt{V_{\mathrm{d}}}$. Thus, highest resolving powers are, under these experimental conditions, achieved at a drift voltage of $V_{\mathrm{d}} \approx 960$ V, corresponding to an electric drift field of $E_{\mathrm{d}} \approx 12$ V cm^{-1}.

This illustrates that the resolving power is damped by the limited ATD peak width. The instruments behaviour is by no means abnormal and has been reported for other IM-MS instruments as well [40]. However, instrument characteristics in terms of peak width and resolving power are generally difficult to investigate and future experiments have yet to address these limitations. Nevertheless, Expression 2.35 suggests that the resolving power R can still be increased by simply extending the length L of the drift tube and linearly scaling up the optimal drift voltage V_{d}, thus, keeping the drift field E_{d} at its maximum feasible value.

---

*This derivation of the IMS resolving power is in accordance with previously published ones [55].

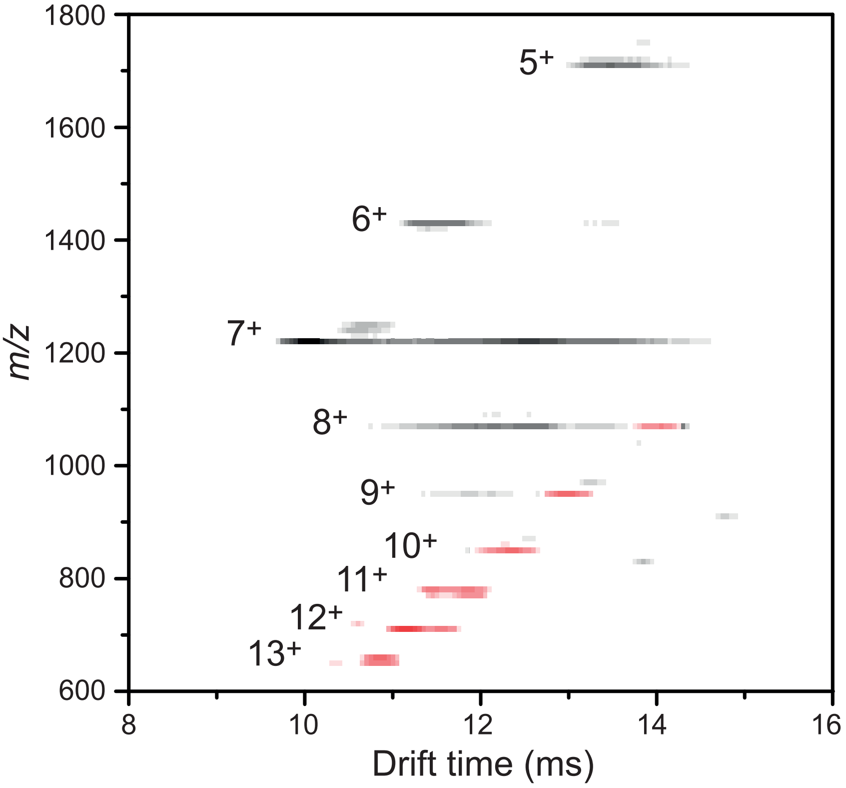

Figure 2.19: Data from nested drift-time TOF measurements of ubiquitin electrosprayed form methanol/water (black) and a similar sample containing 2 % of formic acid (red). TOF spectra were taken in steps of 50 μs and the m/z axis was binned in steps of 10 m/z to improve visualization.

Nested Drift-Time TOF Measurements

As described in the beginning of this section, the DT instrument is capable of acquiring TOF mass spectra of drift-time and m/z-selected ions as a function of any scannable parameter. To quickly obtain a full picture of a sample in terms of m/z and size distributions, it is useful to acquire TOF spectra of the electrosprayed ions as a function of the drift time. To do so, the instrument is operated in ATD-mode (pulsed ion trap) and the quadrupole mass filter only serves as a guide (RF-only). The exact time of the TOF pulse with respect to the time of trap release is then varied over the full drift-time range of all species and mass spectra are acquired at every drift-time step. Subsequently, data can be visualized in a 3D or intensity plot containing m/z as well as drift-time information. In contrast to drift-time measurements of individual ion species, this method effectively yields ATDs of all species within one measurement. It follows the development found in earlier IM-MS instruments [108] as well as in modern, commercial setups (see Section 2.7)

Figure 2.19 exemplarily shows data from drift-time scans of two different ubiquitin samples.

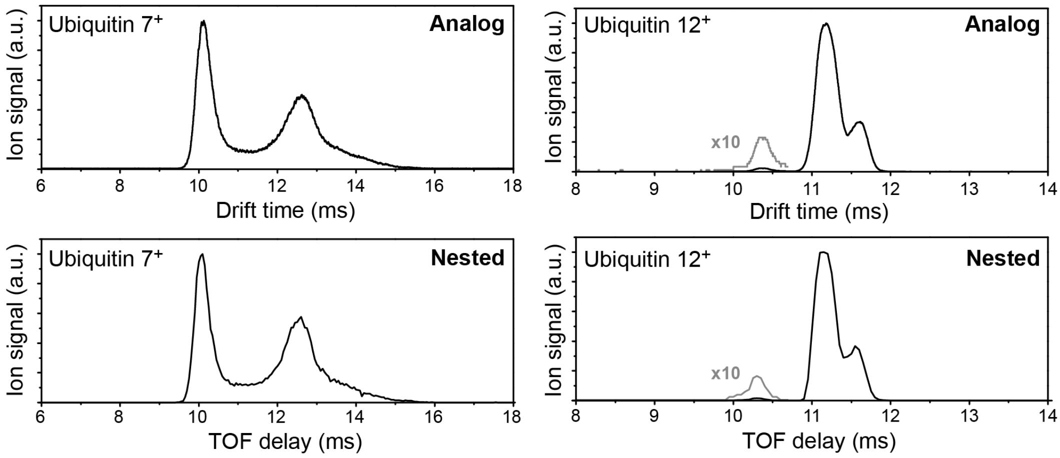

(a) Ubiquitin 7^+ **(b)** Ubiquitin 12^+

Figure 2.20: Comparison of ATDs from analog drift-time measurements (upper panels) to extracted data from nested drift-time TOF measurements (lower panels) as shown in Figure 2.19 for (a) 7^+ and (b) 12^+ ubiquitin ions. ATDs from these two different measurement methods are virtually identical and even low-intensity signals can be equally well resolved.

Ubiquitin electrosprayed from methanol/water (v/v, 50/50) and a similar sample containing 2 % of formic acid is depicted in black and red, respectively. The drift time (x-axis) was scanned in steps of 50 μs and the m/z information (y-axis) was binned in steps of 10 m/z to improve visualization. Hence, each slice in vertical direction represents one TOF mass spectrum, whereas each horizontal slice represents one ATD. The ion intensities in the individual mass spectra are contained in the colour intensity scale. Signals corresponding to charge states 5^+ to 13^+ are apparent and the transition from compact, native-like conformation with relatively short drift times for low charge states to elongated structures with longer drift times of higher charge states can be clearly identified in the signals corresponding to 7^+ and 8^+ ions.

Extraction of a specific m/z channel from these nested drift-time TOF measurements yields ATDs that are virtually identical to the ones from analog drift-time measurement where only one species is investigated at a time. This is illustrated in Figure 2.20 where ATDs from analog (upper panels) and nested (lower panels) drift-time measurements are shown exemplarily for ubiquitin 7^+ (a) and 12^+ (b) ions, respectively. Data from analog and nested measurements are virtually identical and even low-intensity features as the $\sim$ 10.3 ms signal of the 12^+ ions can be equally well resolved using both methods. Thus, the content of information from these nested drift-time TOF measurements illustrated in Figure 2.19 is comparable to the combined information from the mass spectra and ATDs of ubiquitin shown in Figures 1.3 and 1.4, respectively.

2.5.3 Ion Heating and Collisional Unfolding

Under typical experimental conditions, a biomolecular ion undergoes roughly 10^8–10^9 collisions with buffer gas molecules per second inside the the ion source, trap, and drift region. Collisional thermalization, on the other hand, is estimated to require only up to 10^4 collisions [89] and, thus, it can be expected that ions quickly reach thermal equilibrium with surrounding buffer gas molecules after transfer into the gas phase. However, if ions are subjected to more energetic collisions, it is possible to transfer enough energy into the system to induce unfolding of a compact structure or dissociation of larger complexes by breaking non-covalent interactions, or even to generate fragments by dissociating covalent bonds. When performed systematically, collision-induced unfolding (CIU) and subsequent IMS analysis can be useful for the study of, for example, protein or protein-complex structures [19, 109, 110].

In the DT IM-MS setup ions can be activated while injecting them into the drift tube by applying an electric field of up to 200 V cm^{-1} over a distance of $\sim$ 1 cm. However, ion activation can also occur unintentionally by means of RF heating inside ion funnels and the trap region [89, 111]. This plays a crucial role inside the 12 mm middle section of the entrance funnel where the counter-propagating buffer gas flow imposes a drag force onto the ions that needs to be compensated by the electric DC field E_{mid} (see discussion in Section 2.4.3). Here, the close spacial proximity to the entrance funnel electrodes may cause ions to experience the strong, alternating electric fields leading to larger amplitudes of the ions fast oscillating micromotions and, hence, increasing energies of ion-buffer gas molecule collisions. When the electric DC field E_{mid} is on the order of the lower limit for stable ion transmission (Requirement 2.27), an increased transient time subjects ions to an increased number of RF oscillation cycles and therefore increasing the amount of potentially high-energy collisions. Both, collisional unfolding as well as dissociation of covalent bonds inside the entrance funnel has been observed in various experiments on the DT setup. Additional to ion activation inside the entrance funnel, which will be further discussed in the following paragraph, dissociation of non-covalent bonds was also observed occur in the cylindrical ring guide transfer region subsequent to the exit funnel. Here, the mean free path of the ions between collisions with buffer gas molecules is in the mm-regime (see Section 2.4.1), making this region prone to induce post-ion mobility dissociation when the local electric fields are too high. This effect will be further discussed in Chapter 5.

RF Heating

To illustrate the effect of ion heating during injection into the drift tube as well as RF heating inside the entrance funnel middle section, ATDs of the conformationally very heterogeneous ubiquitin 7^+ ions ($m/z \approx 1200$) were recorded for different electric fields in the injection region E_{inj} and the entrance funnel middle section E_{mid}, respectively. Using the Requirement 2.27 it was estimated that for ions of $m/z \approx 1000$ and a size of $\sim$ 1000 Å^2, an electric DC field of at least 20 V cm^{-1} is necessary to safely overcome the drag force of the counter-propagating

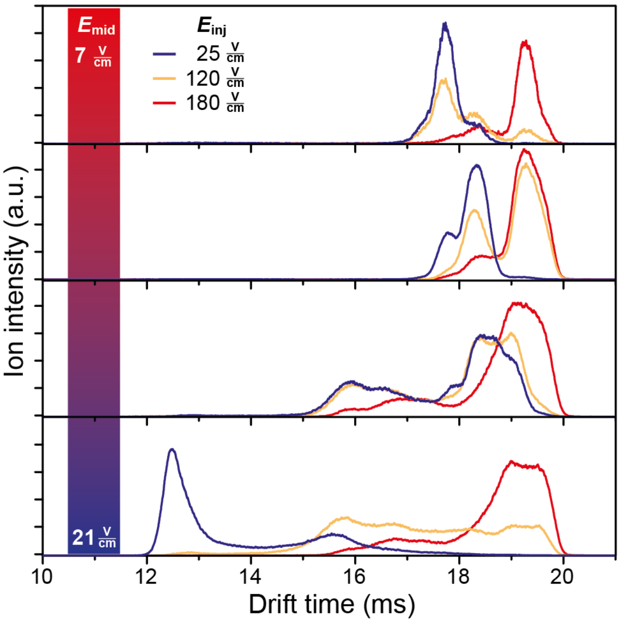

Figure 2.21: ATDs of ubiquitin 7^+ ions at different entrance funnel and injection conditions. The effect of pre-trap RF heating inside the entrance funnel increases with decreasing value of E_{mid} (bottom to top). For different values of E_{mid}, the electric field of the injection region was varied from low (25 V cm^{-1}, blue) to high (180 V cm^{-1}, red) values.

buffer gas. Therefore, the field E_{mid} was varied from 21 V cm^{-1} to 7 V cm^{-1} and for each step ATDs were recorded for different values of E_{inj}. The result is shown in Figure 2.21. The effect of pre-trap activation *via* RF heating increases from the lower to the top panel, whereas the different colours blue, yellow, and red indicate gentle, intermediate, and harsh injection conditions, respectively. It is interesting to observe how the different pre-trap activated species unfold with increasing injection energies (blue to red traces within one panel). At gentle conditions, mainly one compact conformational family is populated, which in terms of size corresponds to the native condensed-phase structure of ubiquitin with a CCS of ~ 1000 Å^2 [20]. When energized during injection into the drift tube, this family of conformers unfolds to a broad distribution of intermediate and unfolded conformers. When a narrower, partially unfolded, initial conformer distribution is generated, the conformational diversity of the final activated ions also seems decreased.

Surprisingly, pre-trap activation *via* RF heating does not lead to the same conformer distributions as activation during injection. This may, however, be attributed to the fact that not only the effect of RF heating increases but also the ion transmission (especially of larger, elongated ions) is affected at low values of E_{mid}. This makes a comparison between the two sections for ion activation inherently difficult. Nevertheless, it can be concluded that an initial narrow distribution of distinct conformers will lead to a similarly narrow distribution of conformers after activation (upper panels), which points to a certain connection between partially folded and extended conformational families of ubiquitin 7^+, as suggested by earlier studies [112] and more in-depth analyzed *via* photodissociation of conformer-selected ubiquitin ions in Chapter 4.

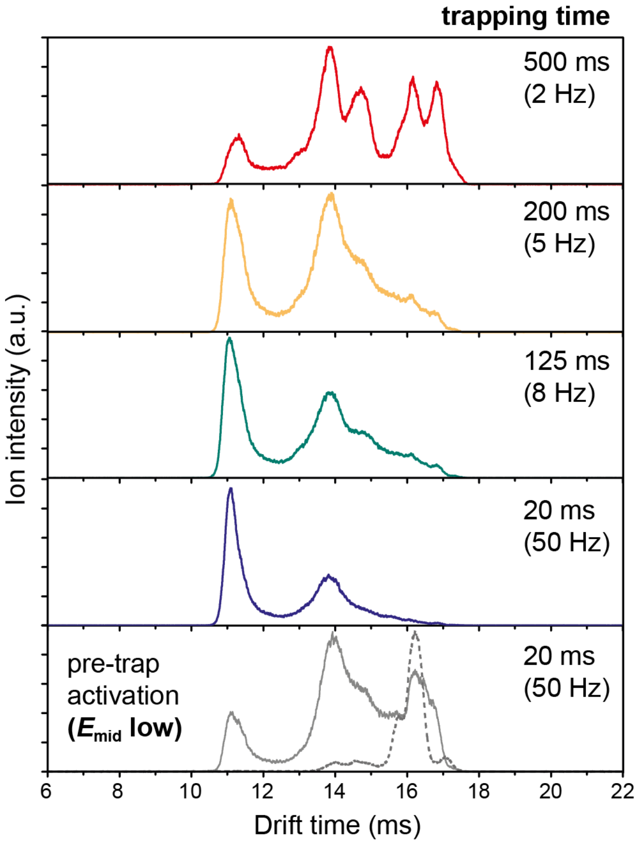

Figure 2.22: ATDs of ubiquitin 7^+ ions at different storage times, illustrating reorganization of gas-phase protein structures. The lower panel depicts ATDs obtained *via* pre-trap activation in the entrance funnel middle section at low values of E_{mid}. ATDs from intermediate and harsh pre-activation conditions are shown as solid and dashed lines, respectively.

Structural Transitions During Ion Storage

The stepwise unfolding and refolding of a protein after its transfer into the gas phase has been subject of earlier studies [24, 113, 114] and will also be focus of Chapter 3 where side-chain backbone interactions will be investigated. As time evolves, the gas-phase proteins are believed to undergo a large structural reorganization [24]. Here, this reorganization is illustrated on the basis of ubiquitin 7^+ ATDs as a function of the ion trapping time, which is given by the repetition rate of the experimental cycle. ATDs of ubiquitin 7^+ at storage times ranging from 20 ms to 500 ms are shown in Figure 2.22. Gentle instrument conditions were applied to observe the native-like compact form of ubiquitin 7^+ with a drift time of $\sim$ 11.2 ms at short a trapping times of 20 ms. At longer trapping times, intermediate structures become more dominant at drift times around 14 ms until elongated conformers with drift times $>$ 15 ms emerge at the longest accessible storage times of 500 ms corresponding to a repetition rate of 2 Hz. Interestingly, the relative intensities of the conformational families after 500 ms storage are somewhat different to those generated *via* collisional heating in the entrance funnel middle section (lower panel) at intermediate (solid line) and harsher conditions (dashed line), where the most extended conformer (drift time $\sim$ 17 ms) was not generated to an appreciable degree. From this it may be concluded, that the here-observed changes in structure after longer storage times are not induced by collisional heating inside the ion trap but are in fact result of a structural reorganization. In this context, it should be noted that the here-presented ATDs are virtually identical to ATDs from previous trapping-time studies on ubiquitin [113].

The elucidation of further structural details, however, is not scope of this discussion. As typical repetition rates lie between 5 Hz and 20 Hz, these results serve as a reminder that care has to be taken when relative populations of conformational families are of interest or when tuning the instrument. The latter especially applies for experiments with the Fritz Haber Institute free electron laser, which at the current stage is limited to 5 Hz operation (see Section 2.6).

2.5.4 Errors in Collision Cross-Section Determination

Generally, the determination of physical quantities is influenced by various systematic or statistical errors. For the determination of collision cross-sections from measured drift times these errors may originate from uncertainties in experimentally determined parameters such as the drift length, the temperature and pressure of the drift gas, and the voltage that is applied over the drift region. Additionally, the drift time itself may be determined incorrectly. To minimize random errors of the latter two quantities, the drift time of a species is typically determined for ten different drift voltages following linear regression of the obtained data points as described earlier in this chapter. Following this procedure, the deviation between independently determined cross-sections does typically not exceed 1.5 %, even with years between measurements.

In addition to random errors that originate from the lack of precision in the individual measurements, the determination of physical quantities are subject to systematic errors that, for example, arise from incorrectly calibrated measuring instruments or display units. Collision cross-sections that are determined at the here presented linear DT setup are generally about 3.5 % higher compared to values that are reported in the literature. A higher cross-section value is a direct result of higher drift times and after careful evaluation of all possible sources of errors, the culprit for this constant error in all measurements was identified to not be inaccurately determined experimental parameters but rather inhomogeneities in the electric field inside the drift region. These may originate from imperfections in the conductive glass drift tubes and are generally very hard to characterize, however, provide a reasonable explanation for the observed discrepancies.

Homogeneous Electric Fields

In the following paragraph it is briefly shown that an homogeneous, constant electric field is necessary to obtain the shortest possible drift time of an ion inside the buffer gas and that any inhomogeneities will cause longer drift times, which lead to cross-sections that are larger than the actual physical cross-section values of the ions.

Borrowing methods from calculus of variations, it can be shown that the integral

$$\boldsymbol{J} = \int_{x_1}^{x_2} f(x, g(x), g'(x))\, \mathrm{d}x\,, \tag{2.36}$$

where the prime denotes a derivative with respect to x, has a stationary value if the Euler-Lagrange differential equation

$$\frac{\partial f}{\partial g} - \frac{\mathrm{d}}{\mathrm{d}x}\left(\frac{\partial f}{\partial g'}\right) = 0 \tag{2.37}$$

is satisfied [115, 116]. Additionally, if f does not explicitly depend on x, then Equation 2.37 simplifies to the Beltrami identity [115, 116]

$$f - g'\frac{\partial f}{\partial g'} = C \tag{2.38}$$

where C is a constant. $\boldsymbol{J}$ can now be identified with the integral form of the drift time

$$t_d = \int_{x_1}^{x_2} \frac{1}{v(x)}\mathrm{d}x = \int_{x_1}^{x_2} \frac{1}{KE(x)}\mathrm{d}x \tag{2.39}$$

where $v(x)$ is the x-dependent drift velocity. In the second step, $v(x)$ is simply replaced using Equation 2.1, in which the (constant) mobility K of the ion is introduced as the proportionality constant between the electric field $E(x)$ and the velocity. Identifying f with $(KE(x))^{-1}$, the Beltrami identity 2.38 now becomes

$$\frac{1}{KE(x)} - E'(x)\underbrace{\frac{\partial}{\partial E'(x)}\left(\frac{1}{KE(x)}\right)}_{=\,0} = C\,. \tag{2.40}$$

This leaves

$$\frac{1}{KE(x)} = C\,, \tag{2.41}$$

and finally

$$E(x) = C'\,, \tag{2.42}$$

where C' is another constant.

This shows that the electric field $E(x)$ inside the drift tube needs to be homogeneous and constant (C') in order to measure the shortest possible drift time t_d at a given voltage difference between the beginning and the end of the drift region.

2.5.5 Ion Transmission

The amount of ions that can be successfully transmitted to the ion detector is crucial for the sensitivity of the instrument. Additionally, for tandem MS experiments, where ions are first drift-time and m/z-selected and subsequently dissociated by irradiation with intense

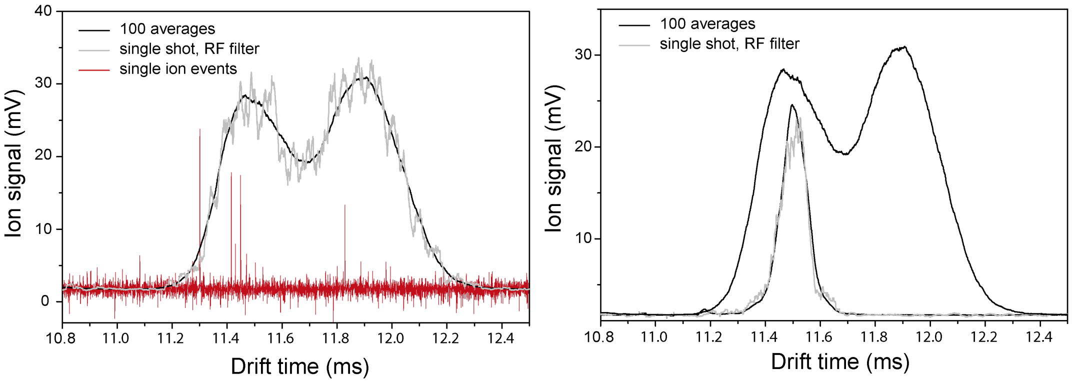

(a) Full ATD **(b)** Sliced ATD

Figure 2.23: ATDs of ubiquitin 11^+ for ion signal characterization. (a) An averaged ATD (black) is depicted with a non-averaged, single shot signal (gray). A 100 kHz low pass was applied to both of these signals to reduce electrical noise. A signal recorded at reduced ion transmission shows at least four sharp features, corresponding to single-ion events (red). (b) A narrow 100 μs *slice* can be selected *via* electrostatic deflection. Averaged signals are shown (black) together with the non-averaged data trace (gray). Also here, low pass filters were applied.

laser light, for example, the ion density needs to be large enough to allow for a significant number of fragments to be generated, which are subsequently analyzed in the TOF mass spectrometer. Many efforts have been made to optimize ion transmission, especially in the ion funnel regions.

To estimate the amount of ions that reach the linear ATD detector within one experimental cycle of a drift-time measurement and, more importantly, the amount of ions that can be provided for further laser experiments, single shot (non-averaged) ATD data traces were compared to the signals that single-ion events generate in the detector. For these test measurements, ubiquitin 11^+ ions were chosen as they will later be subject to further studies. Figure 2.23 (a) shows averaged (black) and single shot (gray) ATDs of ubiquitin 11^+ ions. A 100 kHz low pass was applied to the signal to reduce electrical noise. In order to resolve single-ion events that appear as narrow lines of μs width, the low pass was not applied to the single shot data traces of reduced ion intensity (depicted in red). By dividing the integral of the full ATD by the integral of a single-ion signal, the amount of detected ions can be estimated to $\sim$ 2–4$\cdot 10^3$. Similar numbers result when the total amplification of the ion signal by the detector ($\sim 10^5$) and the current amplifier (10^5) are considered. The charge that that is detected with each pulse of ions yields approximately $2 \cdot 10^{-15}$ C corresponding to roughly 12 000 charges that reach the detector. At a repetition rate of 20 Hz, this induces a total ion current of 40 fA of these particular *m/z*-selected ions, which is comparable to similar custom IM-MS setups.

When ions of a particular range of arrival times are *sliced* out *via* electrostatic deflection for further interrogation, the amount of ions naturally decreases. The corresponding ion

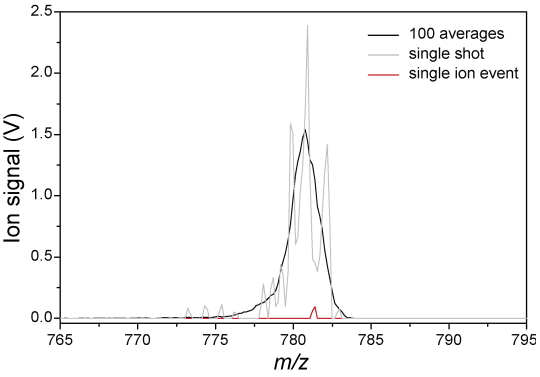

Figure 2.24: Averaged (black) and non-averaged (gray) TOF signal of the 100 μs wide ATD slice of ubiquitin 11^+ ions in Figure 2.23 (b). Reduced ion transmission conditions allowed to observe single-ion events (red) from which the number of ions that reach the detector was estimated.

signal is depicted in Figure 2.23 (b) for a typical 100 μs admittance window. A single shot, non-averaged ion trace of the sliced ATD of ubiquitin 11^+ is depicted here (gray) together with an averaged signal (black). In this particular example, the signal corresponds to roughly 500 ions that can potentially be dissociated by irradiation with laser light. Using different ions for these characterzation experiments, as the singly charged $(\mathrm{CsI})_5\mathrm{Cs}^+$ cluster ions, for example, yields overall similar numbers.

Finally, the number of ions that reach the TOF detector was deduced from similar measurements. Figure 2.24 shows a TOF signal of the m/z 780 ubiquitin 11^+ ions that were pulsed into the mass spectrometer from the narrow 100 μs ATD slice in Figure 2.23 (b). Also here, an averaged ion signal (black) is depicted together with a non-averaged, single shot signal (gray). However, no low pass was applied to these signals of μs width. A single-ion event can be seen in the data trace that was recorded at reduced ion transmission conditions (red). Dividing the integral of the full signal by the one that is generated by a single ion yields that approximately 100 ions reach the TOF detector with each pulse.

2.6 Drift-Time Resolved Laser Experiments

All of the photodissociation (UV and IR) experiments reported in this thesis were performed on the drift-tube (DT) IM-MS instrument described in detail in the preceding sections. Details about the utilized light sources, the experimental procedures, and the extraction of spectral data will be provided on the following pages.

2.6.1 Light Sources

In contrast to direct absorption measurements performed in the condensed phase, a general requirement for gas-phase light-induced dissociation techniques is a high photon flux. The laser systems used to generate the UV radiation for photodissociation experiments at a fixed wavelength and tuneable IR radiation for vibrational spectroscopic investigations are briefly described here.

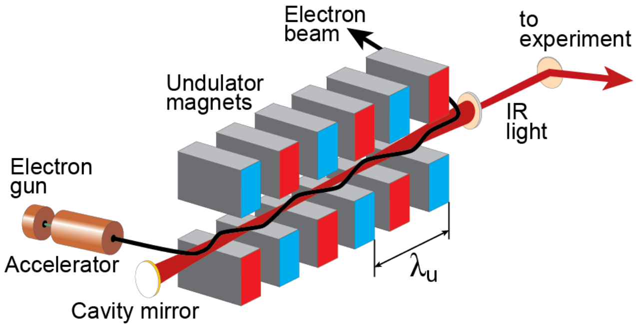

Figure 2.25: Schematic of a free electron laser (FEL). Relativistic electrons are brought on an oscillatory wiggle motion by an array of permanent magnets (undulator). The emitted synchrotron radiation constructively interferes with the electron beam, leading to electron bunching and further amplification of the emitted light inside the cavity. Figure adapted from [35].

UV Excimer Laser

For the generation of UV radiation an Excimer laser (Neweks, PSX-501) was used. Its operation is based on the metastable nature of an excited state and repulsive, dissociative ground state of a noble gas dimer or a noble halide complex. An electrical discharge provides energy for temporarily bound complexes to be formed, which emit monochromatic photons by either spontaneous or stimulated emission and subsequently dissociate. The wavelength of the emitted radiation depends on the utilized molecules and in the here described experiments, a noble gas halide type laser based on the reaction of argon with fluorine was used. Dissociation of temporarily formed ArF complexes yields a wavelength of 193 nm corresponding to a photon energy of 6.4 eV. With this setup, laser pulses of 5 ns length with energies in the lower mJ range can be achieved at repetition rates up to several kHz. During the experiments, however, the repetition rate was limited by the instrument to 10–20 Hz and pulse energies not higher than 1 mJ were applied.

IR Free Electron Laser

In conventional tabletop laser systems, monochromatic and coherent radiation is generated by stimulating transitions between energy levels in atoms and molecules. While this once revolutionary principle is now ubiquitous in todays science and industry applications, it often provides only a limited frequency range and intensities that are too low to perform the here described experiments. On the other hand, free electron lasers (FELs) can provide radiation from microwaves to X-rays [117, 118] with up to kilowatts [119] and even megawatts of power output, which qualifies such highly specialized systems for military use [120]. For the experiments described in this thesis, the more moderately sized Fritz Haber Institute (FHI) FEL setup was used, which can currently generate radiation in the mid-IR range with pulse energies up to 200 mJ [121], corresponding to a power output of 1 W at 5 Hz operation [122].

In Figure 2.25, the setup of an FEL for the generation of IR radiation is shown schematically. The lasing medium of an FEL is a relativistic beam of eponymous *free electrons*, which is generated in pulses by en electron gun and subsequently brought to energies of several MeV by linear accelerators. An array of alternating pairs of oppositely poled permanent magnets with a period length of λ_u (red and blue in Figure 2.25) forces the electrons to describe an oscillatory motion perpendicular to the orientation of the magnetic fields (due to the Lorentz force). This radial acceleration of relativistic and initially randomly distributed electrons causes the emission of synchrotron radiation in a forward-pointing cone. When the intensity of this monochromatic but initially incoherent light is high, interaction of the electrons with the oscillating electromagnetic field of the radiation (due to the ponderomotive force) leads to evenly spaced so-called micro bunches of the electrons at a distance corresponding to one optical wavelength. As a result, the now spacially collimated electrons emit light coherently, which leads to a further increase of the electromagnetic field and enhancing the effect of micro bunching and coherence of the radiation. This positive feedback leads to a gain in light intensities by a factor of 10^6–10^8 and can be achieved by either using very long undulators, as necessary, *e.g.*, for the generation of X-ray radiation, or by placing the undulator array inside a cavity composed of two highly reflective mirrors at a distance equal to a multiple of the generated wavelength. A hole inside one of the cavity mirrors allows to a small fraction of the light to be used for experiments.

At a given undulator period length λ_u and magnetic field strength B_0, the wavelength λ_r of the emitted radiation is given by the resonance condition [123]

$$\lambda_\mathrm{r} = \frac{\lambda_\mathrm{u}}{2\gamma^2}\left(1 + K^2\right) , \tag{2.43}$$

with the Lorentz factor

$$\gamma = \frac{1}{\sqrt{1 - v^2/c^2}} , \tag{2.44}$$

and a dimensionless undulator parameter

$$K = \frac{eB_0\lambda_\mathrm{u}}{\sqrt{8}\pi m_e c} , \tag{2.45}$$

where m_e, v, and c are the mass of the electron, its speed with respect to the rest frame, and the speed of light, respectively. In Equation 2.43 the relativistic nature of the electrons is reflected in a contraction of the emitted wavelength by γ^2 [124]. This effect is essential as the desired wavelengths of the generated light are much shorter than one undulator period λ_u. It is, however, slightly dampened by the factor $(1 + K^2)$, which originates from the oscillatory wiggle motion of the electron itself, as it reduces its velocity component along the undulator axis. The wavelength λ_r is typically manipulated by changing the energy of the electron beam or altering the strength of the magnetic field B_0. The former adjustment coarsely sets the accessible frequency range, while the magnetic field inside the undulator is easily manipulated by changing the distance (gap) between the oppositely poled magnet pairs. A frequency scan is, thus, accomplished by scanning the undulator gap.

The FHI FEL is depicted schematically in Figure 2.26 and was previously described in

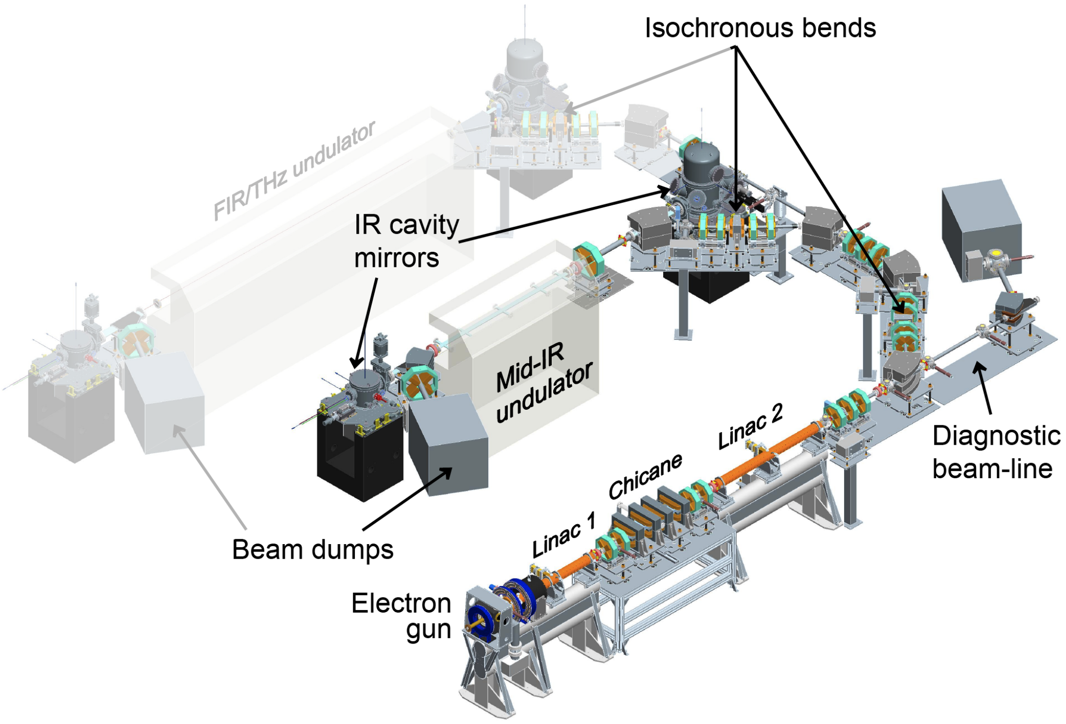

Figure 2.26: Schematic representation of the FHI FEL. The second, far-IR undulator is subject to future installment (grayed out area). Figure adapted from [122].

detail [122]. The electron gun creates and modulates pulses of electrons with a repetition rate of 1 GHz. These micro-pulses of ps length make up macro-pulses of up to 15 μs length. Subsequently, electrons are accelerated to energies of 15–50 MeV by two linear accelerators. Several dipole magnets steer the relativistic electron beam into the mid-IR undulator, which is placed between the gold-plated cavity mirrors. After the generation of IR photons, electrons are steered into a beam dump. Outcoupling of IR light occurs *via* a hole of variable size (1–2.5 mm) in one of the cavity mirrors. A second undulator for generation of far-IR photons is subject to future installment (grayed out in Figure 2.26).

The initial electron pulse structure determines the time structure of the FEL pulses. Thus, light can be generated in pulses of up to 10 μs length, each consisting of GHz micro-pulses of ps length. Different electron energy settings currently allow to generate 4–48 μm IR radiation with macro-pulse energies of more than 100 mJ and a spectral width (FWHM) of 0.5 % [122]. For the IR experiments described within this thesis the FEL was primarily scanned in a wavelength range of 5–10 μm, which can be easily covered at an electron energy of 36 MeV.

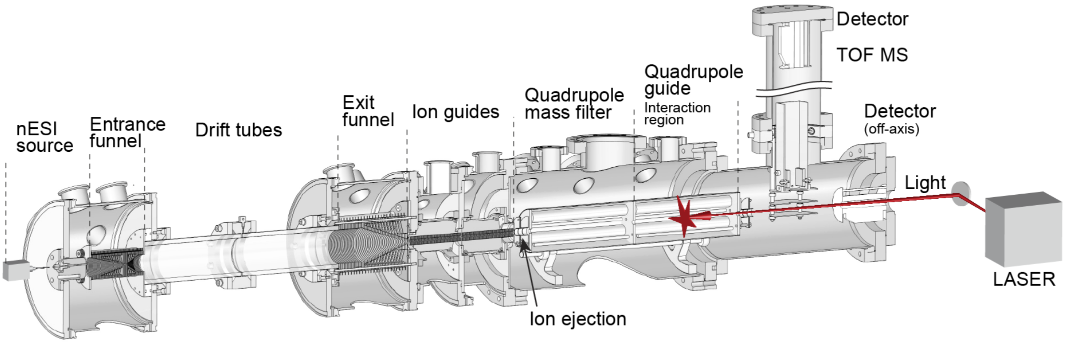

Figure 2.27: Schematic representation of the DT IM-MS setup from a CAD model. A drift-time range (100 μs) is selected *via* electrostatic deflection followed by m/z selection. The path of the laser light and the approximate area of ion-light interaction is indicated in red.

2.6.2 Experimental Scheme & Data Acquisition

In the remainder of this section, details about the experimental procedures for the acquisition of the drift-time and m/z-resolved photodissociation data presented in Chapters 4, 5, and 6 are given. Some redundancy with information from previous sections is intentional.

A detailed representation of the DT instrument from a CAD model is given in Figure 2.27. Details of the experimental setup, the ion source, RF ion guides and separation techniques, have been discussed in Sections 2.4 and 2.5. Here, the path of the laser light and the approximate ion-light interaction region is depicted in red. Light enters the instrument through a CaF_2 window with an optical transparency of 80–90 % (193 nm) or a KRS-5 (Thallium Bromine-Iodide) window with an optical transparency of about 70 % (5–10 μm) for UV and IR experiments, respectively. When IR experiments are performed, light is transported from the FEL to the experimental setup through evacuated beam lines. This is necessary to avoid the absorption of IR light through water and CO_2 in the ambient air. For better accessibility of optical components, however, the last $\sim$ 2 m of the beam line is flushed with dry nitrogen. A combination of a focusing mirror with a fixed focal length (1 m) and an adaptive mirror with a variable focal length of ± 2 m (Kugler GmbH) allows to shift the point of the laser focus from just outside the instrument to approximately the center of the quadrupole guide. This allows to dynamically adapt the laser light during IR experiments from a more collimated beam for higher photon densities (at the cost of laser-ion beam overlap) to a more divergent beam, which increases the overlap with the ions (at reduced photon densities).

A typical trigger pulse sequence for the drit-time selective photodissociation experiments is depicted in Figure 2.28. It is initiated by the ion gate pulse of 100–150 μs length, followed by the 100 μs drift-time admittance window of the ion ejection lens a few ms later. By varying the delay Δt_1, ions of different drift times can be selected. By the time ions traverse the second quadrupole guide, the laser pulse is triggered, which induces fragmentation when the

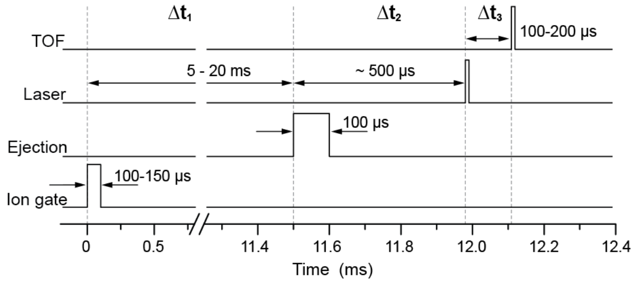

Figure 2.28: Typical pulse sequence and timings for drift-time resolved laser experiments with the DT IM-MS instrument.

light is resonant with a molecular transition. In practice, the time delay Δt_2 is adapted dynamically to yield the optimal overlap with the precursor ions and, thus, the best fragment signal. The TOF measurement is initiated after the delay Δt_3, which represents the time that the precursor ions and its fragments need to exit the quadrupole guide and reach the TOF plates. It is typically in the range of 100–200 μs and is, as the delay Δt_2, strongly dependent on instrument tuning.

Multiple TOF mass spectra are then acquired using the GHz oscilloscope (Section 2.4.5) and averaged to yield a final fragment spectrum. To reduce electrical noise in the TOF measurements and to even the baseline, signals below a threshold of 30 mV are discarded. This approach is justified by the signal intensity that a single ion causes in the TOF detector (50–100 mV, compare Figure 2.24).

Ultraviolet

For drift-time or conformer-selective UV photodissociation experiments, a single ArF Excimer laser pulse (wavelength 193 nm) of 5 ns length was used to effectively dissociate the peptides or proteins under investigation. The pulse energy was about 1 mJ and the laser was not focused, which resulted in an uncollimated beam, roughly 1 cm in diameter at the point of the spacial overlap with the ion beam. A linear relationship between the laser power and the photofragment intensities was observed for the singly protonated pentapeptide [YGGFL + H]$^+$ as well as for the 76 residue protein ubiquitin. This is in accordance with previous studies [68, 69], suggesting that a one-photon process governs the dissociation at 193 nm wavelength and low photon densities.

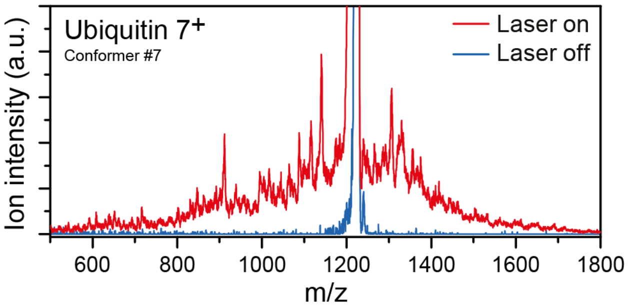

Figure 2.29: UV photofragments of conformer-selected ubiquitin 7^+ ions (red) and the signal corresponding to the undissociated ions (blue). The intensities of the sometimes only partially resolved signals are well above the base line.

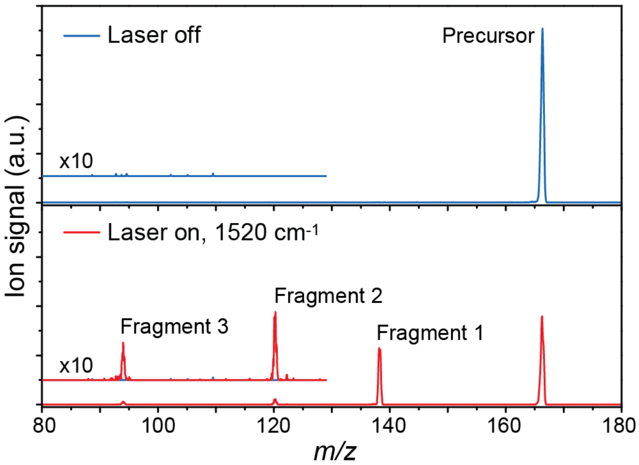

Figure 2.30: IR multiple photon dissociation (IRMPD) TOF mass spectra of isomer-selected, protonated benzocaine with (lower panel) and without (upper panel) resonant IR irradiation. Three fragments are observed upon photon absorption.

UV photodissociation at 193 nm was shown to yield statistically distributed backbone cleavages leading to large numbers of different fragments [72]. When smaller molecules with a manageable amount of dissociation channels are investigated, those photofragments can be well resolved. This is apparent, *e.g.*, from the photofragment spectra of [YGGFL + H]$^+$ shown in Figure 2.3 (Section 2.2), where most fragment signals are well-resolved. As the the size of the molecule of interest increases, however, a growing amount of different dissociation channels leads, at the given resolution and accuracy of the TOF mass analyzer, to sometimes inscrutable photofragment spectra. To illustrate this, Figure 2.29 shows a 193 nm photofragment spectrum of one particular conformer of ubiquitin 7$^+$, together with a (clipped) signal of the undissociated precursor ions. The experimental parameters were chosen such, that roughly 20 % of the precursor ions dissociated. Many, sometimes only partially resolved signals can be observed, most of which have intensities way above the base line and can, thus, clearly be distinguished from noise signals. Similar fragment intensities and signal-to-noise ratios were observed in all UVPD experiments on ubiquitin reported within this thesis. Details can be found in Chapter 4.

Infrared

In order to investigate molecular vibrations, the drift-time and m/z-selected packets of ions were irradiated with a 10 μs pulse of FEL IR radiation with pulse energies of 10–50 mJ. The focus of the laser light was adapted dynamically to yield the required photon density. When resonant with a molecular vibration, the IR light led to the fragmentation of the investigated species. This is exemplarily shown in Figure 2.30 where the TOF mass spectrum of a protonated isomer of benzocaine, a small aromatic molecule frequently used as a local anaesthetic (see Chapter 5), is depicted without (upper panel) and with irradiation (lower panel) with resonant IR photons.

The wavenumber $\tilde{\nu}$ of the FEL was scanned in steps of 3 cm^{-1} and the intensities of the

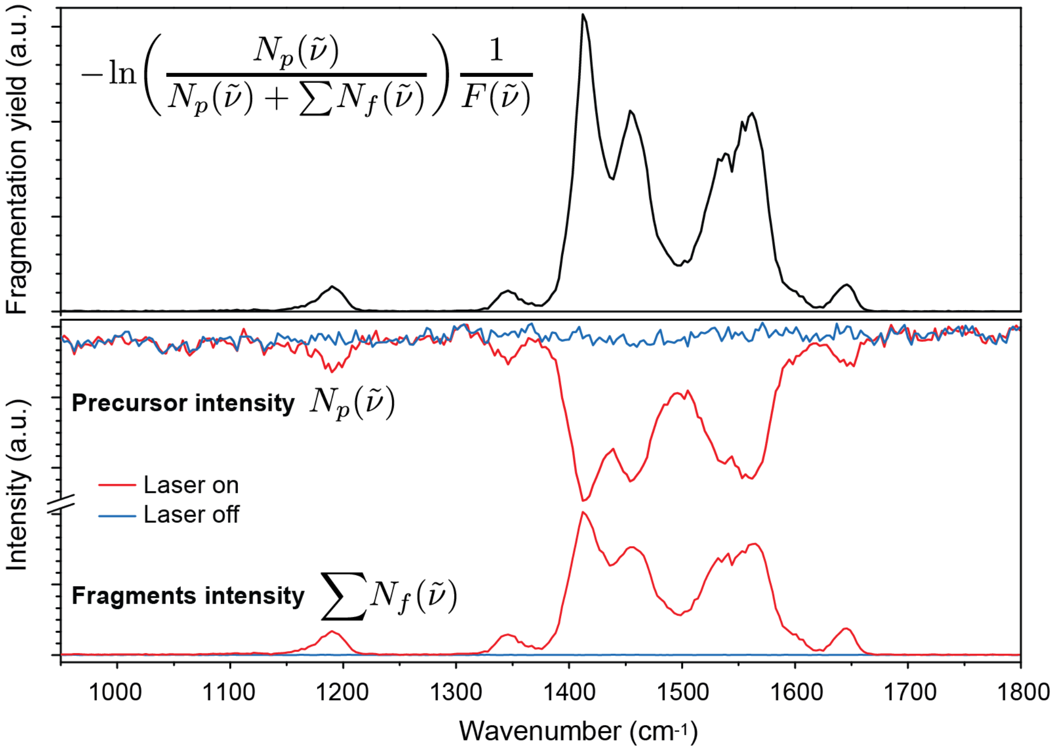

Figure 2.31: IRMPD data of isomer-selected benzocaine from a FEL wavenumber scan (lower panel) and the resulting IR spectrum according to Equation 2.46 (upper panel). The intensity of the precursor ions N_p and the summed intensities of the fragments $\sum N_f$ progress contrarily as a function of the wavenumber (red traces), indicating that little ion losses occur before detection. Monitoring the intensities of the non-irradiated ions (blue traces) helps to determine the stability of the ion source and the background signals of the photofragments.

precursor N_p as well as the fragment signals N_f were monitored to obtain IR multiple photon dissociation (IRMPD) spectra from the IR absorption cross-section $\sigma(\tilde{\nu})$, which, in a first order approximation, can be calculated by rearranging Equation 2.7 to

$$\sigma(\tilde{\nu}) \propto -\ln\left(\frac{N_p(\tilde{\nu})}{N_p(\tilde{\nu})+\sum N_f(\tilde{\nu})}\right)\frac{1}{F(\tilde{\nu})}\,, \tag{2.46}$$

where the total number of ions N_0 was replaced by the sum of precursor and fragment ions $N_p(\tilde{\nu}) + \sum N_f(\tilde{\nu})$. Division by the laser fluence $F(\tilde{\nu})$ (*i.e.* the laser power) accounts for intensity variations of the FEL over the wavenumber range. This approach is strictly valid only when dissociation occurs with a linear photon fluence dependency, however, was shown to yield good qualitative agreement with single-photon and calculated linear absorption spectra also when multiple photon absorption processes are involved [125].

The FEL was operated at a repetition rate of 5 Hz, whereas the DT instrument was operated at 10 Hz. Thus, every other pulse of ions was detected without being subjected to laser light. This conveniently allowed to monitor the stability of the nESI spray during the scans and could furthermore be used to determine the background signal of the fragment ions, which was subtracted from the fragment signal if necessary. The resulting data traces are exemplarily depicted for the selected benzocaine isomer in the lower panel of Figure 2.31. In this particular example, the combined intensity of all fragments $\sum N_f$ almost completely makes up for the loss in intensity of the precursor ions N_p when the light is resonant. This simply implies that all fragments are effectively detected and relatively little ion losses occur. The vibrational spectrum of the molecule can then be calculated as a fragmentation yield using Equation 2.46 (upper panel in Figure 2.31).

The exact wavelength of the FEL radiation depends strongly on instrument tuning and was calibrated after each scan. This is typically achieved by measuring the FEL spectrum with a Czerny-Turner grating spectrometer equipped with a pyroelectric array detector for several wavelength points within the scanned spectral range [122]. The recorded spectra were subsequently corrected. Wavelength scans were usually repeated at least twice and subsequently averaged to minimize experimental errors. The presented experimental procedures apply to all IR spectroscopic experiments reported in this thesis.

2.7 Experimental Setup II: Traveling-Wave IM-MS Instrument Synapt G2-S

A second IM-MS experimental setup, the commercially available Synapt G2-S (Waters Corporation, Manchester, UK), was utilized to investigate ions based on their sizes, mass-to-charge ratios, and CID dissociation patterns. Detailed descriptions of the instrument can be found in earlier publications [126, 127] and the employed experimental techniques are described in the previous sections. Thus, only a brief overview of the instrument shall be given here. The great strength of the instrument lies in its high *m/z*-resolving power and sensitivity that allows the detection and identification of minuscule signals. The high sensitivity is owed to the use of cleverly designed traveling-wave (TW) ring-electrode RF ion guides that facilitate ion transport through regions of elevated pressures, such as the source region, the ion trap and transfer regions, as well as the ion-mobility cell. As the name suggests, electric fields having the form of traveling waves propel ions forward, which is beneficial for ion transport performance [127]. However, in contrast to the ion transport in linear drift-tube (DT) instruments, where constant electric fields drive the ions forward, the ion transport in inhomogeneous electric fields can not be described analytically. Therefore, collision cross-section information can only be obtained indirectly from drift-time measurements *via* calibration with species of known cross sections, which is prone to errors. Nonetheless, the instrument features valuable analytical capabilities. CID fragmentation of *m/z*-selected species can, for example, be induced before and after ion-mobility separation allowing the shape and size of fragments (Chapter 3) or conformer-specific fragmentation (Chapters 4 and 5) to be investigated, respectively.

The instrument is depicted schematically in Figure 2.32. It is equipped with a Z-spray nESI source (Section 2.4.2), followed by TW RF ion guides that transfer ions into high vacuum. A quadrupole mass filter allows to select ions of a specific *m/z* before trapping of ions occurs in an RF trap, filled with argon buffer gas at pressures of 1–5 $\cdot 10^{-2}$ mbar. During injection into the nitrogen-filled IMS cell at 2–3 mbar pressure, ions pass a short region that serves thermalization *via* collisions with helium buffer gas molecules at $\sim 10^{-1}$ mbar pressure (helium cell). Subsequent to IMS separation, ions traverse a second argon-filled transfer cell (1–5 $\cdot 10^{-2}$ mbar) before they are *m/z*-analyzed in a high-resolution TOF mass spectrometer. As stated above, ions can be subjected to energetic collisions with the surrounding argon buffer gas molecules prior (trap dissociation) and after ion-mobility separation (transfer dissociation), which yields highly complementary multi-dimensional sets of data.

In comparison with the DT IM-MS instrument, a few fundamental differences are noticeable. The ion-mobility cell of the Synapt instrument is only 25 cm in length, however, provides an IMS resolving power that is competitive with that of the DT instrument ($\Delta\Omega/\Omega \approx 40$). This compact design comes at the cost of only indirect cross-section measurements that require calibration. Furthermore, in contrast to the DT setup, *m/z*-selection occurs prior IMS separation in the Synapt instrument. Gas-phase reactions that alter the *m/z*-value may therefore occur unnoticed inside or shortly after the drift region of the DT instrument (see

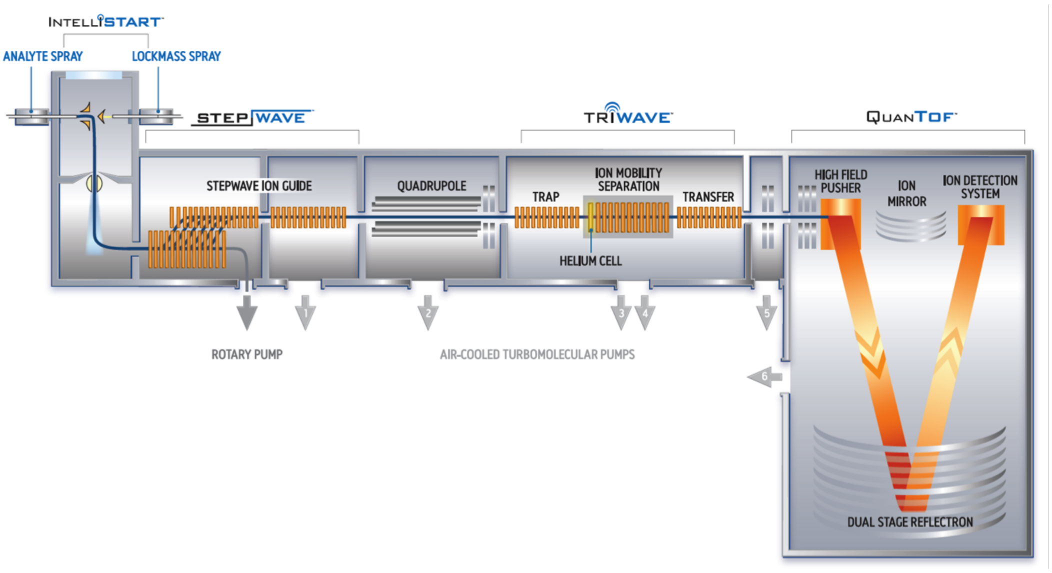

Figure 2.32: The Waters Synapt G2-S traveling-wave (TW) IM-MS instrument. The setup allows to dissociate ions by energetic collisions with argon buffer gas molecules before and after ion-mobility separation. Illustration from Waters Corporation.

Chapter 5), whereas they will be detected at the Synapt as a change in the mass spectrum. A downside of this MS/IMS/MS arrangement is that ions need to be transferred from the high vacuum of the quadrupole region into the mbar regime of the IMS cell, which may lead to collisionally activated ions with elevated internal temperatures [128]. As a result, the DT setup has proven to provide much more gentle conditions, which allowed the investigation of even weakly bound complexes (Chapter 6) that were not observable during this work using the Synapt instrument.

3 The Influence of Side-Chain Microsolvation on Gas-Phase Protein Structure*

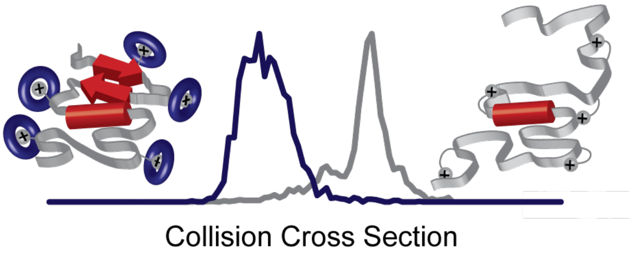

The charge state of a gas-phase protein is often found to be a crucial determinant for the resulting gas-phase structure. It was suggested that charge induced unfolding is not only driven by Coulomb repulsion but that the interaction of the charged sites with the protein's backbone is responsible for loss of native-structural elements [24]. In the following chapter, these side-chain backbone interactions and their influence on the protein's structure are investigated using IM-MS and selective side-chain microsolvation. It will be demonstrated how the inhibition of this charge-backbone interaction can help to preserve more native-like structure in the gas phase.

3.1 Introduction

Today electrospray ionization (ESI) is routinely applied to characterize proteins *via* mass spectrometry (MS) [11, 76]. There is an ongoing discussion about the extent to which native structural elements can be conserved in the gas phase. In recent years, studies have revealed that not only the protein's primary structure but also higher-order structural elements, up to the quaternary architecture of a protein complex, can be retained in the absence of solvent [15, 16, 129, 130]. A subtle balance between attractive inter- and intramolecular forces, including salt bridges, van der Waals interactions, hydrogen bonds, and the repulsive

---

*This chapter is based, in part, on the work published in S. Warnke, G. von Helden, and K. Pagel *J. Am. Chem. Soc.* **2013**, *135*, 1177-1180 http://dx.doi.org/10.1021/ja308528d.
Figures and content adapted with permission. Copyright 2013 American Chemical Society.

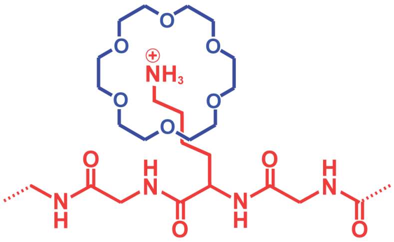

Figure 3.1: Schematic representation of a crown-ether complexed peptidic backbone. The crown ether 18-crown-6 binds preferably to charged lysine residues [132–136].

Coulomb forces between like charges, governs the folding and three-dimensional organization of gas-phase proteins. In this context, one of the crucial determinants has been shown to be the charge state [131]. Low charge states can exhibit compact, globular structures that are governed by a hydrogen-bonding network within the molecule's backbone, whereas high charge states often form extended conformations that are largely dominated by Coulomb repulsion between the charged residues [22]. Intermediate charge states can show a multitude of coexisting conformations (compare also Figure 1.4 in the introductory part of this thesis).

One method to investigate the overall structure of protein ions is ion-mobility spectrometry (IMS) [42, 43, 129, 137, 138], which was introduced in Chapter 1. Besides its ability to separate protein conformations that differ in size, IMS allows to measure absolute collision cross-sections (CCS) and therefore to yield direct information on the molecular shape. The conformations of the proteins cytochrome c and ubiquitin, for example, have been studied thoroughly in the gas phase using IM-MS [20, 114, 131, 139, 140]. Remaining questions concern the extent to which these gas-phase structures resemble conformations of the solvated protein and the underlying mechanisms leading to structural changes. It has been proposed that one of the crucial steps during transfer from solution to the gas phase is the collapse of charged side chains onto the backbone of the protein ion [24]. Here the influence of side-chain solvation and side-chain backbone interactions on the protein's overall structure is investigated.

3.2 Experimental Details

Samples

All samples for IMS-studies were purchased from Sigma Aldrich. The proteins ubiquitin, cytochrome c, and myoglobin were dissolved in 10 mM triethylammonium acetate aqueous solution to 100 μM concentration. In order to desalt the sample solution for cleaner mass spectra all samples were dialyzed for two hours with 10 mM triethylammonium acetate aqueous solution. For this, Slide-A-Lyzer dialysis tubes (MWCO = 2000, Thermo Scientific) were used. For the experiments, the samples were diluted to the desired concentration ($\sim$ 10 μM). Crown ether 18-crown-6 (CE) was dissolved in water and added to the protein solution in a ratio corresponding to 10-100 equivalents.

Experimental Parameters

For ion mobility analysis and tandem IM-MS experiments, the commercial traveling-wave (TW) instrument described in Section 2.7 was used. Samples were ionized using a (nano) electrospray ionization source. After transfer into the vacuum environment of the instrument, the species of interest are *m/z*-selected and can optionally be dissociated *via* energetic collisions prior ion mobility analysis. Typical experimental parameters of the TW IM-MS instrument were: source temperature 20°C; capillary voltage, 0.8 - 1.2 kV; sample cone 20 - 50 V; source offset, 20 V; cone gas, off; trap collision energy, 2 V; transfer collision energy, 4 V; trap gas flow, 2 mL/min; helium cell gas flow, 180 mL min^{-1}; IMS gas flow, 90 mL min^{-1}; trap DC bias 38 - 40 V; IMS wave height, 40 V; IMS wave velocity, 500 - 900 m s^{-1}.

Collision Cross-Section Determination

Drift-time measurements from TW instruments cannot be directly converted into collision cross-sections (CCSs) because of the use of inhomogeneous electric fields inside the drift region. Instead, drift times were calibrated with calibrants of known CCSs following an established calibration protocol [141]. To minimize errors in the calibration, drift times were recorded for various wave velocities and CCS values were averaged. CCSs of the calibrants were determined using the drift-tube (DT) IM-MS instrument described in Section 2.4. Drift-time data of ubiquitin, cytochrome c, and the respective protein-CE complexes were calibrated using CCS values of the bare ions of ubiquitin and cytochrome c, respectively.

3.3 Results and Discussion

To analyze the impact of side-chain backbone interactions on the gas-phase structure of proteins, different amounts of crown ether (CE) (18-crown-6, 264 Da) was non-covalently attached to the proteins ubiquitin and cytochrome c. These CEs are known to coordinate strongly to protonated lysine side chains (see Figure 3.1) [132–136]. The proteins or protein-CE complexes were investigated *via* ion mobility-mass spectrometry (IM-MS) using the commercial traveling-wave (TW) IM-MS instrument (described in Section 2.7) in which ions drift through a buffer gas under the influence of an electric field having the form of a traveling wave [126, 127]. Absolute CCS values for calibration of TW IMS data were determined using the drift-tube (DT) IM-MS instrument described in Section 2.4.

3.3.1 IM-MS of Protein-Crown Ether Complexes

Typical mass spectra of the investigated proteins with charge 5^+ and 7^+ for ubiquitin and cytochrome c, respectively, and varying CE content are shown in the upper panels of Figure 3.2. Under mild source conditions, complexes with up to five CEs can be observed for both proteins. The mass of the utilized CE yields a shift of $\Delta m/z$ 52.8 (= 264/5) and $\Delta m/z$ 37.7

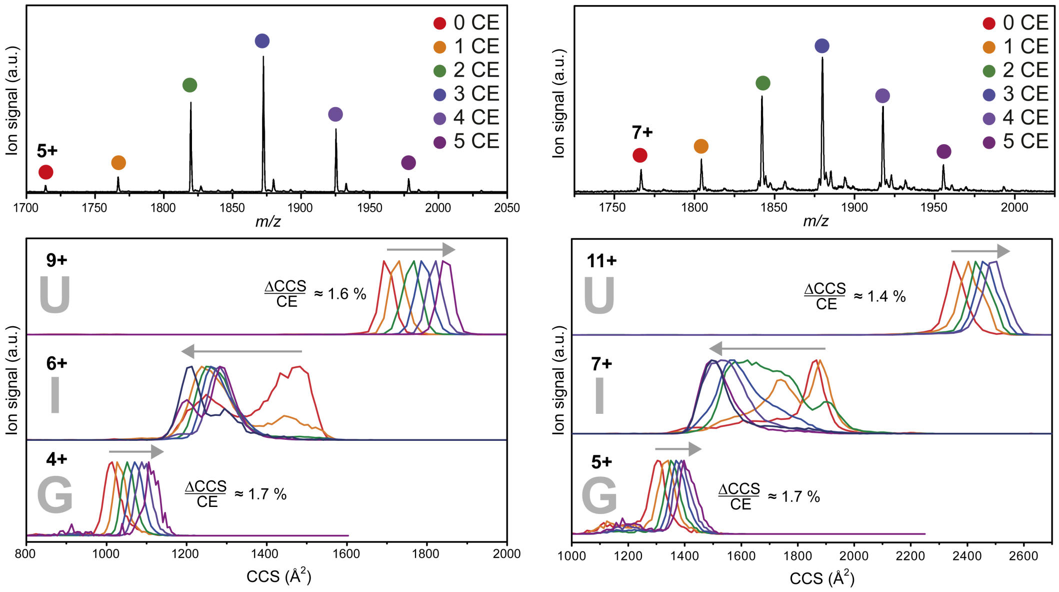

(a) Ubiquitin **(b)** Cytochrome c

Figure 3.2: Mass spectra and ATDs of protein-crown ether (CE) complexes for (a) ubiquitin and (b) cytochrome c. For one charge state, each additional CE leads to a shift in the mass spectrum (upper panels). The change in CCS with addition of CEs to the protein shows a charge state dependence (lower panels); Globular (G) and unfolded (U) ions increase in size whereas intermediate (I) ions undergo a compaction.

(= 264/7) for each additional adduct, respectively. The lower panels of Figure 3.2 show IMS arrival time distributions (ATDs) of the CE-complexed proteins in different charge states and varying numbers of CEs attached. To compare the charge states, the drift times were converted to CCSs (given in Å^2) [141–143]. As has been observed previously [20, 131, 144, 145], the molecules' CCSs increase with increasing charge, reflecting the unfolding of compact, globular (G) structures at low charge ($\leqslant 4^+$ for ubiquitin and $\leqslant 5^+$ for cytochrome c) into extended, unfolded (U) structures at high charge ($\geqslant 9^+$ for ubiquitin and $\geqslant 10^+$ for cytochrome c).

It is interesting to observe the effect of CE attachment on the CCS. For states with low amount of charges (G) as well as for high charge states (U), the CCS increases slightly by 1.4–1.7 % for each additional CE (see Figure 3.2). This observation was expected because of the additional mass of each CE which is added to the complex. However, counterintuitive effects were observed for CE complexes in intermediate (I) charge states, as can be seen exemplarily for 6^+ and 7^+ ions in Figure 3.2. Here, CE binding leads to dramatic decreases in size, with CCSs up to 30 % smaller than those of the bare ions. This indicates significant compaction upon the addition of CEs.

It is noticeable that the compaction of the intermediate charge states of ubiquitin and cytochrome c upon CE binding is not continuous, but that rather specific structures (or ensembles of structures of similar size) are being populated and others depopulated as the

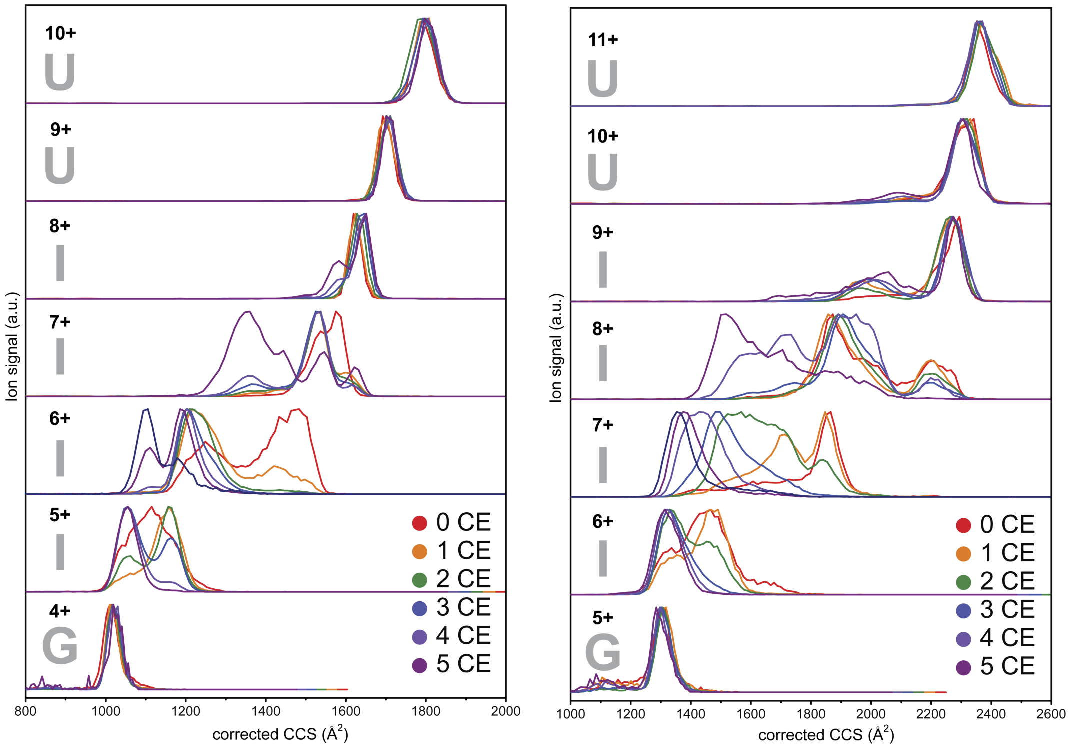

(a) Ubiquitin

(b) Cytochrome c

Figure 3.3: Corrected CCSs of CE-complexed (a) ubiquitin and (b) cytochrome c ions. The average size increase of the protein per additional CE molecule ($\frac{\Delta\text{CCS}}{\text{CE}}$, see Figure 3.2) is substracted from the CCS of the complex to illustrate changes in the population of distinct structures (or ensembles of structures with similar CCSs).

CE content increases. When a compaction effect does not occur after CE addition, however, the CCS of the newly formed complex slightly increases with respect to the uncomplexed molecule, as observed for the globular (G) and unfolded (U) ions. To account for the size of the CE molecule in the protein-CE complex, the average size increase per additional CE ($\frac{\Delta\text{CCS}}{\text{CE}} \approx 1.4$–$1.7$ %, see Figure 3.2) was substracted from the CCS of the protein-CE complex to yield a corrected CCS. The resulting conformer distributions are depicted in Figure 3.3 for charge states 4^+ to 10^+ (ubiquitin) and 5^+ to 11^+ (cytochrome c), covering the full range of the intermediate (I) charge states for both proteins. The now corrected CCSs allow to directly compare changes in relative populations of distinct structures that are being formed upon CE binding.

The conformer distribution of the bare ubiquitin 6^+ ion, for example, consists of mainly two broad features centered around 1250 Å^2 and 1450 Å^2, respectively (Figure 3.3 (a)). The latter becomes depopulated and finally disappears with the addition of the second CE, in favor of the more compact structures around 1250 Å^2. The binding of the fourth CE is accompanied

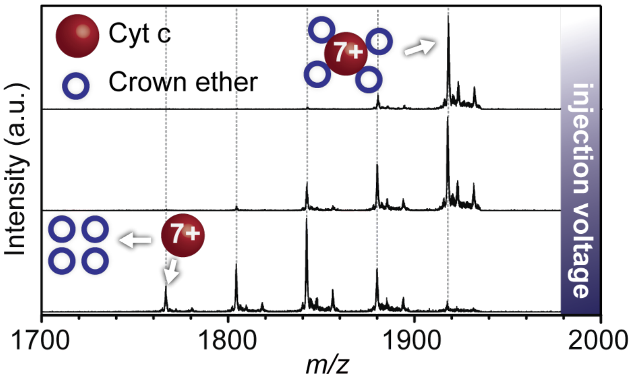

Figure 3.4: Tandem MS spectra of the 7^+ cytochrome c–4CE complex at different injection voltages. Increasing the injection voltage (top, 2 V; middle, 8 V; bottom, 16 V) created all of the lower-order complexes.

by the population of a narrow feature around 1100 Å^2 corresponding to a compact, globular structure, which increases in intensity as the CE content of the complex is further increased. The largest observed protein-CE complex containing six CE molecules mainly adopts this globular structure around 1100 Å^2 and all the signals above 1250 Å^2 corresponding to more elongated structures have vanished. This astounding compaction behavior and the population of rather discrete structures instead of a continuous shift towards smaller species was observed for all intermediate charge states of both proteins investigated here (Figure 3.3).

With a different instrument, conformational transitions as observed here have been shown to depend strongly on the timing parameters, such as the trapping time prior to the injection of the molecules into the drift cell [114]. In addition, in Synapt TW instruments, the ion temperature is known to increase significantly during injection into the drift cell [128, 146]. The compaction effect described here for protein-CE complexes was observed with both the TW and DT IMS instruments, and the ATDs showed no dependence on device timing and IMS injection voltage within the accessible range.

3.3.2 CID of Protein-Crown Ether Complexes

To gain more information on the CE-induced compaction process, tandem IM-MS experiments were carried out on CE-complexed cytochrome c ions. A high-pressure collision cell prior to the IMS cell allowed fragmentation of m/z-selected protein-CE complexes *via* collision-induced dissociation (CID). Subsequent structural changes of the molecule and its fragments could be observed by IMS analysis. Mass spectra of CE-complexed cytochrome c in the 7^+ charge state at three different injection energies are shown in Figure 3.4. Starting with a protein containing four CEs, lower-order complexes could be produced as fragments by increasing the injection voltage (Figure 3.4, top to bottom). Figure 3.5 shows ATDs of the resulting complexes for the

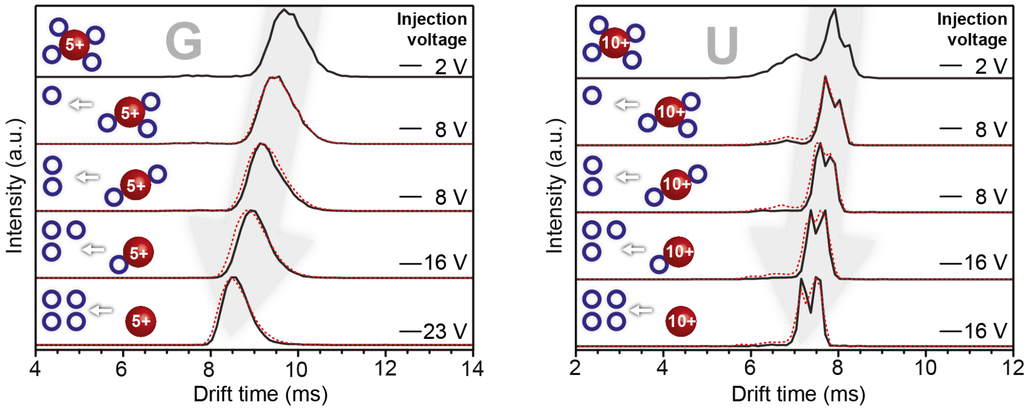

(a) Globular structures **(b)** Unfolded structures

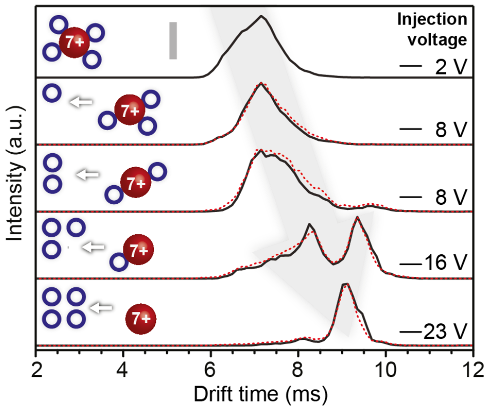

(c) Intermediate structures

Figure 3.5: Structural changes upon CE removal. (a, b) No significant structural changes were observed when CE was removed from low-charge G or high-charge U cytochrome c ions. (c) Cleavage from intermediate charge states induced partial unfolding of the molecule, resulting in an increase in arrival time. Regardless of charge, no difference between the CID-generated CE complexes and those generated directly *via* ESI (red dashed lines; 2 V injection voltage) was observed.

5^+, 7^+, and 10^+ charge states. Ions featuring globular (G, 5^+ and lower) or predominantly unfolded conformations (U, 10^+ and higher) underwent no significant structural changes when CE was removed from the complex (Figure 3.5 (a, b)). However, CE removal from intermediate charge states (6^+ to 9^+) induced partial unfolding of the molecule, leading to longer drift times and larger CCSs (Figure 3.5 (c)). Independent of the charge state, the ATDs obtained after CID were virtually identical to those measured for ions produced directly *via* ESI (Figure 3.5, red dashed lines). This indicates that the CID-generated extended conformations observed for the intermediate charge states result from the loss of CE molecules rather than from the energy deposited into the complex during CID.

3.3.3 Implications for the Gas-Phase Structure

The results observed here indicate that the local environment of charged side chains in the gas phase can severely influence the structure. What can give rise to the observed CE-induced compaction? The addition of CE does not alter the overall charge, and a slight change in the positions of the CE-complexed side chains or the associated changes in local

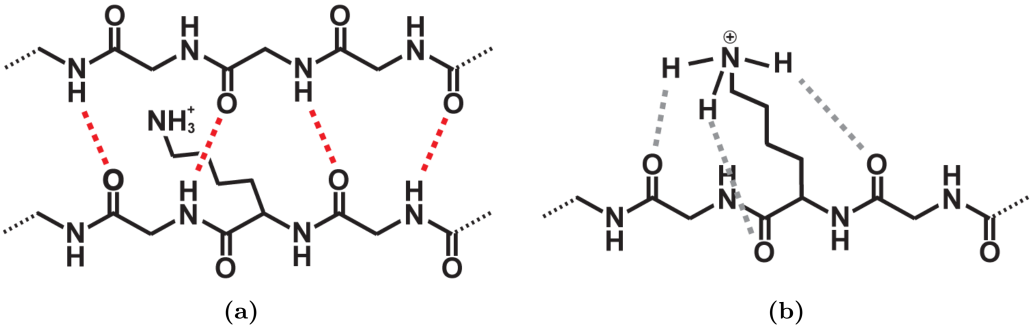

Figure 3.6: (a) Schematic representation of structure-stabilizing hydrogen bonds (red) that will be disrupted when charged side chains interact with backbone carbonyl groups (b) to form non-native hydrogen bonds (gray).

dielectric environment should not significantly affect the overall role of Coulomb repulsion. A more important factor that could have an influence on the structure is the alteration of the interactions between the protonated basic side chains and the protein backbone. In a condensed-phase protein, the charged side chains are involved in salt bridges, coordinate to carbonyl groups of the backbone, or interact with solvent molecules. In the absence of a solvent environment, the side chains will take part in intramolecular interactions and can coordinate to the backbone carbonyl groups, which would then no longer be available to be involved in potentially structure-stabilizing hydrogen bonds (see Figure 3.6). The added CE can take over the role of the solvent, with the result that the side-chain backbone interaction is reduced. This effect is schematically indicated in Figure 3.7, where the charged protein is depicted as a cartoon. Secondary structure elements such as β-sheets and α-helices are depicted in red, unordered structure is depicted as gray strands, and CEs are represented by blue rings. The solvation shell of the molecule is represented as a light-blue sphere. The upper part of the figure shows the stepwise evolution of the protein on its way to the gas phase after ionization *via* ESI as suggested previously [24]. After evaporation of the solvent, the charged side-chain residues collapse onto the molecule's peptidic backbone, forming hydrogen bonds with backbone carbonyls or creating salt bridges with anionic residues. As a result, hydrogen bonds within the protein's backbone can be disrupted. The disappearance of these structure-defining bonds can lead to destabilization of secondary and tertiary structure elements, resulting in structural changes in the protein. This situation is illustrated in the upper-right corner of Figure 3.7. However, when the charged side chains are capped with CE, the collapse after evaporation of the solvent is inhibited, leaving secondary structure elements intact (Figure 3.7, lower-right). As a consequence, a compact and presumably more native-like structure is observed for CE-complexed proteins in intermediate charge states.

Further support for the proposed mechanism comes from a previous study on the much smaller peptide gramicidin S [147]. With a combination of gas-phase IR spectroscopy and

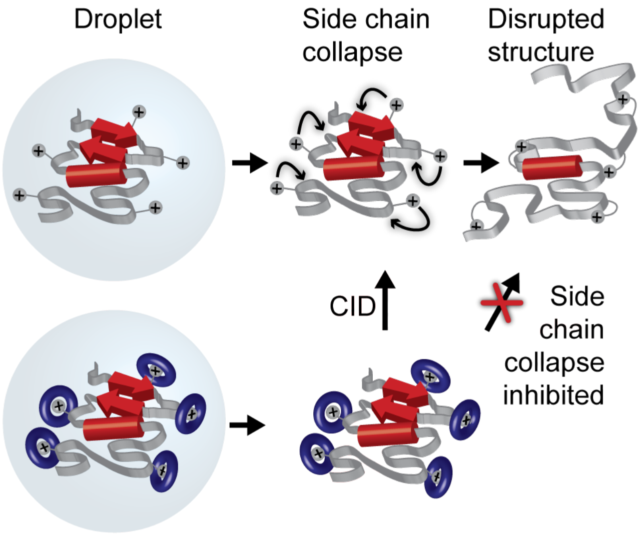

Figure 3.7: Effect of CE side-chain microsolvation on the molecule's structure. Secondary structure elements are shown in red, unordered structure is shown in gray, solvent is shown in light blue, and CEs are shown as blue rings. Collapse of the side chain after evaporation of the solvent is inhibited when the side chain is capped with a CE. See the discussion in the text.

theory, it was found that the charged NH_3^+ groups of the two Orn residues* strongly interact with the peptide backbone, leading to a disruption of intramolecular β-sheet-like hydrogen bonds. In contrast, when the side-chain backbone interaction is inhibited through CE complexation, the hydrogen-bonding pattern that governs the secondary structure remains essentially unaffected. In addition, IM-MS experiments on other CE-complexed proteins such as the non-covalent protein-ligand complex myoglobin (17 kDa) revealed compaction of intermediate charge states similar to that found for ubiquitin and cytochrome c. Therefore, the observed effects are rather general and not limited to the here selected proteins.

3.4 Conclusions

This study demonstrates that the gas-phase structure of proteins such as ubiquitin and cytochrome c can be drastically altered by the non-covalent attachment of CE molecules. On the basis of these results, it can be postulated that interactions between protonated lysine side chains and backbone carbonyls are in direct competition with the intramolecular hydrogen bonding that determines the protein's secondary and tertiary organization. Non-covalent attachment of CEs to the charged side chains of the protein can compensate for these effects by solvating the positively charged ionic groups in a similar way to solvent molecules in the

---

*Ornithine (ORN) is a nonproteogenic amino acid whose side chain is similar to that of lysine but shortened by one methylene group.

condensed phase. In a more general context, this implies that side-chain microsolvation by CEs can be used as a tool to manipulate and tune protein structures in the gas phase.

4 UV Photodissociation of Conformer-Selected Protein Ions

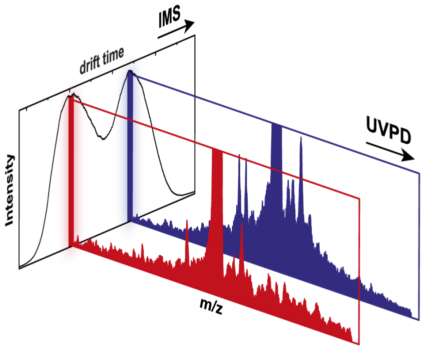

Ultraviolet photodissociation (UVPD) of gas-phase proteins has attracted increased attention in recent years. This growing interest is largely based on the fact that, in contrast to slow heating techniques such as collision induced dissociation (CID), the cleavage propensity after absorption of UV light is distributed over the entire protein sequence, which can lead to a very high sequence coverage as required in typical top-down proteomics applications. In this chapter, the newly constructed IM-MS experimental setup is used in combination with UVPD to obtain conformer-selective UV fragment spectra of various, coexisting gas-phase conformations of the protein ubiquitin. The presented studies aim to answer the question whether UVPD can be used to obtain information about higher order protein structure.

4.1 Inroduction

Understanding the structure and dynamics of proteins is one of the greatest challenges in the life sciences. To experimentally tackle this, a large variety of techniques to investigate samples in the condensed phase have been developed. In the last decades, techniques to study proteins in the absence of solvent, that is, in the gas phase, have emerged as promising additions that provide complementary information. Most of these methods rely on gentle ionization techniques such as electrospray ionization (ESI) followed by mass spectrometry (MS), and together with methods to isolate, energize, and fragment gas-phase molecules, MS is today the work-horse technique in “omics” research [11, 148].

When protein sequence information is of interest, the most commonly applied method in commercially available so-called tandem-MS instruments is collision induced dissociation

(CID) [29]. Here, however, peptide bond cleavages do not occur randomly along the sequence but rather at specific positions when the molecule is slowly heated during CID. As a result, often only little sequence coverage and incomplete information about the primary structure is obtained, which in turn can be problematic, especially for the characterization of unknown compounds. Because of this limitation, over the past few years electron capture dissociation and electron transfer dissociation (ECD/ETD) have received increased attention, since in those methods, cleavages occur less selective along the sequence and therefore greatly increased sequence information can be obtained [149, 150]. Unlike in collisional heating methods, noncovalent interactions can be retained after dissociation of the backbone using ECD/ETD, which can facilitate the investigation of protein complexes and higher order protein structures [31, 32, 150]. However, the ECD/ETD process is most efficient for precursor ions with high charge density [139, 151], which, on the other hand, often leads to unfolding of the gas-phase protein. As a consequence, compact, more native-like gas-phase ions are usually difficult to investigate by ECD/ETD.

A dissociation method, which recently emerged as a promising alternative is based on the absorption of UV photons by the amide backbone and subsequent dissociation [71]. During this ultraviolet photodissociation (UVPD), peptide bond cleavages occur rather statistically over the entire amino acid sequence, which can yield nearly complete sequence coverage for intact proteins in low charge states [60, 67, 72, 152] and even noncovalent protein assemblies [153]. Furthermore, UVPD can be applied to a large variety of instruments with only relatively few modifications.

It was demonstrated in Chapters 1 and 3 that a protein can adopt a multitude of different conformations in the gas phase depending on solvent conditions and the amount of charged sites. They can be compact and native-like with a high content of noncovalent, intramolecular interactions, or unfold to extended conformations dominated by charge repulsion when the charge state of the molecule is increased [154]. It is, at this point, not clear if this structural diversity can have an influence on UVPD. This question is founded on the notion that the energy of the absorbed UV photon does not dissipate over the molecule, but may lead to a local excitation followed by a quick dissociation process.

Ion mobility spectrometry has, in combination with MS, proven useful to separate and analyze structural differences of protein ions [43, 137, 138, 155], which was also demonstrated earlier in this thesis. The ability to obtain absolute collision cross-sections (CCS) from drift-time measurements does, furthermore, provide a chance to validate model structures by comparing theoretical and experimental CCSs. The ability to select ions of a particular m/z and shape and provide those ions for further investigations is a unique property of gas-phase experiments. Such selectivity is often difficult to achieve in the condensed phase, where different protonation states, conformations, and aggregation states can be in a dynamic equilibrium for which typically only a distribution can be probed. Most importantly, however, when one tries to elucidate higher order structures, it has to be kept in mind that the structural preferences of biological molecules in the gas phase may be different from those in the condensed phase, because the global free energy minimum in solution is usually only a local minimum in the absence of solvent (see also Figure 1.2 in the introduction of this thesis). This ambiguity of a correlation between gas-phase structures and solution structures has been discussed earlier [12, 13] and it has been shown in many experiments that when the molecules are handled gently, condensed-phase structural elements can be retained after transfer into the gas phase [13, 17, 18].

The question arises whether the combination of IM-MS to preselect molecular shapes, with UVPD can be used to deduce direct structural information from fragmentation patterns of different structures. For a multitude of reasons, this question is difficult to address. The observed fragmentation pattern as well as the conformation of the molecule will both depend on the charge state. As a result, it is very difficult to disentangle the influence of the charge and the conformation on the fragmentation behavior within one experiment.

In the following chapter, first results on conformer- and *m/z*-selective UVPD are presented. Experiments were performed, once again, on ubiquitin ions. The reason for its omnipresence in experiments reported within this thesis is the existence of a comprehensive groundwork for this molecule. And even though it has been investigated extensively in all possible forms, it still holds many secrets about its structure. Results from earlier studies will here be used to calculate model structures to explain the results from conformer-selective UVPD experiments. It will be concluded that coexisting, extended gas-phase structures may be a result of the relatively large energy barriers between *cis* and *trans* isomers of a peptide bond preceding one particular proline residue. The second part of this chapter is devoted to finding structural similarities between partially folded and extended species of ubiquitin ions. Also here, the results point towards the special role of proline residues in the protein sequence.

4.1.1 Experimental and Computational Details

The following description of experimental details applies to both experiments on ubiquitin 11^+ and 7^+ ions in Sections 4.2 and 4.3, respectively.

Samples

Human ubiquitin was purchased from R&D Systems (Wiesbaden, Germany) and used without further purification. Solvents were purchased from Sigma-Aldrich (Taufkirchen, Germany). For (nano) electrospray ionization, an aqueous 1 mM ubiquitin stock solution was diluted with water/methanol, v/v 50/50, to yield a concentration of 10 μM. Formic acid (1.5 %) was added to generate high charge states. For ionization $\sim$ 5 μL of sample was loaded into in-house-prepared Pd/Pt coated borosilicate capillaries, and a voltage of 0.8–1.0 kV were applied [85].

Conformer-Selective UVPD

For conformer-selective UV photodissociation (UVPD), the experimental drift-tube (DT) setup described in Section 2.4 was used. Briefly, ions are generated in a (nano) electrospray ionization source (nESI) and transferred into the vacuum. An electrodynamic ion funnel collects and pulses ions into the drift region where they drift through helium buffer gas under the influence of a weak electric field ($\sim$ 10 V cm^{-1}). A second electrodynamic ion funnel guides the conformer-separated ions into ultrahigh vacuum. Here, ions of specific drift times can be selected following *m/z* selection by a quadrupole mass spectrometer. UVPD *via* irradiation with a 193 nm excimer laser pulse occurs approximately 100 μs prior to TOF mass analysis. The UV pulse length and energy are about 5 ns and 1 mJ, respectively, and the beam diameter is about 1 cm. Under those conditions, the absorption of multiple photons is not expected. Further, the laser power dependence of the fragmentation yield is observed to be linear, in line with a one-photon process. A detailed description of the experiment can be found in Section 2.6.2.

Collision Cross-Section Determination

For comparison with calculated structures and other experiments, the time axes of the arrival time distributions (ATDs) were converted to collision cross-sections (CCSs). Conversion of ATDs from DT IMS instruments, which utilize a uniform electric fields in the drift region, can be achieved using Equation 2.4. CCS values reported here are in good agreement with previously published values for ubiquitin [113, 156].

Conformer-Selective CID

Conformer-resolved collision induced dissociation (CID) experiments were performed on the Waters Synapt G2-S traveling-wave (TW) IM-MS instrument described in Section 2.7. Typical experimental settings were: source temperature, 20°C; capillary voltage, 0.8–1.0 kV; sample cone, 40 V; source offset, 20 V; cone gas, off; trap collision energy, 2 V; trap gas flow, 2 mL min^{-1}; helium cell gas flow, 180–200 mL min^{-1}; IMS gas flow, 70–100 mL min^{-1}; trap DC bias 34–35 V; IMS wave height, 40 V; IMS wave velocity, 650–800 m s^{-1}.

In TW instruments the effective ion temperature can increase substantially during injection and transmission through the IMS cell [128, 146]. To observe compact or partially folded conformations of ubiquitin 7^{+}, the instrument therefore required careful tuning to gentle conditions, which was mainly achieved by reducing RF amplitudes, increasing the gas flow of the helium cell (which serves thermalization of the ions prior entering the IMS region), and decreasing the IMS pressure and injection voltage (trap DC bias). For the acquisition of conformer-resolved CID spectra, the collision voltage in the argon-filled collision cell after conformer selection (*i.e.* the transfer cell) was raised until substantial fragmentation was observed (transfer CE 53.0–54.5 V).

Molecular Dynamics (MD) Simulations*

All MD simulations and part of the analysis were carried out with the Gromacs suite of programs (version 4.6.3) [157]. The ff99SB-ILDN [158] parameter set of the Amber force field was used for the protein. The four ubiquitin models named *ttt*, *ctt*, *tct*, and *ttc* (see description in the following paragraphs) were briefly equilibrated, and then for each of the four systems six MD simulations of 100 ns were performed with an integration step size of 0.5 fs. The temperature was 300 K, coupled to the velocity-rescaling thermostat by Bussi, Donadio, and Parrinello [159]. No cut-offs for non-bonded interactions and no bond constraints were applied. Only the last 60 ns of the 100 ns trajectories were considered for analysis.

4.2 Ubiquitin 11$^+$: Cis/Trans Isomers of Proline Peptide Bonds†

Here, the first UVPD fragmentation spectra of protein ions, which are both *m/z*- and conformer-selected are presented. The well-characterized 76-residue protein ubiquitin is used to show that the gas-phase structure of the protein has a considerable impact on the fragments formed *via* UVPD. With the help of molecular dynamics (MD) simulations it is found that the most significant differences arise from cleavage around one particular proline residue.

4.2.1 Results and Discussion

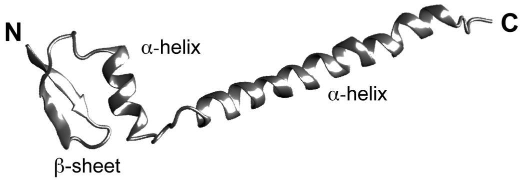

Figure 4.1: The A-state of ubiquitin, a partially denatured structure found in the condensed phase (structure based on [160]).

Ubiquitin in the Gas Phase

Ubiquitin – one of the most commonly occurring proteins in eukaryotes – has as such been studied extensively in the gas phase using a variety of techniques [20, 25, 140, 152, 161]. Pioneering work in the groups of Clemmer and Bowers for example showed that ubiquitin can adopt a multitude of defined and partially interchangeable conformations in the gas phase [13, 19, 20, 113, 145] of which some are closely linked to those of ubiquitin in the condensed phase [20, 23]. A particularly interesting example of those gas-phase conformers

---

[*] Calculations were performed by Carsten Baldauf in the Theory department of the Fritz Haber Institute.

[†] This chapter is based on the work published in S. Warnke, C. Baldauf, M. T. Bowers, K. Pagel, and G. von Helden *J. Am. Chem. Soc.* **2014**, *136*, 10308-10314 http://dx.doi.org/10.1021/ja502994b.

Figures and content adapted in accordance with the Creative Commons CC-BY Usage Agreement. Copyright 2014 American Chemical Society.

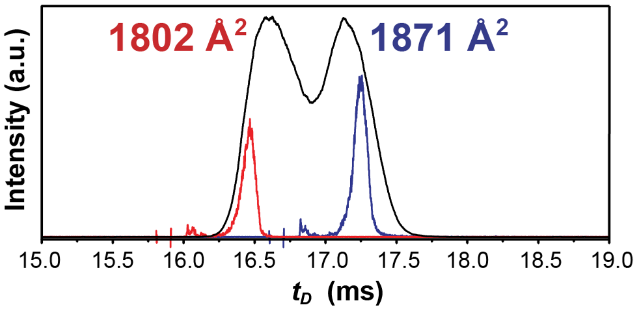

Figure 4.2: Arrival time distribution (ATD) of 11^+ ubiquitin. For conformer-selective photodissociation experiments, 100 μs fractions of each species were isolated (red and blue) and transmitted to the interaction region.

is a group of structures occurring for high charge states. There, structures are observed that, unlike ubiquitin in its native fold, are not compact but rather extended [20, 145]. In the condensed phase an extended structure with a native-like β-hairpin motif near the N-terminus and a predominantly helical C-terminal domain can be observed in water/methanol mixtures [160, 162, 163]. The structure of this so-called A-state (Figure 4.1) is compatible with the sizes of some of the highly charged ubiquitin ions in the gas phase as determined in IM-MS experiments [20]. Here, ubiquitin in the 11^+ charge state is investigated, for which two dominant gas-phase conformers with structures compatible with the A-state have been observed previously [20].

UV Photodissociation of Selected Ubiquitin 11^+ Conformers

Ubiquitin ions, which are size- and m/z-separated using the experimental drift-tube (DT) setup described in Section 2.4, are either directly transferred to a detector to record arrival time distributions (ATDs) or irradiated by a UV excimer laser at 193 nm followed by time-of-flight mass analysis of the resulting fragments.

In Figure 4.2, an ATD of ubiquitin ions in the 11^+ charge state is shown. Clearly, two peaks can be seen, resulting from two distinct conformations or conformational families. Their corresponding drift times can be converted into CCSs, which both are comparable to those determined previously for extended structures of ubiquitin [20, 113].

From the two peaks in the ATD shown in Figure 4.2, a small 100 μs fraction can be isolated by electric deflection of the other ions. The isolated fraction representing the conformer occurring at earlier drift times (1802 Å^2) and the isolated fraction representing the more extended conformer (1871 Å^2) are shown as red and blue traces in Figure 4.2, respectively. Those m/z- and conformer-selected ions can now be irradiated with a single 193 nm pulse of an ArF excimer laser, and the resulting photofragmentation spectra are shown in Figure 4.3. Both spectra consist of many peaks, some of which are only partially resolved. Some peaks clearly occur in both spectra; others, however, are prominent in only one. Among the most

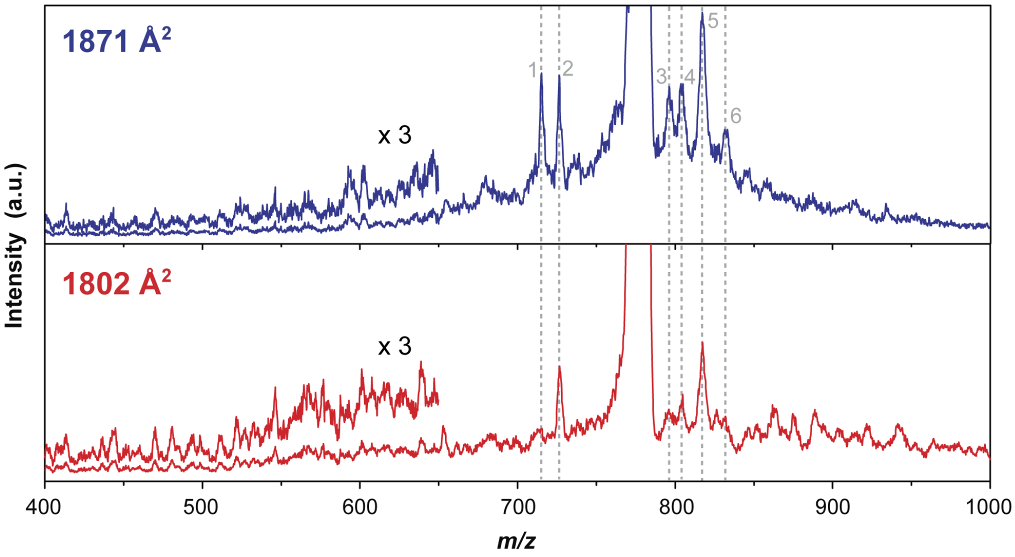

Figure 4.3: UVPD spectra of conformer-selected 11^+ ubiquitin. Spectra are shown for the compact conformation (1802 Å^2, lower panel, red) and for the more extended conformation (1871 Å^2, upper panel, blue). The dashed lines indicate the positions of the most prominent differences at m/z 716 (#1), 726 (#2), 795 (#3), 805 (#4), 817 (#5), and 833 (#6).

prominent features and striking differences are the peaks at m/z 716, 726, 795, 805, 817, and 833, which are numbered consecutively from 1 to 6 in Figure 4.3.

The observation of a different fragmentation behavior is interesting by itself – especially when considering that conformer-selective CID does not yield distinct fragmentation patterns (see Section 4.2.1 below) [164]. The mass spectra in Figure 4.3 both stem from the same molecules in the same charge state that merely differ in conformation. Those two conformers might also differ in their internal charge distribution. Both factors could influence the observed fragmentation pattern and are typically difficult to disentangle. The impact of distinct charge localization has recently been investigated extensively for a small model peptide system [165]. In that study, structural differences could not be linked to different charge distributions. Furthermore, the approach applied there is difficult to transfer to the here considered larger species. Here, the goal is to determine whether structural differences are sufficient to explain the differences observed in the UV induced fragmentation patterns of the two distinct ATD peaks.

CID of Confomer-Selected Ubiquitin 11^+

To test whether the widly used fragmentation method, collision induced dissociation (CID), is similarly sensitive to the protein's higher order structure, conformer-selective CID fragment spectra were recorded for the two conformers of ubiquitin 11^+ using the TW IM-MS instrument

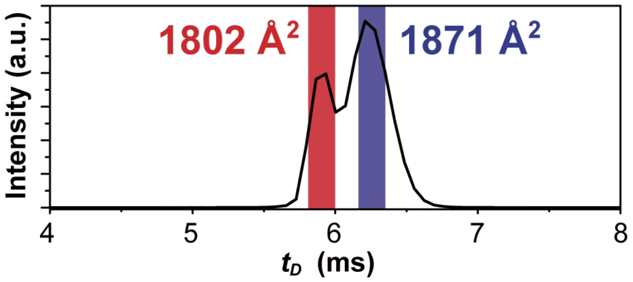

Figure 4.4: ATD of ubiquitin 11^+ from the travelling-wave (TW) IM-MS instrument. For conformer-selective CID, fragment spectra of the compact (red) and more elongated (blue) conformer are extracted for drift-time ranges as indicated in red and blue (see Figure 4.5 for the fragment spectra).

described in detail in Section 2.7.

The ATD of ubiquitin 11^+ as measured on this instrument (Figure 4.4) is virtually identical to the dirft-tube data (Figure 4.2) in peak positions and very similar relative intensities. The latter, however, is a matter of experimental parameters of both instruments. The drift-time ranges that are selected for the extraction of CID fragment spectra are indicated in red and blue for the 1802 Å^2 and the 1871 Å^2 species, respectively, and the resulting mass spectra are shown in Figure 4.5. The regions of low fragment intensities are magnified as indicated. Generally, the CID fragment intensities and relative abundances change significantly with the applied collision voltage, and therefore fragment spectra for higher collision energies for the high mass range are also shown (inset in Figure 4.5). For comparison with the UVPD data, the positions of the intense photofragments labeled #1–#6 in Figure 4.3 are indicated as dashed lines.

Apart from several of the intense UV fragment signals that coincide with signals in the CID spectra (fragments #2, #4, #5, and #6), the CID fragmentation patterns in Figure 4.5 differ significantly from the photofragment spectra in Figure 4.3. This is not unexpected considering the inherently different dissociation mechanisms of UVPD and CID. Comparison between the CID spectra of the different conformers, on the other hand, does not reveal considerable differences. The vast majority of fragments can be clearly identified in the CID spectra of both conformers and only minuscule differences are observed (insets in Figure 4.5). However, the intensities of the peaks in question and their relative differences are usually very low ($< 1\%$ relative to the main fragment). In addition both conformers lead to a different dissociation yield, which, given their difference in CCS and internal potential energies, might not be surprising. Therefore, these small differences in the CID spectra are not considered to be significant in the context of this study.

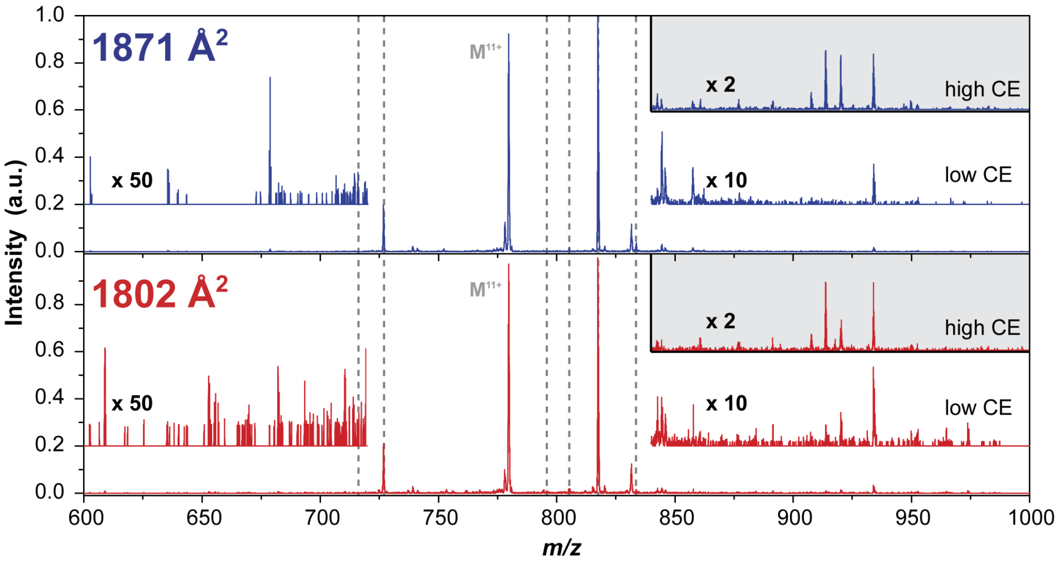

Figure 4.5: Collision induced dissociation fragment spectra of the two ubiquitin 11$^+$ drift peaks (Figure 4.4) for low collision energies (1802 Å^2: 29 V; 1871 Å^2: 26 V) and higher collision energies (inset highlighted in grey, 1802 Å^2: 33 V; 1871 Å^2: 32 V). The intense UV photofragments labeled #1–#6 in Figure 4.3 are indicated as dashed lines for comparison.

UVPD Fragment Assignment

To classify the differences in the UVPD fragment spectra in Figure 4.3 according to the underlying cleavage position, it is necessary to assign the corresponding photofragments. Due to the limited resolution of the spectra, an assignment purely based on the data presented here is difficult. Aided by high-resolution UVPD spectra of non-conformer selected ions obtained by the group of Jennifer S. Brodbelt [72], however, all prominent and most of the weaker features could be identified (for a list of all assigned fragments see Appendix A). Fragment #3 in Figure 4.3, for example, is an N-terminal a^{36} fragment (5$^+$) occurring from the cleavage of the peptidic backbone between residues Ile^{36} and Pro^{37}. The most apparent differences in the fragment spectra, however, originate from cleavage around a single residue: Pro^{19}. The corresponding fragments are y^{57} (#1, 9$^+$, and #4, 8$^+$), y^{58} (#2, 9$^+$, and #5, 8$^+$), and y^{59} (#6, 8$^+$), which are formed *via* cleavage of the peptide bonds between the residues Pro^{19}-Ser^{20}, Glu^{18}-Pro^{19}, and Val^{17}-Glu^{18}, respectively. Based on this assignment, it can, therefore, be concluded that differences in the fragmentation behavior around Pro^{19} are responsible for the majority of differences in the mass spectra in Figure 4.3.

In order to provide a semiquantitative picture about the prevalence of cleavages along the sequence, relative intensity were assigned to each identifiable and assignable peak in the mass spectra using values from 0 to 3. In this scheme, 0 means no distinct peak and 1 a clearly visible peak. The six intense fragment peaks in Figure 4.3 were assigned a relative intensity

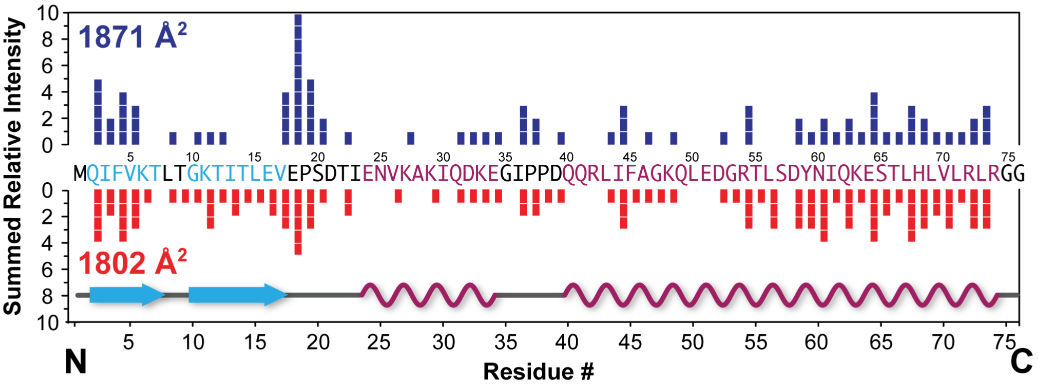

Figure 4.6: UVPD fragmentation propensity of the two conformers of 11^{+} ubiquitin. The bars show the combined relative intensities of all fragments that originate from the same cleavage site for the compact conformer (1802 Å^2, lower panel, red) and the more extended form (1871 Å^2, upper panel, blue). The structure shown in the lower part of the figure is based on the A-state.

of 2 and, if differentiation between fragment abundances was necessary, the highest intensity level 3 was assigned (relative intensities are included in the list of assigned fragments in Appendix A). Subsequently, the intensities were grouped according to the cleavage position along the sequence, and the corresponding histogram plot is shown in Figure 4.6.

One clear result is that sequence coverage is generally very high. This is in good agreement with previous studies, which showed that for ubiquitin, a coverage of almost 100 % can be achieved [72]. Both conformers also feature an enhanced formation of C-terminal fragments as well as a lower cleavage propensity for the middle part of the protein. However, there are also very clear differences, which on the basis of the crude intensity assignment can be considered relevant when the relative intensity varies by more than two. The most prominent of these differences is the enhanced cleavage around Pro^{19} for the higher CCS conformer as already apparent in Figure 4.3. This difference is especially pronounced at the N-terminal side between Glu^{18} and Pro^{19} with a summed relative intensity of 5 for the lower and 10 for the higher CCS conformer. Interestingly, it has been observed previously that Xxx-Pro peptide bonds can show an enhanced cleavage propensity upon activation using slow heating techniques such as CID [166]. Even though this proline effect has been shown to not be relevant in UVPD [67], a strong preference for cleavage of the Glu^{18}-Pro^{19} bond is observed here, while no such preference is observed for the Xxx-Pro bonds of Pro^{37} and Pro^{38}.*

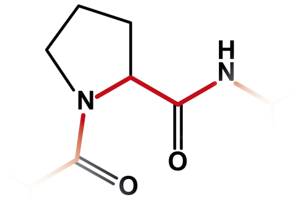

Figure 4.7: The heterocyclic backbone of a proline residue inside a peptidic backbone (red) restricts its conformational flexibitity.

The Special Role of Pro^{19}

Proline generally plays a very special role in protein folding. In peptides (Figure 4.7), its heterocyclic backbone considerably restricts the conformational flexibility, which is the reason for proline to be often involved in the formation of loops and turns. In addition, while all other amino acids almost exclusively form *trans* peptide bonds, a considerable amount of Xxx-Pro peptide bonds are found to exist in *cis* conformation (10-40 %). For ubiquitin in the condensed phase, *cis/trans* isomerization of peptide bonds preceding proline has been found to play an important role in the folding dynamics [167–169]. For unfolded, condensed-phase ubiquitin, about 9 % of Pro^{19}, 14 % of Pro^{37}, and 19 % of Pro^{38} are involved in *cis* peptide bonds [168]. Pro^{19}, however, occupies a somewhat strategic position for folding since the native hydrogen bonded structure can only be formed when Pro^{19} is preceded by a *cis* peptide bond [168]. In contrast, *cis* peptide bonds preceding Pro^{37} and Pro^{38} are less important for the overall structure [168]. Furthermore, *cis/trans* isomerization is responsible for rather slow folding dynamics and represents a kinetic bottleneck [168].

Also in the gas phase, *cis/trans* isomerization of the Xxx-Pro peptide bond was recently shown to significantly influence the structure of smaller peptides. A detailed analysis of different variants of the nonapeptide bradykinin, for example, revealed that *cis/trans* isomerization of prolyl-peptide bonds is responsible for the formation of multiple distinct coexisting gas-phase conformations [165]. Analysis of a wide number of proline-containing peptides furthermore showed that this effect is rather general and not limited to bradykinin [170]. Additionally, in a work related to this thesis, it was recently demonstrated how *cis/trans* isomerization is influenced by interactions with monovalent cations [171].

The observation of two (or more) peaks in an ATD means that two (or more) different conformations with different cross-sections are stable in the gas phase and do not interconvert on a millisecond time scale at 300 K. This implies that rather large free energy barriers separate their corresponding conformational space. A large number of hydrogen bonds that need to be broken simultaneously in order to change conformation could give rise to such a barrier. When the structural differences are large, as for example for a folded and extended structure, this would be expected. In the case of ubiquitin 11^{+}, however, both structures are extended, for which case it is much more difficult to imagine a substantial free energy

---

[*] Qualitatively identical results are found when using a simplified intensity scale of 0 (peak not observed) and 1 (peak observed) for composing the cleavage propensity plot (Figure 4.6).

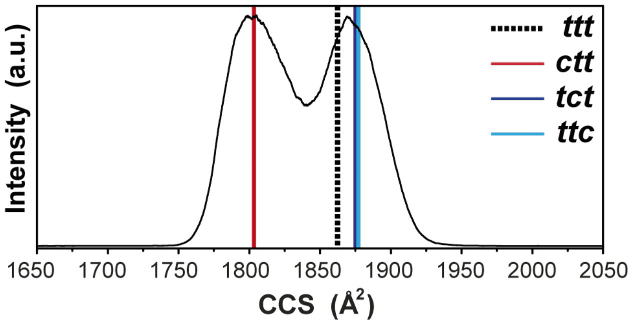

Figure 4.8: Collsision cross-sections (CCSs) of 11^+ ubiquitin. The time axis in the ATD was converted to CCS, and theoretical CCSs of four types of structures are shown as lines.

barrier that is governed by differences in the hydrogen bond pattern. The observation that both structures generating the ATD in Figure 4.2 mostly show differences in the UVPD fragmentation behavior around Pro^{19} points to a special role of this residue. *Cis/trans* isomerization of an associated peptide bond could explain both the apparent presence of a large free energy barrier and the difference in fragmentation behavior of the two conformers.

Molecular Dynamics Simulations*

In order to shed more light on the possible role of proline *cis/trans* isomerization, molecular dynamics (MD) simulations of ubiquitin were performed, with the peptide bond preceding residues Pro^{19}, Pro^{37}, and Pro^{38} in all *trans*- (*ttt*) as well as mixed *cis/trans* (*ctt*, *tct*, and *ttc*) conformations using the Amber force field (ff99SB-ILDN) [158] and the program package Gromacs [157]. For most charge states of ubiquitin, many possibilities of how protons are distributed over the various basic sites exist. The 11^+ charge state is an exception, however, since 11^+ is very likely formed by protonation of all four arginines, all seven lysines, and the N-terminus, with the C-terminus being the only deprotonated site. As starting point, structures resembling those of the condensed-phase A-state were chosen as described before [156, 172, 173]. For each *ttt*, *ctt*, *tct*, and *ttc* conformer, six MD runs at a temperature of 300 K with a duration of 100 ns were performed. Generally, in all simulations, structures remained in conformations that featured the secondary structure of the A-state, namely, an N-terminal β-hairpin that ranges almost to Pro^{19} and two helical segments that are extended by charge repulsion of the protonated side chains of the lysine and arginine residues. The simulations of the individual *cis/trans* conformer types reveal local structural differences around the proline residues. *Cis/trans* isomerization of the peptide bonds around proline is not observed to occur over the course of a simulation.

For quantitative comparison with the experimental data, theoretical CCSs of the four conformers *ttt*, *ctt*, *tct*, and *ttc* were obtained by averaging CCS values of 3600 structures

---

[*] Calculations were performed by Carsten Baldauf in the Theory department of the Fritz Haber Institute.

taken at 0.1 ns intervals from the MD trajectories (the first 40 ns of the trajectory were left for equilibration and were not considered in the analysis).

Figure 4.8 shows the ATD of 11^+ ubiquitin where the time axis is converted into CCS; the vertical lines represent the calculated CCSs of the *ttt*, as well as the *cis* Xxx-Pro bond containing structures *ctt*, *tct*, and *ttc*. CCS calculations were performed using the exact hard sphere scattering (EHSS) model [174], and the resulting cross-sections were scaled by 0.97 to account for systematic errors in the calculation procedure. Surprisingly, only the structure with a *ctt* conformation yields a CCS that is substantially different from the all-*trans* (*ttt*) species. Considering the estimated relative error of the method of about 1 %, the CCSs of the *tct* and *ttc* conformers are virtually indistinguishable from those of the all *trans* species *ttt*. The absolute values of the calculated CCSs might suffer from systematic errors in the EHSS model as well as in the geometries obtained from the MD simulations. The relative differences between the *ctt* and the other conformations should, however, suffer much less from those systematic errors. Thus, it is likely that the more compact conformer (1802 $Å^2$) corresponds to the conformer of ubiquitin 11^+ with the peptide bond preceding Pro^{19} in *cis* conformation, while the more extended conformer (1871 $Å^2$) is due to molecules with the peptide bond preceding Pro^{19} in *trans* conformation.

Implications for the Fragmentation Mechanism

How can the conformational change in Pro^{19} peptide bonds from *trans* to *cis* give rise to such significant changes in the UVPD signature? One possibility is that the UV absorption behavior of the molecule changes with *cis/trans* isomerization at Pro^{19}. A shift in band position, a difference in oscillator strength, or a different nature of the excited state between the *cis* and *trans* peptide bond could result in differing fragmentation propensities.

A second reason for a difference in fragmentation behavior around the Pro^{19} residue could be the UVPD mechanism itself. After photoexcitation, an excited electronic state will either induce direct dissociation or undergo a transition to the ground electronic state, followed by an intramolecular vibrational redistribution (IVR) of the energy gained from photon absorption (6.4 eV). This amount of energy when distributed over all vibrational modes of the molecule in its electronic ground state is probably not enough to cause dissociation on the experimental time scale. Further, the barrier for *cis/trans* isomerization is typically 50-80 kJ mol^{-1} [175], several times lower than that required for dissociation. Thus, if dissociation occurs from the electronic ground state, it would occur from a hot molecule that likely had the opportunity to undergo *cis/trans* isomerization. In that case, one would expect a similar fragmentation behavior for originally *cis* or *trans* molecules. However, a difference in the branching ratio between dissociation from an excited electronic state and transition back to the ground state could result in a different fragmentation behavior. In that case, an electronic excitation around the *cis* peptide bond would have a higher propensity for relaxation and therefore show less fragmentation.

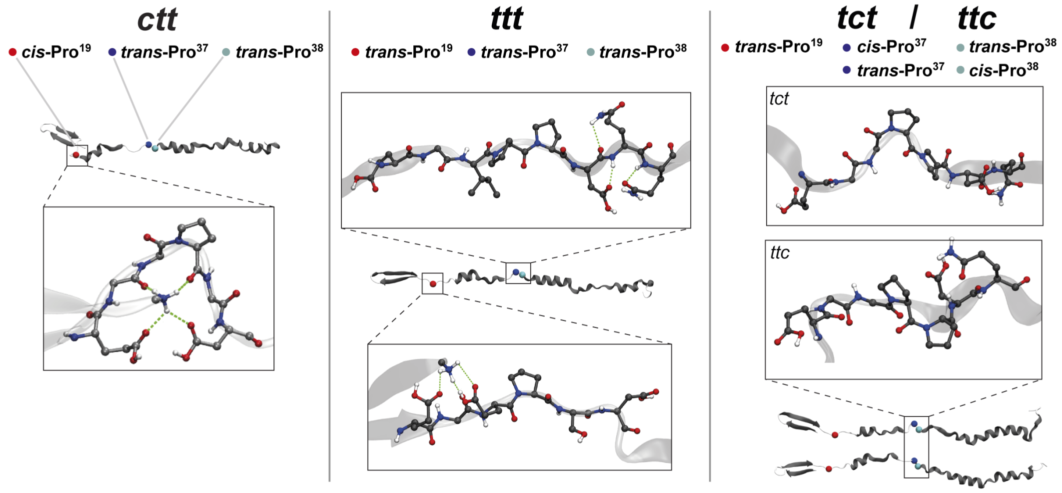

Figure 4.9: Representative MD snapshots of 11^+ ubiquitin from MD simulations. (Left) MD structure with Pro^{19} in *cis* and all other prolines in *trans* conformation (*ctt*); (middle) MD structure with all prolines in *trans* conformation (*ttt*); (right) MD structures with either Pro^{37} or Pro^{38} in *cis* conformation. The regions around the proline residues are magnified and hydrogen bonds are illustrated by dashed lines. Only the *ctt* structure exhibits extended hydrogen bonding network around the Pro^{19} residue when in *cis* conformation.

A third possible explanation arises from differences in the local structure of the molecules. Representative structures of the four model systems *ctt*, *ttt*, *tct*, and *ttc* are shown in Figure 4.9. In the *ctt* conformation, a stable turn-like structure around Pro^{19} is formed, which is conserved over the entire duration of the simulation. This turn promotes multiple hydrogen bond formation in the N-terminal region of the protein. On the other hand, when the peptide bond preceding Pro^{19} is in *trans* conformation (Figure 4.9 middle), no hydrogen-bonding networks in the proximity of the Pro^{19} residue are found. This is also the case for both *cis* and *trans* conformations of the residues Pro^{37} and Pro^{38} (Figure 4.9 right) where stable hydrogen bond networks are not formed over the simulation time.

To examine the potential influence of the hydrogen bond network on the fragmentation pattern, the number of contacts (all atoms closer than 0.3 nm) between two fragments after hypothetical cleavage of a peptide bond is plotted as a function of the cleavage position in the upper panel of Figure 4.10. For all structures, this plot shows a maximum in the number of contacts for a cleavage near the turn of the β-sheet segment, as the two adjacent strands are closely linked with each other. All along the backbone, the *ttt*, *tct*, and *ttc* conformations have a very similar number of contacts between their hypothetical N- and C-terminal fragments, in line with their very similar structures and CCSs. The *ctt* molecule on the other hand shows an enhanced number of contacts up to the end of the β-sheet region, most pronounced around the Pro^{19} residue. In Figure 4.10, lower panel, the difference in the number of contacts between *ttt* and the other structures is shown. Clearly, a large enhancement for *ctt* around

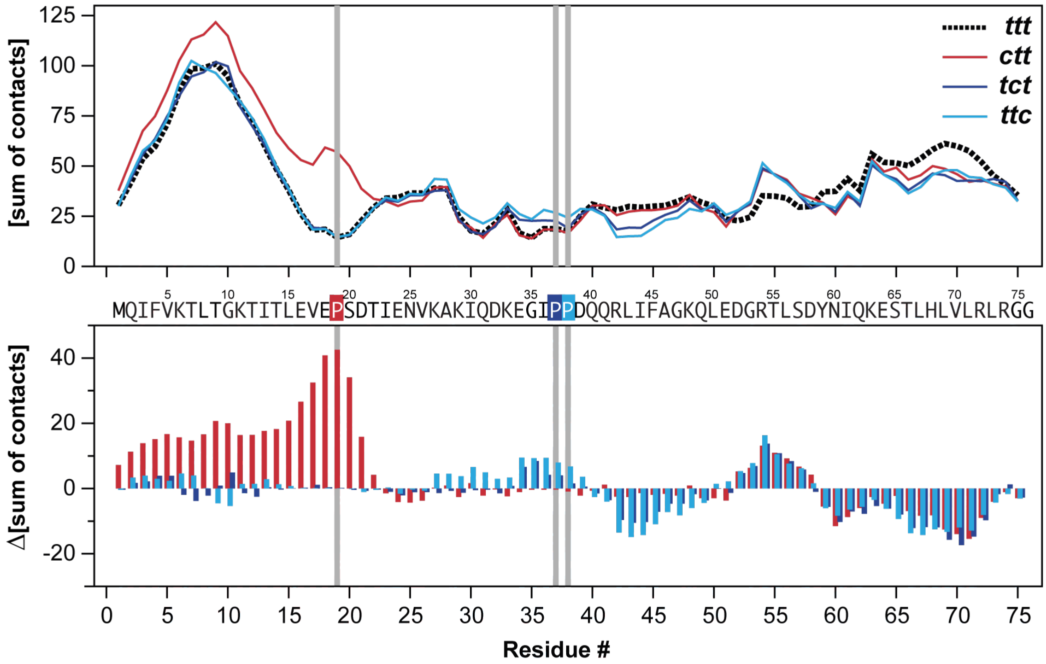

Figure 4.10: Number of intramolecular contacts below 0.3 nm. (Upper panel) number of contacts (atoms being closer than 0.3 nm) between the right and left part of the molecule after a hypothetical cleavage of a peptide bond, where the x-axis corresponds to the cleavage position; (lower panel) difference relative to the *ttt* structure. The *ctt* (red) structure shows a considerably elevated number of contacts between the N- and C-terminal fragments when cleaved around Pro^{19}.

Pro^{19} is observed. That is, the N- and C-terminal fragments formed *via* cleavage around Pro^{19} are located in close spatial proximity with an enhanced number of noncovalent contacts. Enhanced hydrogen bonding and salt bridges in proteins was previously shown to decrease the abundance of fragment peaks in other high-energy dissociation methods such as ETD [32, 153]. In those instances, additional post-ETD collisional activation was necessary to break the noncovalent interactions between fragments after cleavage of the peptide backbone. It is conceivable that the same effect leads to a decreased abundance of fragments from backbone cleavages around Pro^{19} in the *ctt* conformation. This would cause differences in the detection efficiency of fragment ions and lead to the observed differences in UVPD spectra.

Which of the three possibilities described above gives rise to the fragmentation differences reported here is not completely unambiguous although the evidence is most consistent with the third possibility; that is, for ubiquitin 11$^+$ *cis/trans* isomerization of the peptide bond preceding Pro^{19} is very likely the origin for the differences in UVPD fragmentation behavior. What is unambiguous, however, is that the ubiquitin structure and UVPD fragmentation pattern are closely linked. Other possible issues, like the detailed location of charges, await further investigation.

4.2.2 Conclusions

In summary, the presented study reports first experimental evidence for the conformational dependency of UV photofragmentation of a protein at 193 nm. In contrast, collision induced dissociation proved not to sensitive on higher order protein structure. In conjunction with MD simulations, results obtained from the combined IM-MS/UVPD experiment indicate that the *cis/trans* isomerization of proline is responsible for stable A-state-like gas-phase conformations of ubiquitin in high charge states. The *cis/trans* isomerization of the peptide bond preceding Pro^{19} was shown to have the biggest influence on the protein's overall structure when extended, as in the A-state. Seen from a broader perspective, these data furthermore demonstrate the potential of conformer-selective UVPD to serve as tool for the structural analysis of proteins in the gas phase.

4.3 Ubiquitin 7^+: Connections Between Conformers*

Using IM-MS in conjunction with UVPD, it was demonstrated in Section 4.2 that higher order structure of a protein can drastically influence its photofragmentation behavior at 193 nm. The UVPD spectra of two different elongated structures of the 8.5 kDa protein ubiquitin in charge state 11^+ showed a significant variation in the fragment pattern, which was attributed to a difference in the intramolecular hydrogen bond pattern as a consequence of *cis/trans* isomerization of a single peptidyl-prolyl bond. Here, conformer-selective UVPD data for ubiquitin 7^+ ions is presented. These protein ions of *intermediate* charge are known to adopt a large variety of compact and extended conformations in the gas phase (compare Figure 1.4). The data indicates that UVPD is also structure-sensitive for this conformationally much more diverse charge state. Furthermore, the study presents evidence for a connection between certain conformers, which show similar UVPD dissociation patterns even if they exhibit vastly different CCSs. From that it is concluded that groups of structures with considerably different CCSs but similar structural features within one group exist.

4.3.1 Results and Discussion

Ion Mobility-Mass Spectrometry of Ubiquitin 7^+

In both environments, solution and the gas phase, ubiquitin has been observed to adopt various distinct conformations, ranging from compact, globular to unfolded, extended structures [13, 145, 160, 162, 176]. As for most proteins, the charge state of the ions was found to be most influential on the structure after transfer into the gas phase. Compact conformations require low charge states whereas more elongated structures are dominantly found for higher charge states (see also Figure 1.4 in the introductory chapter of this thesis). Moreover, recent studies have shown that the gas-phase conformation of ubiquitin is also closely linked to the solution conditions the ions originate from [21, 112, 145, 156]. When electrosprayed from aqueous or more denaturing solvents, ubiquitin was shown to adopt compact, native-like conformations, as well as a more elongated α-helix rich structure (the so-called A-state in Figure 4.1) [112, 156], which are similar to those existing in the condensed phase [160, 162, 176]. Using IMS-based techniques, it was furthermore shown that there is a certain connection between distinct folded and unfolded structures of gas-phase ubiquitin, which was attributed to structural features that are preserved during the unfolding process [19].

This study focuses on ubiquitin ions of the intermediate charge state 7^+ in which attractive and repulsive intramolecular interactions are balanced and multiple different structures are observed simultaneously using IM-MS. For these ions, the distribution of gas-phase conformers strongly depends on instrument parameters such as source conditions and injection energy. At gentle conditions, a compact species with a CCS of ~ 1000 Å^2 can be observed, which

---

*This chapter is based on the work published in S. Warnke, G. von Helden, and K. Pagel *Proteomics* **2015**, *15*, 2804–2812. http://dx.doi.org/10.1002/pmic.201400480
Figures and content reprinted with permission. Copyright 2015 WILEY-VCH Verlag GmbH & Co. KGaA.

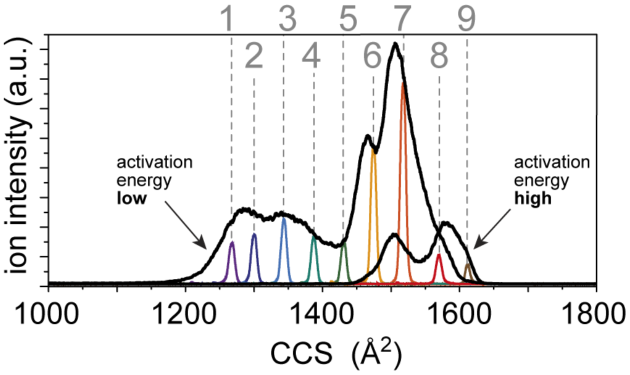

Figure 4.11: Arrival time distributions (ATDs) of ubiquitin 7^+ at two different trap settings. The time axis was converted to collision cross-section (CCS). The narrow peaks labeled consecutively from 1–9 are the selected portions of the ATDs transmitted for UV photodissociation. A previously reported more compact conformation ($\sim$ 1000 Å^2) was not studied within this work [145, 156].

unfolds to intermediate and extended structures with CCSs ranging from 1200 Å^2 to 1600 Å^2 when the molecules are energized.

In Figure 4.11 typical arrival time distributions (ATDs) of ubiquitin 7^+ measured at two different trap conditions are shown with drift times converted to CCSs. At intermediate conditions, the ATD exhibits a variety of partially folded (1200–1450 Å^2) and extended structures ($>$ 1450 Å^2) all of which having been observed previously [20, 112]. A more compact conformer around 1000 Å^2 was also observed but not studied in detail here due to very low ion intensities. At harsher trap conditions, *i.e.* higher voltage gradients and RF amplitudes inside the ion trap, at least two more extended structures were observed with CCSs of $\sim$ 1500 Å^2 and $\sim$ 1600 Å^2, respectively. The narrow peaks consecutively labeled with numbers 1–9 are the slices of the ATDs that have been selected at the ion ejection lens and were transmitted for UV photodissociation.

UV Photodissociation of Selected Ubiquitin 7^+ Conformers

After drift-time and m/z-selection, the isolated ions are subjected to a single unfocused 193 nm ArF excimer laser pulse ($\sim$ 1 mJ) and fragment spectra are recorded for each selected conformer individually by averaging over 500 TOF pulses. The so obtained UV photofragment spectra of the nine different ubiquitin 7^+ structures from the ATD in Figure 4.11 are shown in Figure 4.12. The spectra are normalized to the intensity of the precursor ion signal and then equally scaled to the level of the fragment intensities. The roman numerals I–VIII denote the strongest ion signals. As expected from previous studies [72] and from experiments described in Section 4.2, a vast variety of different fragments is formed, which in turn results in rich

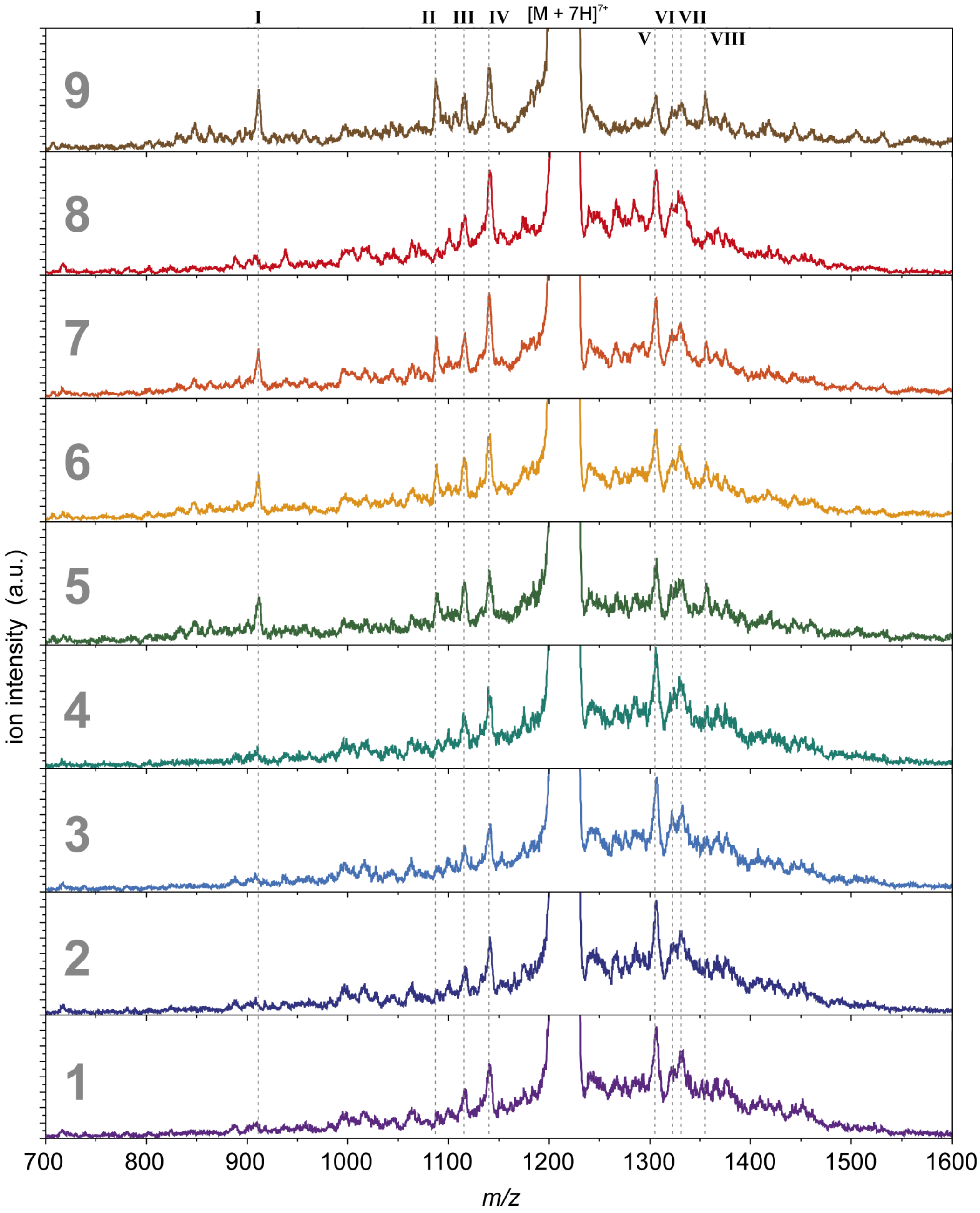

Figure 4.12: UVPD fragment spectra of the selected portions of the ATD labeled 1–9 in Figure 4.11. The spectra are normalized to the intensity of the precursor ion signal and then equally scaled to the level of the fragments. The dashed lines highlight the most prominent signals I–VIII. Conformers that occur at both trap settings (Figure 4.11) yield identical UVPD spectra.

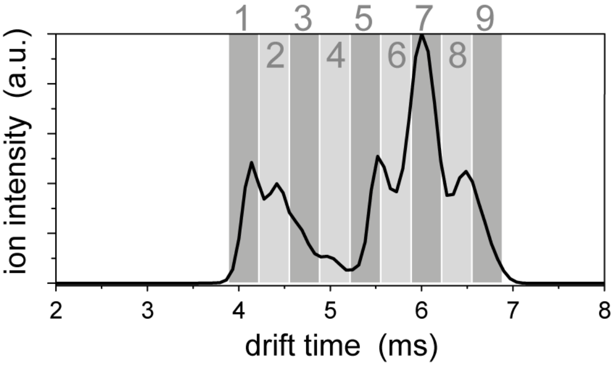

Figure 4.13: ATD of ubiquitin 7^+, measured on the traveling-wave (TW) instrument. The conformer distribution observed here and on the drift-tube (DT) instrument (Figure 4.11) are virtually identical. The gray bars labeled 1–9 consecutively indicate the regions of the ATD that were selected for extraction of CID fragment spectra.

fragment spectra with many, often only partially resolved signals. All ion signals, however, can be clearly distinguished from the noise level. A comparison between mass spectra of undissociated and dissociated ubiquitin 7^+ ions can be found in Figure 2.29 of Chapter 2.

Many of the fragment signals in Figure 4.12 can be found in all nine spectra; others, however, are only present in some. Among the most apparent differences are the fragments labeled I, II and VIII, which are of higher intensities in the fragment spectra of the ATD slices labeled 5, 6, 7, and 9 than in the spectra labeled 1, 2, 3, 4, and 8. In addition the fragment V is of considerably higher intensity in the latter set of spectra.

Even without further assignment of the peaks, two aspects can already be concluded from the spectra in Figure 4.12. First, ubiquitin 7^+ ions show a different UVPD fragmentation behavior depending on their conformation. This interesting observation was first made for the 11^+ ubiquitin ions in the previous section and indicates once more that UVPD is structure-sensitive to a certain extent. Second, some of the fragmentation spectra along the conformer distribution are rather similar, which points to a link between certain conformers.

CID of Selected Ubiquitin 7^+ Conformers

For the highly charged, extended ubiquitin ions in Section 4.2, fragment spectra from low-energy CID did not prove to hold structural information. The universality of this result, however, cannot be affirmed at this point. To test whether the high structural diversity of the ubiquitin 7^+ ions has any impact on the CID fragmentation patterns, conformer-resolved fragmentation experiments were performed on the TW IM-MS instrument described in detail in Section 2.7. CID fragments were generated after conformer-separation of the *m/z*-selected ions and fragment spectra were acquired with high *m/z* resolution, allowing an unambiguous fragment assignment using a complete list of possible fragments.

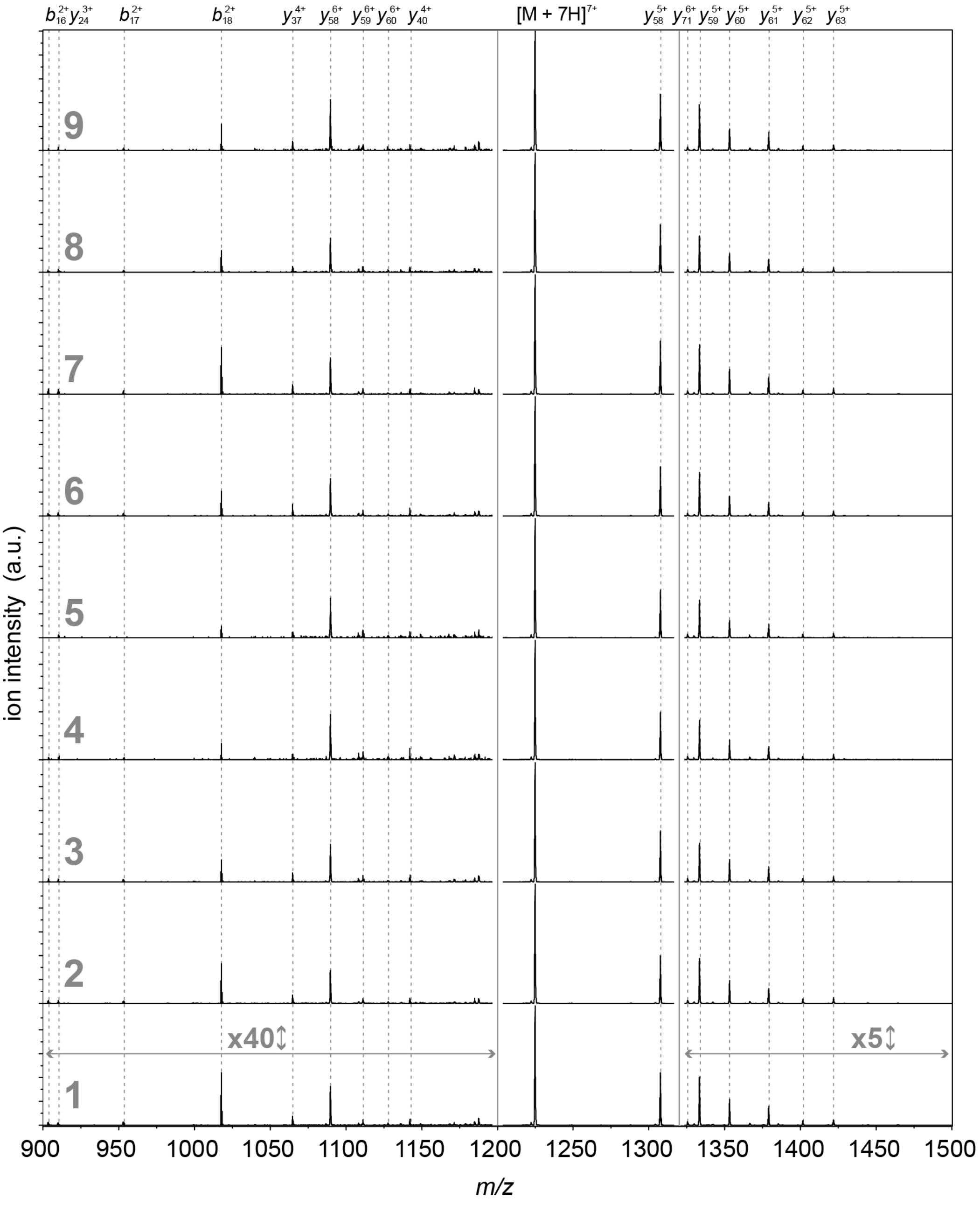

Figure 4.14: CID fragment spectra of the selected regions labeled 1–9 in the ATD in Figure 4.13. The spectra are normalized to the intensity of the precursor ion signal. The lower and higher m/z ranges are magnified by factors of 40 and 5, respectively. The variation in intensity of the fragment at m/z 1020 (b_{18}^{2+}) lies within 0.5 % and 2.5 % of the strongest fragments and is therefore not considered significant here.

A typical ATD of ubiquitin 7^+ from this experiment is shown in Figure 4.13. The distribution and relative abundances of the partially folded and extended structures are virtually identical to those observed at the DT instrument in Figure 4.11. Indicated in gray and consecutively labeled 1–9, are the drift-time windows for which fragment spectra were extracted from the data. Each of these drift-time windows was selected such that a direct comparison to the UVPD spectra of the nine different conformers from the ATD in Figure 4.11 is possible. The corresponding CID fragment spectra are shown in Figure 4.14. The lower and higher m/z ranges are magnified by factors of 40 and 5, respectively. The dashed lines indicate the positions of the assigned fragment types that are annotated at the top of the figure.

As reported previously, fragment spectra from low energy CID of ubiquitin ions are largely dominated by b- and y-type fragments stemming from cleavages N-terminal to proline or C-terminal to acidic residues [72, 73, 166, 177, 178]. A similar trend is also observed in this experiment and leads to a prominent series of C-terminal y-type fragments (starting at m/z 1306), which stem from cleavages of the peptide bonds between Glu^{18}-Pro^{19} (y_{58}^{5+}) and the five preceding residues Val^{17}-Glu^{18} (y_{59}^{5+}), Glu^{16}-Val^{17} (y_{60}^{5+}), Leu^{15}-Glu^{16} (y_{61}^{5+}), Thr^{14}-Leu^{15} (y_{62}^{5+}), and Ile^{13}-Thr^{14} (y_{63}^{5+}) with decreasing signal intensity for fragmentation towards the N-terminus. A second series of peaks stems from the same fragments at a higher charge state (6^+), but their intensity is considerably reduced corresponding to only a few percent of the lower-charged equivalents.

Unlike in the UVPD experiments, however, no significant differences between the CID fragment spectra of the nine ubiquitin 7^+ conformers can be observed. The insensivity of CID fragmentation towards higher order protein structure was similarly observed for the highly charged ubiquitin ions in Section 4.2 and was the outcome of earlier studies [164]. It is noteworthy, that a variation in abundance of a low intensity fragment signal at m/z 1017 can be observed. However, the absolute intensity of this b_{18}^{2+} fragment, which is the N-terminal counterpart of the most intense y_{58}^{5+} fragment, only varies between 0.5 % and 2.5 % of the y_{58} signal and furthermore follows the relative intensity distribution of the precursor ion signal (compare relative intensities in Figure 4.13). It is likely that the intensity variation of this low abundance signal is an artefact of the measurement and is therefore considered to be not significant in the context of this study.

UVPD Fragment Assignment

A deeper understanding of the observed dependence of UV photofragmentation on the protein conformation requires an unambiguous assignment of the obtained fragments. As in the case of the UV photofragments of ubiquitin 11^+ ions discussed in the previous section, the limited resolution of the TOF mass spectrometer used here does not permit fragment assignment purely based on the presented UVPD fragment spectra. Considering the mass accuracy (m/z ± 1.5) and resolution ($\Delta \mathrm{m/m} \sim 500$) of the instrument, up to five distinct photofragments can be hypothetically assigned to each of the signals labeled I–VIII (Table 4.1). For the similarly

Table 4.1: Possible UVPD fragments in a ±1.5 Da window around the observed species I–VIII. Bold numbers denote Pro residues. Fragments observed previously by UVPD for other charge states are marked with “x” when present or “xx” when particularly prominent in the reference spectra. Fragments observed in the CID experiment are marked with “x”.

Label	m/z	m/z	Type	Sequence	prev. observed	
	(exp.)	(th.)		position	in UVPD[a]	in CID[b]
I	912.8	912.1	c_{16}	16	-	-
		913.7	y_{48}	29	x	-
		913.8	y_{40}	**37**	xx	-
		914.3	b_{41}	41	-	-
		914.4	b_{49}	49	-	-
II	1089.0	1089.2	z_{38}	**38**	xx	-
		1089.6	y_{58}	**19**	xx	x
III	1118.1	1116.7	c_{30}	47	-	-
		1117.4	z_{10}	67	x	-
		1117.8	y_{39}	**38**	x	-
		1118.4	c_{20}	20	-	-
IV	1141.4	1141.3	x_{50}	27	-	-
		1142.1	y_{40}	**37**	xx	x
		1142.3	x_{30}	47	x	-
		1142.3	z_{20}	57	x	-
		1142.6	b_{41}	41	-	-
V	1307.6	1307.0	b_{47}	47	-	-
		1307.3	y_{58}	**19**	xx	x
		1308.3	x_{70}	7	-	-
		1309.7	y_{46}	31	x	-
VI	1323.7	1325.1	a_{24}	24	-	-
		1325.2	a_{36}	**36**	x	-
		1325.3	y_{71}	6	x	x
VII	1333.1	1332.1	a_{48}	48	-	-
		1333.1	y_{59}	**18**	xx	x
		1333.8	z_{47}	30	x	-
		1333.9	y_{35}	42	x	-
		1334.6	b_{36}	**36**	x	-
VIII	1356.4	1356.1	z_{24}	53	x	-
		1356.9	a_{72}	72	-	-
		1357.6	a_{37}	**37**	x	-

[a] in UV fragment spectra of ubiquitin 10^+ and 11^+ [72] (unpublished data).
[b] in CID fragment spectra of 7^+ ions within this study.

complex photofragment spectra of the 11^+ ions in Section 4.2 an assignment was still possible because high-resolution reference fragment spectra of thenformer resolved ubiquitin 11^+ ions were made available by the group of Jennifer Brodbelt [72]. For the here considered 7^+ ions this is not the case. To still narrow down the list of possible candidates, the unambiguously identified photofragments of 10^+ and 11^+ ubiquitin ions observed in the high-resolution experiments [72] were compared to the list of possible fragments observed here for the 7^+ ions (Table 4.1). For each signal I–VIII, at least two fragment candidates have been previously observed in UVPD of 10^+ and 11^+ ubiquitin. These fragments are marked with an "x" or, if the fragments are particularly prominent in the reference spectra, with "xx" in Table 4.1. It is interesting to note that for each of the features I–VIII at least one fragment is observed that stems from cleavage of a peptide bond involving one of the three proline residues that are present at positions 19, 37, and 38 in the sequence of ubiquitin. In addition, the fragments involving proline residues are generally among the most prominent signals in the UVPD spectra of the higher charged species [72] (and unpublished data).

Comparison of the photofragment spectra with the fragments observed in the low-energy CID experiment can yield further information about fragment identities. Despite the inherently different dissociation mechanisms involved in UVPD and CID, several fragments of ubiquitin 11^+ were found in both, the UVPD and the CID experiment in Section 4.2. Intriguingly, five C-terminal y-type CID fragments of the 7^+ ions are also among the previously observed UV photofragments of ubiquitin 10^+ and 11^+. Those fragments are marked with "x" in Table 4.1. Most of these fragments, namely y_{58} (5^+, 6^+), y_{40} (4^+), and y_{59} (5^+), stem from cleavage of peptide bonds preceding proline residues.

A dissociation method that was previously shown to depend on the higher order structure of ubiquitin is ECD [25, 150, 179]. Using this dissociation technique for ubiquitin 7^+, however, mainly leads to c- and z-type ions [179], none of which having been observed in previous UVPD experiments of ubiquitin 10^+ and 11^+.

Taken together, there is still a certain ambiguity in the identification of possible fragments for the eight most prominent signals in Figure 4.12. Similar to the dissociation propensities found for 11^+ ubiquitin, however, there is clear evidence for a prevalence of fragments stemming from cleavages of peptide bonds involving proline residues. Such a proline-effect is well known for slow heating techniques such as CID [166, 177], but was previously shown to be not significant in UVPD [67]. The present study and the results presented in Section 4.2 clearly contradict these findings. However, it is important to note that the tentative fragment assignment made here only involves the eight most prominent of the hundreds of different fragments observed in the experiment and does, thus, not contradict earlier studies where rather non-specific backbone cleavage is found upon photodissociation at 193 nm.

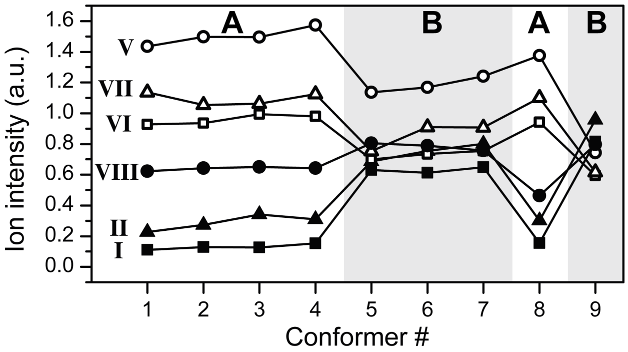

Figure 4.15: Intensity dependence on conformation of the most abundant UVPD fragments. The signals labeled III and IV in Figure 4.12 show only little variation and are not included here. On the basis of these fragment intensities, the nine conformers can be classified into two groups, A and B.

Connection between conformers

To gain more insight into the apparent link between certain structures, the intensities of the fragments that exhibit noticeable intensity variations along the conformer distribution are plotted in Figure 4.15. For clarity, open and solid symbols are used, indicating two different types of curve progressions. The fragments labeled I, II and VIII in Figure 4.12, each increase in intensities for conformers 5, 6, 7, and 9, whereas the opposite is the case for the fragments labeled V, VI, and VII, which are of higher intensities in the fragment spectra of the conformers 1, 2, 3, 4, and 8. This observation supports the hypothesis that certain structures are connected. Accordingly, the nine different structures of ubiquitin 7^+ can be classified into two groups of conformers with similar photofragmentation patterns, namely structures 1-2-3-4-8 (group A) and structures 5-6-7-9 (group B).

The fact that the photofragmentation patterns of two distinct conformers are different must be a result of a difference in structure. One premise for the coexistence of multiple structures at a temperature of 300 K is the existence of sufficiently high energy barriers that separates their corresponding conformational space and prevents group A and group B structures from interconverting on the timescale of the experiment. In solution studies on ubiquitin, *cis/trans* isomerization of peptide bonds involving loop and turn-inducing proline residues has been identified to form such a barrier, which is typically around 50-80 kJ mol^{-1} [175]. Especially the residue Pro^{19} was found to be of particular importance for the protein structure [168], and in Section 4.2 it was shown that *cis/trans* isomerization of the peptide bond preceding the residue Pro^{19} is likely the reason for coexisting gas-phase structures of 11^+ ubiquitin. Similar conclusions have been drawn for smaller proline containing model peptides where multiple coexisting gas-phase conformations were attributed to isomerization of peptidyl-prolyl bonds [165, 170].

The here performed tentative fragment assignment suggests that for ubiquitin 7^+, like in the

11^+ case, many differences in fragment identities and relative abundances arise from cleavage around Xxx-Pro peptide bonds, which leads to the conclusion that isomerization of these peptide bonds plays an important role for the 7^+ ions as well. The two different structural groups A and B are, therefore, likely to differ in the isomerization state of peptidyl-prolyl bonds. Such a subtle difference in local structure, on the other hand, can severely influence the entire intramolecular hydrogen bonding network of the protein (Section 4.2.1). In ECD and ETD experiments [25, 32, 180], as well as vacuum UVPD on protein-ligand complexes [181] it was found that the retention of non-covalent interactions after cleavage of the backbone can lead to distinct fragmentation patterns. It is not unlikely, that similar effects are responsible for the differences in the UVPD spectra observed here.

Fragment spectra from low energy CID experiments do not contain information about differences in higher order structure. This is not surprising because the internal energy of the molecule is increased gradually with each collision until it reaches the dissociation threshold, which typically exceeds the barrier for *cis/trans* isomerization of Xxx-Pro peptide bonds [182]. The situation is different, however, when unfolding rather than the dissociation of the molecule is monitored after subjection to collisions with inert gas molecules. In a recent series of studies on collision induced unfolding (CIU) of different gas-phase conformations of ubiquitin 7^+, it was concluded that partially folded and unfolded structures can retain certain structural aspects of the compact species from which they originated [19, 112]. In other words, certain structures are linked over an unfolding path, with shared structural motifs. The here presented results support this hypothesis and indicate that the similarities in the photofragmentation pattern within one group arise from shared structural features, which are maintained over the group's entire conformational space (i.e. 1-2-3-4-8 for group A and 5-6-7-9 for group B).

4.3.2 Conclusions

UVPD recently emerged as a promising technique for peptide and protein sequencing because nearly complete sequence coverage can be achieved within a relatively simple experiment. Using a combined IM-MS-UVPD-TOF MS approach where ions can be size- and *m/z*-selected before photodissociation at 193 nm, it is shown here, that UVPD is sensitive to the underlying higher order structure of conformationally highly diverse 7^+ ubiquitin ions. Considerable differences in fragment identities and abundances were observed in the photofragment spectra of different pre-selected conformations. These results are in good agreement with the data on two extended conformers of 11^+ ubiquitin in Section 4.2, which showed a significantly different UVPD fragmentation behavior.

At the current state, however, the present data also implies that specific conformers not necessarily yield unique UVPD fragment spectra. Instead, repeating fragment patterns are found, which indicate that certain structures within the ensemble are closely connected. Based on these results, the conformers of 7^+ ubiquitin can be categorized into two groups, A and B, each of which exhibiting various structures with different CCSs but a similar UVPD fragmentation behavior. This leads to the assumption that, despite their difference in CCS, the conformers within one group share a common structural feature, which is retained over the entire gas-phase unfolding pathway, while a relatively large energy barrier prevents interconversion between both groups on the timescale of the experiment. For 11^+ ubiquitin ions, *cis/trans* isomerization of Xxx-Pro peptide bonds was identified as a possible cause for the varying photodissociation pattern. Even though the limited mass resolution in the photofragment spectra of ubiquitin 7^+ ions reported here does not allow an unambiguous assignment of all fragments, it is likely that the observed differences in the UVPD spectra are also originating from *cis/trans* isomerization of peptidyl-prolyl bonds.

From a more general perspective, the present study implies that the conformational families often observed for gas-phase proteins, are in fact groups of dynamically interconverting structures that are separated by a relatively large energy barrier. While UVPD is not sensitive to the conformational aspects within one group, it can well be used to distinguish between different groups – for example to identify proline *cis/trans* isomers, which are known to have a significant impact on the folding of proteins in both, solution and the gas phase.

5 Isomer-Selective IR Spectroscopy: Protomers of Benzocaine*

"And now for something completely different."
– Monty Python

The immediate environment of a molecule can have a profound influence on its properties. Thus, care has to be taken when the applied method of investigation imposes an environment on the molecule other than the one of interest. This can be the case when gas-phase methods are applied for the investigation of biological molecules, or molecules that are active in a biological context. Condensed-phase properties of the molecule can then not directly be deduced from these experiments but require the knowledge of how condensed-phase and gas-phase properties are correlated. A prerequisite for this is, of course, a detailed understanding of the experimental observations.

This chapter describes the structural investigation of the local anaesthetic benzocaine using ion mobility-mass spectrometry in conjunction with IR spectroscopy in a wavenumber range of 950–1800 cm^{-1}. The observed vibrations of, for example, C=O, N-H$_2$, or N-H$_3$ groups of two drift-time separated species are then assigned to different structures of the same molecule by comparison to quantum chemical calculations. This combination of experiment and theory allows the unambiguous identification of two different structures of gas-phase benzocaine, whose relative populations highly depend on the solvent conditions that are used for electrospray ionization. This observation of multiple coexisting species is attributed to the different dielectric properties of the solution- and the vacuum environment of the experimental apparatus. Further calculations suggest that a carbonyl group, rather than an amine group, is, somewhat unexpectedly, the preferred protonation site when the molecule resides in an environment of low relative permittivity, such as the vacuum or the hydrophobic protein environment of an ion channel.

After the different species of benzocaine are identified, it finally becomes apparent that not their difference in size but rather differences in the ion-neutral interactions are responsible for

---

*This chapter is based on the work published in S. Warnke, J. Seo, J. Boschmans, F. Sobott, J. H. Scrivens, C. Bleiholder, M. T. Bowers, S. Gewinner, W. Schöllkopf, K. Pagel, and G. von Helden *J. Am. Chem. Soc.* **2015**, *137*, 4236-4242. http://dx.doi.org/10.1021/jacs.5b01338
Figures and content reprinted in accordance with the Creative Commons CC-BY Usage Agreement. Copyright 2015 American Chemical Society.

their ion mobility separation. These results emphasize that the interaction of the ion with the drift gas can play an important role and has to be carefully considered for the calculation of collision cross-sections from model structures.

5.1 Introduction

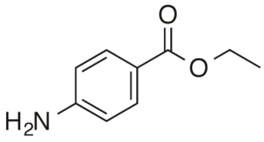

Figure 5.1: Chemical structure of the local anaesthetic benzocaine, the ethyl-ester of *para*-aminobenzoic acid.

All atoms and molecules interact with their surroundings, which can be highly diverse ranging from a weakly interacting gas to a strongly interacting liquid or solid. The interactions of molecules with the environment will influence them by perturbing and shifting energy levels, thereby possibly altering their structures, reactivities, and other properties. Biological systems can offer a wide range of different environments. Those can be polar and protic in an aqueous medium or nonpolar and hydrophobic in a protein environment or inside a membrane. The corresponding relative permittivities ϵ_r can range from $\epsilon_r = 80$ for water to below $\epsilon_r = 2$ in nonpolar surroundings. The different environments will have profound effects on the solubility, charge distribution, and the structures of molecules.

An interesting class of molecules, which are biologically active in (vastly) different dielectric environments, is comprised of the esters of *para*-aminobenzoic acid, some of which find a clinical application as local anaesthetics (LAs) [183, 184].

In contrast to aminobenzoic acid, which can act as both acid or base in aqueous solution, its esters are lacking an acidic group and can only act as a base, a common feature of all LAs [185]. Their mode of action involves inhibition of signal conduction through the neuronal cell membrane by blocking the flux of Na^+ ions through voltage-gated sodium channels [183, 184, 186–188]. In aqueous solutions at physiological conditions (pH 7.4, 150 mM NaCl), most LAs exist as both charged and neutral particles. However, the LA benzocaine (Figure 5.1), the ethyl ester of *para*-aminobenzoic acid, will not be protonated to an appreciable degree under these conditions because of its low pK_a value of 2.5. This property sets benzocaine apart from other LAs. In addition, the hydrophobic nature of benzocaine leads to a poor solubility in aqueous solutions at physiological conditions [189]. Despite these differences, benzocaine can still act as a sodium channel blocker, and the formation of a benzocaine-Na^+ complex inside the pore has been suggested to be the active form to solve this apparent paradox [190].

For the analysis and identification of drugs and related compounds, mass spectrometry (MS)-based methods are indispensable today. To understand and quantify the results obtained, it is important to find clear correlations between condensed-phase properties and those in the gas phase. Recent research is especially directed toward the implementation of ion mobility spectrometry (IMS), a method to separate different isobaric gas-phase structures, as a standard technique in conjunction with MS to aid compound analysis. In this context, it is essential to unambiguously link experimental and calculated results.

Here, the structure and protonation propensities of benzocaine is investigated when sprayed from solution into a solvent-free environment with relative permittivity, ϵ_r, of 1. In terms of electric properties, such an environment resembles a hydrophobic membrane or the interior of a protein. Ion mobility-mass spectrometry (IM-MS) in employed in conjunction with structure-sensitive spectroscopy in the mid-IR range using a free electron laser (FEL). With these methods, the structure of benzocaine when electrosprayed from both protic and aprotic solvents is probed with a goal of determining changes in the relative protomeric populations.

5.2 Experimental and Computational Details

Samples

Benzocaine and all solvents were purchased from Sigma-Aldrich (Taufkirchen, Germany) and used without further purification. Solutions of 100 μM benzocaine were prepared with methanol/water (v/v, 50/50) and pure acetonitrile as solvents, respectively. For (nano)electrospray ionization, $\sim$ 5 μL of sample were loaded into in-house-prepared Pd/Pt-coated borosilicate capillaries, and voltages of 0.8–1.0 kV were applied [85].

Isomer-Selective CID

Drift-time resolved collision induced dissociation (CID) experiments were performed on the commercial traveling wave (TW) IM-MS instrument described in Section 2.7. After (nano)electrospray ionization, the species of interest were *m/z*-selected by a quadrupole mass filter following isomer separation in an ion mobility (IM) cell. An argon-gas filled collision cell was used to generate CID fragments of the now drift-time separated ions, which are subsequently mass-analyzed by means of TOF MS.

Typical experimental setting were: source temperature, 20°C; capillary voltage, 0.8–1.0 kV; sample cone, 40 V; source offset, 20 V; trap collision energy, 2 V; trap gas flow, 2 mL min^{-1}; helium cell gas flow, 180 mL min^{-1}; IMS gas flow, 80 mL min^{-1}; trap DC bias, 40 V; IMS wave height, 40 V; IMS wave velocity, 1000 m s^{-1}. The collision voltage in the transfer cell was raised until fragmentation was observed (12–20 V).

Isomer-Selective IR Spectroscopy

To preselect gas-phase isomers prior to irradiation with intense IR light, the drift-tube (DT) IM-MS experimental setup described in Section 2.4 was used. After ionization with a (nano) electrospray ionization source ions are separated based on their ion mobilities in the IMS region of the instrument, which is (here) filled with nitrogen buffer gas at $\sim$ 3 mbar pressure. Ions subsequently entered the high-vacuum region where *m/z*-selection occurred in the quadrupole mass filter. For isomer-selective irradiation with IR light, a narrow drift-time window of 100 μs width can be selected by electrostatic deflection prior mass selection. These *m/z*- and drift-time/isomer-selected ions are then irradiated by a 10 μs pulse of IR photons with typical pulse energies between 10 and 40 mJ. The wavelength-dependent photofragmentation is monitored by means of TOF MS and per wavelength step of 3 cm^{-1}, 15 TOF photofragment spectra were averaged. IR spectra are composed by computing the fragmentation yield for each wavelength step. Each spectrum shown below is acquired at least twice.

IR light is generated by a free electron laser [191] housed in the Fritz Haber Institute and transported through an evacuated beamline until it reaches the experimental setup.

More details about the experimental procedures can be found in Chapter 2.6.2 of this thesis.

Computational Details*

Optimized geometries, relative energies, and harmonic vibrational frequencies of O- and N-protonated benzocaine were calculated at the B3LYP level of density functional theory with a def2-TZVP basis set using TURBOMOLE v6.6. [192] Vibrational frequencies are scaled by a factor of 0.975 and convoluted with a Gaussian profile of 1.5 % width to fit the experimental spectra. Proton affinities E_{pa} were calculated by determining single-point energies of the lowest-energy structures of the O- and N-protonated species, using the COSMO solvation model [193] for different relative permittivities, ϵ_r, of the surrounding media and subsequent subtraction from the energy of the neutral.

Theoretical collision cross-sections (CCSs) of the obtained model structures were calculated using the projection superposition approximation (PSA) [194–197] and the trajectory method (TM) [198, 199].

5.3 Results and Discussion

IM-MS experiments were performed using the in-house constructed drift-tube (DT) instrument and the commercially available traveling-wave (TW) instrument that have been described in Sections 2.4 and 2.7, respectively. In both experimental setups, ions are generated *via* (nano) electrospray ionization (nESI) and transferred into the low-pressure environment of the instrument. Here, ions are trapped, and short pulses are released into a nitrogen-filled drift region, which they traverse under the influence of a weak electric field at velocities that are related to their corresponding size. Quadrupole- and TOF mass spectrometry allows further selection and analysis of the ions.

Figures 5.2 (a) and (b) show typical TW and DT arrival time distributions (ATDs) of positively charged benzocaine electrosprayed from different solvents, respectively. Interestingly,

---

*The calculation of optimized geometries was performed by Jongcheol Seo in the Molecular Physics department of the Fritz Haber Institute. Theoretical collision cross-sections were calculated by Christian Bleiholder in the Department of Chemistry, Florida State University.

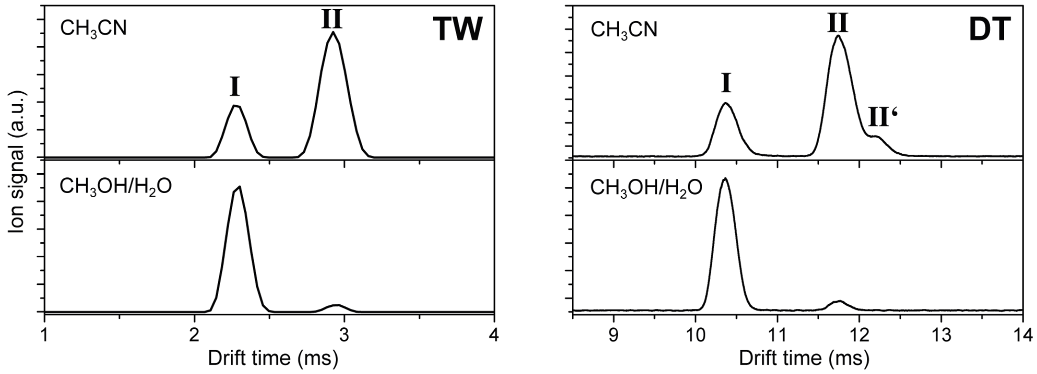

(a) Traveling-wave ATDs **(b)** Drift tube ATDs

Figure 5.2: Arrival time distributions (ATDs) from (a) traveling-wave (TW) and (b) drift-tube (DT) measurements of positively charged benzocaine, electrosprayed from acetonitrile (upper panels) and an aqueous solution (lower panels). Species II' is only observed in the DT instrument.

two well-separated drift peaks can be observed on both instruments, which change in relative intensity when the solvent composition is changed; a feature of high mobility with a drift time of ${}^{\mathrm{TW}}2.25$ / ${}^{\mathrm{DT}}10.30$ ms (I) is predominantly observed for an aqueous solution (CH_3OH/H_2O, lower panels) and a second, lower mobility feature at a drift time of ${}^{\mathrm{TW}}2.9$ / ${}^{\mathrm{DT}}11.75$ ms (II) is the strongest signal when the nonprotic solvent acetonitrile is used (CH_3CN, upper panels). When the DT instrument is used, species II additionally exhibits a smaller, unresolved component at a higher drift time (${}^{\mathrm{DT}}12.2$ ms, II').

The observation of two drift peaks that differ in ${}^{\mathrm{DT}}$drift time by approximately 14 % is unusual for a molecule of this size and mass (m/z 166) because it implies the coexistence of at least two isomers, differing in size to a similar extent as the respective drift times. In Fact, the corresponding collision cross-sections (CCSs) are determined to be 135 and 155 Å^2 for species I and II, respectively (Table 5.3). This difference in CCS must be a consequence of a difference in structure. From the chemical structure of benzocaine (Figure 5.1), very little structural diversity can be envisaged. The presence of *trans* and *gauche* isomers, which differ in the rotation angle of the ester group is conceivable (Figure 5.3 (b)). However, such a rotation seems at the first glance rather unlikely to yield a drift-time and CCS difference of 14 %. Another possibility is the formation of different protomers (Figure 5.3 (a)), with the proton residing on either the amine nitrogen (N-protonated) or on the carbonyl oxygen (O-protonated). In aqueous solutions, the N-protonated species is certainly favored because of the basicity of the amine group, however, the situation can be very different in the absence of solvent molecules [200].

On the basis of results from studies where either (IM)-MS or spectroscopy have been employed independently, the existence of different gas-phase protomers has been suggested for smaller analogues of benzocaine, such as *para*-aminobenzoic acid [201–203] or *para*-

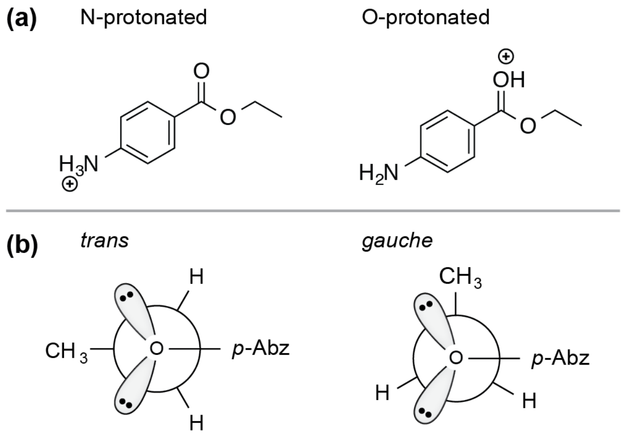

Figure 5.3: Potential sources of isomerism for protonated benzocaine. (a) Benzocaine can be protonated at the NH_2 group (left) or the carbonyl oxygen (right). (b) In addition, *trans/gauche* isomers, in which the relative orientation of the ethyl group is altered, are conceivable. p-Abz denotes the position of the p-aminobenzoyl moiety.

hydroxybenzoic acid [204–206]. Also for these smaller systems with similar constituents and chemical structure, an influence of the solvent composition on the gas-phase ions has been reported, and evidence for both N- and O-protonated species was found.

5.3.1 Drift-Time Resolved CID

Collision induced dissociation (CID) is the standard-tool for ion fragmentation in MS applications [58], and can, especially in combination with IMS, alleviate structure analysis [207]. Here, using the TW instrument, the shape- and m/z-selected ions were subjected to collisions with an inert neutral gas (argon) and fragments were subsequently analyzed by means of TOF MS. The gray bars in the upper panel of Figure 5.4 represent the drift-time windows from which the fragment information of the two peaks I and II were extracted. The resulting fragment spectra of the species I and II for collision voltages of 12 V and 20 V, respectively, are shown in the lower two panels of Figure 5.4.

The most abundant fragment for both species is formed by the loss of the ethene molecule (C_2H_4), which results in a strong ion signal at m/z 138. Other fragment signals in the lower m/z range are substantially weaker in intensity and are therefore magnified by factors of 10^2 and 10^3 in the fragment spectra of species I and II, respectively. In both cases subsequent loss of CO_2 is observed forming m/z 94 followed by loss of NH_3 to form m/z 77. However, higher collision energies and magnification factors were required for species II than for species I, reflecting its greater dissociation threshold. Furthermore, a signal at m/z 120, which indicates the loss of water from the m/z 138 fragment, could only be found in the spectrum of species I. Further discussion of the observed differences in dissociation will be provided below, together

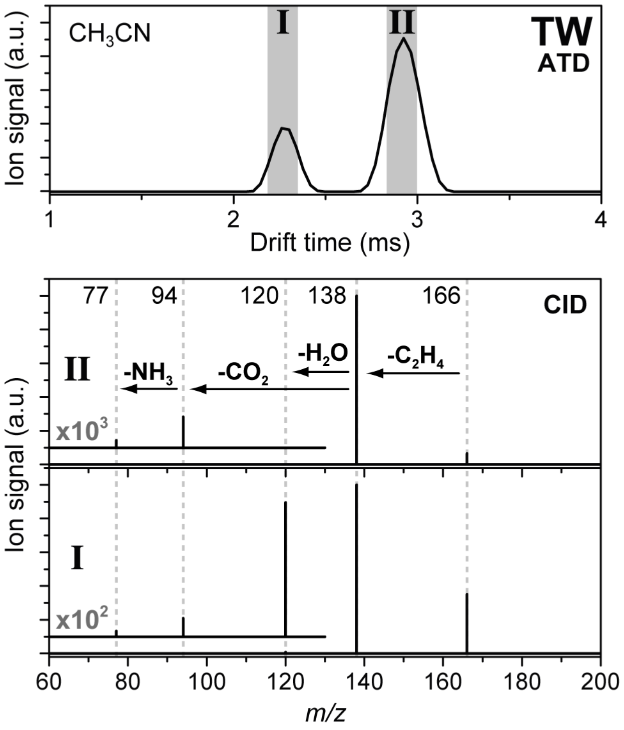

Figure 5.4: CID fragment spectra (lower two panels) of the drift-time separated species I and II from the traveling-wave (TW) instrument. The drift-time windows from which fragment spectra were extracted are indicated in gray in the ATD (upper panel). The lower mass range in the fragment spectra is magnified by factors of 10^2 and 10^3, respectively. For both species I and II dissociation is observed, accompanied by the loss of neutral compounds as annotated in the fragment spectrum of II.

with results from spectroscopic investigations.

5.3.2 Drift-Time Resolved IR Spectroscopy

To gain further insight into the identity of the two species of benzocaine found in the IM-MS experiments, vibrational gas-phase spectra of the two isomers were recorded individually. Intramolecular vibrations strongly depend on the molecular structure, which makes vibrational spectroscopy, especially at frequencies in the mid-IR range, a valuable tool to deduce structural information. A common method to obtain IR spectra in the gas phase is to employ IR multiple photon dissociation (IRMPD) on *m/z*-selected ions [35] (see Section 2.3). Here, infrared lasers of high intensity are needed to allow for the absorption of multiple photons at IR-active sites, which results in increased internal energies and dissociation of covalent bonds. For these IRMPD experiments, the Fritz Haber Institute FEL is coupled to the DT IM-MS experimental setup, which enables spectroscopic investigation of drift-time separated species. Subsequent

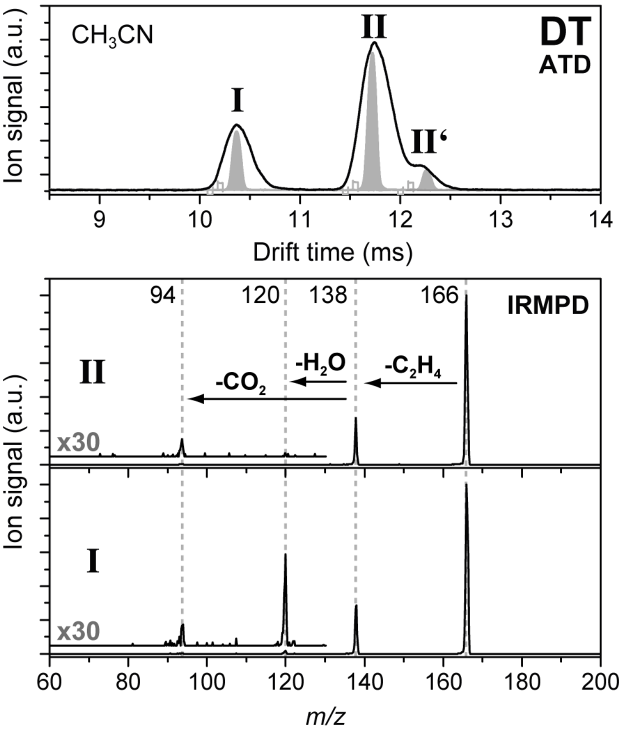

Figure 5.5: IR photofragment spectra of the drift-time separated species I and II (lower two panels) at resonant wavelengths as measured on the drift-tube (DT) instrument. The narrow 100 μs signals (in gray) in the ATD (upper panel) are the portions of the isomer distribution that were transmitted for irradiation with IR photons. The identity of the fragments was confirmed by collision-induced dissociation experiments where identical fragmentation patterns were observed (compare Figure 5.4).

to drift-time and *m/z* separation, ions within a narrow drift-time window can be selected and irradiated by a pulse of intense IR light. Fragment analysis occurs by means of TOF MS. An action spectrum is recorded by monitoring the intensity of the precursor ion signal and the corresponding fragment signals as a function of the laser wavelength.

IR Photodissociation and Spectra

The narrow (100 μs) fractions of the ATD in the upper panel of Figure 5.5 are the fractions of species I, II, and II' that were isolated and transmitted for irradiation with IR photons following mass analysis. Typical IRMPD fragment spectra of species I and II at resonant wavelengths are depicted in the lower two panels of Figure 5.5. The lower *m/z* ranges are magnified by a factor of 30. The fragmentation patterns and characteristics observed upon IRMPD are virtually identical to the ones observed in the CID experiment. Also here, the most abundant fragment , *m/z* 138 (loss of CO or C_2H_4), undergoes further fragmentation

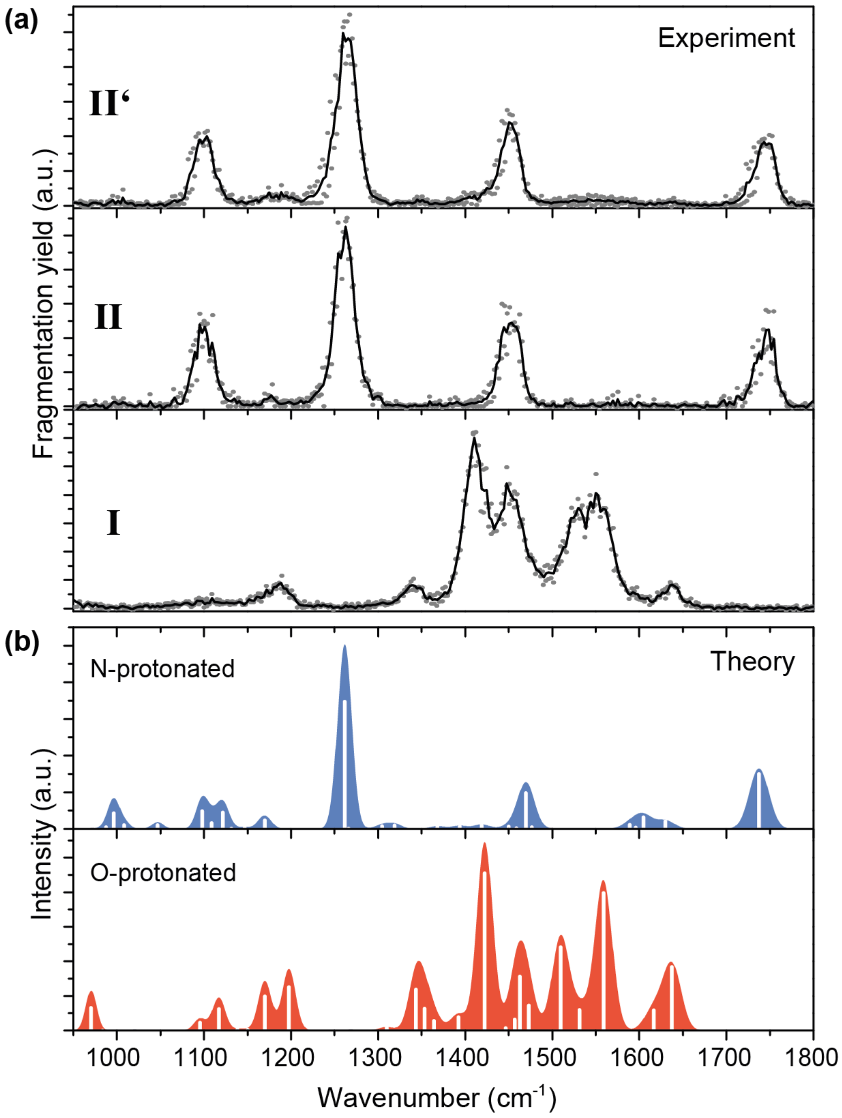

Figure 5.6: (a) Gas-phase IR spectra of the three drift-time selected species of benzocaine observed in the ATD in Figure 5.5. Data from two individual scans per species are depicted as gray dots. The solid lines represent an average of these two individual scans. (b) Computed vibrational spectra of the lowest-energy structures of N-protonated (upper panel) and O-protonated (lower panel) benzocaine ions. The theoretical spectra were scaled by a factor of 0.975 and convoluted with a Gaussian profile of 1.5 % width to match the experiment

to yield substantially weaker fragment signals at *m/z* 120 (loss of H_2O) and *m/z* 94 (loss of CO_2). As in the CID experiment, species II exhibits a lower dissociation yield than I, and thus, higher laser power was required for the photodissociation of II. Additionally, species II does not form the *m/z* 120 fragment to a considerable extent. The photofragmentation characteristics of species II', which was only observed in the DT instrument, are virtually identical to the ones observed for II.

The resulting IR spectra in a wavenumber range of 950 to 1800 cm^{-1} are presented in Figure 5.6 (a). The solid lines represent an average of two individual scans, which are depicted as gray dots. Surprisingly, the spectra of I and II/II' are completely different. The latter set of spectra mainly consists of four strong bands at wavenumbers 1100, 1260, 1450, and 1745 cm^{-1} with a width of approximately 25 cm^{-1} each, whereas the spectrum of I holds strong, partially resolved features between 1375 and 1600 cm^{-1} and some weaker bands at 1190, 1340, and 1635 cm^{-1}.

Comparison with Theoretical Spectra*

To clarify the identities of species I and II/II', it is crucial to assign the vibrational bands of the experimental spectra. Therefore, model structures of benzocaine with N- and O-protonated sites as well as different orientations of the ethyl group (*trans* and *gauche*), which result from rotation of the ester bond, were computed (Figure 5.7). Theoretical spectra were calculated using the B3LYP functional with the def2-TZVP basis set. For both protomers, the *trans* isomer is favored by 2.1–3.3 kJ mol^{-1} (Figure 5.7), and their most prominent vibrational bands are summarized in Tables 5.1 (a) and (b) for O- and N-protonated species, respectively . For comparison with experimental data, the calculated vibrational frequencies were scaled by a factor of 0.975 and convoluted with a Gaussian curve profile of 1.5 % width. The resulting theoretical spectra are shown in Figure 5.6 (b) in red for O-protonated (lower panel) and blue for N-protonated species (upper panel).

The theoretical spectrum of the N-protonated species is in excellent accord with the experimental spectra of II and II', and all of the observed vibrations can be found in the predicted spectrum within the width of the experimental bands. Therefore, the observed bands at 1745 and 1450 cm^{-1} can be assigned to C=O stretching and NH_3 umbrella modes, respectively. More complex asymmetric and symmetric stretching vibrations of C-C and the ester-bonded ethyl group (C-OEt) can be assigned to the observed bands at 1260 and 1100 cm^{-1}, respectively. The nonlinear relation between laser power and band intensity in this multiple photon process is likely to be the reason for the absence of predicted lower-intensity vibrations in the experimental spectrum. The spectrum of species I, however, is in good agreement with the calculated spectrum of the O-protonated molecule. The individual vibrational modes, however, are mostly predicted to be not well-separated, which explains the more convoluted experimental spectrum. Nevertheless, a characteristic band in the spectrum

---

*The calculation of optimized geometries was performed by Jongcheol Seo in the Molecular Physics department of the Fritz Haber Institute.

Table 5.1: Experimental and theoretical vibrational frequencies of (a) O-protonated and (b) N-protonated benzocaine. The strongest features of the calculated and experimental spectra are listed.

(a) O-protonated

IR bands (cm^{-1})		vibrational mode
observed	calculated	
1635	1637	NH_2 scissor
	1616	NH_2 scissor + C-C stretch (ring)
1550	1559	C-C, C-OEt asymmetric stretch (ester) + C-C stretch (ring)
1530	1510	C-C, C-OEt asymmetric stretch (ester) + in-plane C-H bend (ring)
1450	1459	CH_3 scissor + CH_2 scissor
	1448	CH_3 twist
1410	1423	$C{=}OH^+$ stretch
1340	1343	CH_2 wag
1190	1198	in-plane C-H bend (ring)
	1170	in-plane C-H bend (ring) + in-plane $O{=}H^+$ bend

(b) N-protonated

IR bands (cm^{-1})		vibrational mode
observed	calculated	
1745	1738	C=O stretch
1450	1470	NH_3 umbrella
1260	1262	C-C, C-OEt asymmetric stretch (ester) + CH_2 wag
1100	1121	C-C, C-OEt symmetric stretch (ester)
	1098	CH_3 antisymmetric bend

of the O-protonated species, which arises from the stretching vibration of the protonated carbonyl ($C\text{-}OH^+$) at 1423 cm^{-1}, is particularly noteworthy because it can exclusively be found in the experimental spectrum of I, whereas the band corresponding to the stretching vibration of the free carbonyl (C=O) in an N-protonated molecule is absent. In summary, on the basis of the gas-phase IR spectra, the drift peaks I and II/II' in Figure 5.2 can unambiguously be assigned to O- and N-protonated species of benzocaine, respectively. Hypothetically, the molecule could also be protonated at the aromatic ring, as has been observed for protonated aniline [208]. For benzocaine, however, such structures are not energetically favorable nor do the experimental IR spectra show features characteristic for ring protonation, so they can therefore be excluded here (for details, see Appendix B).

The aforementioned differences in the CID- and IRMPD-fragment spectra of species I and II can now be explained on the basis of O- and N-protonated structures. The loss of water from the *m/z* 138 fragment, which results in a *m/z* 120 signal, is a feature observed in the fragment spectra of the O-protonated species I. It is likely that this dissociation channel is suppressed when the proton resides at the amine group and it is therefore not observed

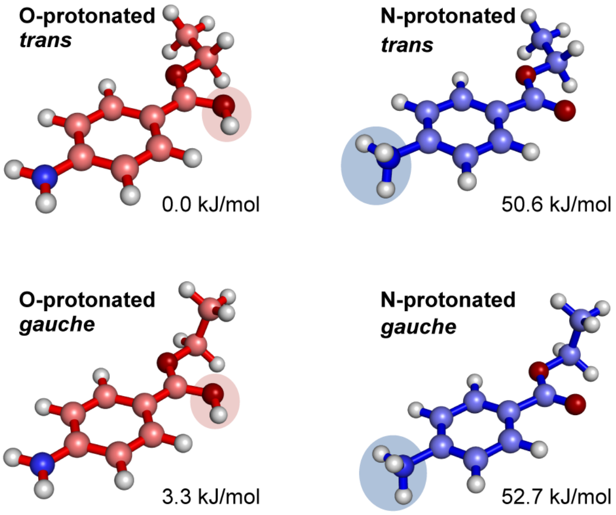

Figure 5.7: Calculated lowest-energy structures of O- and N-protonated benzocaine in *trans* and *gauche* conformation and corresponding relative energies. Structures were obtained using TURBOMOLE v6.6 at the B3LYP level of density functional theory with a def2-TZVP basis set.

in the CID and IRMPD fragment spectra of species II/II', respectively. The corresponding fragmentation pathways are illustrated in Figure 5.8.

Origin of the II' Species

Identical fragmentation patterns and IR spectra are observed for species II and II', which thus implies that both structures carry the charge at the amine nitrogen. Additionally, their difference in drift time implies a size difference of approximately 4 %, which is unlikely to result from conformational changes considering the low flexibility of the molecule. When measured on the TW instrument, the ATDs do not exhibit this additional II' component (Figure 5.2). Unlike in this instrument, however, the here-utilized DT instrument does not allow m/z selection prior to drift-time separation, and it is therefore possible that partially solvated N-protonated molecules traverse the drift tube and subsequently lose the weakly bound solvent molecules in the transfer region toward high vacuum before m/z selection occurs. These partially solvated benzocaine molecules will be larger than fully desolvated molecules and hence have slightly increased drift times, but they will be detected as fully desolvated molecules. This post-IM dissociation has been observed in other studies on this and other DT instruments [209] and provides a reasonable explanation for the observation of the II' species.

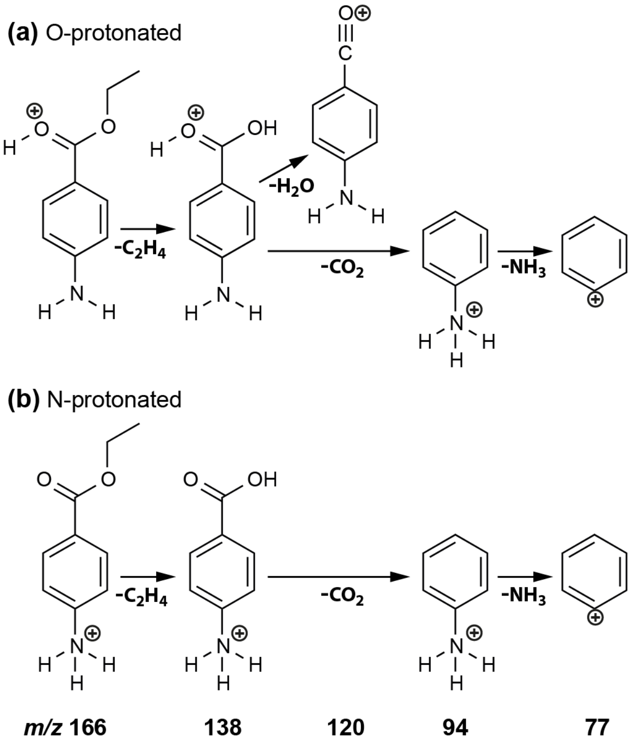

Figure 5.8: Fragmentation of O-protonated (a) and N-protonated (b) benzocaine. The loss of H_2O cannot occur when the proton resides at the amine group. Thus, no *m/z* 120 signal is observed in the CID fragment spectra of species II (Figure 5.4) and the IRMPD fragment spectra of species II/II' (Figure 5.5).

5.3.3 CCS Calculation

After the unambiguous identification of the O- and N-protonated species of benzocaine, it remains to explain the baseline separation of these rather similar structures in the IM-MS experiments on the basis of the theoretical models. For this purpose, theoretical CCSs of the different protomers as well as their rotational *trans* and *gauche* isomers were calculated. Generally, several methods are available to achieve this, with the projection approximation (PA) method being the simplest [210, 211]. In its standard form, a CCS is estimated by calculating the projected area (*i.e.*, the shadow) of a molecule for many different orientations. A more refined version, the projection superposition approximation (PSA) [194–197], takes errors into account that arise from concave molecular structures and performs well for larger molecules. Effects that result from the charge distribution within the molecule, however, are ignored in these two methods. In the trajectory method (TM) [198, 199], realistic ion-molecule interaction potentials, which can include charge-induced dipole interactions, are taken into account. This method is well-suited for smaller molecules such as benzocaine; however, it is of high computational cost for larger species.

Table 5.3: Experimental and theoretical CCSs

Benzocaine isomer	CCS_{calc} (Å^2)		CCS_{exp} (Å^2)
	PSA[a]	*TM*[b]	
O-protonated / *trans*	131.1	132.7	135
O-protonated / *gauche*	131.6	132.5	
N-protonated / *trans*	133.3	144.0	155
N-protonated / *gauche*	129.5	144.0	

[a] Projection superposition approximation
[b] Trajectory method

Here, the calculation of theoretical CCSs was performed using the PSA and TM methods, which were both parametrized for nitrogen drift gas. Calculated CCSs of the *trans* and *gauche* conformers yield virtually identical values, which is in stark contrast to the vastly differing experimental CCSs of 135 and 155 Å^2 for I and II, respectively (Table 5.3). Furthermore, the calculations suggest that the experimentally observed differences in drift time are likely a result of different electrostatic interactions with the nitrogen buffer gas molecules rather than distinct sizes of the structures. Although PSA calculations, which lack an explicit treatment of charge-induced interactions, yield essentially identical CCSs for all model structures, a difference in CCS of approximately 8 % between the O- and N-protonated species is predicted by TM, which accounts for charge-induced dipole interactions. The theoretical CCS of the O-protonated model structure thus reproduces the experimental CCS of species I within the error of the method, whereas species II exhibits an experimental CCS that is still 6 % higher than the calculated value of the N-protonated model structure. These results imply that the CCS calculation methods need to be further refined to account more thoroughly for charge effects in polarizable drift gases such as nitrogen.

The underlying reason for a much longer drift time of the N-protonated species with respect to the O-protonated molecule is likely to be found in differences in charge density distribution between the two different protomers. These are illustrated in Figure 5.9 (a) and (b) for the lowest-energy model structures of the O- and N-protonated species, respectively. For the former, the mesomeric effect leads to delocalization of the charge, in contrast to an N-protonated benzocaine, where the charge density is much more localized. In Figure 5.9 (b), this is indicated by red (more negative) and blue (more positive) color. This N-protonated ion, however, will experience a stronger interaction with the polarizable, neutral nitrogen molecules than the molecule with a delocalized charge, leading to longer drift times and higher CCSs in the IMS experiment.

5.3.4 Influence of the Surrounding Medium

The solvent composition has been observed to have a great influence on relative abundances of the electrosprayed O- and N-protonated species of benzocaine in the gas phase.

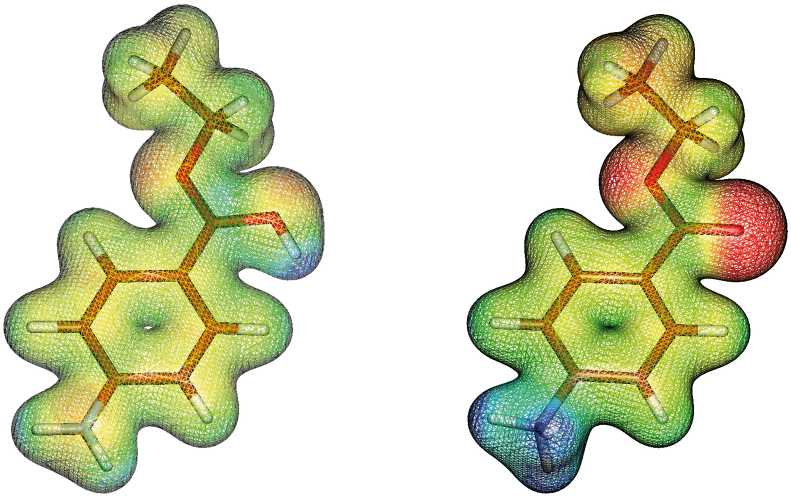

(a) O-protonation **(b)** N-protonation

Figure 5.9: Calculated charge density distributions of the O-protonated (a) and N-protonated (b) forms of benzocaine. The mesomeric effect leads to delocalization of the charge in the case of O-protonation. Thus, charge-induced ion-molecule interaction is stronger for N-protonated species.

A methanol/water solution facilitates protonation at the carbonyl oxygen, whereas species with a protonated amine are predominantly observed when acetonitrile is used as a solvent. These observations are in line with previous findings on the influence of the solvent on the gas-phase structures of positively and negatively charged smaller analogs of benzocaine [201, 202, 205, 206].

To shed more light on the influence of the surrounding media on the molecular structure, proton affinities, E_{pa}, of O- and N-protonated species of benzocaine as a function of the medium's relative permittivity ϵ_r were calculated (Figure 5.10). These calculations suggest that in a polar solution protonation will most likely occur at the amine rather than the ester group (up to 50 kJ mol^{-1} more stable). Considering the pK_a value of the amine group, this is the expected behavior for the molecule in an aqueous solution. When the relative permittivity of the surrounding medium decreases, however, the carbonyl oxygen becomes the preferred protonation site. This can be attributed to a conjugation between the amine and the charged carbonyl group in the absence of solvent molecules [212, 213]. The electron-density-donating neutral amine and the density-withdrawing positively charged ester group both work in favor of the conjugated π-system, thus stabilizing protonation at the carbonyl oxygen.

If protonation at the oxygen is favored under vacuum conditions, then why are both protomers observed in the gas phase and why does their relative abundance depend on the solvent medium? The observation of energetically unfavored N-protonated species in the gas phase (by 50 kJ mol^{-1}) must be a consequence of the electrospray process. In the electrospray process, the molecule undergoes a transition from a solvated to a desolvated state. When

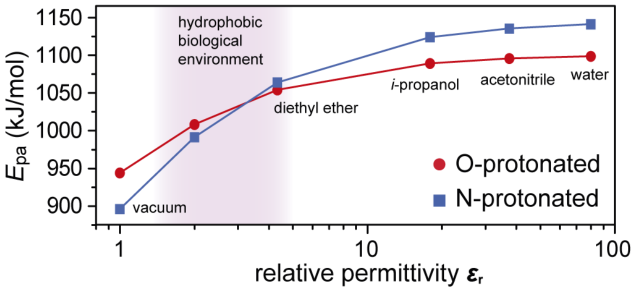

Figure 5.10: Proton affinity of N- and O-protonated species. Single-point energies of the lowest-energy structures of the two protomeric species were calculated for different relative permittivities ϵ_r of the surrounding media and subtracted from the energy of the neutral molecule to yield the negative of the proton affinity, -E_{pa}. Solvated in water, the proton will be attached to the amine nitrogen, whereas carbonyl-oxygen protonation is favored in environments of lower relative permittivity.

a protic solvent as methanol/water is used, the presence of many protic solvent molecules facilitate relocation of the charge to the preferred site within the last solvation shell; hence, the O-protonated species can be observed. However, an aprotic solvent like acetonitrile does not allow this structural reorganization in the last steps of the transition from solution to the gas phase, and the solution structure is therefore kinetically trapped [201, 202, 213], leading to the formation of N-protonated benzocaine. Nonetheless, O-protonation can be facilitated by residual water inside the aprotic solvent.

These results can also be interpreted from a physiological point of view. Benzocaine is known to act as a local anaesthetic by blocking sodium channels [183, 184, 187, 188]. The majority of sodium channel blockers act as charged molecules, blocking the transit of Na^{+} ions inside the pore, whereas benzocaine is commonly assumed to act as a neutral [183, 184, 187, 188]. However, the proton affinity of benzocaine is dependent on the permittivity of the surrounding medium. The estimated relative permittivity of a lipid bilayer or a transmembrane protein is estimated to be $\epsilon_r \approx 2$–6, which is much smaller than typical for *in vitro* conditions (Figure 5.10). Whether benzocaine acts on the sodium channel as a charged or neutral molecule cannot be deduced from the experiments presented here. However, if protonation plays a role in the underlying mechanism, then the proton will most likely be located at the carbonyl oxygen because of the hydrophobicity of the ion channel.

5.4 Conclusions

Ion-mobility-resolved IR spectroscopy provides the first direct evidence for different protomeric populations of the local anaesthetic benzocaine, the ethyl ester of *para*-aminobenzoic acid. At least two well-separable gas-phase species can be found in IM-MS experiments. Vibrational spectra of these both m/z- as well as ion-mobility-selected species were recorded in the mid-IR range using a free electron laser, and two different protomers, O- and N-protonated benzocaine, were unambiguously identified by comparison with calculated spectra from density functional theory calculations. Distinct photofragmentation and collision induced dissociation fragment patterns as well as calculated collision cross-sections of model structures further support the structural assignment. For the latter the incorporation of charge-induced dipole terms is crucial because the differences in drift time of the two species do not arise from their conformational diversity but rather from different charge distribution within the molecules. These results confirm earlier studies on structurally similar molecules where the existence of different gas-phase protomers was suggested [201, 202, 205, 206, 214].

Calculated proton affinities further suggest that the preferred protonation site may vary significantly with the electric properties of the surrounding medium. Although the amine nitrogen is the most basic site in aqueous environments, the carbonyl oxygen becomes energetically favorable for protonation when the relative permittivity decreases. Consequently, a protic solvent, such as methanol/water, facilitates rearrangement of the proton to the preferred site on the way from the ion source into the gas phase, whereas an aprotic solvent leads to kinetic trapping of the most stable solution structure [201, 202, 213]. These results may have an impact on studies of molecules as benzocaine in hydrophobic environments, such as a membranes or ion channels, which in terms of relative permittivity, ϵ_r, resemble the gas phase more than an aqueous solution.

6 β-Sheet Formation in Peptide Amyloid Assemblies*

"Of all the ways that proteins can go bad,
becoming an amyloid is surely one of the worst." [6]

After successful demonstration of the advantages that the combined IM-MS IR spectroscopic approach entails for the investigation of molecular structure in Chapter 5, the method is here applied to much larger systems of different aggregating hexapeptides. Such systems are interesting in the light of amyloid diseases where peptides and proteins are commonly found to form insoluble fibril structures that all share a common structural motif – β-sheets. The present study aims to identify peptide oligomers that are in a transition stage from an unordered to a highly ordered β-sheet structure. IM-MS is capable of separating different oligomeric states that are otherwise identical in their m/z values. Gas-phase IR spectra of these oligomer-separated species are then recorded in a wavenumber range of 1000–1850 cm^{-1} where structure-characteristic C=O stretching and N-H bending vibrations are expected. Comparison of the observed absorption bands with condensed-phase reference data finally allows to identify structural predispositions of the isolated oligomer species. This approach is commonly used for structural assignment in condensed-phase IR spectroscopic methods and is here for the first time successfully applied to molecular aggregates in the gas phase.

6.1 Introduction

The assembly of peptides and proteins into insoluble, β-sheet-rich fibrils is a common hallmark of all amyloid diseases [3, 5, 215]. In the disease case, however, small soluble oligomers rather than mature fibrils have been suggested as the toxic species. Oligomers of amyloidogenic peptides such as the β-amyloid peptide [216–218], α-synuclein [219], islet amyloid polypeptide [220, 221], insulin [222, 223], and several others are suspected to be responsible for Alzheimer's, Pakinson's, type II diabetes, and so on. Exploring the structure of those oligomers is not

---

*This chapter is based on a recently submitted manuscript entitled *"An Infrared Spectroscopy Approach to Follow β-Sheet Formation in Peptide Amyloid Assemblies"* by the authors Jongcheol Seo, Waldemar Hoffmann, Stephan Warnke, Xing Huang, Sandy Gewinner, Wieland Schöllkopf, Michael T. Bowers (UCSB), Gert von Helden, and Kevin Pagel. The reprint of figures and content is conform with the publishers copyright policies. Peptides where synthesized and characterized with condensed-phase methods by W.H., gas-phase experiments were performed by J.S., W.H., and S.W., data was analyzed by J.S. and W.H., and the manuscript was co-written by all authors.

only crucial to develop a better understanding of the underlying molecular details of amyloid assembly, but is also key for the development of novel diagnostic and therapeutic methods.

Extensive structural studies using X-ray diffraction, nuclear magnetic resonance spectroscopy (NMR), and electron microscopy (EM) have revealed that highly ordered β-sheets maintained by cross-β spines are dominant in mature fibrils [223–227]. Moreover, circular dichroism (CD) and infrared (IR) spectroscopy studies revealed that large secondary structural transitions from partially helical or unordered structures into repeating β-sheets occur during the assembly process [228–230]. Thus, determining secondary structure of pre-fibrillar oligomers and identifying the specific states responsible for the secondary structural transitions to β-sheet should be the first step in investigating the assembly of amyloid proteins and peptides. However, structural investigations of amyloid oligomers are inherently challenging, as such oligomeric systems are polydisperse and often polymorph, *i.e.*, they do not exhibit a defined oligomerization state but rather form a dynamic equilibrium between multiple species of different oligomer sizes and can, for one and the same oligomeric state, coexist in multiple conformations. As a result, traditional condensed-phase methods are of limited use for structural studies of these systems because they only yield ensemble-averaged results. Thus, several methods based on mass spectrometry (MS) and ion mobility spectrometry (IMS) have been applied to study amyloid assembly [26–28, 231–237]. With its unique capability to isolate and detect molecular ions of a specific mass-to-charge ratio and measure collision cross-sections (CCS), recent IM-MS studies successfully isolated size and shape-specific oligomer states of amyloidogenic peptides and extract structural as well as oligomer distribution information.

The peptide VEALYL, which corresponds to segment 12–17 of the insulin B chain, was recently shown to form amyloid fibrils that later evolve into microcrystals in solution [26, 226, 227]. X-ray studies have revealed that the peptides assemble into a so-called steric zipper – a repeating pattern of antiparallel β-sheets with densely packed, interdigitated side-chains [224, 226, 227]. IM-MS methods found that a structural transition from a compact to a more extended structure appears early in the assembly process [26]. IM-MS is, however, not sensitive to the secondary structure itself; it only gives information about the overall shape of a molecule, and relies on comparison with modeling studies to obtain structural information.

To address this limitation IR spectroscopy is here combined with the IM-MS to probe the structure of shape and *m/z* selected ions. IR spectroscopy is a versatile tool for identifying secondary structure [33, 34]. The stretching mode of C=O groups (amide I) in the peptide backbone can be especially diagnostic for different types of secondary structure (see Table 6.1). Highly ordered structures such as α-helices and β-sheets yield major amide I bands at 1650–1660 cm^{-1} and 1620–1640 cm^{-1}, respectively [34]. Random coils and several turn structures on the other hand, yield amide I features at 1640–1650 cm^{-1}and 1660–1685 cm^{-1} which are both distinct from those of β-sheets [33, 34]. The drift-tube IM-MS instrument described in Section 2.4 within this thesis facilitated IR spectroscopic investigations on *m/z*- and/or ion-mobility selected molecular ions. Irradiating the isolated molecular ions with light

Table 6.1: Correlations between common protein structural motifs and observed amide I positions [33, 34].

Secondary structure	Amide I band ($\mathrm{cm^{-1}}$)
antiparallel β-sheets / aggragated strands	1675–1695
3_{10}-helix	1660–1670
type II β-turn	1660–1685
α-helix	1648–1660
random coil	1640–1648
β-sheet	1620–1640
aggregated strands	1610–1628

from the Fritz Haber Institute's FEL (Section 2.6.1) – an intense, tunable IR-laser – can lead to the absorption of multiple IR photons and subsequent dissociation as discussed in Section 2.2. Plotting the fragmentation yield as a function of IR wavelength gives a gas-phase IR multiple photon dissociation (IRMPD) spectrum, which resembles the condensed-phase IR absorption spectrum. In the following paragraphs the oligomers of VEALYL and its sequence-scrambled control peptides, VELYAL and YVEALL were investigated using these techniques.

6.2 Experimental Details

Materials

All solvents were purchased from Sigma-Aldrich and used without further purification. The three reported hexapeptides were synthesized* using standard Fmoc (9-fluorenyl-methoxycarbonyl) solid-phase peptide synthesis (SPPS). SPPS was carried out on a fully automated peptide synthesizer, Activo-P11 (Activotec, Cambridge, UK) or Syro XP-1 (Multi-Syn Tech GmbH, Witten, Germany). After removal of all protection groups and cleavage from the resin, the synthesized peptides were further purified by reverse-phase HPLC and subsequently verified by nESI-MS using a Synapt G2-S HDMS mass spectrometer (Waters Corporation, Manchester, UK). Sample solutions were prepared by dissolving peptides in water/methanol (1/1, v/v) to the final concentration of 2 mM. The pH of each sample solution was determined to be ~ 3.0 by using a WTW pH526 pH meter equipped with an InLab Micro electrode (Mettler Toledo, Giessen, Germany).

---

*Peptides where synthesized by Waldemar Hoffmann from the Molecular Physics department of the Fritz Haber Institute.

Transmission Electron Microscopy (TEM)*

Aliquots of the peptide sample solutions (2 mM, pH $\sim$ 3) were deposited onto a carbon coated Cu grid by drop-casting. After being dried in ambient air, they were put into an FEI aberration-corrected Titan 80–300 microscope operated at 300 kV where TEM micrographs were obtained.

Solid State Fourier Transform-Infrared (FT-IR) Spectroscopy†

Peptide solutions (2 mM) were incubated under stirring at 37°C for 24 hours. Subsequently, the formed precipitates were isolated from the solution by centrifugation at 12.000 G for 10 minutes. The supernatants were transfused and the precipitations were freeze-dried. The background-corrected FT-IR spectra (650–4000 cm^{-1}) of the precipitates were measured using a JASCO FT/IR-4100 spectrometer (JASCO Inc., Easton, MD, USA) in the transmission mode. Solid samples for the non-fibril forming sequence VELYAL were prepared by quick-freezing the incubated sample solution and further freeze-drying. Solid FT-IR spectra of freshly dissolved sample solutions were prepared as described for the incubated VELYAL sample solution.

IM-MS and Drift-Time Selective IR Spectroscopy

Peptide solutions were further diluted to the desired concentration (0.15–2 mM), loaded into Pd/Pt-coated (nano) electrospray ionization (nESI) emitters, and electrosprayed on the drift-tube IM-MS instrument described in Section 2.4. The collision cross-section (CCS) of a particular oligomer was calculated from the measured arrival time distributions as described in Section 2.5.2. Oligomer-selective IRMPD spectroscopy was performed by selecting a narrow fraction of the drift-time distribution (100 μs) prior to m/z-selection and subsequent irradiation of the ions with IR radiation provided by the Fritz Haber Institute's FEL [122]. The absorption of multiple photons leads to fragmentation and emerging fragments are detected by the TOF mass analyzer. The final IRMPD spectra are composed by plotting the fragmentation yield as a function of the IR wavenumber as described in Section 2.6.2.

6.3 Results and Discussion

The hexapeptide VEALYL is well known to form amyloid fibrils [223, 224, 226, 227]. This manifests itself in the formation of an insoluble deposition immediately after the incubation of VEALYL in water/methanol at room temperature. Figure 6.1 (a) shows a transmission electron micrograph (TEM) of amyloid fibrils that are formed within minutes after dissolving

---

[*] TEM was performed by Xing Huang in the Department of Inorganic Chemistry of the Fritz Haber Institute.

[†] FT-IR experiments were performed by Waldemar Hoffmann from the Molecular Physics department of the Fritz Haber Institute.

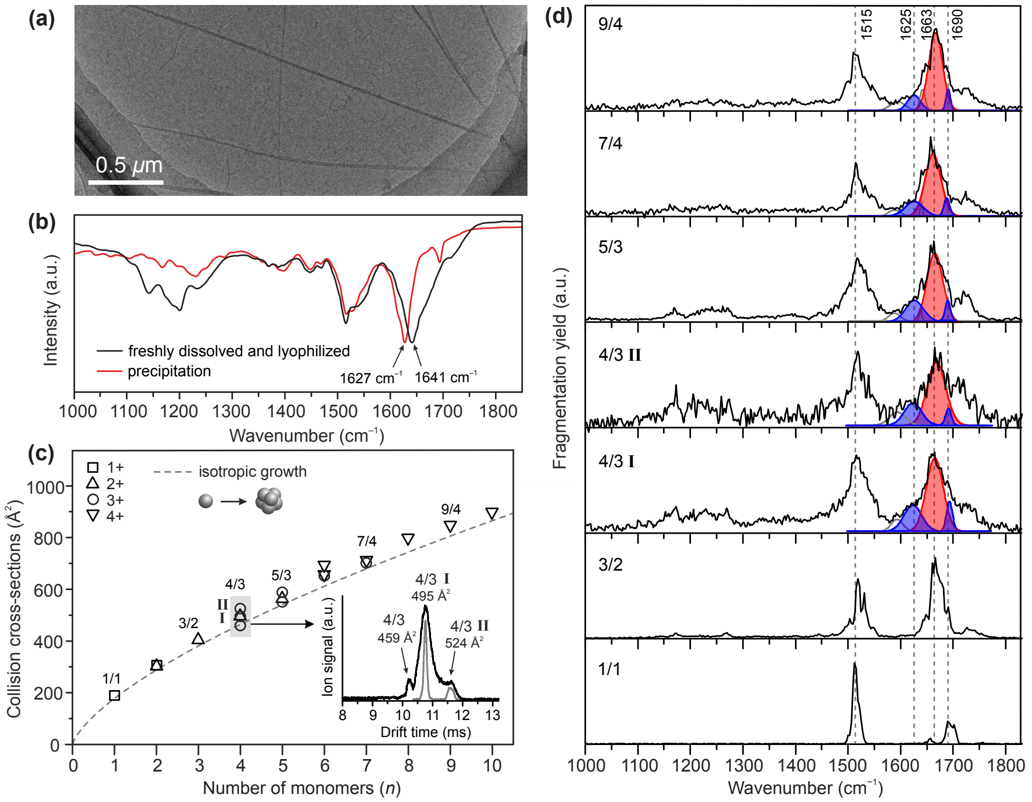

Figure 6.1: (a) Transmission electron micrograph (TEM) of an incubated VEALYL solution. (b) Solid FT-IR spectra of VEALYL precipitate obtained after 24 hour incubation at a temperature of 37°C and freshly dissolved VEALYL without precipitation after lyophilization. (c) Measured collision cross-sections (CCSs) of VEALYL oligomers as a function of the number of monomers (n). The dashed line denotes the expected CCSs assuming isotropic growth. The inset shows a typical arrival time distribution (ATD) of the triply charged tetramer (4/3) where multiple conformers with distinct CCS are observed. (d) IRMPD spectra of m/z- and drift-time selected VEALYL oligomer ions from the singly-protonated monomer (1/1) up to quadruply-protonated nonamer (9/4) measured in the wavenumber range of 1000–1850 cm^{-1}. Fractions of the amide I band that are representative for β-sheet (centered at 1625 and 1690 cm^{-1}) and turn-like structures (centered at 1665 cm^{-1}) are represented in blue and red, respectively.

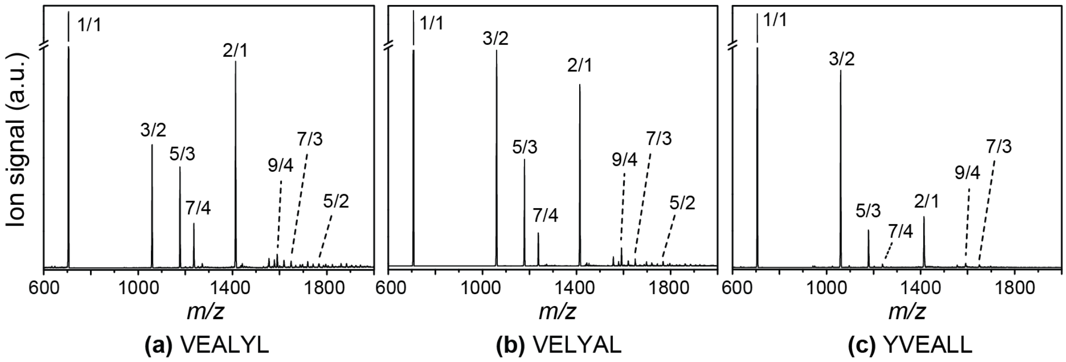

Figure 6.2: TOF mass spectra of 2 mM samples of VEALYL (a), VELYAL (b), and YVEALL (c). Upon electrospraying the sample into the drift-tube IM-MS instrument, a wide distribution of oligomers can be observed. The data is scaled to the intensities of higher oligomers.

the VEALYL sample. The secondary structure of non-soluble VEALYL fibrils was previously found to be dominated by β-sheets [223–227]. Solid-state FT-IR spectroscopy, especially in the amide I region where C=O vibrations are probed, is sensitive to the secondary structure. Highly ordered antiparallel β-sheets are expected to yield amide I bands at 1620–1640 cm^{-1}and ~1690 cm^{-1}, whereas signals at 1640–1650 cm^{-1} and 1660–1690 cm^{-1} indicate random coils and several types of turn structures, respectively (compare Table 6.1) [33, 34]. A comparison between FT-IR spectra of freshly dissolved VEALYL and the precipitate is shown in Figure 6.1 (b). For the freshly dissolved sample (black), the maximum of the amide I band at 1641 cm^{-1} together with several broad features up to 1700 cm^{-1} indicate the presence of unordered and turn-like structures. In contrast, the IR spectrum of the VEALYL precipitate (red) shows a narrower and red-shifted amide I band centered at ~1627 cm^{-1}. This suggests that the VEALYL precipitate predominantly consists of highly ordered β-sheets.

6.3.1 IM-MS of VEALYL Oligomers

A disadvantage of condensed-phase methods is that in solution they can only provide ensemble-averaged results of all aggregation states. Structural details of the individual pre-fibrillar oligomers are, thus, impossible to obtain with these methods. This limitation was here overcome by using IM-MS based techniques. These allow clear separation of oligomer number (n) and conformation, as well as providing absolute collision cross-sections (CCSs). When a freshly dissolved VEALYL sample is electrosprayed, a wide distribution of multiply charged peptide oligomers is observed (Figure 6.2 (a)). The CCS values of each individual VEALYL conformer were measured and the results are shown in Figure 1c. The dashed line represents an ideal isotropic (*i.e.* globular) growth m/z following $\sigma = \sigma_1 \cdot n^{2/3}$, where σ_1 denotes the CCS of the monomer [26]. This CCS plot clearly shows the polydisperse and polymorph nature of VEALYL oligomers, featuring oligomers with various stoichiometries ranging from the singly-protonated monomer ($n/z = 1/1$) to the quadruply-protonated decamer ($n/z = 10/4$).

The inset in Figure 1c shows an ATD of the triply-protonated tetramer ($n/z = 4/3$) for which multiple species with different CCSs were observed. Interestingly, VEALYL oligomers larger than the trimer ($n > 3$) exhibit CCS values that are larger than predicted by the isotropic model. This deviation from the isotropic growth line may be indicative of the presence of soluble, β-sheet-rich intermediates on the way to fibril formation, as suggested by earlier studies [26, 226].

6.3.2 IR Spectroscopy of VEALYL Oligomers

Although ion mobility data contain information about the overall sizes of oligomer ions, it cannot provide clear evidence for a specific secondary structure. To obtain information about structural details of individual oligomer ions, the IM-MS instrument was used as a preparative tool to pre-select ions of a specific size and m/z, followed by irradiation with intense IR laser pulses generated by the Fritz Haber Institute's free electron laser [122]. An IRMPD spectrum can then be generated from the wavelength-dependent dissociation of the pre-selected ions as described in Section 2.6.2. The resulting IRMPD spectra of individual VEALYL oligomers up to the quadruply-protonated nonamer ($n/z = 9/4$) measured in a wavenumber range of 1000–1850 cm^{-1} are shown in Figure 6.1 (d). The spectra consist of two major bands at 1600–1700 cm^{-1} and 1450–1550 cm^{-1}, which can be assigned as amide I and II vibrations, respectively. IR features above 1700 cm^{-1} originate from carboxylic acid vibrations either from the C-terminus or the side chain of glutamic acid. Weaker features in the wavenumber range 1100–1300 cm^{-1} can be assigned to Tyr and amide III vibrations [33, 238]. For the singly-protonated monomer ($n/z = 1/1$), well-separated features can be observed in the amide I region at 1655, and 1695–1705 cm^{-1}, as well as a very weak feature at 1750 cm^{-1}. Compared to the amide I bands of higher oligomers, these monomer features are found at higher wavenumbers. This is not surprising, since the extent of hydrogen bonding inside the hexapeptide monomer is expected to be rather low and, thus, provide little perturbation of the individual C=O oscillators. As the size of the oligomer increases, amide I features are shifted towards lower wavenumbers. The spectra of higher oligomers ($n = 3$–9) feature amide I bands that are centered around 1660–1670 cm^{-1}, which is indicative of turn-like structures (Table 6.1). Most interesting, however, is the observation of typical β-sheet IR bands in the amide I region (1620–1640 cm^{-1}) for the tetramer and higher oligomers, which clearly have larger CCSs than predicted by the isotropic growth model. To qualitatively ascertain relative abundances of ordered β-sheet and turn-like structures, the amide I region (1600–1700 cm^{-1}) of these oligomers ($n = 4$–9) was deconvoluted with multiple Gaussian curves (Figure 6.1 (d)). Each of these Gaussians represents a specific motif: antiparallel β-sheets centered at 1625 and 1690 cm^{-1} (blue) and small turns at 1665 cm^{-1} (red). This analysis indicates a significant proportion of β-sheet in higher VEALYL oligomers of $n \geqslant 4$.

Compared to the clear evidence for β-sheets in the solid FT-IR spectra of the mature VEALYL fibrils (Figure 6.1 (b)), β-sheet signatures in the IRMPD spectra of VEALYL

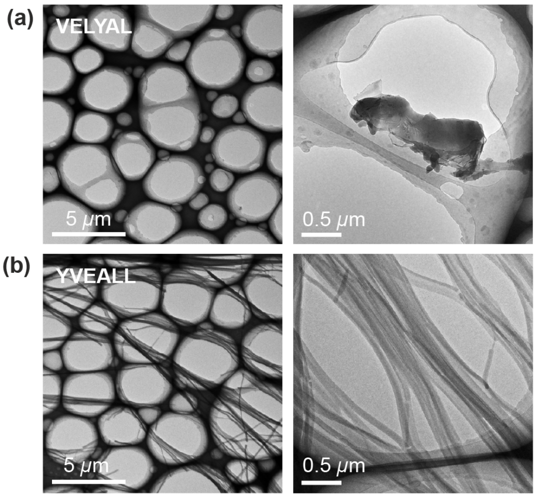

Figure 6.3: TEM micrographs of (a) VELYAL and (b) YVEALL obtained after incubation at room temperature for 29 days and subsequent evaporation of the solvent. No fibrils, but only the TEM grid was observed for VELYAL, whereas fibril formation was observed for YVEALL.

oligomers (Figure 6.1 (d)) are weaker and exhibit little variation over the different oligomer sizes. This makes it difficult to correlate the IRMPD results with the observed CCSs and to pinpoint specific oligomers that are involved in structural transitions. For VEALYL, however, a relatively fast rate of fibril formation was observed. Once an intermediate β-sheet-rich structure is formed, it may well rapidly proceed to form insoluble fibrils, leaving only soluble intermediates with less β-sheet content in solution before the IMS and spectroscopy analysis is performed.

6.3.3 Scrambling the VEALYL Sequence

In order to generate comparable peptides that may be less prone to amyloid formation, the VEALYL sequence variants VELYAL and YVEALL were synthesized and investigated. Keeping the overall amino acid composition unchanged helps to minimize differences in the IR spectra that arise due to different amino acid side chain absorptions and greatly facilitates the comparison between different sets of IR data. As shown in the TEM image in Figure 6.3 (a), VELYAL does not appear to form amyloid fibrils. Likewise, no visible precipitate was formed after several days of incubation. FT-IR spectra of the lyophilized VELYAL sample (Figure 6.4 (a)) exhibit an amide I peak at 1638 cm^{-1} and broad features up to 1750 cm^{-1}, which indicates that mostly unordered structures are present and no β-sheets are formed. Taken together, these results show that VELYAL is a non-amyloid forming sequence, which makes it an ideal reference for further comparison. VELYAL does form oligomers that can be transferred into the IM-MS instrument at considerable intensities (Figure 6.2 (b)), allowing further investigation by IM-MS and IRMPD. However, their CSSs more closely follow the isotropic growth curve than either of the other two peptides, which indicates a compact and rather globular set of conformations. In addition, the IRMPD spectra show almost no sign of β-sheet formation and point to a predominantly unordered or turn-like conformation (for the full set of IRMPD spectra see Figure C.1 Appendix C). These results emphasize that the

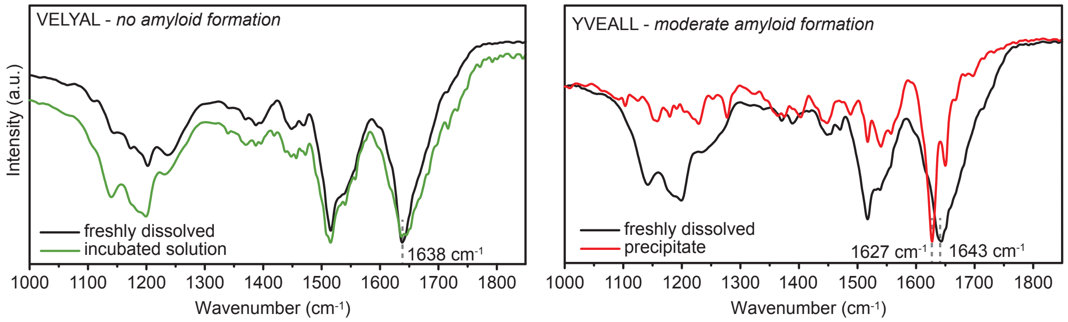

(a) FT-IR VELYAL **(b)** FT-IR YVEALL

Figure 6.4: Solid FT-IR spectra of the non-amyloid forming peptide VELYAL (a) and the moderately amyloid forming peptide YVEALL (b). Spectra are shown for freshly dissolved (black) and for an incubated (green) sample and for the precipitate (red), respectively.

increased β-sheet content observed for VEALYL is a real effect and not just an artefact of the IRMPD measurements.

In stark contrast to the non-amyloidogenic variant VELYAL, the TEM micrographs of YVEALL clearly point to the formation of amyloid fibrils (Figure 6.3 (b)). This is further supported by the FT-IR spectra of the precipitate (Figure 6.4 (b)), which exhibit a sharp IR band at 1627 cm^{-1}, indicating the presence of highly ordered β-sheets. However, the rate of fibril formation was observed to be considerably slower than in the original sequence VEALYL, which makes YVEALL an ideal candidate for the spectroscopic investigation of intermediate amyloid oligomers.

In IM-MS a wide distribution of oligomers of different size and charge are observed for YVEALL (Figure 6.2 (c)). The CCS evolution of different oligomers as a function of the oligomer number n is shown in Figure 6.5 (a). For species up to the tetramer (n = 1–4), only little deviation from the isotropic growth model (dashed line) is observed. Larger oligomers ($n > 4$), however, exhibit significantly higher CCSs than predicted by the isotropic model. Figure 6.5 (b) shows an ATD of the triply protonated pentamers (5/3), for which at least four distinct conformers can be separated (labeled I–IV). The size of the smallest observed pentamer (5/2) fits to the isotropic model, whereas the largest pentamer (5/3 IV) is $\sim$ 23 % larger in CCS compared to isotropic oligomers. YVEALL pentamers are therefore highly polymorph and represent a transition from globular species close to the isotropic line to much more extended states.

6.4 IR Spectroscopy of VEALYL Variant Oligomers

The IRMPD spectra of each 5/3 conformer are given in Figure 6.5 (c). All spectra show strong amide II and I features in the 1500–1580 cm^{-1} and 1600–1700 cm^{-1} region, respectively, and additionally exhibit pronounced signals at 1100–1300 cm^{-1}, corresponding to Tyr

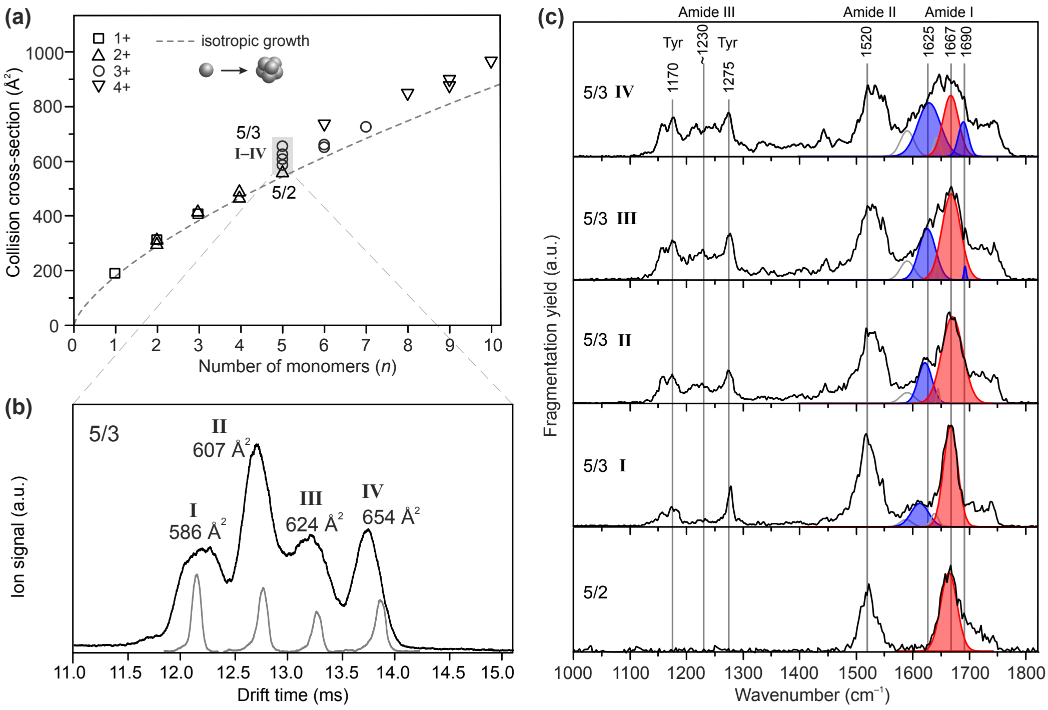

Figure 6.5: (a) CCSs of YVEALL oligomers as a function of the number of monomers n. The dashed line denotes isotropic growth. (b) An ATD of the triply protonated pentamer (5/3) for which multiple conformers with distinct CCSs are observed. The narrow peaks depicted in gray correspond to the portions of the oligomer distribution that were selected for further IRMPD-spectroscopic analysis. (c) IRMPD spectra of the doubly-protonated pentamer (5/2) and the drift-time selected species (I–IV) of the triply protonated YVEALL pentamers (5/3). The amide I region (1600–1720 cm^{-1}) was deconvoluted by fitting multiple Gaussian curves. The red and blue Gaussians represent IR bands corresponding to turn-like (centered at 1665 cm^{-1}) and β-sheet structures (centered at 1625 and 1690 cm^{-1}), respectively.

and amide III vibrations. It is interesting to observe how the individual IR bands change when the pentamers become more extended. The amide II band only undergoes a small blue-shift and broadening as the CCS increases. This is not surprising, since the amide II band consists of N-H and C-N bending modes which are only marginally affected by changes in the secondary structure [234]. The diagnostic amide I band, however, shows a strong variation between different pentamers. For the doubly-protonated pentamer (5/2) the amide I modes are centered at 1667 cm^{-1} and do not exhibit IRMPD features in the typical β-sheet range of 1620–1640 cm^{-1} (Table 6.1). However, as the cross-section of the polymorphic pentamers increase (species I–IV), typical β-sheet amide I features centered at 1625 cm^{-1} and 1690 cm^{-1} make up a considerable fraction of the overall spectrum. In order to allow a more quantitative assessment, the IR traces of the individual pentamers (I–IV) were deconvoluted in the amide I region by fitting multiple Gaussians as shown in

Figure 6.5 (c). The curves in blue represent the characteristic β-sheet bands and curves in red correspond to turn-like features. Clearly the β-sheet bands increase as the CCS increases. The most extended pentamer IV exhibits IRMPD features centered at 1625 cm^{-1} and 1690 cm^{-1} that are both highly characteristic for the existence of antiparallel β-sheet structures.

Further support for a possible transition in secondary structure is provided by the increasing intensities of the IR bands around 1220–1240 cm^{-1} for conformations with increasing CCS. These bands can be tentatively assigned to amide III bands typical for antiparallel β-sheets [33, 35]. Additional structural information can be drawn from amino acid side chain vibrations. According to X-ray crystallography studies, half of all amino acid side chains in amyloid fibrils only weakly interact with other side chains or the peptide backbone. For globular oligomers, on the other hand, extensive interactions between side chains or with the backbone are essential in order to maintain the compact structure [223, 226]. These characteristics are also reflected in the IRMPD spectra of the corresponding structures, leading to signatures of free side chains for fibril-like species and less pronounced features for globular types. This behaviour can be found in the spectra of the polymorph YVEALL pentamers in Figure 6.5 (c). IR bands that can be assigned to C-O-H bending (1170 cm^{-1}) and C-OH stretching (1275 cm^{-1}) vibrations of free tyrosine residues [33] as well as signals at 1700–1750 cm^{-1} that correspond to C=O stretching vibrations of free or weakly bound carboxylic acids can all be identified with increasing intensities for species with increasing cross-section. Taken together, the presented results from IM-MS and IRMPD spectroscopic experiments strongly suggest that pentamers of the fibril-forming sequence YVEALL are soluble, early intermediates that undergo secondary structural transitions from a compact unordered structure to an extended assembly of repeating β-sheets.

In order to correlate the deviation in CCS from the isotropic growth model with the IRMPD spectroscopic results, the fraction of β-sheet in all investigated species was calculated by dividing the summed area of β-sheet structures in the IRMPD spectra (blue curves) by the total area of the amide I band (compare IR spectra in Figures C.1 and C.2 and Tables C.1–C.3 in Appendix C). The result is shown in Figure 6.6. Oligomers of VELYAL barely deviate from the isotropic line (less than 5 %), and feature β-sheet signatures that make up less than 10 % of the total amide I band. The amyloid forming sequences VEALYL and YVEALL on the other hand show more pronounced deviations in CCSs, with up to 61 % β-sheet content for the largest of the four different pentameric species (5/3) of YVEALL (solid circles). The data convincingly demonstrates the positive correlation between relative size and ordered β-sheet structure, and therefore support recent IM-MS approaches where such a correlation was suggested [26–28, 233–235].

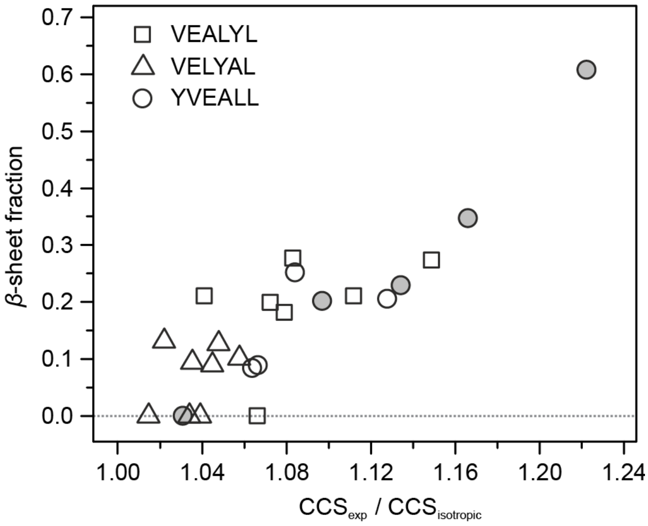

Figure 6.6: Fraction of β-sheet in the amide I band of VEALYL (squares), VELYAL (triangles), and YVEALL (circles) oligomers as a function of relative deviation in CCS from the isotropic growth model. Solid circles denote the polymorph pentamers (5/2 and 5/3, I–IV) of YVEALL, which are discussed in detail in Figure 6.5

6.5 Conclusions

The combination of IM-MS and IR spectroscopy enabled to directly measure the onset of β-sheet structure formation in isolated, early soluble oligomers of the insulin B-chain fragment VEALYL, which was previously shown to form β-sheet rich amyloid fibrils and microcrystals [227]. In addition, the critical transition from a compact and unordered to an extended β-sheet structure was monitored for highly polymorph pentamers of the amyloidogenic VEALYL sequence variant YVEALL. Compact YVEALL pentamers were shown to predominantly adopt turn-like or unfolded structures while a considerably increased content of β-sheet was observed for more extended analogs. Further support for this structural assignment was found in amide III and side chain vibrations, which follow the evolution of β-sheet characteristic amide I features and strongly suggest that the peptide assemblies consist of repeating antiparallel β-sheets. Taken together, the data represent the first spectroscopic study that successfully identifies specific pre-fibrillar oligomer states involved in the critical transition from an unordered to a β-sheet-rich structure. For the systems investigated here, oligomers consisting of as little as four to nine peptide strands were found to exhibit a considerable fraction of β-sheet.

Furthermore, the results presented here demonstrate that there is a clear correlation between a large collision cross-section that deviates from the isotropic growth model and the presence of β-sheet structures. This correlation greatly strengthens the interpretation given in recent IM-MS studies of amyloid systems [26–28, 233–235] and demonstrates how IR-spectroscopy combined with IM-MS can be of great use for this field of research. These combined techniques offer new possibilities to explore the secondary structures of soluble, pre-fibrillar oligomers, which will be greatly beneficial for developing effective strategies to manipulate or hinder the amyloid assembly process [28, 233, 236, 237] and may ultimately help to understand the molecular basis of amyloidogenic diseases.

7 Summary and Future Perspectives

Ion mobility spectrometry, combined with mass spectrometry to IM-MS, evolved to a widely-used technique in various branches of science to investigate molecular ions in the gas phase. Together with methods to dissociate size and m/z-selected species, IM-MS has proven useful to obtain information about molecular structures and is applicable to a wide range of different molecules. Each of the combined methods can provide additional, complementary information about different structural aspects. The comparison of experimental results to properties deduced from calculated model structures using molecular dynamics and/or quantum chemical calculations can ultimately help to pinpoint specific structures or structural details that cannot be derived from the experiment alone.

7.1 Summary

Using a commercial instrument, IM-MS was successfully applied to investigate the influence of charged sites on gas-phase protein structures. It was found that not only the repulsion of like charges is responsible for the unfolding of a protein in the gas phase when the total amount of charge is increased. The charged site itself interacts with the protein's backbone thereby destroying native-like structural elements, followed by unfolding as earlier suggested [24].

Furthermore, a new IM-MS experimental setup was presented that, in addition to *traditional* IM-MS measurements, allows the study of photofragmentation properties of conformer, isomer, or oligomer-selected gas-phase ions. Using this instrument, it was first shown how UV photodissociation at 193 nm wavelength can be sensitive to the higher order structure of the protein ubiquitin. In conjunction with molecular dynamics calculations, differences in fragmentation propensities of different conformations of the protein ubiquitin could be attributed to one particular peptide bond preceding a proline residue being in a *cis* or *trans* isomeric state.

When tuneable light sources are used, the wavelength-dependent fragmentation of molecules can be monitored and a spectrum can be generated. With the aid of intense and tuneable IR radiation generated by the Fritz Haber Institute's free electron laser, it was possible to obtain highly informative vibrational spectra from the isolated species. By obtaining IR spectra of drift-time separated ions of the small local anaesthetic benzocaine, two different isomeric species were found to coexist in the gas phase, with each species possessing completely different vibrational signatures. Their identity was confirmed by comparison with quantum chemical calculations and it was found that the dielectric properties of the molecule's immediate surrounding can significantly influence its preferred protonation site.

In the last part of this thesis the focus was shifted towards monitoring structural changes in aggregating systems. In the light of neurodegenerative diseases, such systems represent one of the key elements. Aggregating peptide and protein strands that finally form insoluble amyloid fibrils are suspected to be the pathogenic species in the disease case. The aim of this study was to identify oligomeric species that are on the verge of a structural reorganization towards a highly ordered β-sheet-rich architecture – the scaffold of an amyloid fibril. In particular, the structural preferences of the amyloidogenic peptide sequence VEALYL from the insulin B-chain were investigated, which was previously shown to form insoluble amyloid fibrils in solution [223–227]. Oligomer-specific gas-phase IR spectroscopy of VEALYL and two of its sequence-scrambled versions could successfully demonstrate that already early oligomers with as few as four or five monomer subunits can undergo a transition from a random assembly to a β-sheet-rich structure. Here, conclusions from the experimentally obtained vibrational spectra were drawn by comparison with reference data from condensed-phase measurements. This study represents the first where IM-MS in combination with IR spectroscopy was used to identify structural transitions in polydisperse and polymorph systems and, furthermore, highlights the unique advantages that gas-phase experiments provide for the study of molecular structures even of complex molecular assemblies.

7.2 Perspective for Future Research

The success of the here combined methods in isolating specific molecular ions based on their *m/z* and size and investigating their structure with spectroscopic methods may have a significant impact on the field of structure analysis of gas-phase molecular ions. The versatility of this approach in terms of molecular types and size makes it widely applicable for structure identification not only of biological molecules as presented in this thesis.

Future Field of Research. Ongoing research further exploits the capability of the drift-tube instrument to separate homo-molecular aggregates of identical *m/z* values as performed in Chapter 6 to investigate oligomers of amyloidogenic peptides. Having demonstrated the applicability of the method to small aggregating amino acid segments it will now be extended to larger aggregating systems with direct biological relevance, *e.g.*, to probe the structures of the pathologic assemblies of the 42-residue form of the amyloid β-protein, which is linked to Alzheimer's disease.

However, it is not only research in the field of neurodegenerative diseases that may benefit from the latest developments in instrumentation using gas-phase approaches. Non-covalently bound metastable (*meta*)clusters that are formed, *e.g.*, on an amino acid level are also of medical interest. They play a central role in a range of different metabolic disorders. Two examples are the disorders called *phenylketonuria* and *tyrosinemia* where a lack of the enzymes needed to metabolize the amino acids phenylalanine and tyrosine, respectively, can lead to unusually high amino acid concentrations in the body. This, in turn, can cause the highly abundant species to form clusters, presenting a hazard to liver, kidneys, or brain. Also here will a detailed knowledge about the oligomer structures be helpful for understanding the disorders on a molecular basis.

Related research is concerned with identifying segments in the amino acid sequence of proteins that are prone to promoting aggregation and predicting their aggregation propensities [239]. Pairwise interaction between residues of the same types (polar/non-polar, acidic/basic, *etc.*) typically drives the self-assembly, giving reason to separately and systematically investigate the cluster growth of amino acids with similar side chains. The metastable nature of such amino acid clusters allows a non-destructive transfer into the gas phase and further investigation using MS methods [240–243]. The here presented possibility to directly probe the structure of a specific cluster using IR spectroscopy presents an opportunity to shed more light into the structure of metaclusters. This research is not only aimed at developing an understanding of protein aggregation but may ultimately present a step towards the prediction of protein structure solely from the amino acid sequence information – a maturing field with a long way to go.

Future Instrumentation. The drift-tube IM-MS instrument will, in a near and distant future, undergo modifications in order to satisfy the urge for increased resolution with respect to IMS drift-time and m/z-separation as well as separation of vibrational bands. IMS resolving power is easily improved by increasing the drift voltage according to Equation 2.35, or, if the resulting electric fields exceeds a range where a safe operation is not possible, by increasing the length of the drift tube at constant electric field. Little more effort is required to increase m/z-resolving power, however, the modular instrument design allows to modify time-of-flight components as required. The spectral resolution, on the other hand, cannot that easily be improved and requires more modification. While the current setup yields IRMPD spectra of satisfactory resolution, the minimum achievable band width will always be limited by the high internal temperature of the probed molecular ions.

Strategies to improve spectral resolution are based on, *e.g.*, cooling the ions of interest *via* collisions with cold buffer gas molecules in ion traps cooled by liquid nitrogen or helium [244]. At low internal temperatures, vibrational states of higher energies are depleted and the molecules can be probed spectroscopically from low energy levels that are less disperse. Direct probing of cold molecules with IR light, however, will lead to vibrational heating during the IRMPD process. This, in turn, results in broadened vibrational bands in an experimental spectrum. In order to avoid this heating, which is inherent to the IRMPD process, a range of different techniques have been developed [244], one of which includes the tagging of the analyte ion with non-covalently, weakly bound species that presents only little disturbance to the analyte's original structure. This newly formed complex can then be dissociated with

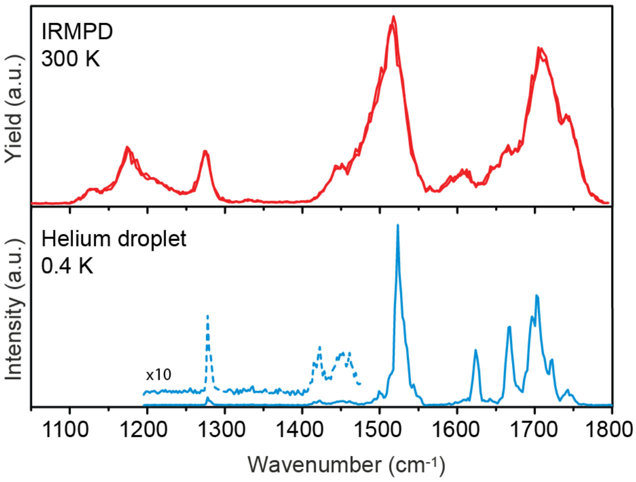

Figure 7.1: IR spectra of singly protonated YGGFL ions. Two consecutive scans acquired using the drift-tube IM-MS instrument show partially unresolved features of internally hot ions (upper panel). The same molecular ions yield narrow vibrational bands when the internal energy is low (lower panel). This data was acquired using the helium-droplet matrix isolation technique in which ions are cooled down to 0.4 K prior spectroscopic investigation [245].

relatively little energy intake, thus leading to higher vibrational resolution in the spectrum.

In an alternative approach gas-phase molecules are embedded in a cold matrix, *e.g.*, argon or helium, following spectroscopic interrogation [246]. Recent instrument development established this method also for ionic biomolecular species [245]. Figure 7.1 shows IR spectra of singly protonated YGGFL ions as measured at the drift-tube instrument (upper panel) using IRMPD spectroscopy at room temperature and as obtained using a matrix isolation method (lower panel) where ions of interest are embedded in superfluid helium droplets at a temperature of 0.4 K [245]. The difference in spectral resolution is striking and in the case of the helium droplets, the resolution is further limited by the bandwidth of the free electron laser used to generate the IR photons (~ 0.5 %). A combination of the drift-tube instrument with methods to obtain high-resolution vibrational spectra is, thus, desirable. However, cold ion trap methods require less sophisticated experimental setups than the helium-droplet competitor and can achieve spectra of similar quality for biological molecular ions [69, 245].

A schematic representation of a future drift-tube setup, which will allow to store and cool drift-time and m/z-selected ions in a helium-cooled ion trap following spectroscopic investigation is depicted in Figure 7.2. After drift-time and m/z-selection, the ion trajectories are bent by 90° in a quadrupole bender. Ions are subsequently loaded into a hexapole RF ion trap, which is mounted on a helium cryostat and filled with low pressure helium buffer gas to cool the internal energy of the ions *via* collisions. The cold ions will here be tagged with, *e.g.*, rare gas atoms, depending on the minimum temperature that can be achieved with this setup. This is followed by irradiation with IR light generated by the FHI FEL and the dissociation of the ion-rare gas complex will be monitored with the TOF MS. Just as in the case of the original IRMPD spectra presented here, the depletion of the precursor ion signal and the appearance of the fragment signal will be used to generate IR spectra of cold, m/z and conformer-selected molecular ions. A Cu-cold shield will be installed to prevent the hexapole trap to be exposed to blackbody radiation emitted by the surrounding

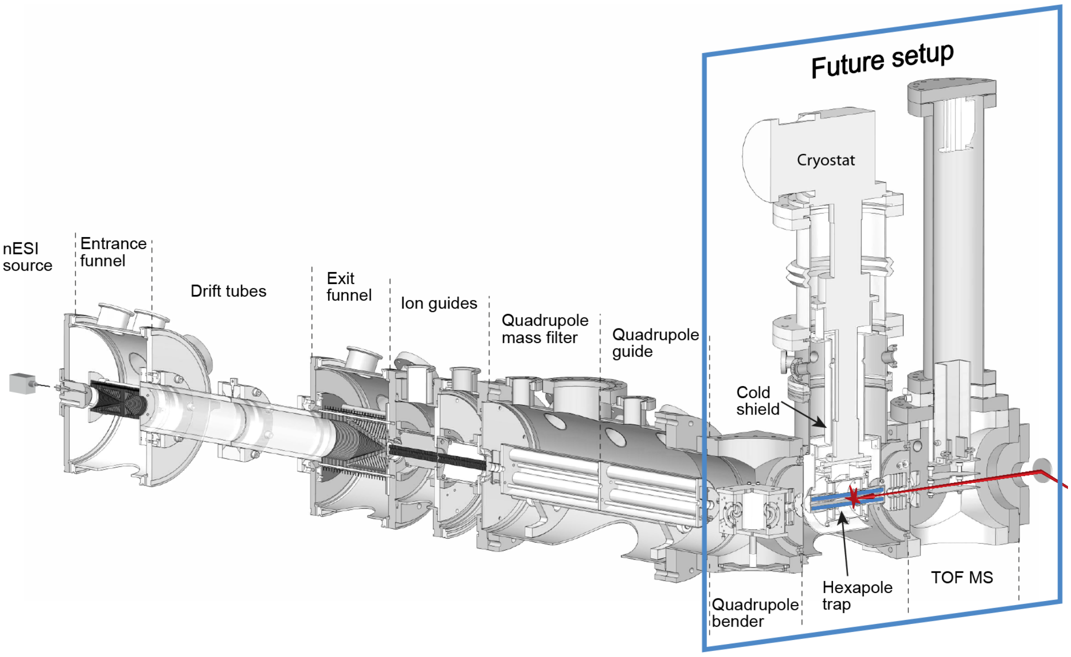

Figure 7.2: Future drift-tube IM-MS setup. Drift-time and *m/z*-selected ions will be loaded into a helium-cooled hexapole RF trap and tagged with, *e.g.*, rare gas atoms to form weakly-bound complexes. The FHI FEL provides IR radiation that, when in resonance with a molecular vibration, leads to dissociation of the complex. Fragmentation of the precursor complex can then be monitored using the TOF MS.

vacuum chambers. The minimum achievable temperature of the trap, however, is difficult to assess but will certainly range well-above 4 K (the minimum temperature of a helium cryostat).

The combination of IM-MS with orthogonal, structure-sensitive as well as computational methods will doubtlessly raise large interest as the new gas-phase approach presents many opportunities for structure determination of molecular ions and offers a large range of potential applications in life sciences.

Appendix A
UV Photofragments of Ubiquitin

UVPD Fragment Assignment for Ubiquitin 11^+

For a deeper understanding about the observed differences in UV photofragmentation of different ubiquitin 11^+ conformers in Section 4.2, an assignment of the fragment signals is required. Unfortunally, an unambiguous assignment purely based on the obtained fragment mass spectra was not possible due to the limited resolution of the in-house built mass spectrometer. However, high-resolution UVPD mass spectra of non-conformer selected ubiquitin 11^+ from an orbitrap instrument was provided by the group of Jennifer Brodbelt [72]. Direct comparison with our conformer-selected UVPD data allowed the identification of all intense peaks and many of the weaker features. To do so, the experimental fragment spectra were overlaid with the high-resolution reference spectra and fragments were assigned manually according to the peak positions. If two fragment peaks in the reference spectra are in such close proximity that they appear as one single signal in our mass spectra, an intensity was assigned to both peaks. A list of all assigned fragments and their assigned relative intensities can be found in Table A.1. The relative intensities were used to compose the fragmentation propensity as a function of the protein sequence shown in Figure 4.6 in Section 4.2.

fragment type	label	sequence position	*m/z*	charge state	relative intensity 1st peak at 1802 Å^2	relative intensity 2nd peak at 1871 Å^2
a	2	2	232.11	1	1	1
b	2	2	260.11	1	1	1
z	3	73	273.14	1	1	1
c	2	2	277.13	1	1	1
y	5	71	279.68	2	1	1
y	3	73	289.16	1	1	1
x	3	73	315.14	1	1	1
z	6	70	328.21	2	1	1
y	6	70	336.20	2	1	0
a	3	3	345.20	1	1	1
x+	6	70	349.71	2	1	0
a+	6	6	360.72	2	1	0
b	3	3	373.19	1	1	1
y	7	69	385.75	2	1	1
z	4	72	386.23	1	1	1
x	7	69	398.74	2	1	0
y	4	72	402.25	1	1	1
z	11	65	406.92	3	1	0
a+	11	11	407.58	3	1	0
c	11	11	422.25	3	1	0
x+	4	72	429.23	1	1	0
z	12	64	435.90	3	1	0
y	8	68	442.29	2	1	1
z	16	60	451.77	4	1	0
x	8	68	455.28	2	1	0
y	20	56	460.66	5	1	0
a+	13	13	478.95	3	1	0
z	17	59	480.28	4	1	1
b	8	8	481.28	2	1	1
y	13	63	484.20	3	1	1
a	4	4	492.20	1	1	1
a+	4	4	493.20	1	1	1
z	9	67	502.80	2	1	1
y	9	67	510.82	2	1	1
z	18	58	521.04	4	1	1
z	14	62	521.65	3	1	1
x	9	67	523.81	2	1	1
y	14	62	526.98	3	1	1
b	9	9	531.80	2	1	0
x+	18	58	531.80	4	1	0
y-	23	53	534.50	5	1	0
x	14	62	535.64	3	1	0
y	24	52	546.10	5	1	1
a+	10	10	546.82	2	1	1
z	15	61	564.33	3	1	1
y	10	66	567.37	2	1	1
z	20	56	571.56	4	1	0
y-	20	56	578.30	4	1	0
a	5	5	591.30	1	1	1
a+	5	5	592.30	1	1	1
z	21	55	599.83	4	1	0
z	16	60	602.02	3	1	1
y	16	60	607.36	3	1	0
x	32	44	607.66	6	1	0
a+	11	11	610.87	2	1	1
x+	16	60	616.36	3	1	1
y	11	65	617.90	2	1	1
b	5	5	619.32	1	1	1
a-	17	17	626.04	3	1	1
a+	29	29	638.60	5	1	0
z	17	59	640.04	3	1	0
a-NH_3	12	12	652.38	2	1	1
y-H_2O	12	64	652.40	2	1	1
z	12	64	653.40	2	1	1
a-NH_3	18	18	663.37	3	0	1
b	18	18	678.40	3	0	1
y-	30	46	679.97	5	0	1
x	49	27	697.25	8	0	1
z	44	32	711.39	7	0	1
y	57	19	715.50	9	1	3
y	58	18	726.28	9	2	3
x	32	44	728.99	5	1	1
a	33	33	735.20	5	1	1
z	59	17	738.84	9	1	1
y-	33	43	746.21	5	1	1
a	54	54	753.41	8	0	1
c	54	54	759.04	8	1	1
y-	40	36	761.00	6	1	1
a+	34	34	761.21	5	1	1
a+	48	48	761.28	7	1	1
z	54	22	764.92	8	1	1
a	36	36	795.24	5	1	2
x	56	20	797.18	8	1	2
a	64	64	802.21	9	1	2
y-	57	19	803.69	8	2	2
y	72	4	805.04	10	2	2
a	58	58	805.43	8	1	1
a	37	37	814.45	5	1	2
y	58	18	816.94	8	2	3
a	44	44	820.62	6	1	2
y-	74	2	830.96	10	1	2
y	59	17	832.94	8	1	2
x	22	54	847.12	4	1	1
a	68	68	850.90	9	1	1
y-	37	39	851.27	5	1	1
y-	45	31	851.46	6	1	1
a+	54	54	861.04	7	1	0
y-	61	15	861.46	8	1	0
b	46	46	861.63	6	1	0
c	47	47	873.98	6	1	0
x	31	45	874.22	4	1	0
y	38	38	874.47	5	1	0
y	62	14	875.72	8	1	0
y	54	22	876.34	7	1	0
a	32	32	886.99	4	1	0
y	63	13	888.35	8	1	0
a+	16	16	889.52	2	1	0
y	39	37	893.89	5	1	0
b	16	16	903.01	2	1	0
y-	58	18	933.36	7	0	1
a	67	67	940.00	8	1	0
a	59	59	943.65	7	1	0
b	26	26	963.52	3	1	0
b	18	18	1017.07	2	1	1

Table A.1: Assigned UVPD fragments of the two ubiquitin 11^+ conformers and relative intensities of the fragments. N-terminal fragments are of type a, b, and c, C-terminal fragments are of type x, y, and z. "+" or "−" signs refer to a shift in mass of 1 Da.

Appendix B
Protomers of Benzocaine

Hypothetical Ring-Protonation of Benzocaine

Besides the two possible protonation sites of benzocaine that are discussed in Section 5, a third possible protomeric species could arise from a protonation of the benzene ring, which plays a role in the gas-phase structures of aniline [208]. To rule out this possibility for benzocaine, theoretical model structures and corresponding spectra were computed. The four different ring-protonated structures considered here, are at least 59.0 kJ mol^{-1} higher in energy than the lowest-energy structure of the O-protonated form and 6.3 kJ mol^{-1} higher than the most stable N-protonated species (see insets in Figure B.1 (b)). Additionally, the theoretical spectra (Figure B.1 (b)) do not reproduce the experimental data of species I and II (Figure B.1 (a)). Energy optimization and calculation of theoretical spectra was carried out in analog to Section 5. The theoretical spectra were convoluted with a Gaussian profile of 1.5 % width and scaled by a factor of 0.975.

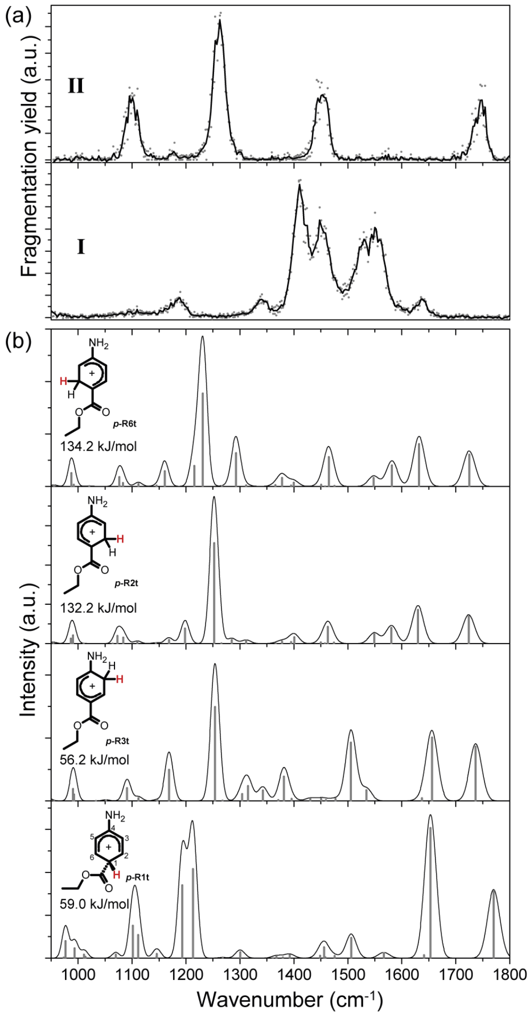

Figure B.1: Theoretical vibrational spectra of ring-protonated species of benzocaine (b). The insets show the chemical structures of the respective ring-protonated model structures and the corresponding energies with respect to the lowest-energy O-protonated structure. None of the calculated spectra give a good match to the experimental data which are reproduced in (a).

Appendix C
Peptide Oligomers – IR Spectra and CCSs

Gas-Phase IR Spectra of Peptide Oligomers

Figures C.1 and C.2 show the gas-phase IR spectra of higher oligomers of VELYAL and YVEALL, respectively. Spectra of the original sequence VEALYL are shown in Figure 6.1. Roman numerals denote multiple conformations of the same oligomeric species (n/z) that could be resolved in the IM-MS experiment. The amide I region was fitted with multiple Gaussian curves to assess the content of β-sheet within each investigated oligomer. Blue curves represent signals that correspond to β-sheet features and denoted on the right is the fraction of those signals in the total integral of the amide I region.

CCSs and β-Sheet Content of Peptide Oligomers

The Tables C.1–C.3 contain the measured cross-sections of all observed oligomers of the peptides VEALYL, VELYAL, and YVEALL as well as their relative size $\mathrm{CCS}_{\mathrm{exp}}/\mathrm{CCS}_{\mathrm{isotropic}}$ with respect to the isotropic model $\sigma = \sigma_1 \cdot n^{2/3}$, where σ_1 denotes the CCS of the monomer. The right columns contain the relative content of spectral features indicating β-sheet structures in the amide I region of the IRMPD spectra in Figures C.1 and C.2 (area of blue Gaussians divided by total area of the amide I band).

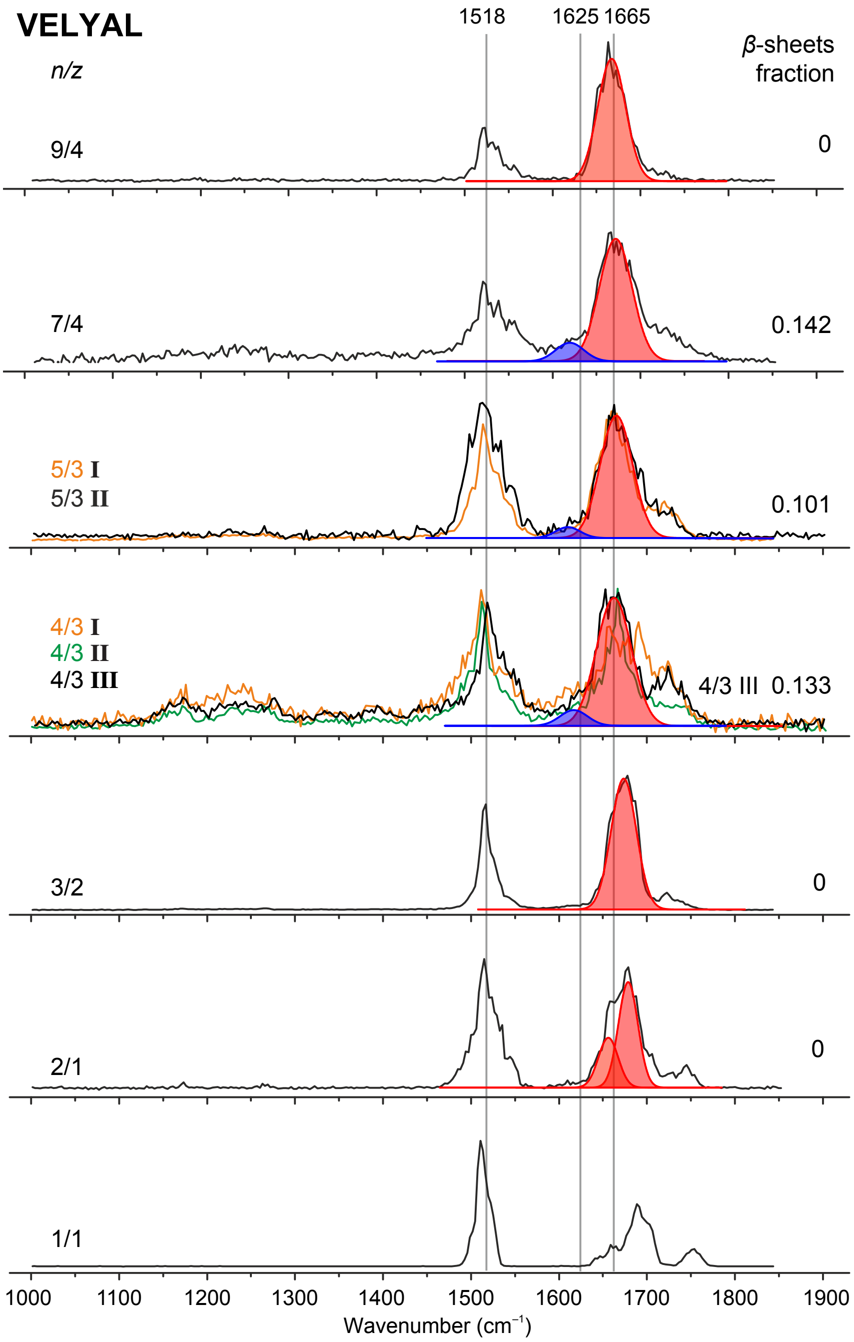

Figure C.1: IRMPD spectra of oligomer-selected VELYAL species.

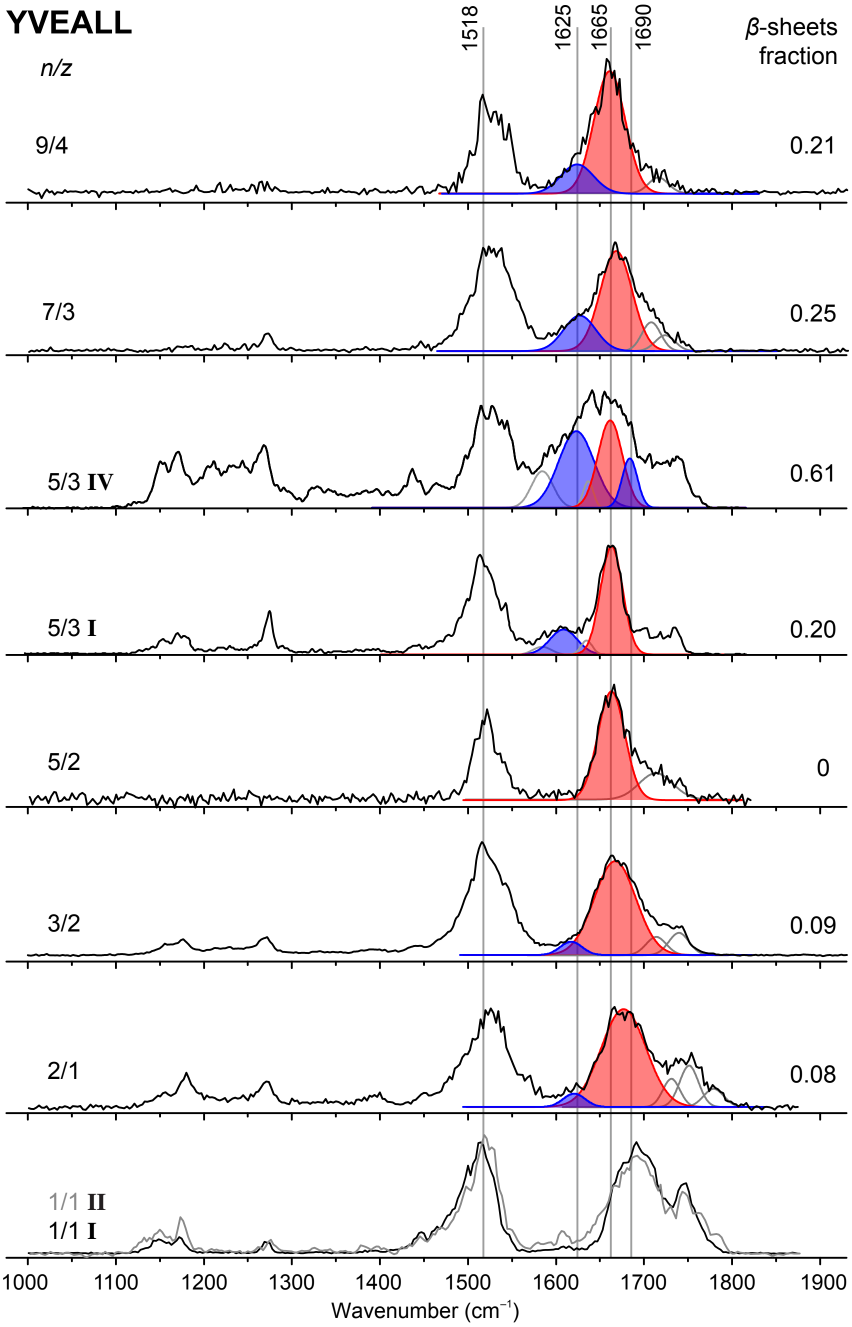

Figure C.2: IRMPD spectra of oligomer-selected YVEALL species.

Table C.1: Collision cross-sections and β-sheet fractions of peptide oligomers

(a) VEALYL

n	z	$\mathrm{CCS_{exp}}$ (Å^2)	$\mathrm{CCS_{exp}/CCS_{isotropic}}$	β-sheet fraction in amide I
1	1	190	1.05	0
2	1	306	1.06	0
2	2	315	1.09	
3	2	409	1.08	0
4	2	495	1.09	
		524	1.14	
4	3	459	1.00	
		495	1.08	0.29
		524	1.15	0.27
5	2	563	1.06	
5	3	551	1.04	0.21
		588	1.11	0.21
6	3	652	1.09	
6	4	656	1.09	
7	3	702	1.06	
7	4	710	1.07	0.20
8	4	796	1.10	
9	4	845	1.08	0.18
10	4	895	1.07	

(b) YVEALL

n	z	$\mathrm{CCS_{exp}}$ (Å^2)	$\mathrm{CCS_{exp}/CCS_{isotropic}}$	β-sheet fraction in amide I
1	1	191	1.04	
2	1	309	1.06	0.084
2	2	297	1.02	
		314	1.08	
3	2	406	1.06	0.089
4	2	461	1.00	
		486	1.05	
5	2	558	1.04	0
5	3	586	1.10	0.20
		607	1.13	0.22
		624	1.16	0.34
		654	1.22	0.61
6	3	661	1.10	
6	4	729	1.21	
7	3	726	1.08	0.25
8	4	853	1.17	
9	4	893	1.12	0.21
10	4	936	1.10	

Table C.3: Collision cross-sections and β-sheet fractions of VELYAL oligomers

n	z	CCS_{exp} (Å^2)	$CCS_{exp}/CCS_{isotropic}$	β-sheet fraction in amide I
1	1	192	1.00	
2	1	302	1.00	
2	2	309	1.01	
3	1	397	1.00	
3	2	413	1.00	
4	2	488	1.01	
		502	1.04	
4	3	471	1.00	0.14
		494	1.02	0.10
		507	1.05	0.13
		546	1.12	
5	2	563	1.00	
5	3	553	1.00	0.10
		601	1.07	0.10
6	2	638	1.00	
6	3	648	1.02	
6	4	629	1.00	
		649	1.02	
		671	1.06	
7	3	710	1.01	
7	4	713	1.01	0
8	3	777	1.01	
8	4	805	1.05	
9	3	829	1.00	
9	4	863	1.04	0
10	4	913	1.00	
10	5	893	1.02	
11	4	948	1.00	
		959	1.01	
11	5	987	1.04	
12	4	1009	1.00	
15	5	1183	1.01	

Bibliography

[1] Linderstrom-Lang, K. U. *Lane Medical Lectures: Proteins and Enzymes*; Stanford University Press, 1952; Vol. 6.

[2] Dobson, C.; Sali, A.; Karplus, M. *Angewandte Chemie* **1998**, *37*, 868–893.

[3] Dobson, C. *Nature* **2003**, *426*, 884–890.

[4] Dill, K. A.; Chan, H. S. *Nature Structural Biology* **1997**, *4*, 10–19.

[5] Selkoe, D. *Nature* **2003**, *426*, 900–904.

[6] Schnabel, J. *Nature* **2010**, *464*, 828–829.

[7] Goldschmidt, L.; Teng, P. K.; Riek, R.; Eisenberg, D. *Proceedings of the National Academy of Sciences of the United States of America* **2010**, *107*, 3487–3492.

[8] Schubert, F.; Ph.D. thesis; Freie Universität Berlin; 2014.

[9] Fraenkel, E.; Pabo, C. *Nature Structural Biology* **1998**, *5*, 692–697.

[10] Krishnan, V.; Rupp, B. *Macromolecular Structure Determination: Comparison of X-ray Crystallography and NMR Spectroscopy*; John Wiley & Sons, 2012.

[11] Aebersold, R.; Mann, M. *Nature* **2003**, *422*, 198–207.

[12] Meyer, T.; Gabelica, V.; Grubmüller, H.; Orozco, M. *Wiley Interdisciplinary Reviews: Computational Molecular Science* **2013**, *3*, 408–425.

[13] Wyttenbach, T.; Pierson, N. A.; Clemmer, D. E.; Bowers, M. T. *Annual Review of Physical Chemistry* **2014**, *65*, 175–196.

[14] Siuzdak, G.; Bothner, B.; Yeager, M.; Brugidou, C.; Fauquet, C.; Hoey, K.; Chang, C. *Chemistry & Biology* **1996**, *3*, 45–48.

[15] Loo, J. A. *Mass Spectrometry Reviews* **1997**, *16*, 1–23.

[16] Heck, A. J. R.; Heuvel, R. H. H. v. d. *Mass Spectrometry Reviews* **2004**, *23*, 368–389.

[17] Ruotolo, B. T.; Giles, K.; Campuzano, I.; Sandercock, A. M.; Bateman, R. H.; Robinson, C. V. *Science* **2005**, *310*, 1658–1661.

[18] Heck, A. J. R. *Nature Methods* **2008**, *5*, 927–933.

[19] Koeniger, S. L.; Merenbloom, S. I.; Sevugarajan, S.; Clemmer, D. E. *Journal of the American Chemical Society* **2006**, *128*, 11713–11719.

[20] Wyttenbach, T.; Bowers, M. T. *Journal of Physical Chemistry B* **2011**, *115*, 12266–12275.

[21] Shi, H.; Clemmer, D. E. *Journal of Physical Chemistry B* **2014**, *118*, 3498–3506.

[22] Mao, Y.; Ratner, M.; Jarrold, M. *Journal of Physical Chemistry B* **1999**, *103*, 10017–10021.

[23] Shi, H.; Pierson, N. A.; Valentine, S. J.; Clemmer, D. E. *Journal of Physical Chemistry B* **2012**, *116*, 3344–3352.

[24] Breuker, K.; McLafferty, F. W. *Proceedings of the National Academy of Sciences of the United States of America* **2008**, *105*, 18145–18152.

[25] Skinner, O. S.; McLafferty, F. W.; Breuker, K. *Journal of the American Society for Mass Spectrometry* **2012**, *23*, 1011–1014.

[26] Bleiholder, C.; Dupuis, N. F.; Wyttenbach, T.; Bowers, M. T. *Nature Chemistry* **2011**, *3*, 172–177.

[27] Bleiholder, C.; Do, T. D.; Wu, C.; Economou, N. J.; Bernstein, S. S.; Buratto, S. K.; Shea, J.-E.; Bowers, M. T. *Journal of the American Chemical Society* **2013**, *135*, 16926–16937.

[28] Young, L. M.; Cao, P.; Raleigh, D. P.; Ashcroft, A. E.; Radford, S. E. *Journal of the American Chemical Society* **2014**, *136*, 660–670.

[29] Papayannopoulos, I. A. *Mass Spectrometry Reviews* **1995**, *14*, 49–73.

[30] Sinz, A. *Analytical and Bioanalytical Chemistry* **2010**, *397*, 3433–3440.

[31] Zhang, H.; Cui, W.; Gross, M. L.; Blankenship, R. E. *FEBS Letters* **2013**, *587*, 1012–1020.

[32] Lermyte, F.; Konijnenberg, A.; Williams, J. P.; Brown, J. M.; Valkenborg, D.; Sobott, F. *Journal of the American Society for Mass Spectrometry* **2014**, *25*, 343–350.

[33] Barth, A. *Biochimica et Biophysica Acta (BBA) - Bioenergetics* **2007**, *1767*, 1073–1101.

[34] Jackson, M.; Mantsch, H. *Critical Reviews in Biochemistry and Molecular Biology* **1995**, *30*, 95–120.

[35] Oomens, J.; Sartakov, B. G.; Meijer, G.; von Helden, G. *International Journal of Mass Spectrometry* **2006**, *254*, 1–19.

[36] Valle, J.; Eyler, J.; Oomens, J.; Moore, D.; van der Meer, A.; von Helden, G.; Meijer, G.; Hendrickson, C.; Marshall, A.; Blakney, G. *Review of Scientific Instruments* **2005**, *76*.

[37] Rijs, A. M.; Oomens, J. *Topics in Current Chemistry: Gas-Phase IR Spectroscopy and Structure of Biological Molecules*; Springer, 2015; Vol. 364.

[38] Masson, A.; Kamrath, M.; Perez, M.; Glover, M.; Rothlisberger, U.; Clemmer, D.; Rizzo, T. *Journal of the American Society for Mass Spectrometry* **2015**, *26*, 1444–1454.

[39] Voronina, L.; Rizzo, T. R. *Physical Chemistry Chemical Physics* **2015**, *17*, 25828–25836.

[40] Kemper, P. R.; Dupuis, N. F.; Bowers, M. T. *International Journal of Mass Spectrometry* **2009**, *287*, 46–57.

[41] Collins, D.; Lee, M. *Analytical and Bioanalytical Chemistry* **2002**, *372*, 66–73.

[42] Kanu, A. B.; Dwivedi, P.; Tam, M.; Matz, L.; Hill, H. H. *Journal of Mass Spectrometry* **2008**, *43*, 1–22.

[43] Bohrer, B. C.; Merenbloom, S. I.; Koeniger, S. L.; Hilderbrand, A. E.; Clemmer, D. E. *Annual Review of Analytical Chemistry* **2008**, *1*, 293–327.

[44] Bowers, M. T. *International Journal of Mass Spectrometry* **2014**, *370*, 75–95.

[45] Baumbach, J. *Analytical and Bioanalytical Chemistry* **2006**, *384*, 1059–1070.

[46] Westhoff, M.; Litterst, P.; Freitag, L.; Urfer, W.; Bader, S.; Baumbach, J.-I. *Thorax* **2009**, *64*, 744–748.

[47] Willis, R. C. *Modern Drug Discovery* **2002**, *5*, 28–30.

[48] Lokhnauth, J.; Snow, N. *Journal of Separation Science* **2005**, *28*, 612–618.

[49] Makinen, M. A.; Anttalainen, O. A.; Sillanpaa, M. E. T. *Analytical Chemistry* **2010**, *82*, 9594–9600.

[50] Makinen, M.; Nousiainen, M.; Sillanpaa, M. *Mass Spectrometry Reviews* **2011**, *30*, 940–973.

[51] Ewing, R.; Atkinson, D.; Eiceman, G.; Ewing, G. *Talanta* **2001**, *54*, 515–529.

[52] Cumeras, R.; Figueras, E.; Davis, C. E.; Baumbach, J. I.; Gracia, I. *Analyst* **2015**, *140*, 1376–1390.

[53] Cumeras, R.; Figueras, E.; Davis, C. E.; Baumbach, J. I.; Gracia, I. *Analyst* **2015**, *140*, 1391–1410.

[54] Langevin, P. *Annales de Chimie et de Physique* **1905**, *5*, 245–288.

[55] Revercomb, H. E.; Mason, E. A. *Analytical Chemistry* **1975**, *47*, 970–983.

[56] Mason, E. A.; McDaniel, E. W. *Transport properties of ions in gases*; Wiley: New York, 1988.

[57] Einstein, A. *Annalen der Physik* **1905**, *322*, 549–560.

[58] Sleno, L.; Volmer, D. *Journal of Mass Spectrometry* **2004**, *39*, 1091–1112.

[59] Demtröder, W. *Atoms, Molecules and Photons: An Introduction to Atomic-, Molecular- and Quantum Physics*; Springer, 2010.

[60] Reilly, J. P. *Mass Spectrometry Reviews* **2009**, *28*, 425–447.

[61] McLuckey, S. A. *Journal of the American Society for Mass Spectrometry* **1992**, *3*, 599–614.

[62] Lehmann, K. K.; Scoles, G.; Pate, B. H. *Annual Review of Physical Chemistry* **1994**, *45*, 241–274.

[63] Paizs, B.; Suhai, S. *Mass Spectrometry Reviews* **2005**, *24*, 508–548.

[64] Roepstorff, P.; Fohlman, J. *Biomedical Mass Spectrometry* **1984**, *11*, 601.

[65] Polfer, N. C.; Oomens, J. *Mass Spectrometry Reviews* **2009**, *28*, 468–494.

[66] Black, J. G.; Yablonovitch, E.; Bloembergen, N.; Mukamel, S. *Physical Review Letters* **1977**, *38*, 1131–1134.

[67] Choi, K. M.; Yoon, S. H.; Sun, M.; Oh, J. Y.; Moon, J. H.; Kim, M. S. *Journal of the American Society for Mass Spectrometry* **2006**, *17*, 1643–1653.

[68] Bari, S.; Gonzalez-Magana, O.; Reitsma, G.; Werner, J.; Schippers, S.; Hoekstra, R.; Schlathölter, T. *Journal of Chemical Physics* **2011**, *134*.

[69] Burke, N. L.; Redwine, J. G.; Dean, J. C.; McLuckey, S. A.; Zwier, T. S. *International Journal of Mass Spectrometry* **2015**, *378*, 196–205.

[70] Bowers, W. D.; Delbert, S. S.; Hunter, R. L.; McIver, R. T. *Journal of the American Chemical Society* **1984**, *106*, 7288–7289.

[71] Ly, T.; Julian, R. *Angewandte Chemie* **2009**, *48*, 7130–7137.

[72] Shaw, J. B.; Li, W.; Holden, D. D.; Zhang, Y.; Griep-Raming, J.; Fellers, R. T.; Early, B. P.; Thomas, P. M.; Kelleher, N. L.; Brodbelt, J. S. *Journal of the American Chemical Society* **2013**, *135*, 12646–12651.

[73] O'Brien, J. P.; Li, W.; Zhang, Y.; Brodbelt, J. S. *Journal of the American Chemical Society* **2014**, *136*, 12920–12928.

[74] Moore, J. H.; Coplan, M. A.; Davis, C. C. *Building scientific apparatus: a practical guide to design and construction*; Addison-Wesley: London, 1983.

[75] Dole, M.; Mack, L. L.; Hines, R. L. *Journal of Chemical Physics* **1968**, *49*, 2240–2249.

[76] Fenn, J. B.; Mann, M.; Meng, C. K.; Wong, S. F.; Whitehouse, C. M. *Science* **1989**, *246*, 64–71.

[77] Fenn, J. B. *Angewandte Chemie* **2003**, *42*, 3871–3894.

[78] Smith, D. P. H. *IEEE Transactions on Industry Applications* **1986**, *22*, 527–535.

[79] Kebarle, P.; Verkerk, U. H. *Mass Spectrometry Reviews* **2009**, *28*, 898–917.

[80] Wilm, M.; Mann, M. *Analytical Chemistry* **1996**, *68*, 1–8.

[81] Lord Rayleigh, F. R. S. *Philosophical Magazine Series 5* **1882**, *14*, 184–186.

[82] Kebarle, P. *Journal of Mass Spectrometry* **2000**, *35*, 804–817.

[83] Valascovic, G. A.; Kelleher, N. L.; Little, D. P.; Aaserud, D. J.; McLafferty, F. W. *Analytical Chemistry* **1995**, *67*, 3802–3805.

[84] Wende, T.; Ph.D. thesis; Freie Universität Berlin; 2012.

[85] Hernandez, H.; Robinson, C. V. *Nature Protocols* **2007**, *2*, 715–726.

[86] Heine, N.; Ph.D. thesis; Freie Universität Berlin; 2014.

[87] Kelly, R. T.; Tolmachev, A. V.; Page, J. S.; Tang, K.; Smith, R. D. *Mass Spectrometry Reviews* **2010**, *29*, 294–312.

[88] Douglas, D.; Frank, A.; Mao, D. *Mass Spectrometry Reviews* **2005**, *24*, 1–29.

[89] Wester, R. *Journal of Physics B - Atomic Molecular and Optical Physics* **2009**, *42*, 1–12.

[90] Friedburg, H.; Paul, W. *Naturwissenschaften* **1951**, *38*, 159–160.

[91] Bennewitz, H. G.; Paul, W.; Schlier, C. *Zeitschrift für Physik* **1955**, *141*, 6–15.

[92] Paul, W.; Reinhard, H. P.; von Zahn, U. *Zeitschrift für Physik* **1958**, *152*, 143–182.

[93] Paul, W. *Reviews of Modern Physics* **1990**, *62*, 531–542.

[94] Earnshaw, S. *Transactions of the Cambridge Philosophical Society* **1842**, *7*, 97.

[95] Jackson, J. D. *Classical Electrodynamics*, 3rd ed.; John Wiley & Sons, 1998.

[96] Gerlich, D. *Advances in Chemical Physics* **1992**, *82*, 1–176.

[97] Abramowitz, M.; Stegun, I. A. *Handbook of Mathematical Functions with Formulas, Graphs, and Mathematical Tables*; Dover Publications Inc., 1972.

[98] Vedel, F. *International Journal of Mass Spectrometry and Ion Processes* **1991**, *106*, 33–61.

[99] Prestage, J. D.; Williams, A.; Maleki, L.; Djomehri, M. J.; Harabetian, E. *Physical Review Letters* **1991**, *66*, 2964–2967.

[100] Dehmelt, H. G. *Advances in Atomic and Molecular Physics* **1967**, *3*, 54–72.

[101] Shaffer, S.; Tang, K.; Anderson, G.; Prior, D.; Udseth, H.; Smith, R. *Rapid Communications in Mass Spectrometry* **1997**, *11*, 1813–1817.

[102] Tolmachev, A.; Kim, T.; Udseth, H.; Smith, R.; Bailey, T.; Futrell, J. *International Journal of Mass Spectrometry* **2000**, *203*, 31–47.

[103] Warnke, S.; Diploma thesis; Eberhard Karls Universität Tübingen; 2010.

[104] Wiley, W. C.; McLaren, I. H. *Review of Scientific Instruments* **1955**, *26*, 1150–1157.

[105] Demtröder, W. *Experimentalphysik 2: Elektrizität und Optik*; Springer-Verlag Berlin, 2013; Vol. 6.

[106] Fernandez-Lima, F. A.; Becker, C.; Gillig, K.; Russell, W. K.; Chaer Nascimento, M. A.; Russell, D. H. *Journal of Physical Chemistry A* **2008**, *112*, 11061–11066.

[107] Maier-Borst, M.; Löffler, P.; Petry, J.; Kreisle, D. *Zeitschrift Für Physik D – Atoms Molecules and Clusters* **1997**, *40*, 476–478.

[108] Hoaglund, C.; Valentine, S.; Sporleder, C.; Reilly, J.; Clemmer, D. *Analytical Chemistry* **1998**, *70*, 2236–2242.

[109] Hopper, J. T. S.; Oldham, N. J. *Journal of the American Society for Mass Spectrometry* **2009**, *20*, 1851–1858.

[110] Niu, S.; Ruotolo, B. T. *Protein Science* **2015**, *24*, 1272–1281.

[111] Tolmachev, A.; Vilkov, A.; Bogdanov, B.; Pasa-Tolic, L.; Masselon, C.; Smith, R. *Journal of the American Society for Mass Spectrometry* **2004**, *15*, 1616–1628.

[112] Shi, H.; Atlasevich, N.; Merenbloom, S. I.; Clemmer, D. E. *Journal of the American Society for Mass Spectrometry* **2014**, *25*, 2000–2008.

[113] Myung, S.; Badman, E. R.; Lee, Y. J.; Clemmer, D. E. *The Journal of Physical Chemistry A* **2002**, *106*, 9976–9982.

[114] Badman, E. R.; Hoaglund-Hyzer, C. S.; Clemmer, D. E. *Analytical Chemistry* **2001**, *73*, 6000–6007.

[115] Jeffreys, H.; Jeffreys, B. *Methods of Mathematical Physics*, 3rd ed.; Cambridge University Press, 1999.

[116] Nolting, W. *Grundkurs Theoretische Physik 2: Analytische Mechanik*; Springer Berlin Heidelberg New York, 2006.

[117] McNeil, B. W. J.; Thompson, N. R. *Nature Photonics* **2010**, *4*, 814–821.

[118] Ullrich, J.; Rudenko, A.; Moshammer, R. *Annual Review of Physical Chemistry* **2012**, *63*, 635–660.

[119] Jefferson Lab, Free Electron Laser. Retrieved from https://www.jlab.org/FEL.

[120] Whitney, R.; Douglas, D.; Neil, G.; 2005; Airborne megawatt class free-electron laser for defense and security. United States. Retrieved from http://www.osti.gov/scitech/servlets/purl/841301.

[121] Wieland Schöllkopf, *private communication*, 2015.

[122] Schöllkopf, W.; Gewinner, S.; Junkes, H.; Paarmann, A.; von Helden, G.; Bluem, H.; Todd, A. M. M.; The new IR and THz FEL Facility at the Fritz Haber Institute in Berlin. *Proceedings of SPIE 2015*, Prague, Czech Republic, April 13-16, 2015.

[123] Onuki, H.; Elleaume, P. *Wigglers, Undulators and their Applications*; Taylor & Francis, 2003.

[124] Marshall, T. *Free Electron Lasers*; Macmillan Publishing Company, 1985.

[125] Oomens, J.; Tielens, A.; Sartakov, B.; von Helden, G.; Meijer, G. *Astrophysical Journal* **2003**, *591*, 968–985.

[126] Pringle, S. D.; Giles, K.; Wildgoose, J. L.; Williams, J. P.; Slade, S. E.; Thalassinos, K.; Bateman, R. H.; Bowers, M. T.; Scrivens, J. H. *International Journal of Mass Spectrometry* **2007**, *261*, 1–12.

[127] Giles, K.; Williams, J. P.; Campuzano, I. *Rapid Communications in Mass Spectrometry* **2011**, *25*, 1559–1566.

[128] Merenbloom, S. I.; Flick, T. G.; Williams, E. R. *J. Am. Soc. Mass Spectrom.* **2012**, *23*, 553–62.

[129] Benesch, J. L. P.; Ruotolo, B. T.; Simmons, D. A.; Robinson, C. V. *Chemical Reviews* **2007**, *107*, 3544–3567.

[130] Hilton, G. R.; Benesch, J. L. P. *Journal of the Royal Society Interface* **2012**, *9*, 801–816.

[131] Shelimov, K. B.; Clemmer, D. E.; Hudgins, R. R.; Jarrold, M. F. *Journal of the American Chemical Society* **1997**, *119*, 2240–2248.

[132] Julian, R.; Beauchamp, J. *International Journal of Mass Spectrometry* **2001**, *210*, 613–623.

[133] Cunniff, J.; Vouros, P. *Journal of the American Society for Mass Spectrometry* **1995**, *6*, 1175–1182.

[134] Julian, R.; Ly, T. *Journal of the American Society for Mass Spectrometry* **2006**, *17*, 1209–15.

[135] Hilderbrand, A. E.; Myung, S.; Clemmer, D. E. *Analytical Chemistry* **2006**, *78*, 6792–6800.

[136] Weimann, D. P.; Winkler, H. D. F.; Falenski, J. A.; Koksch, B.; Schalley, C. A. *Nature Chemistry* **2009**, *1*, 573–577.

[137] Wyttenbach, T.; Bowers, M. *Gas-phase conformations: The ion mobility/ion chromatography method*; Topics in Current Chemistry, Vol. 225; Springer-Verlag Berlin, 2003.

[138] Uetrecht, C.; Rose, R. J.; van Duijn, E.; Lorenzen, K.; Heck, A. J. R. *Chemical Society Reviews* **2010**, *39*, 1633–1655.

[139] Horn, D. M.; Breuker, K.; Frank, A. J.; McLafferty, F. W. *Journal of the American Chemical Society* **2001**, *123*, 9792–9799.

[140] Koeniger, S. L.; Merenbloom, S. I.; Clemmer, D. E. *Journal of Physical Chemistry B* **2006**, *110*, 7017–7021.

[141] Ruotolo, B. T.; Benesch, J. L. P.; Sandercock, A. M.; Hyung, S.-J.; Robinson, C. V. *Nature Protocols* **2008**, *3*, 1139–1152.

[142] Scarff, C. A.; Thalassinos, K.; Hilton, G. R.; Scrivens, J. H. *Rapid Communications in Mass Spectrometry* **2008**, *22*, 3297–3304.

[143] Bush, M. F.; Hall, Z.; Giles, K.; Hoyes, J.; Robinson, C. V.; Ruotolo, B. T. *Analytical Chemistry* **2010**, *82*, 9557–9565.

[144] Shelimov, K. B.; Jarrold, M. F. *Journal of the American Chemical Society* **1996**, *118*, 10313–10314.

[145] Li, J.; Taraszka, J. A.; Counterman, A. E.; Clemmer, D. E. *International Journal of Mass Spectrometry* **1999**, *185-187*, 37–47.

[146] Morsa, D.; Gabelica, V.; De Pauw, E. *Analytical Chemistry* **2011**, *83*, 5775–5782.

[147] Kupser, P.; Pagel, K.; Oomens, J.; Polfer, N.; Koksch, B.; Meijer, G.; Helden, G. v. *Journal of the American Chemical Society* **2010**, *132*, 2085–2093.

[148] Dettmer, K.; Aronov, P. A.; Hammock, B. D. *Mass Spectrometry Reviews* **2007**, *26*, 51–78.

[149] Syka, J. E.; Coon, J. J.; Schroeder, M. J.; Shabanowitz, J.; Hunt, D. F. *Proceedings of the National Academy of Sciences of the United States of America* **2004**, *101*, 9528–9533.

[150] Zubarev, R. A.; Kelleher, N. L.; McLafferty, F. W. *Journal of the American Chemical Society* **1998**, *120*, 3265–3266.

[151] Ledvina, A. R.; McAlister, G. C.; Gardner, M. W.; Smith, S. I.; Madsen, J. A.; Schwartz, J. C.; Stafford, J., G. C.; Syka, J. E.; Brodbelt, J. S.; Coon, J. J. *Angewandte Chemie* **2009**, *48*, 8526–8.

[152] Guan, Z.; Kelleher, N. L.; O'Connor, P. B.; Aaserud, D. J.; Little, D. P.; McLafferty, F. W. *International Journal of Mass Spectrometry and Ion Processes* **1996**, *157-158*, 357–364.

[153] Zhang, Z.; Browne, S. J.; Vachet, R. W. *Journal of the American Society for Mass Spectrometry* **2014**, *25*, 604–613.

[154] Hall, Z.; Robinson, C. V. *Journal of the American Society for Mass Spectrometry* **2012**, *23*, 1161–1168.

[155] Lanucara, F.; Holman, S. W.; Gray, C. J.; Eyers, C. E. *Nature Chemistry* **2014**, *6*, 281–294.

[156] Segev, E.; Wyttenbach, T.; Bowers, M. T.; Gerber, R. B. *Physical Chemistry Chemical Physics* **2008**, *10*, 3077–3082.

[157] Hess, B.; Kutzner, C.; van der Spoel, D.; Lindahl, E. *Journal of Chemical Theory and Computation* **2008**, *4*, 435–447.

[158] Lindorff-Larsen, K.; Piana, S.; Palmo, K.; Maragakis, P.; Klepeis, J. L.; Dror, R. O.; Shaw, D. E. *Proteins* **2010**, *78*, 1950–1958.

[159] Bussi, G.; Donadio, D.; Parrinello, M. *Journal of Chemical Physics* **2007**, *126*, 014101.

[160] Brutscher, B.; Bruschweiler, R.; Ernst, R. R. *Biochemistry* **1997**, *36*, 13043–13053.

[161] Freitas, M. A.; Hendrickson, C. L.; Emmett, M. R.; Marshall, A. G. *International Journal of Mass Spectrometry* **1999**, *185-187*, 565–575.

[162] Wilkinson, K. D.; Mayer, A. N. *Archives of Biochemistry and Biophysics* **1986**, *250*, 390–399.

[163] Pan, Y.; Briggs, M. S. *Biochemistry* **1992**, *31*, 11405–11412.

[164] Badman, E. R.; Hoaglund-Hyzer, C. S.; Clemmer, D. E. *Journal of the American Society for Mass Spectrometry* **2002**, *13*, 719–723.

[165] Pierson, N. A.; Chen, L.; Russell, D. H.; Clemmer, D. E. *Journal of the American Chemical Society* **2013**, *135*, 3186–3192.

[166] Breci, L. A.; Tabb, D. L.; Yates, r., J. R.; Wysocki, V. H. *Analytical Chemistry* **2003**, *75*, 1963–1971.

[167] Kim, P. *Annual Review of Biochemistry* **1990**, *59*, 631–660.

[168] Briggs, M. S.; Roder, H. *Proceedings of the National Academy of Sciences of the United States of America* **1992**, *89*, 2027–2021.

[169] Nall, B. T. *Comments on Molecular and Cellular Biophysics* **1985**, *3*, 123–143.

[170] Counterman, A. E.; Clemmer, D. E. *Analytical Chemistry* **2002**, *74*, 1946–1951.

[171] Baldauf, C.; Pagel, K.; Warnke, S.; von Helden, G.; Koksch, B.; Blum, V.; Scheffler, M. *Chemistry A European Journal* **2013**, *19*, 11224–11234.

[172] Cordier, F.; Grzesiek, S. *Biochemistry* **2004**, *43*, 11295–112301.

[173] Kony, D. B.; Hunenberger, P. H.; van Gunsteren, W. F. *Protein Science* **2007**, *16*, 1101–1118.

[174] Shvartsburg, A. A.; Jarrold, M. F. *Chemical Physics Letters* **1996**, *261*, 86–91.

[175] Pal, D.; Chakrabarti, P. *Journal of Molecular Biology* **1999**, *294*, 271–288.

[176] Vijay-Kumar, S.; Bugg, C. E.; Cook, W. J. *Journal of Molecular Biology* **1987**, *194*, 531–544.

[177] Vaisar, T.; Urban, J. *Journal of Mass Spectrometry* **1996**, *31*, 1185–1187.

[178] Reid, G. E.; Wu, J.; Chrisman, P. A.; Wells, J. M.; McLuckey, S. A. *Analytical Chemistry* **2001**, *73*, 3274–81.

[179] Breuker, K.; Oh, H.; Horn, D. M.; Cerda, B. A.; McLafferty, F. W. *Journal of the American Chemical Society* **2002**, *124*, 6407–6420.

[180] Zhang, H.; Cui, W.; Wen, J.; Blankenship, R. E.; Gross, M. L. *Analytical Chemistry* **2011**, *83*, 5598–5606.

[181] Canon, F.; Milosavljevic, A. R.; van der Rest, G.; Refregiers, M.; Nahon, L.; Sarni-Manchado, P.; Cheynier, V.; Giuliani, A. *Angewandte Chemie* **2013**, *52*, 8377–8381.

[182] Pierson, N. A.; Clemmer, D. E. *International Journal of Mass Spectrometry* **2015**, *377*, 646–654.

[183] Hille, B. *The Journal of General Physiology* **1977**, *69*, 497–515.

[184] Schwarz, W.; Palade, P. T.; Hille, B. *Biophysical Journal* **1977**, *20*, 343–368.

[185] Nardi, A.; Damann, N.; Hertrampf, T.; Kless, A. *ChemMedChem* **2012**, *7*, 1712–1740.

[186] Hille, B. *Ion Channels of Excitable Membranes*, 3rd ed.; Sinauer Associates, 2001.

[187] Lipkind, G. M.; Fozzard, H. A. *Molecular Pharmacology* **2005**, *68*, 1611–1622.

[188] Boiteux, C.; Vorobyov, I.; French, R. J.; French, C.; Yarov-Yarovoy, V.; Allen, T. W. *Proceedings of the National Academy of Sciences of the United States of America* **2014**, *111*, 13057–13062.

[189] Ávila, C. M.; Martínez, F. *Journal of Solution Chemistry* **2002**, *31*, 975–985.

[190] Tikhonov, D. B.; Bruhova, I.; Zhorov, B. S. *FEBS Letters* **2006**, *580*, 6027–6032.

[191] Schöllkopf, W.; et al.; The New IR FEL Facility at the Fritz-Haber-Institut in Berlin. *Proceedings of FEL 2014*, Basel, Switzerland, August 25-29, 2014; WEB04.

[192] *TURBOMOLE V6.6 2014*, a development of University of Karlsruhe and Forschungszentrum Karlsruhe GmbH, 1989-2007, TURBOMOLE GmbH, since 2007; available from `http://www.turbomole.com`.

[193] Klamt, A.; Schüürmann, G. *Journal of the Chemical Society, Perkin Transactions 2* **1993**, 799.

[194] Bleiholder, C.; Wyttenbach, T.; Bowers, M. T. *International Journal of Mass Spectrometry* **2011**, *308*, 1–10.

[195] Anderson, S. E.; Bleiholder, C.; Brocker, E. R.; Stang, P. J.; Bowers, M. T. *International Journal of Mass Spectrometry* **2012**, *330-332*, 78–84.

[196] Bleiholder, C.; Contreras, S.; Do, T. D.; Bowers, M. T. *International Journal of Mass Spectrometry* **2013**, *345-347*, 89–96.

[197] Bleiholder, C.; Contreras, S.; Bowers, M. T. *International Journal of Mass Spectrometry* **2013**, *354-355*, 275–280.

[198] Mesleh, M. F.; Hunter, J. M.; Shvartsburg, A. A.; Schatz, G. C.; Jarrold, M. F. *The Journal of Physical Chemistry* **1996**, *100*, 16082–16086.

[199] Campuzano, I.; Bush, M. F.; Robinson, C. V.; Beaumont, C.; Richardson, K.; Kim, H.; Kim, H. I. *Analytical Chemistry* **2012**, *84*, 1026–1033.

[200] Kebarle, P.; Peschke, M. *Analytica Chimica Acta* **2000**, *406*, 11–35.

[201] Tian, Z.; Kass, S. *Angewandte Chemie* **2009**, *121*, 1347–1349.

[202] Schmidt, J.; Meyer, M. M.; Spector, I.; Kass, S. R. *Journal of Physical Chemistry A* **2011**, *115*, 7625–7632.

[203] Campbell, J. L.; Le Blanc, J. C.; Schneider, B. B. *Analytical Chemistry* **2012**, *84*, 7857–7864.

[204] Tian, Z.; Wang, X. B.; Wang, L. S.; Kass, S. R. *Journal of the American Chemical Society* **2009**, *131*, 1174–1181.

[205] Steill, J. D.; Oomens, J. *Journal of the American Chemical Society* **2009**, *131*, 13570–13571.

[206] Schröder, D.; Budesinsky, M.; Roithova, J. *Journal of the American Chemical Society* **2012**, *134*, 15897–15905.

[207] Hoadlund-Hyzer, C.; Li, J.; Clemmer, D. *Analytical Chemistry* **2000**, *72*, 2737–2740.

[208] Lalli, P. M.; Iglesias, B. A.; Toma, H. E.; de Sa, G. F.; Daroda, R. J.; Silva Filho, J. C.; Szulejko, J. E.; Araki, K.; Eberlin, M. N. *Journal of Mass Spectrometry* **2012**, *47*, 712–719.

[209] Bowers, M. T.; Thanh, D. D. *Analytical Chemistry* **2015**, *87*, 4245–4252.

[210] von Helden, G.; Hsu, M. T.; Gotts, N.; Bowers, M. T. *The Journal of Physical Chemistry* **1993**, *97*, 8182–8192.

[211] Wyttenbach, T.; Helden, G.; Batka, J. J.; Carlat, D.; Bowers, M. T. *Journal of the American Society for Mass Spectrometry* **1997**, *8*, 275–282.

[212] Tang, M.; Isbell, J.; Hodges, B.; Brodbelt, J. *Journal of Mass Spectrometry* **1995**, *30*, 977–984.

[213] Chang, T. M.; Prell, J. S.; Warrick, E. R.; Williams, E. R. *Journal of the American Chemical Society* **2012**, *134*, 15805–15813.

[214] Lapthorn, C.; Dines, T. J.; Chowdhry, B. Z.; Perkins, G. L.; Pullen, F. S. *Rapid Communications in Mass Spectrometry* **2013**, *27*, 2399–2410.

[215] Caughey, B.; Lansbury, P. *Annual Review of Neuroscience* **2003**, *26*, 267–298.

[216] Walsh, D.; Klyubin, I.; Fadeeva, J.; Cullen, W.; Anwyl, R.; Wolfe, M.; Rowan, M.; Selkoe, D. *Nature* **2002**, *416*, 535–539.

[217] Goedert, M.; Spillantini, M. G. *Science* **2006**, *314*, 777–781.

[218] Lesne, S.; Koh, M.; Kotilinek, L.; Kayed, R.; Glabe, C.; Yang, A.; Gallagher, M.; Ashe, K. *Nature* **2006**, *440*, 352–357.

[219] Winner, B.; et al. *Proceedings of the National Academy of Sciences of the United States of America* **2011**, *108*, 4194–4199.

[220] Lin, C.-Y.; Gurlo, T.; Kayed, R.; Butler, A. E.; Haataja, L.; Glabe, C. G.; Butler, P. C. *Diabetes* **2007**, *56*, 1324–1332.

[221] Gurlo, T.; Ryazantsev, S.; Huang, C.-j.; Yeh, M. W.; Reber, H. A.; Hines, O. J.; O'Brien, T. D.; Glabe, C. G.; Butler, P. C. *American Journal of Pathology* **2010**, *176*, 861–869.

[222] Chiti, F.; Dobson, C. M. *Annual Review of Biochemistry* **2006**, *75*, 333–366.

[223] Ivanova, M. I.; Sievers, S. A.; Sawaya, M. R.; Wall, J. S.; Eisenberg, D. *Proceedings of the National Academy of Sciences of the United States of America* **2009**, *106*, 18990–18995.

[224] Nelson, R.; Sawaya, M.; Balbirnie, M.; Madsen, A.; Riekel, C.; Grothe, R.; Eisenberg, D. *Nature* **2005**, *435*, 773–778.

[225] Stromer, T.; Serpell, L. *Microscopy Research and Technique* **2005**, *67*, 210–217.

[226] Sawaya, M. R.; Sambashivan, S.; Nelson, R.; Ivanova, M. I.; Sievers, S. A.; Apostol, M. I.; Thompson, M. J.; Balbirnie, M.; Wiltzius, J. J. W.; McFarlane, H. T.; Madsen, A. O.; Riekel, C.; Eisenberg, D. *Nature* **2007**, *447*, 453–457.

[227] Matthes, D.; Daebel, V.; Meyenberg, K.; Riedel, D.; Heim, G.; Diederichsen, U.; Lange, A.; de Groot, B. L. *Journal of Molecular Biology* **2014**, *426*, 362–376.

[228] Cerf, E.; Sarroukh, R.; Tamamizu-Kato, S.; Breydo, L.; Derclaye, S.; Dufrene, Y. F.; Narayanaswami, V.; Goormaghtigh, E.; Ruysschaert, J.-M.; Raussens, V. *Biochemical Journal* **2009**, *421*, 415–423.

[229] Soledad Celej, M.; Sarroukh, R.; Goormaghtigh, E.; Fidelio, G. D.; Ruysschaert, J.-M.; Raussens, V. *Biochemical Journal* **2012**, *443*, 719–726.

[230] Buchanan, L. E.; Dunkelberger, E. B.; Tran, H. Q.; Cheng, P.-N.; Chiu, C.-C.; Cao, P.; Raleigh, D. P.; de Pablo, J. J.; Nowick, J. S.; Zanni, M. T. *Proceedings of the National Academy of Sciences of the United States of America* **2013**, *110*, 19285–19290.

[231] Bernstein, S. L.; Dupuis, N. F.; Lazo, N. D.; Wyttenbach, T.; Condron, M. M.; Bitan, G.; Teplow, D. B.; Shea, J.-E.; Ruotolo, B. T.; Robinson, C. V.; Bowers, M. T. *Nature Chemistry* **2009**, *1*, 326–331.

[232] Dupuis, N. F.; Wu, C.; Shea, J.-E.; Bowers, M. T. *Journal of the American Chemical Society* **2011**, *133*, 7240–7243.

[233] Do, T. D.; LaPointe, N. E.; Economou, N. J.; Buratto, S. K.; Feinstein, S. C.; Shea, J.-E.; Bowers, M. T. *Journal of Physical Chemistry B* **2013**, *117*, 10759–10768.

[234] Do, T. D.; Economou, N. J.; Chamas, A.; Buratto, S. K.; Shea, J.-E.; Bowers, M. T. *Journal of Physical Chemistry B* **2014**, *118*, 11220–11230.

[235] Do, T. D.; LaPointe, N. E.; Sangwan, S.; Teplow, D. B.; Feinstein, S. C.; Sawaya, M. R.; Eisenberg, D. S.; Bowers, M. T. *Journal of Physical Chemistry B* **2014**, *118*, 7247–7256.

[236] Young, L. M.; Saunders, J. C.; Mahood, R. A.; Revill, C. H.; Foster, R. J.; Tu, L.-H.; Raleigh, D. P.; Radford, S. E.; Ashcroft, A. E. *Nature Chemistry* **2015**, *7*, 73–81.

[237] Zheng, X.; Liu, D.; Klaerner, F.-G.; Schrader, T.; Bitan, G.; Bowers, M. T. *Journal of Physical Chemistry B* **2015**, *119*, 4831–4841.

[238] Cai, S.; Singh, B. *Biochemistry* **2004**, *43*, 2541–2549.

[239] Caflisch, A. *Current Opinion in Chemical Biology* **2006**, *10*, 437–444.

[240] Hodyss, R.; Julian, R.; Beauchamp, J. *Chirality* **2001**, *13*, 703–706.

[241] Schalley, C.; Weis, P. *International Journal of Mass Spectrometry* **2002**, *221*, 9–19.

[242] Spencer, E. A. C.; Ly, T.; Julian, R. R. *International Journal of Mass Spectrometry* **2008**, *270*, 166–172.

[243] Atlasevich, N.; Holliday, A. E.; Valentine, S. J.; Clemmer, D. E. *Journal of Physical Chemistry B* **2012**, *116*, 11442–11446.

[244] Rizzo, T. R.; Stearns, J. A.; Boyarkin, O. V. *International Reviews in Physical Chemistry* **2009**, *28*, 481–515.

[245] González Flórez, A. I.; Ahn, D.-S.; Gewinner, S.; Schöllkopf, W.; von Helden, G. *Physical Chemistry Chemical Physics* **2015**, *17*, 21902–21911.

[246] Toennies, J.; Vilesov, A. *Angewandte Chemie* **2004**, *43*, 2622–2648.

List of Publications

Papers relating to this thesis:

Protein structure in the gas phase: The influence of side-chain microsolvation
S. Warnke, G. von Helden, and K. Pagel
J. Am. Chem. Soc. **2013**, *135*, 1177-1180.

Photodissociation of conformer-selected ubiquitin ions reveals site-specific cis/trans isomerization of proline peptide bonds
S. Warnke, C. Baldauf, M. T. Bowers, K. Pagel, and G. von Helden
J. Am. Chem. Soc. **2014**, *136*, 10308-10314.

Analyzing the higher order structure of proteins with conformer-selective ultraviolet photodissociation
S. Warnke, G. von Helden, and K. Pagel
Proteomics **2015**, *16*, 2804-2812.

Protomers of benzocaine: solvent and permittivity dependence
S. Warnke, J. Seo, J. Boschmans, F. Sobott, J. H. Scrivens, C. Bleiholder, M. T. Bowers, S. Gewinner, W. Schöllkopf, K. Pagel, and G. von Helden
J. Am. Chem. Soc. **2015**, *137*, 4236-4242 .

An infrared spectroscopy approach to follow β-sheet formation in peptide amyloid assemblies
J. Seo, W. Hoffmann, S. Warnke, X. Huang, S. Gewinner, W. Schöllkopf, M. T. Bowers, G. von Helden, and K. Pagel
2015, submitted for review.

Additional papers not directly related to this thesis

How cations change peptide structure
C. Baldauf, K. Pagel, S. Warnke, G. von Helden, B. Koksch, V. Blum, and M. Scheffler
Chem. Eur. J. **2013**, *19*, 11224-11234.

Exploring the conformational preferences of 20-residue peptides in isolation: Ac-Ala$_{19}$-Lys + H^{+} vs. Ac-Lys-Ala$_{19}$ + H^{+} and the current reach of DFT
F. Schubert, M. Rossi, C. Baldauf, K. Pagel, S. Warnke, G. von Helden, F. Filsinger, P. Kupser, G. Meijer, M. Salwiczek, B. Koksch, M. Scheffler, and V. Blum
Phys. Chem. Chem. Phys. **2015**, *17*, 7373-7385.

Native like helices in a specially designed beta peptide in the gas phase
F. Schubert, K. Pagel, M. Rossi, S. Warnke, M. Salwiczek, B. Koksch, G. von Helden, V. Blum, C. Baldauf, and M. Scheffler
Phys. Chem. Chem. Phys. **2015**, *17*, 5376-5385.

Online monitoring the isomerization of an azobenzene-based dendritic bolaamphiphile using ion mobility-mass spectrometry
L. H. Urner, B. N. S. Thota, O. Nachtigall, S. Warnke, G. von Helden, R. Haag, and K. Pagel
Chem. Commun. **2015**, *51*, 8801-8804.

Following the structural evolution of metallo-supramolecular [7]catenanes by ion mobility-mass spectrometry
K. Pagel, D. Sattler, S. P. Black, S. Warnke, A. R. Stefankiewicz, J. R. Nitschke, G. von Helden, and C. A. Schalley
2015, submitted for review.

Photooxygenation and Gas-Phase Reactivity of Multiply Threaded Pseudorotaxanes
K. Nowosinski, S. Warnke, K. Pagel,D. Komáromy, W. Jiang, and C. A. Schalley
2015, submitted for review.

Curriculum Vitae

Der Lebenslauf ist in der Online-Version aus Gründen des Datenschutzes nicht enthalten.

For reasons of data protection, the curriculum vitae is not included in the online version.

Acknowledgements

An dieser Stelle werde ich mich bei einigen Leuten bedanken, ohne die ich diese Doktorarbeit nicht, oder nicht in dieser Form hätte fertigstellen können. An erster Stelle stehen hier Gert von Helden und Kevin Pagel. Gert hatte mir schon als Diplomand größtes Vertrauen geschenkt, als er mir den Aufbau einer neuen Apparatur anvertraute. Seitdem habe ich viel gelernt, jedoch gab es bis zuletzt Laborsituationen in denen ausgedehnte Fehlersuchen nur durch Gerts Handauflegen gelöst werden konnten. Durch Kevin habe ich die ersten FEL Experimente miterlebt. Er dachte sich wahrscheinlich, dass ich neben der vielen Bastelei etwas Abwechselung vertragen könnte und nahm mich mit nach Nieuwegein zu FELIX. Dort konnte man des Nachts, während langer Messzeiten in Doppel- und Dreifachschichten, auf der Gerard Meijer-Brücke stehend, auch mal über anderes als Wissenschaft reflektieren. Es folgten etliche gemeinsame Projekte an denen Gert und Kevin gleichermaßen beteiligt waren, was deren Erfolg womöglich umso größer ausfallen ließ.

Das Alles konnte natürlich nur geschehen weil Gerard Meijer, als damaliger Direktor der Abteilung, den beiden Physikstudenten aus Tübingen (die er natürlich sofort als Pärchen entlarvt hatte) die Türen öffnete, um ihnen mit der außerordentlichen Infrastruktur seiner Abteilung die Anfertigung ihrer Abschlussarbeiten zu ermöglichen. Jedem, der diese durch Inga von Dölln und Andrea Braaker meisterlich organisierte Abteilung einmal betreten hat dürfte klar sein, dass diese Infrastruktur nicht nur materieller Natur ist, sondern auch eine große soziale Komponente anzubieten hat. Hinter der jeweils richtigen Tür findet man sowohl tatkräftige, als auch moralische Unterstützung bei Problemen aller Art. Davon konnte meine Arbeit substantiell profitieren. Das Experiment wäre nicht so weit gekommen, wenn nicht Wolfgang Erlebach oder Henrik Haak ein Auge (oder eine Schieblehre) über etliche Konstruktionszeichnungen hätten wandern lassen. Deren fachgerechte Umsetzung sei der Feinwerktechnik unter der damaligen Leitung von Horst Schwäricke gedankt. Wollte ich selbst den Hammer in die Hand nehmen, konnte ich mir von Manfred Erdmann und anschließend von Petrik Bischoff stets die passenden Nägel geben lassen. Sie hielten auch gleich die Zange bereit um die krummen Nägel wieder zu ziehen. Die ständige technische Unterstützung von Georg Hammer und Andreas Liedke sorgte darür, dass der Laboralltag reibungslos ablief. Für Spannung (auch für sehr abwechslungsreiche) sorgte Viktor Platschkowski, der mit den Kollegen im ELab die Lötkolben nie kalt werden lässt. Sandy Gewinner und Wieland Schöllkopf haben ebenfalls viel Energie für meine Experimente aufgebracht – in Form von Photonen. Diese kamen zu jeder Tages- und Nachtzeit um die Unbekannten meiner Moleküle näher zu beleuchten.

Auch auf die Laborbevölkerung – die Doktoranden und Postdocs – ist immer Verlass. Sei es für fachliche, oder auch vollkommen fachfremde Diskussionen. Insbesondere bin ich den Mitgliedern aus den Arbeitsgruppen von Gert und Kevin zu Dank verpflichtet. Waldemar Hoffmann und Jongcheol Seo[*] waren an Teilen dieser Arbeit direkt beteiligt. Ich bin sehr erleichtert, dass sie sich auch in Zukunft um meine auf den Namen *iMob* getaufte Maschine kümmern werden. Für die angenehme Gesellschaft im Büro war Johanna Hofmann verantwortlich. Nicht nur deswegen, sondern auch wegen der vielen Chemikalieneinkäufe war sie essenziell für das Gelingen dieser Arbeit. Dem Rest der Gruppe danke ich nicht zuletzt für das Korrekturlesen meiner Doktorarbeit.

Den externen Wissenschaftlern, wie z.B. Michael T. Bowers oder Frank Sobott, die entweder meine Arbeit durch ihre Besuche bereichert haben, mich in ihren Laboren haben arbeiten lassen, oder Details zu Versuchsaufbauten und Experimenten zu Verfüfung stellten, danke ich für ihre Kooperation.

Der langen Liste von Doktoranden, Postdocs und Gruppenleitern, die die Abteilung Molekülphysik mittlerweile verließen, all jenen die ich hier nannte, und all denjenigen, die ich aufgrund des Schlafentzuges nicht mehr im Gedächtnis hatte, verdanke ich eine unvergessliche Zeit. Euch danke ich von Herzen.

Und dann gibt es noch eine Person in dieser Abteilung, die eine besondere Rolle spielt. Mit ihr teile ich beinahe alle Erfahrungen seit Beginn meines Physikstudiums. Alle Höhen und Tiefen der letzten Jahre erlebte sie aus erster Hand, teilte Freud und Leid, und zeigte vor Allem sehr viel Verständnis. Dir, Ana Isabel González Flórez, möchte ich an dieser Stelle ganz besonders danken. Ich blicke gespannt auf unsere gemeinsame Zukunft.

Stephan Warnke
Berlin, Oktober 2015

---

[*] Sorry, no english. The bottom line is: Thank you!